First-Principles Studies of Complex Oxide Materials

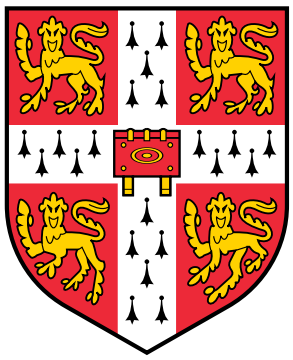

Can Philipp Koçer

Theory of Condensed Matter Group
Department of Physics
University of Cambridge

This thesis is submitted for the degree of
Doctor of Philosophy

King's College

May 2021

Declaration

I hereby declare that except where specific reference is made to the work of others, the contents of this dissertation are original and have not been submitted in whole or in part for consideration for any other degree or qualification in this, or any other university. This dissertation is my own work and contains nothing which is the outcome of work done in collaboration with others, except as specified in the text. This dissertation contains fewer than 60,000 words including abstract, tables, footnotes, and appendices and has fewer than 150 figures.

Chapter 3 is the outcome of "First-Principles Study of Localised and Delocalised Electronic States in Crystallographic Shear Phases of Niobium Oxide", Can P. Koçer, Kent J. Griffith, Clare P. Grey, Andrew J. Morris, *Phys. Rev. B*, **99**, 075151 (2019). I carried out all of the hands-on research for this chapter and the associated publication, and was the main author of the article.

Chapter 4 is based on "Cation Disorder and Lithium Insertion Mechanism of Wadsley–Roth Crystallographic Shear Phases from First Principles", Can P. Koçer, Kent J. Griffith, Clare P. Grey, Andrew J. Morris, *J. Am. Chem. Soc.*, **141**, 15121–34 (2019). I carried out the research and was the main author of the article.

Chapter 5 was published in "Lithium Diffusion in Niobium Tungsten Oxide Shear Structures", Can P. Koçer, Kent J. Griffith, Clare P. Grey, Andrew J. Morris, *Chemistry of Materials*, **32**, 3980–3989 (2020). I carried out the research and was the main author of the article.

Chapter 6 is the result of "Efficient lattice dynamics calculations for correlated materials using DFT+DMFT", Can P. Koçer, Kristjan Haule, G. Lucian Pascut, Bartomeu Monserrat, *Phys. Rev. B*, **102**, 245104 (2020). I carried out the research and was the main author of the article.

First-Principles Studies of Complex Oxide Materials

Can Philipp Koçer

Abstract

This thesis uses first-principles methods to study complex oxide materials. The first part of the thesis deals with complex oxide materials that have applications as lithium-ion battery electrodes. In the second part, a new method for the calculation of vibrational properties of correlated materials, specifically transition metal oxides, is developed.

After introducing the relevant background and computational methods in Chapters 1 and 2, three chapters are devoted to the study of Wadsley–Roth crystallographic shear phases. This family of niobium-based oxides has attracted significant attention due to their promise as high-rate lithium-ion battery electrodes. Chapter 3 is devoted to the study of the electronic structure and magnetism of niobium suboxides. An electronic structure analysis establishes the coexistence of flat and dispersive energy bands, corresponding to localised and delocalised electron states. These states are shown to be inherent features of the crystal structures. A localisation-delocalisation transition occurs as the structural capacity for localised electrons is exceeded. The results shed light on the experimentally observed electrical and magnetic properties of the niobium suboxides.

Chapter 4 examines cation disorder and lithium insertion mechanism of crystallographic shear phases, making use of an enumeration approach to generate sets of cation configurations and lithium-vacancy configurations. A three-step lithium insertion mechanism is revealed, discernible in the evolution of lattice parameters and the voltage profile. A predicted theoretical voltage curve is in good agreement with available experimental data. A distinctive change in the local structure is also discovered: transition metal oxygen octahedra become more symmetric on lithium insertion. The electronic structure behaves as expected for crystallographic shear phases, given the results of the previous chapter: small amounts of localised electrons are present during initial lithium insertion, but on further lithiation, metallicity results.

Chapter 5 investigates the lithium diffusion mechanism of niobium tungsten oxide shear structures. Building on the results of the previous two chapters, transition state searches and molecular dynamics simulations were used to obtain hopping barriers and diffusion coefficients. Overall, a quasi-1D diffusion mechanism is observed with low activation barriers (80–300 meV) and high diffusion coefficients (10^{-12}–10^{-11} m^2s^{-1}). Structure-property relationships for crystallographic shear phases are discussed in detail in relation to battery performance.

Chapter 6 develops a robust and efficient method to calculate phonons in correlated materials with DFT+DMFT. The method combines a DFT+DMFT force implementation with the direct method for lattice dynamics, using non-diagonal rather than diagonal supercells. In addition, a fixed self-energy approximation is proposed. The method is tested for a set of typical correlated materials, and shown to drastically reduce computational costs compared to previous work.

Acknowledgments

Over the last 3 1/2 years, I had the privilege of working with many amazing people, some of whom I would like to thank here. First I would like to thank my supervisor, Andrew Morris, for his support and for giving me a free hand in picking the topics I wanted to work on. I also especially want to thank Kent Griffith for introducing me to the fascinating field of complex niobium-based oxides, and the great collaboration we have established over the past years. I would like to thank Clare Grey for support during my work on complex oxides and many interesting discussions. My PhD would have been a lot less enjoyable without the members of the Morris group, and I specifically want to thank James Darby and Angela Harper for the fun and relaxed atmosphere in our office, and Matt Evans and Bora Karasulu for their help with many different issues. I would like to thank Tomeu Monserrat and the members of his group for allowing me to join them in group meetings and our collaboration on DMFT phonon calculations. Kristjan Haule and especially Lucian Pascut introduced me to the exciting field of dynamical mean field theory and correlated materials, and I want to thank them for our fruitful collaboration. Antonios Alvertis, Angela Harper, Jordan Dorrell, Annalena Genreith-Schriever, and James Darby were kind enough to proofread parts of this thesis. On a technical note, I would like to thank Dr Michael Rutter for his help with various computer-related issues.

At an institutional level, I would like to thank the Winton Programme for the Physics of Sustainability for providing a PhD studentship, and the Theory of Condensed Matter group for the welcoming work environment. Most of the research presented herein was done using generous allocations of computational resources on the HPC Midlands+ machine; 500,000 CPUhs for a start-up project in November and December 2017, 1.75M for a substantial project in the period January to June 2018, a Tier 2 Rapid Access allocation of 5M CPUhs for the period July 2018 – June 2019, and another Tier 2 Rapid Access allocation of 3M CPUhs for the period July 2019 – June 2020. A smaller fraction of the calculations were also performed on the UK supercomputer ARCHER, and on the Cambridge CSD3 machine.

Finally, I would like to thank my family, especially my parents, for their continued support over the years.

Table of Contents

List of Figures

List of Tables

Chapter 1

Introduction and Background

1.1 Overview

This thesis presents the results of research performed between October 2017 and May 2021 in the Theory of Condensed Matter Group of the Cavendish Laboratory, University of Cambridge.

The research presented herein is concerned with first-principles quantum mechanical studies of complex oxides. The first part of the thesis focuses on the Wadsley–Roth family of crystallographic shear phases, which have attracted significant attention due to their promise as lithium-ion battery electrodes. For these materials, the complexity arises from their large and hierarchical crystal structures that can host different metal cations. Interesting phenomena occur when these materials are electrochemically exposed to lithium. The last chapter of the thesis is concerned with the calculation of lattice dynamics and associated properties in oxides which show complex interplays between multiple degrees of freedom – atomic, electronic and magnetic.

The thesis is structured as follows: the remainder of this chapter summarises the background and context of the research, introducing relevant aspects of lithium-ion batteries, complex oxide battery materials, and the theory of correlated electron materials. **Chapter 2** describes the electronic structure methods used in this work, specifically density-functional theory and dynamical mean field theory. The next three chapters present the results of my research into the properties of complex niobium-based oxide materials: **Chapter 3** deals with the electronic structure of niobium suboxides Nb_2O_{5-x}, **Chapter 4** investigates structural aspects of complex niobium tungsten oxides and their lithium insertion mechanism, and **Chapter 5** examines lithium diffusion within these materials. In **Chapter 6**, a method for the calculation of lattice dynamics with DFT+DMFT is developed. Conclusions and possible directions for future research are presented in **Chapter 7**.

1.2 Motivation

The modern age presents our species with many challenges. Among the most difficult of these are climate change and ocean acidification, caused by carbon dioxide emissions from the combustion of fossil fuels. To prevent drastic changes to the ecology of our planet we are forced to revolutionise

our energy infrastructure. While the precise energy mix of the future is still being debated, a shift away from fossil fuels and towards renewables, such as solar and wind, is inevitable. The development of new and improved energy technologies facilitates this shift.

Any energy technology relies fundamentally on the availability of appropriate materials. Within a device, materials with specific properties are integrated into the working mechanism to perform specific functions. The goal of materials research is to find materials with better properties to perform these functions. In the present work, the focus is on materials for electrochemical energy storage, i.e. batteries. The lithium-ion battery is a breakthrough technology of the last century, enabling the portable electronics revolution. Devices such as cellphones and laptops are nowadays exclusively powered by lithium-ion batteries, due to their superior energy density as compared to other battery types. Governments worldwide have recognized the key role of electrochemical energy storage in the electrification of transport. The UK recently introduced the Faraday Institution to rise to this challenge [1]. Outside of consumer applications, electrochemical energy storage on the grid scale is projected to play a role in relieving the intermittency of renewable energy resources [2]. Many different materials have been proposed for use in batteries, with different chemistries for each application. However, the road from laboratory demonstration to commercialisation is long and difficult, involving multiple years of development.

Developing and improving materials is challenging because it is very difficult to 'see' what goes on inside a material during operation in a device. Experimental evidence is always indirect and can be hard to interpret. But for the human that does the research, 'seeing' is very much key to understanding. Material scientists, chemists and physicists have all been educated to think in terms of models of atomic and electronic structure. Interpreting the experimental data in terms of one of these models – or proposing a new one – is what constitutes understanding in this field. Computer simulations of materials play an important role in this regard by bridging the gap between experimental data and the underlying atomic and electronic mechanisms that give rise to the observed behaviour. Thanks to improvements in computer power and algorithmic efficiency, *ab initio* quantum mechanical calculations can nowadays be performed on a wide range of materials. The most popular technique used in condensed matter physics, materials science and chemistry is density-functional theory (DFT), which offers a good balance of accuracy and efficiency. The battery materials field is no exception in this regard. DFT calculations can provide insight into the electrochemical profile, structural evolution and ionic diffusion pathways of a material [3, 4]. Together with the experimental data, DFT calculations allow us to understand how a material works and to suggest strategies to improve its performance. Todays powerful supercomputers enable calculations to be performed in a high-throughput fashion, working with thousands, if not tens of thousands, of structures to compute properties or screen for a desired outcome. In this context, Chapters 3, 4, and 5 present results of computational simulations of complex oxide Wadsley–Roth phases, a family of promising battery anodes.

Taking a broader view of the computational materials physics field, it is clear that DFT is still the main workhorse. However, modelling certain classes of compounds and properties requires more advanced methods. For complex transition metal oxides in particular, the strong electron-electron interactions in *d*-orbitals pose problems for DFT. Combining DFT with dynamical mean

field theory (DMFT) results in an advanced electronic structure method capable of accurately modelling the electronic structure of correlated materials. However, as with most beyond-DFT methods, only some aspects of materials physics can be modelled. DMFT is usually limited to calculations of electronic structure, and does not allow the calculation of nuclear dynamics, for example phonons. This motivates the work presented in Chapter 7, where a method for the calculation of lattice dynamics with DFT+DMFT is developed.

1.3 Battery Science

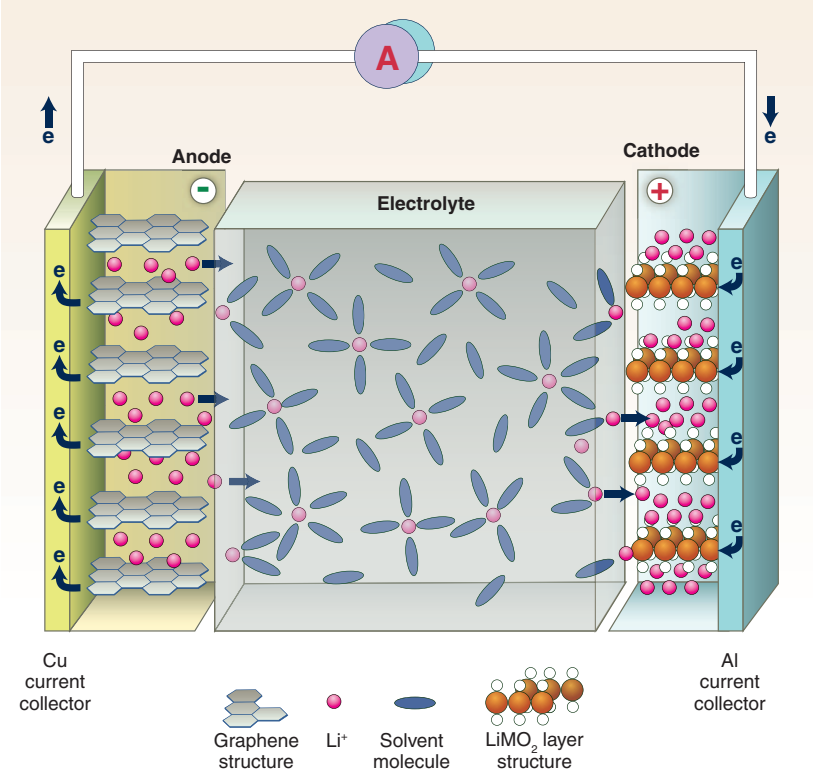

Figure 1.1: Operating principle of a Li-ion battery. During the discharge, both electrons and lithium ions flow from the anode to the cathode. Ions flow through the electrolyte while electrons flow through the external circuit. The anode is graphitic carbon and the cathode is $LiMO_2$ ($LiCoO_2$), a layered transition metal oxide. From Ref. [2], reproduced with permission from AAAS and based on public domain material in Ref. [5].

Operating Principle and Thermodynamics

A battery is an electrochemical device that stores energy. All batteries consist of three main parts; an anode, a cathode, and an electrolyte. The electrodes (anode and cathode) are electronically and ionically conductive, while the electrolyte only conducts ions. During the discharge of the battery, the active ions (lithium ions in lithium-ion batteries) flow from the anode to the cathode, passing through the electrolyte. The electrons flow through the external circuit and do work (Fig. 1.1). By separating the flow of ions and electrons, the chemical energy stored in the device is converted to

electrical energy. Transfer of lithium ions from anode to cathode produces a thermodynamically more stable arrangement of atoms and chemical bonds, reducing the Gibbs free energy of the system. The chemistry of the electrode materials determines the amount of charge that can be shuttled between the electrodes and the change in Gibbs free energy on doing so, which ultimately limits both the capacity and the operating potential of the cell. The cell reaction illustrated in Figure 1.1 – the same as in most portable electronic devices – is

$$\begin{aligned}
\text{Anode: } & \mathrm{LiC_6} \longrightarrow \mathrm{Li_{1-x}C_6} + x\,\mathrm{Li^+} + x\,\mathrm{e^-} \\
\text{Cathode: } & \mathrm{Li_{1-x}CoO_2} + x\,\mathrm{Li^+} + x\,\mathrm{e^-} \longrightarrow \mathrm{LiCoO_2} \\
\text{Full: } & \mathrm{LiC_6} + \mathrm{Li_{1-x}CoO_2} \longrightarrow \mathrm{Li_{1-x}C_6} + \mathrm{LiCoO_2}
\end{aligned}$$

Electrode materials are classified according to the changes they undergo during cycling [6]. Graphite and $\mathrm{LiCoO_2}$ (Fig. 1.1) are insertion electrode materials, as are the transition metal oxides that form the subject of later chapters. In such an insertion electrode, lithium ions are inserted into empty sites in the lattice and the material undergoes only small structural changes during operation. The lithium is ionised and the electron occupies empty states at the Fermi level. The second type, alloying electrodes such as phosphorus, show more pronounced structural changes on reaction with lithium [7]. Chemical bonds change and the materials undergo large volume expansion. A third type, conversion electrodes, consists of a binary transtion metal compound, $\mathrm{M_aX_b}$ which on reaction with lithium yields a microstructure composed of metallic nanoparticles in a matrix of $\mathrm{Li_yX}$. The vast majority of commercial devices use insertion electrodes, which are the subject of later chapters. Cathode materials are usually late first-row transition metal oxides. Common anode materials are graphitic carbon, main group alloying compounds such as silicon or germanium, or compounds of early or second-row transition metals. Organic liquids are the most prominent electrolyte, but solid state electrolytes are attracting attention for their improved safety characteristics.

The capacity of an electrode is the amount of charge that can be stored in a certain amount of mass or volume of material. The gravimetric capacity (in mAh/g) is calculated according to

$$\text{capacity} = \frac{zF}{M \cdot 3.6\ \text{C/mAh}} \tag{1.1}$$

where z is the number of electrons transferred during the reaction, F is the Faraday constant, and M is the molar mass of the electrode material. The volumetric capacity is found by multiplying the gravimetric capacity by the density of the material. The voltage V is determined by the combination of electrodes and generally changes over the course of the discharge. The energy stored in the battery is determined by the integral of the voltage over the charge q

$$\text{energy} = \int_0^Q V(q)\ dq \tag{1.2}$$

where Q is the total amount of charge stored in the battery. Normalising the energy by mass or volume of the materials (or the entire cell) gives the gravimetric or volumetric energy density. Note that all measures of battery performance are usually given in terms of mass/volume of

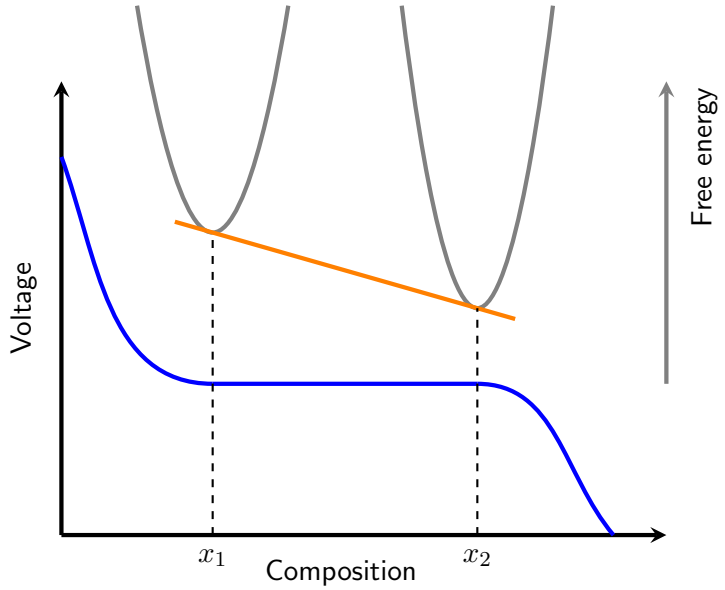

Figure 1.2: Voltage profile (blue) and free energy of two distinct phases (grey) during a first-order phase transition. The free energy of the system is minimized between x_1 and x_2 by forming a two-phase mixture, represented by the orange line (tangent to grey curves). The sloping parts at the start and end of discharge correspond to single-phase regions. Adapted from Ref. [9].

active electrode materials, without any binder material, electrolyte, or auxilliary cell components. Charge/discharge rates are usually given in terms of the C-rate, which is the number of times the battery can be fully discharged within one hour. For example, a rate of 10C would mean the discharge takes 6 minutes. If the capacity of the cell is 200 mAh/g, this implies a discharge current of 2000 mA/g. Voltage and rate are not independent of each other – at higher discharge rates the voltage of a battery will necessarily drop due to the development of an overpotential [8].

The reactions that take place in a battery are governed by both thermodynamic and kinetic factors. If the battery is discharged slowly enough, the reaction can be treated as taking place under equilibrium conditions. For a reaction

$$\delta x \ \mathrm{Li} + \mathrm{Li}_x\mathrm{A} \rightarrow \mathrm{Li}_{x+\delta x}\mathrm{A}$$

where A denotes an unspecified material reacting with lithium, the change in the Gibbs free energy per formula unit is

$$\Delta G = G(\mathrm{Li}_{x+\delta x}\mathrm{A}) - G(\mathrm{Li}_x\mathrm{A}) - \delta x \ G(\mathrm{Li}) \tag{1.3}$$

and the (open circuit) voltage V_{oc} measured between the two electrodes is given by

$$\Delta G = -nFV_{oc} \tag{1.4}$$

where n is the number of mols of charge that is transferred during the reaction, and F is the Faraday constant. Note that V_{oc} is the voltage measured if no current is allowed to flow and is therefore the change in the Gibbs free energy of the system per amount of charge. Since the Gibbs free energy and the voltage are directly related, thermodynamic quantities can be obtained from

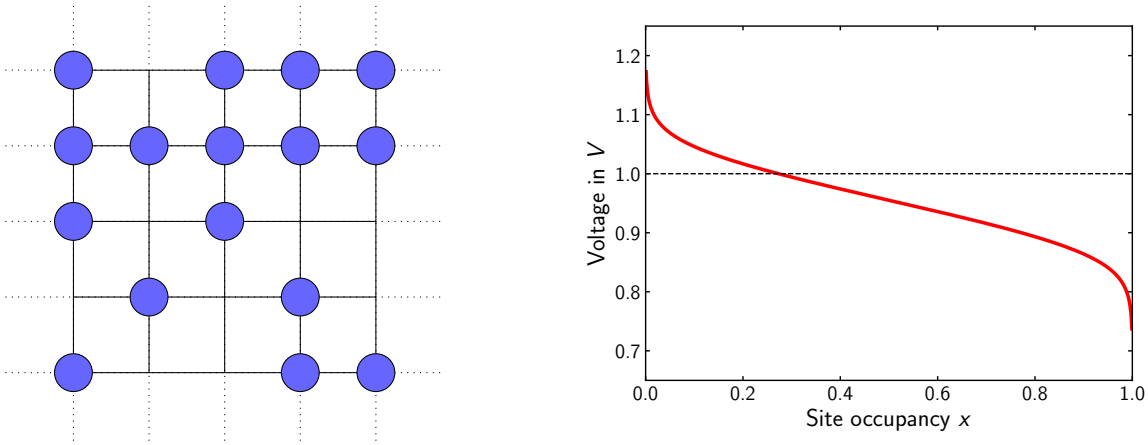

Figure 1.3: Lattice model for the chemical potential of a solid solution. The voltage is plotted for $\mu_0 = 0$ with $\epsilon = -1$ eV, $U = 90$ meV, and $k_B T = 25$ meV. The voltage drops below the single particle insertion energy before $x = 0.5$ due to the repulsive interaction U.

measurements of the voltage profile.

Two general features are commonly observed in voltage profiles: flat regions with constant voltage, and sloping regions where the voltage varies as a function of capacity (Fig. 1.2). Flat regions in voltage profiles mark the coexistence of two phases. Consider the region between the points x_1 and x_2 in Figure 1.2; the two grey half-curves between x_1 and x_2 represent the (hypothetical) free energies of the two phases, if they were to adopt compositions between those points. However, since the Gibbs free energy is a convex function of composition, its minimal value between x_1 and x_2 is given by the orange tangent. On the tangent the Gibbs free energy is $G = (1-f)G_1 + fG_2$, where f is the fraction of phase 2, and G_1 and G_2 are the Gibbs free energies of compositions x_1 and x_2. The tangent line has a constant slope, which results in a constant voltage within the region $x_1 < x < x_2$.

Sloping regions indicate the presence of a single phase, with a voltage that changes over the course of the discharge. Consider the voltage measured for an infinitesimal composition change δx

$$V_{oc} = -\frac{\Delta G}{nF} = \lim_{\delta x \to 0} -\frac{\Delta G}{\delta x} = \frac{1}{e}\left(\mu_0 - \lim_{\delta x \to 0} \frac{G(\mathrm{Li}_{x+\delta x}A) - G(\mathrm{Li}_x\mathrm{A})}{\delta x}\right) = \frac{\mu_0 - \mu(x)}{e} \tag{1.5}$$

where μ_0 is the chemical potential of bulk lithium and $\mu(x)$ is the chemical potential of lithium at the reacting electrode. In contrast to the previous case of a two phase reaction, lithium is inserted into a single phase for which the lithium chemical potential is changing as a function of composition x. This so-called solid solution behaviour is often observed in insertion electrodes. A simple model for a solid solution is the lattice gas [9]. In this model, we assume that insertion of a single lithium into an otherwise empty lattice leads to an energy decrease of ϵ. The lattice in question has N equivalent sites, which are randomly occupied by lithium atoms. For a fractional occupancy of x, the entropy is

$$S = k_B \ln(\Omega) = k_B \ln\left(\frac{N!}{(N - n_{\mathrm{Li}})!\; n_{\mathrm{Li}}!}\right) = -N k_B (x \ln(x) + (1-x)\ln(1-x)) \tag{1.6}$$

where $n_{\mathrm{Li}} = xN$ and we have used Stirling's approximation to simpify the expression. As $G = H - TS$, and $\mu_{\mathrm{Li}}(x) = \frac{dG}{dn_{\mathrm{Li}}}$, the entropy makes the following contribution to the chemical potential

$$-T\frac{dS}{dn_{\mathrm{Li}}} = -T\frac{1}{N}\frac{dS}{dx} = k_B T \ln\left(\frac{x}{1-x}\right) \tag{1.7}$$

Interaction between lithium atoms is modelled by a linear term Ux, where U represents the energy change per lithium if all sites of the lattice are occupied. In total, we have that

$$\mu_{\mathrm{Li}}(x) = \epsilon + Ux + k_B T \ln\left(\frac{x}{1-x}\right) \tag{1.8}$$

An example of the voltage profile of a solid solution is shown in Figure 1.3. In summary, a two-phase region is characterised by a flat part of the voltage profile, while single-phase solid solutions show a sloping voltage. The study of voltage profiles can provide information on the phase transitions that occur within materials during battery operation. This is demonstrated in Chapter 4, where the voltage profile of the Wadsley–Roth phases (exhibiting both solid-solution and two-phase reaction behaviour) is studied from first principles.

Experimental Characterisation

Electrochemical studies on battery materials provide both important performance data and information on the phase diagram as a function of charge state. However, the structural changes that occur inside a battery material can not be studied using electrochemistry alone. Techniques that can provide this information include X-ray (powder) diffraction (XRD), Nuclear magnetic resonance spectroscopy (NMR), and X-ray absorption spectroscopy (XAS). XRD measurements provide information on the crystal symmetry of phases and changes of lattice parameters during cycling. NMR measurements are very sensitive to the local atomic environment of the nucleus under study, and can in some cases be matched to specific atomic coordination numbers and oxidation states. XAS probes core-to-valence electronic transitions providing a wealth of information on both local geometric as well as electronic structure. All of these techniques can be performed *post mortem*, i.e. after disassembling the battery at a certain state of charge, or *in situ*, during operation of the device. NMR and *post mortem* XRD experiments can be done in a regular lab, while *in situ* XRD and all XAS experiments require powerful synchrotron beamlines. Often different behaviour is observed for *in situ* vs. *post mortem* – a testament to the fact that the cycling rate plays an important role in determining the phase transformation mechanism of the material.

Most of the experimental data acquired from these methods can be compared to first-principles DFT predictions of the same phenomena. This approach has been very successful in the study of alloying electrodes, such as lithium and sodium phosphide [7], lithium and sodium anodes of tin [10, 11], and the Li-FeS_2 conversion anode [12]. Of particular relevance to this work are XRD measurements and XANES (X-ray absorption near-edge structure) recorded on the Wadsley–Roth phases as a function of charge state, providing direct experimental information regarding the relationship between structural evolution and electrochemistry [13]. In Chapter 4, the mechanisms behind the local and long-range structural evolution of these materials are studied using first-

principles calculations, and linked to the electrochemical properties.

Kinetic Factors

The thermodynamic principles underlying battery operation have been described above. Kinetic factors are equally important, because the ability to quickly charge and discharge devices is crucial for most applications. Both electronic and ionic conductivity contribute to rate performance, and we shall discuss each in turn. Lithium is a highly electropositive element and thus usually exists as $Li^+ + e^-$ within solid-state materials. Both the ion and the electron need to be accommodated. In insertion electrodes, lithium ions occupy empty lattice positions, while the electrons fill the lowest energy unoccupied electronic states in the material. In transition metal oxide electrodes, these states are predominantly of transition metal d-orbital character. We can separate two cases in this regard: TMOs in which the d-orbitals form delocalised band-like states, and TMOs in which the d-orbitals remain atomic-like, with strong Coulomb repulsion between electrons in those orbitals [9]. If band states are filled by the electrons, the resulting material is a metal and shows good electronic conductivity, with the Fermi level shifting up and down depending on the charge state. In the case of localised d-orbitals, the electronic conductivity is often poor since the electrons cannot move freely through the material. There are a number of different effects that can lead to localisation: the material might be a Mott insulator, or the electrons are trapped as polarons. In Chapters 3 and 4, the electronic structure of n-doped Wadsley–Roth phases is examined, and we discover a coexistence of both types of electronic behaviour in those materials.

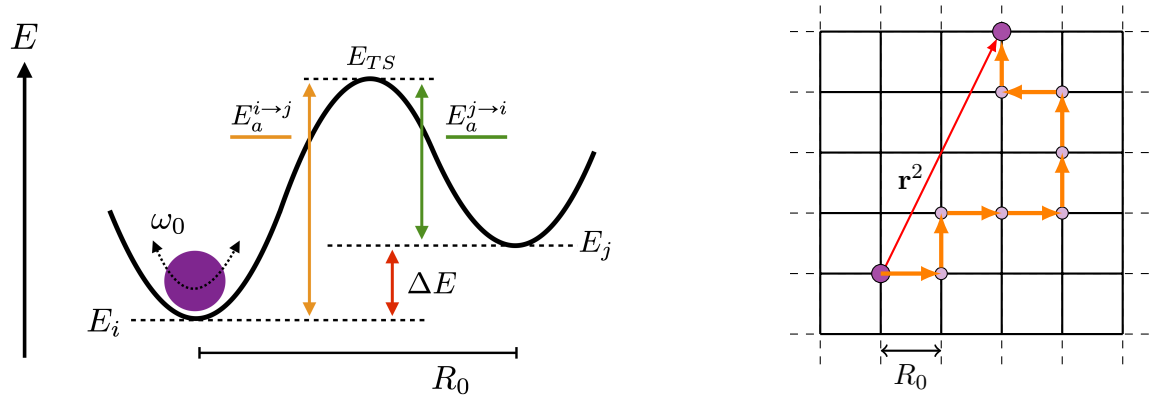

Figure 1.4: Schematic potential energy surface during ionic motion in solid-state materials. Two minima are separated by a real-space distance of R_0. Within each minimum the ion has a characteristic vibrational frequency ω_0. The activation energy E_a depends on the direction of the hop. On the right, a single particle is shown performing a single instance of a random walk on a 2D lattice.

High ionic conductivity is an essential requirement for all battery materials. A prerequisite for ionic motion is that the lattice is only partially filled, so that ions have an empty site next to them into which they can move. The rate of this process is governed by structure of the potential energy surface (PES) of the material. The typical shape of a PES for ion hopping is shown in Fig. 1.4, with two minima i and j corresponding to stable positions, and a maximum between them that is referred to as the transition state (TS) or activated complex. The calculation of reaction rates is a well-developed field of theoretical chemistry, and the most commonly used theory to calculate

rates in practice is transition-state theory (TST), a detailed description of which is available in Refs [14, 15]. For ionic motion, a simple expression is often used for the rate of hopping $\Gamma_{i\to j}$ from a site i to an adjacent site j

$$\Gamma_{i\to j} = A \cdot \exp\Big(-\frac{E_a^{i\to j}}{k_B T}\Big) \tag{1.9}$$

where E_a is the activation energy, k_B is Boltzmann's constant, T is the temperature, and A is a prefactor determined by TST. The prefactor contains the ratio of the partition functions of the transition state and the initial state, and is commonly approximated by a single attempt frequency ω_0 for ionic diffusion in solids. Note that the activation energy E_a is the potential energy difference between the transition state and the initial state, and therefore depends on the direction of hopping. If the two sites i and j have different potential energies, the $i \to j$ and $j \to i$ hops will have different rates. Under equilibrium conditions, the populations of sites i and j (P_i and P_j) are given by the Boltzmann distribution $P_j/P_i = \exp(-\frac{\Delta E}{k_B T})$, and rates and populations satisfy the detailed balance condition $P_i \cdot \Gamma_{i\to j} = P_j \cdot \Gamma_{j\to i}$. Given the exponential dependence of the rate on the activation energy and the temperature, it is common to ignore the prefactor and discuss ion kinetics in terms of the magnitude of the activation energy alone.

Diffusion of particles on a lattice can be described as a random walk (Fig. 1.4). For a single particle diffusing on a 2D square lattice (Fig. 1.4) the walk consists of a sequence of N steps $R_{0,i}$ where $i = 1, ..., N$. The quantity we are interested in is the mean squared displacement as a function of time $\langle \mathbf{r}^2(t)\rangle$:

$$\begin{aligned}\langle \mathbf{r}^2(t)\rangle &= \Big\langle \Big(\sum_{i=1}^{N} \mathbf{R}_{0,i}\Big) \cdot \Big(\sum_{j=1}^{N} \mathbf{R}_{0,j}\Big)\Big\rangle = \Big\langle \sum_{i=1}^{N} \mathbf{R}_0^2 + \sum_{i=1}^{N}\sum_{\substack{j=1\\ i\neq j}}^{N} \mathbf{R}_{0,i}\cdot\mathbf{R}_{0,j}\Big\rangle \\ &= \langle N\rangle R_0^2 + \sum_{\substack{i,j\\ i\neq j}} \langle \mathbf{R}_{0,i}\cdot\mathbf{R}_{0,j}\rangle = \langle N\rangle R_0^2.\end{aligned} \tag{1.10}$$

The cross term is zero because on average the particle is equally likely to move into any of the four adjacent sites at any step. Time and number of steps are related as follows: Since the number of steps N is a Poisson-distributed random variable with rate Γ, the average number of steps $\langle N\rangle$ in time interval t is given by $N = \Gamma t$. It therefore follows that

$$\langle \mathbf{r}^2(t)\rangle = R_0^2 \Gamma t \tag{1.11}$$

The diffusion coefficient D_{sp} is defined as the long-time limit of the time derivative of the mean squared displacement. For this case of a single particle diffusing on a simple lattice, it is possible to find an expression of the diffusion coefficient D_{sp} in terms of the rate Γ and jump distance R_0

$$D_{sp} = \frac{1}{2d}\lim_{t\to\infty}\frac{d\langle \mathbf{r}^2(t)\rangle}{dt} = \frac{R_0^2\Gamma}{2d} \tag{1.12}$$

where d is the number of dimensions. The subscript emphasises that this applies to the case of a single particle diffusing on an otherwise empty lattice. This expression is often given in the form

$D_{sp} = R_0^2\tilde{\Gamma}$, where $\tilde{\Gamma} = \Gamma/2d$ is the hopping frequency per bond.

The general principles introduced above hold true even for more complicated lattices in real materials, for which a fraction c of sites is occupied by diffusing particles. In the case of many particles, we define two different diffusion coefficients: the tracer diffusion coefficient D^* and the jump diffusion coefficient D_J

$$D^* = \frac{1}{2d}\lim_{t\to\infty}\frac{d}{dt}\frac{1}{n}\sum_{i=1}^{n}\langle \mathbf{r}_i^2(t)\rangle \tag{1.13}$$

$$D_J = \frac{1}{2d}\lim_{t\to\infty}\frac{d}{dt}\frac{1}{n}\Big\langle \big[\sum_{i=1}^{n}\mathbf{r}_i(t)\big]^2\Big\rangle \tag{1.14}$$

where n is the number of diffusing particles. The tracer diffusion coefficient captures the ability of a single tagged particle to diffuse through the medium, while the jump diffusion coefficient measures the diffusivity of the center of mass of the particles, and hence is relevant for mass transport. While the mean squared displacement of an individual particle still grows linearly with time, the motion is impacted by interactions. In the simplest (mean-field) model, the interactions are taken into account by a factor of $(1-c)$, to approximate $D^* = (1-c)D_{sp}$. Beyond a mean-field model, it becomes much more complicated to treat effects of inter-particle correlations on the tracer diffusion coefficient. For non-zero values of c, but the same values of Γ and R_0, the tracer diffusion coeffient will not be equal to the expression given in Eqn. 1.12 due to particle-particle interactions, and in general it is not possible to find simple expressions for it in terms of Γ, R_0, and c. Note that the jump diffusion coefficient D_J is unaffected by interactions, and has the value $R_0^2\tilde{\Gamma}$ for all c [16]. The importance of the diffusion coefficient lies in its relationship to transport and ionic conductivity. The chemical diffusion coefficient D_c (closely related to D_J) enters Fick's law and determines Li-ion flux in the presence of chemical potential gradients. Via the Einstein relation, it also determines mobility in the presence of electric fields. The rate at which a battery can be cycled is therefore ultimately determined by the lithium diffusion within the active materials.

There are a variety of experimental techniques that can determine the diffusivity and the activation energies of ionic motion in solid-state materials. A simple measurement is the cycling of batteries at different rates. This gives direct performance data but it is difficult to disentangle the many complex factors contributing to this measurement to obtain intrinsic material characteristics. Techniques that are relevant to the materials studied in this work are NMR relaxometry and PFG (pulsed-field gradient) NMR. NMR relaxometry is a technique to obtain data on activation barriers of ionic motion. PFG NMR on the other hand allows direct measurements of diffusion coefficients in solid-state materials. In combination with first-principles simulations of the ionic hopping pathways and activation barriers, these techniques can provide detailed insight into the ionic motion in materials, as demonstrated in Chapter 5.

1.4 Complex Oxide Battery Materials

A vast number of materials have been studied as lithium-ion battery electrodes. The present work is concerned with the study of a family of complex niobium-based oxides, variously known

as Wadsley–Roth phases, crystallographic shear phases, or block-type structures. These can be found in the phase diagrams of Nb_2O_5, Nb_2O_5–WO_3, TiO_2–Nb_2O_5. Common to this family is a specific type of crystal structure that is made up of *blocks* (Fig. 1.5). The blocks are formed by connecting the constituent metal–oxygen octahedra via corner-sharing to form units that are n octahedra wide and m octahedra long. The blocks are then stacked together and connected via edge-sharing to form the crystal structure of the material. Within their plane, blocks are connected via edge-sharing of octahedra, while perpendicular to the plane, they connect via corner-sharing to form columns. In some structures, tetrahedrally coordinated metal ions fill voids at the corners of the blocks.

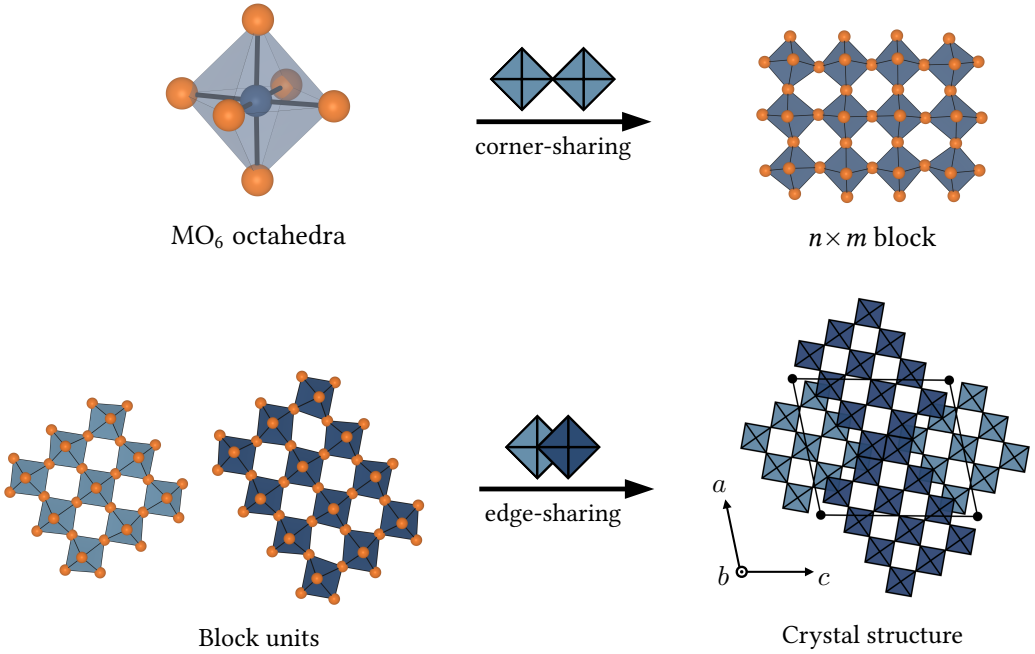

Figure 1.5: Building a block-type crystal structure, specifically $Nb_{22}O_{54}$. Metal–oxygen octahedra are connected via corner-sharing to form a $n \times m$ block. Block units are stacked together and connected via edge-sharing to form the crystal.

The planes along which the blocks are connected are referred to as crystallographic shear planes, due to the fact that the blocks connected by one of these planes are sheared relative to each other by half the size of an MO_6 octahedron. It is often useful to think of these structures as modifications of a perfect infinite array of corner-shared octahedra, equivalent to the ReO_3 structure (which in turn can be described as a perovskite lacking the A-site cation). Compared to a ReO_3 structure, the two in-plane directions in block-type structures are interrupted by a series of crystallographic shear planes, leading to an array of quasi-one-dimensional columns. This confinement has important ramifications for the electronic structure and ion transport properties of the materials, as detailed in Chapters 4 and 6.

To set the context of the present work, it is worth providing a short historical overview. The first comprehensive studies of block-type structures were done by Wadsley and Roth [17, 18, 19, 20]. In a series of seminal papers in the 1960s, Wadsley and Roth established the phase diagrams of the binary systems Nb_2O_5–WO_3 and TiO_2–Nb_2O_5. In doing so, they also introduced the so-called

"block principle" that underpins the structural description of these phases [20]. One of the essential characteristics of these compounds is their ability to sustain small changes in stoichiometry, which do not lead to isolated defect formation, but instead result in changes to the crystal structure as a whole. This adaptability leads to very complex phase diagrams, since any small change in stoichiometry leads to the formation of a new phase with a distinct crystal structure. Two examples of how this adaptability is manifested are unit cell-level intergrowths, and planar defects along which the blocks deviate from the typical size.

A systematic and comprehensive study of lithium insertion into Wadsley–Roth phases was reported by Cava et al. in 1983 [21] (14 different compounds). This was motivated by observations made on ReO_3, which on lithium insertion undergoes a sequence of structural distortions [22]. As the octahedra in ReO_3 twist about their shared corners, the diffusion channels are obstructed, inhibiting lithium diffusion and resulting in poor electrochemical performance. The structural distortions are associated with rotations of the octahedra, similar to what is commonly observed in perovskite oxides. In contrast, Wadsley–Roth phases feature crystallographic shear planes which, due to edge-sharing between octahedra, frustrate octahedral tilts and rotations. The diffusion channels remain open, allowing facile lithium intercalation.

A few years after the electrochemical study, Cava et al. reported that the Wadsley–Roth phase $Nb_{12}O_{29}$ is a metallic antiferromagnet with an ordering temperature of 4 K [23]. $Nb_{12}O_{29}$ is a suboxide of Nb_2O_5 belonging to a series of phases Nb_2O_{5-x} formed by n-doping of the parent oxide, i.e. incorporating a small amount of Nb^{4+}. Measurements of the electrical and magnetic properties of Nb_2O_{5-x} were reported by Cava et al. and Rüscher, and provide interesting indications regarding the interplay of electronic and crystallographic structure in the Wadsley–Roth phases [24, 25, 26, 27]. These are interpreted in the light of first-principles calculations in Chapter 4.

Wadsley–Roth phases are oxides of early transition metals with characteristic intercalation voltages of 1–2 V vs. Li/Li^+ and operate as anodes. The graphite anode used in commercial devices suffers from a number of problems that make oxide anodes attractive alternatives. One major problem is the low operating voltage of graphite, which promotes electrolyte reduction, lithium plating, and dendrite growth, leading to possible short circuiting of the device. Oxide anodes generally operate in a safer voltage window > 1 V vs. Li/Li^+ and do not show these issues, although the higher operating voltage leads to lower full-cell voltages and energy densities. The primary commercial oxide anode material is LTO ($Li_4Ti_5O_{12}$). Two recent developments have led to a surge of interest in anode applications of the Wadsley–Roth phases. The first of these is the report of Wadsley–Roth $TiNb_2O_7$ (TNO) as an anode by Goodenough [28] as a possible alternative to the LTO ($Li_4Ti_5O_{12}$) anode. While LTO suffers from low ionic and electronic conductivity, TNO does not, and shows higher capacity and better rate performance than LTO. TNO is attracting much attention at the moment, including commercial development efforts by Toshiba [29]. A second recent development is the report of high-rate performance and high energy densities achieved with niobium tungsten oxides [13]. These materials show the highest measured diffusion coefficients of any electrode material. Motivated by these developments, Chapters 4, 5, and 6 examine the electronic structure, lithium insertion mechanism, and lithium diffusion in Wadsley–Roth phases, and niobium tungsten oxides specifically.

1.5 Correlated Transition Metal Oxides

Transition metal compounds display a diverse range of physical phenomena, including metal–insulator transitions, multiferroicity, and high-T_c superconductivity. Transition metal oxides (TMO) in particular are of great interest for both applications and fundamental science. Many of the phenomena that occur in TMOs are due to electronic correlation, defined here as the effect of strong interactions between electrons. Key concepts for our understanding of correlated materials will be introduced here, while the details of computational methods will be discussed in the next chapter.

Consider two limits of describing the electronic structure of solids: fully itinerant, and fully localised. If the electrons are fully itinerant, the electronic states of the solid are Bloch states characterised by a wavevector $\mathbf{k}$, which is a good quantum number. Many properties of solids arise naturally from this description: bandstructures, densities of states, and the distinction between metals and insulators. On the other hand, we can think of the solid as an assembly of atoms. If the intra-atomic interactions between electrons are much larger than the inter-atomic interactions, it is reasonable to describe the physics of these solids in terms of concepts of atomic physics. Both of these limits are represented to certain degrees in real materials. Simple metals like lithium and potassium, and semiconductors like silicon are examples of the first limit, while isolated dopants embedded in an inert host serve as example of the second limit. Excitation processes, driven by light, provide good illustrations of their behaviour. In the case of silicon, the excitations are well described as transitions between delocalised band states. On the other hand, for transition metal dopants in gemstones, the excitation process is very accurately described as being purely local, while the solid might only provide a perturbing field that breaks symmetries.

Simple lattice models exist for both cases. In the delocalised limit, a nearest-neighbour tight-binding model is often used, with a Hamiltonian of the form

$$\hat{H} = -t \sum_{\langle ij \rangle, \sigma} (\hat{c}^\dagger_{i\sigma} \hat{c}_{j\sigma} + \hat{c}^\dagger_{j\sigma} \hat{c}_{i\sigma}) \tag{1.15}$$

where $t > 0$ is the hopping parameter, $\hat{c}^\dagger_{i\sigma}$ and $\hat{c}_{i\sigma}$ are creation and annihilation operators for an electron with spin σ at lattice site i. The sum is over pairs of nearest neighbors, denoted by $\langle ij \rangle$. This Hamiltonian is easily solved by transforming to the Bloch basis, defined by $\hat{c}^\dagger_{\mathbf{k}\sigma} = \sum_i e^{i\mathbf{k}\cdot\mathbf{r}_i} \hat{c}^\dagger_{i\sigma}$ and equivalently for $\hat{c}_{\mathbf{k}\sigma}$. The eigenstates have well-defined $\mathbf{k}$ vectors, and for n-cubic lattices the dispersion is $\epsilon(\mathbf{k}) = -2tz\cos(\mathbf{k}\cdot\mathbf{a})$ where z is the number of neighbours and $\mathbf{a}$ the vector of lattice constants. DFT in its most commonly used form can be viewed as a first-principles version of these ideas, leading to a materials-specific, parameter-free, and reasonably accurate computational method.

The other extreme is the atomic limit, for which eigenstates are solutions to the atomic problem. In multi-orbital atoms this results in term symbols. Taking the simplest case of an array of hydrogen-like atom with a single orbital and neglecting interactions, the Hamiltonian that defines the system is

$$\hat{H} = U \sum_i \hat{n}_{i\uparrow} \hat{n}_{i\downarrow} \tag{1.16}$$

where $U > 0$ is the inter-electronic repulsion term and $\hat{n}_{i\sigma} = \hat{c}^\dagger_{i\sigma}\hat{c}_{i\sigma}$ is the number operator for an electron with spin σ at lattice site i. If we consider only a single site, there are four eigenstates: $|0\rangle$ with 0 e^- and $E = 0$, $|\uparrow\rangle$ and $|\downarrow\rangle$ with 1 e^- and $E = 0$, and $|\uparrow\downarrow\rangle$ with 2 e^- and $E = U$.

Correlated solids usually lie in between these two extremes and have a Hamiltonian that contains terms of both types. The simplest model to describe this behaviour is the Hubbard model

$$\hat{H} = -t \sum_{\langle ij\rangle,\sigma} \hat{c}^\dagger_{i\sigma}\hat{c}_{j\sigma} + \hat{c}^\dagger_{j\sigma}\hat{c}_{i\sigma} + U \sum_i \hat{n}_{i\uparrow}\hat{n}_{i\downarrow} \tag{1.17}$$

where the terms have the same meaning as described above. Despite its apparent simplicity, the model leads to a very rich phase diagram, and due to its mixed localised-itinerant character, cannot be solved analytically except in one dimension. Of particular difficulty is the regime $t \approx U$. The Hubbard model is the starting point for the description of correlated materials. The spatial extent of d or f orbitals is generally smaller than that of s or p electrons, and Coulomb interactions between d or f electrons are correspondingly much stronger. It is therefore d or f electrons that show strong correlation effects and require treatment beyond band theory[1]. However, compared to the simple Hubbard model with one orbital, real materials are much more complex due to the presence of additional degrees of freedom (spin and orbital) inherent to d and f electrons. DFT+DMFT, which is a method to model strongly correlated materials from first principles, will be introduced in the next chapter.

The interplay between spin, charge, and orbital degrees of freedom – coupled to the itineracy – leads to a large number of different phenomena and properties. Additionally, different degrees of freedom often compete. Changes in external parameters such as temperature or pressure can tip the balance of factors, making correlated materials quite sensitive and easily tuned. The most notable example of competition between localisation and itineracy is the Mott metal-insulator transition. In the case of the Hubbard model, the first term favours delocalisation (metal) whereas the second term favours localisation (insulator). The balance is governed by the ratio of the Coulomb repulsion U to the hopping t. Changes in pressure or temperature can favour one or the other behaviour, tipping the balance with drastic changes in physical properties during metal-insulator transitions.

The rich phenomenology and sensitivity to changes of external parameters make them interesting but challenging systems to study from first principles. Computational techniques appropriate for correlated materials are much more expensive and difficult to use than DFT, while usually only allowing the calculation of a small number of properties compared to DFT. To extend the capabilities of these techniques, Chapter 7 develops methods to calculate phonons in correlated materials.

[1] That is not to say that electrons in materials that are well-described by band theory do not interact. However, the interactions tend to be weaker and not strongly local, such that the interacting system is a perturbed or renormalised version of the non-interacting system (e.g. Fermi-liquid theory of metals).

Chapter 2

Electronic Structure Theory

The following sections present a brief account of aspects of electronic structure theory relevant to this thesis. The first part deals with density-functional theory, with a focus on the planewave pseudopotential method. The second part introduces Green's function methods, specifically dynamical mean-field theory (DMFT). More detailed explanations can be found in Refs [30, 31, 32] (DFT) and Refs [33, 34, 35, 36] (Green's functions, DMFT) on which much of the following is based.

2.1 The Electronic Structure Problem

The electronic structure of assemblies of atoms is governed by the laws of quantum mechanics. The full Hamiltonian for a molecule or solid is

$$\begin{aligned}\hat{\mathcal{H}} = &-\frac{\hbar^2}{2M_I}\sum_{I=1}^{M}\nabla_I^2 - \frac{\hbar^2}{2m_e}\sum_{i=1}^{N}\nabla_i^2 + \frac{e^2}{8\pi\epsilon_0}\sum_{I=1}^{M}\sum_{\substack{J=1\\I\neq J}}^{M}\frac{Z_I Z_J}{|\mathbf{R}_I-\mathbf{R}_J|}\\ &-\frac{e^2}{4\pi\epsilon_0}\sum_{I=1}^{M}\sum_{i=1}^{N}\frac{Z_I}{|\mathbf{R}_I-\mathbf{r}_i|} + \frac{e^2}{8\pi\epsilon_0}\sum_{i=1}^{N}\sum_{\substack{j=1\\i\neq j}}^{N}\frac{1}{|\mathbf{r}_i-\mathbf{r}_j|}\end{aligned} \tag{2.1}$$

where the nuclear masses, coordinates and charges are denoted by M_I, $\mathbf{R}_I$ and Z_I respectively. The electronic coordinates are labelled by $\mathbf{r}_i$, M and N are the numbers of nuclei and electrons. The Hamiltonian $\hat{\mathcal{H}}$ consists of terms representing the nuclear and electron kinetic energies, the nuclear-nuclear, nuclear-electron, and electron-electron interactions. The time-independent Schrödinger equation is

$$\hat{\mathcal{H}}\Psi_n(\{\mathbf{R}\},\{\mathbf{r}\}) = E_n\Psi_n(\{\mathbf{R}\},\{\mathbf{r}\}) \tag{2.2}$$

where $\{\mathbf{R}\}$ and $\{\mathbf{r}\}$ denote the sets of nuclear and electronic coordinates, respectively, and E_n and Ψ_n represent the energy and wavefunction of the nth state. The full Schrödinger equation includes both nuclear and electronic degrees of freedom, and is impossible to solve for any but the simplest systems.

To make progress, we separate the electronic and nuclear degrees of freedom. Electrons are much heavier than nuclei, and move much faster if in equilibrium. We can therefore assume that the electronic ground state adjusts instantaneously to changes in the nuclear positions, and that the electrons always remain in their ground state. This is commonly referred to as the *adiabatic approximation*. The subsequent *Born-Oppenheimer approximation* assumes that the potential energy of a nuclear configuration is equal to the ground state electronic energy of that configuration, ignoring certain correction terms. The electronic energies are obtained from solutions of the electronic Schrödinger equation into which the the nuclear positions enter as parameters.

Solving the electronic Schrödinger equation is by far the more difficult task, and therefore we will concern ourselves exclusively with the electronic Schrödinger equation in the following. The Hamiltonian for the electrons in atomic units ($\hbar = m_e = e = 4\pi\epsilon_0 = 1$) is given by

$$\hat{H}_e = -\frac{1}{2}\sum_{i=1}^{N}\nabla_i^2 - \sum_{I=1}^{M}\sum_{i=1}^{N}\frac{1}{|\mathbf{R}_I - \mathbf{r}_i|} + \frac{1}{2}\sum_{i=1}^{N}\sum_{\substack{j=1\\ i\neq j}}^{N}\frac{1}{|\mathbf{r}_i - \mathbf{r}_j|} + V_{nn} \tag{2.3}$$

where V_{nn} denotes the Coulomb interaction between nuclei, which is included for completeness. Solving the electronic Schrödinger equation is still extremely difficult, and the only systems for which analytic solutions exist are very simple (such as the hydrogen atom). In order to make further progress, we have to make additional approximations. Two very important approximate methods of treating multi-electron systems are the Hartree-Fock method and *practical* density-functional theory.

Before moving on, let us consider the implications of the Born-Oppenheimer approximation. Given that we have an electronic structure method that provides us with the ground-state electronic energy of any nuclear configuration, we can treat the nuclear motion as an entirely separate problem. We then have a choice of considering the nuclear motion to be either classical or quantum mechanical in nature. A large number of possible applications follow directly from this: if we choose to make the *classical nuclei approximation*, we can optimise the nuclear positions to the minimum of the potential energy surface (PES), we can perform molecular dynamics to obtain thermodynamic quantities, or obtain transition states using specialised search methods. Treating the nuclei quantum mechanically is far less common, but can be done with methods such as path integral molecular dynamics (PIMD). The important point is that after we have separated nuclear and electronic degrees of freedom, the electronic structure method can be treated as a blackbox and replaced as desired. All properties that are defined in terms of the PES can be obtained with different descriptions of the electronic structure. An example of this is the work in Chapter 7, where instead of using DFT to calculate phonons, we use DFT+DMFT.

2.2 Hartree-Fock Method

The Hartree-Fock approach relies on the variational principle of quantum mechanics, which states that the expectation value of the energy $\tilde{E}$ for a normalised trial wavefunction Ψ that satisfies the boundary conditions of the problem will always be larger than or equal to the true ground state

energy

$$\widetilde{E} = \langle \Psi | \hat{H}_e | \Psi \rangle \geq E_0 \tag{2.4}$$

Within Hartree-Fock, the trial wavefunction is chosen to be a Slater determinant of single-particle orbitals, since this ansatz directly satisfies the required antisymmetry under electron exchange

$$\Psi(\{\mathbf{r}\}) = \frac{1}{\sqrt{N!}} \begin{vmatrix} \psi_1(\mathbf{r}_1) & \psi_2(\mathbf{r}_1) & \dots & \psi_n(\mathbf{r}_1) \\ \psi_1(\mathbf{r}_2) & \psi_2(\mathbf{r}_2) & \dots & \psi_n(\mathbf{r}_2) \\ \vdots & \vdots & \ddots & \vdots \\ \psi_1(\mathbf{r}_n) & \psi_2(\mathbf{r}_n) & \dots & \psi_n(\mathbf{r}_n) \end{vmatrix} \tag{2.5}$$

with $\int \psi_i^* \psi_j \ \mathrm{d}\mathbf{r} = \delta_{ij}$. The $\frac{1}{\sqrt{N!}}$ prefactor ensures $\langle \Psi | \Psi \rangle = 1$. Evaluating Eqn. 2.4 with the Slater determinant, we find that

$$\begin{aligned} \widetilde{E} = &-\frac{1}{2} \sum_i \int \psi_i^* \nabla_i^2 \psi_i \ \mathrm{d}\mathbf{r}_i + \frac{1}{2} \iint \frac{\rho(\mathbf{r}')\rho(\mathbf{r})}{|\mathbf{r} - \mathbf{r}'|} \, \mathrm{d}\mathbf{r} \, \mathrm{d}\mathbf{r}' \\ &-\frac{1}{2} \sum_{ij} \iint \frac{\psi_i^*(\mathbf{r}) \psi_j(\mathbf{r}) \psi_j^*(\mathbf{r}') \psi_i(\mathbf{r}')}{|\mathbf{r} - \mathbf{r}'|} \, \mathrm{d}\mathbf{r}' \, \mathrm{d}\mathbf{r} - \sum_I Z_I \int \frac{\rho(\mathbf{r})}{|\mathbf{R}_I - \mathbf{r}|} \, \mathrm{d}\mathbf{r} \end{aligned} \tag{2.6}$$

where $\rho(\mathbf{r}) = \sum_i |\psi_i|^2$ is the electron density. To find the best approximation to the true ground state wavefunction, the energy is minimised with respect to each of the ψ_i by using variational calculus [37]. Orthonormalisation of the orbitals is added as a constraint with a Lagrange multiplier Λ_{ij}

$$E + \sum_{ij} \Lambda_{ij} \ \Big[\int \psi_i^* \psi_j \, \mathrm{d}\mathbf{r} - \delta_{ij} \Big]. \tag{2.7}$$

By minimising with respect to ψ_i^* (which can be treated as independent to ψ_i), we arrive at N coupled single-particle equations

$$\left[-\frac{1}{2} \nabla_i^2 + \int \frac{\rho(\mathbf{r}')}{|\mathbf{r} - \mathbf{r}'|} \, \mathrm{d}\mathbf{r}' + \hat{V}_n \right] \psi_i(\mathbf{r}) - \sum_j \psi_j(\mathbf{r}) \int \frac{\psi_j^*(\mathbf{r}') \psi_i(\mathbf{r}')}{|\mathbf{r} - \mathbf{r}'|} \, \mathrm{d}\mathbf{r}' = \sum_j \Lambda_{ij} \psi_j(\mathbf{r}). \tag{2.8}$$

The first term in the square brackets is the kinetic energy operator, the following one is the Hartree potential, and the third term denotes the Coulomb potential due to the nuclei. The last term is the Fock exchange operator. Through a unitary transformation $\psi_i' = S_{ij} \psi_j$ these are transformed into N eigenvalue equations for the single-particle orbitals

$$\left[-\frac{1}{2} \nabla_i^2 + \int \frac{\rho(\mathbf{r}')}{|\mathbf{r} - \mathbf{r}'|} \, \mathrm{d}\mathbf{r}' + \hat{V}_n \right] \psi_i(\mathbf{r}) - \sum_j \psi_j(\mathbf{r}) \int \frac{\psi_j^*(\mathbf{r}') \psi_i(\mathbf{r}')}{|\mathbf{r} - \mathbf{r}'|} \, \mathrm{d}\mathbf{r}' = \epsilon_i \psi_i(\mathbf{r}). \tag{2.9}$$

These equations are not independent of each other, and have to be solved self-consistently.

In the Hartree-Fock method, the energy E_{HF} is decomposed into a series of progressively smaller terms: the electron kinetic energy T, the electron-nuclear interaction energy E_{e-n}, the

Hartree energy E_H, and the exchange energy E_X

$$E_{HF} = T + E_{e-n} + E_H + E_X. \tag{2.10}$$

The remaining difference between E_{HF} and the true ground state energy E_0 is referred to as the correlation energy E_C. While the correlation energy is by far the smallest term in this decomposition, it is nontheless very important for an accurate description of electronic structure. Breaking the total energy down into a series of terms is common in all of electronic structure theory, but not all theories use the exact same definitions of exchange and correlation. For example, 'exchange' has a different meaning in the context of DFT than in HF. Due to the complete lack of correlation, Hartree-Fock is not a very accurate method by itself. Quantum chemistry techniques, such as coupled-cluster and configuration interaction, include correlation effects by adding further Slater determinants to the HF trial wavefunction. In contrast, DFT takes a different approach and tries to treat exchange and correlation on the same footing, as described in the next section.

2.3 Density-Functional Theory

2.3.1 Foundation of DFT

Density-functional theory is traditionally more popular than Hartree-Fock within the solid-state physics community, and treats the electron density as the fundamental variable rather than the wavefunction. Within the full Hamiltonian of a many-body system (Eqn. 2.1), the interaction term between the electrons and the nuclei is referred to as the external potential (external to the interacting electron system). The external potential plays an important role in the two foundational theorems of DFT, proven by Hohenberg and Kohn [38]:

Theorem I: The ground state charge density $\rho_0(\mathbf{r})$ for a system of interacting particles uniquely determines the external potential $V_{ext}(\mathbf{r})$, up to a constant.

The proof is by contradiction. Suppose there are two external potentials, $V_{ext}^{(1)}(\mathbf{r})$ and $V_{ext}^{(2)}(\mathbf{r})$, which differ by more than a constant and give two different hamiltonians, $\hat{H}^{(1)}$ and $\hat{H}^{(2)}$, with two different ground state wavefunctions $\Psi_0^{(1)}$ and $\Psi_0^{(2)}$ which, however, have the same ground state charge density $\rho_0(\mathbf{r})$. The variational principle of quantum mechanics requires that

$$\begin{aligned} E_1 &= \left\langle \Psi_0^{(1)} \middle| \hat{H}^{(1)} \middle| \Psi_0^{(1)} \right\rangle < \left\langle \Psi_0^{(2)} \middle| \hat{H}^{(1)} \middle| \Psi_0^{(2)} \right\rangle \\ &= \left\langle \Psi_0^{(2)} \middle| \hat{H}^{(2)} \middle| \Psi_0^{(2)} \right\rangle + \left\langle \Psi_0^{(2)} \middle| \hat{H}^{(1)} - \hat{H}^{(2)} \middle| \Psi_0^{(2)} \right\rangle \\ &= E_2 + \int [V_{ext}^{(1)} - V_{ext}^{(2)}]\ \rho_0(\mathbf{r})\, \mathrm{d}\mathbf{r} \end{aligned} \tag{2.11}$$

and similarly

$$\begin{aligned} E_2 &= \left\langle \Psi_0^{(2)} \middle| \hat{H}^{(2)} \middle| \Psi_0^{(2)} \right\rangle < \left\langle \Psi_0^{(1)} \middle| \hat{H}^{(2)} \middle| \Psi_0^{(1)} \right\rangle \\ &= \left\langle \Psi_0^{(1)} \middle| \hat{H}^{(1)} \middle| \Psi_0^{(1)} \right\rangle + \left\langle \Psi_0^{(1)} \middle| \hat{H}^{(2)} - \hat{H}^{(1)} \middle| \Psi_0^{(1)} \right\rangle \\ &= E_1 + \int [V_{ext}^{(2)} - V_{ext}^{(1)}]\ \rho_0(\mathbf{r})\, \mathrm{d}\mathbf{r}. \end{aligned} \tag{2.12}$$

The last two statements added imply $E_1 + E_2 < E_2 + E_1$, which is impossible. Therefore the initial assumption of different V_{ext} leading to the same ground state charge density must be wrong. The ground state charge density determines the external potential up to a trivial constant, and thereby the Hamiltonian. Since the Hamiltonian is fully determined by the ground state charge density, so are all other properties of the system, including the total energy, ground state and all excited state wavefunctions.

Theorem II: A universal functional for the energy in terms of the density $E[\rho]$ exists, valid for any external potential $V_{ext}(\mathbf{r})$. For a given $V_{ext}(\mathbf{r})$, the ground state energy is the global minimum of this functional and the density $\rho(\mathbf{r})$ that minimizes this functional is the exact ground state density.

The following proof assumes that electron densities are V-representable, i.e. can be obtained from ground state wavefunctions of electronic Hamiltonians with some external potential V_{ext}. For these densities all properties, including the Hamiltonian, ground state wavefunction, and total energy, are uniquely determined by the density ρ as shown in theorem I. The energy is therefore a functional of the electron density, $E[\rho]$. Given a Hamiltonian $\hat{H}$ with ground state density ρ_0 and wavefunction $\Psi_0[\rho_0]$, any other density $\tilde{\rho}$ that corresponds to the ground state of a different Hamiltonian with a different ground state wavefunction $\tilde{\Psi}[\tilde{\rho}]$ will have an energy expectation value $\tilde{E}$ that is larger than the ground state energy E_0

$$E[\tilde{\rho}] = \tilde{E} = \left\langle \tilde{\Psi}[\tilde{\rho}] \middle| \hat{H} \middle| \tilde{\Psi}[\tilde{\rho}] \right\rangle > \langle \Psi_0[\rho_0] | \hat{H} | \Psi_0[\rho_0] \rangle = E_0 = E[\rho_0]. \tag{2.13}$$

This follows simply from the variational principle. Minimising $E[\rho]$ with respect to ρ yields the exact ground state energy and density. We can decompose the energy functional as $E[\rho] = F[\rho] + E_{n-n} + \int \rho \cdot V_{ext}\, \mathrm{d}\mathbf{r}$. The term $F[\rho]$ is independent of the external potential, and applies to all electronic systems (it is a "universal" functional).

Levy [39] later reformulated DFT in terms of a constrained search. In Levy's formulation, the universal functional is defined as

$$F[\rho] = \min_{\Psi \to \rho} \left\{ \langle \Psi | \hat{T} + \hat{V}_{ee} | \Psi \rangle \right\} \tag{2.14}$$

where $\hat{T}$ and $\hat{V}_{ee}$ are the kinetic energy operator and the electron-electron interaction, respectively (first and third terms in Equation 2.3). The Levy functional searches over all wavefunctions that give rise to the specified density ρ to return the minimal value of the sum of electron kinetic and interaction energies. With this definition of $F[\rho]$ we only require that the density is N-

representable, meaning that ρ can be obtained from an antisymmetric wavefunction. Since the conditions for this N-representability are known, the constrained search formulation is more general than the original HK theorems.

2.3.2 Kohn-Sham DFT

The exact functional $F[\rho]$ of DFT is unknown. As shown above, $F[\rho]$ captures the electron kinetic energy and electron-electron interaction energies, but unfortunately, approximations to $F[\rho]$ are not accurate enough for simulations of molecules and materials. The Kohn-Sham (KS) approach to DFT introduces an auxiliary system of non-interacting electrons to circumvent this issue. For non-interacting electrons, the analytic expression for the kinetic energy is known, as are certain contributions to the electron-electron interaction energy. KS-DFT maps the fully interacting system onto a non-interacting system and expresses all the major contributions to the total energy in terms of single-particle concepts. All of our ignorance regarding true many-body effects is relegated to the exchange-correlation functional, $E_{xc}[\rho]$. With this, the total energy functional is

$$E[\rho] = \sum_i -\frac{1}{2}\int \phi_i^* \nabla_i^2 \phi_i \, \mathrm{d}\mathbf{r} + \frac{1}{2}\iint \frac{\rho(\mathbf{r})\rho(\mathbf{r}')}{|\mathbf{r}-\mathbf{r}'|}\,\mathrm{d}\mathbf{r}\,\mathrm{d}\mathbf{r}' + V_{e-n} + E_{xc}[\rho] \tag{2.15}$$

for a set of Kohn-Sham orbitals ϕ_i, which are required to reproduce the true ground state charge density $\rho_0(\mathbf{r}) = \sum_i |\phi_i|^2$. According to the second HK theorem, the true ground state density is the global minimum of this functional. By variational calculus, the energy is minimised under constraints of orthonormality, similar to Hartree-Fock, leading to the Kohn-Sham equations

$$\hat{H}_{KS}\phi_i(\mathbf{r}) = \Big[-\frac{1}{2}\nabla^2 + V_H + V_{ext} + \frac{\delta E_{xc}}{\delta \rho}\Big]\phi_i(\mathbf{r}) = \epsilon_i \phi_i(\mathbf{r}) \tag{2.16}$$

where V_H is the Hartree potential, V_{ext} is the electron-nuclear interaction and $\frac{\delta E_{xc}}{\delta \rho}$ is the exchange-correlation potential. The electron density forms both input and output of these equations. The equations therefore have to be solved self-consistently.

2.3.3 Approximations to the Exchange-Correlation Functional

The exact form of the exchange-correlation functional $E_{xc}[\rho]$ is unknown. Different levels of approximations are used in practice. The simplest approximation is the local density approximation (LDA). The LDA expression for the exchange-correlation energy is

$$E_{xc}[\rho] = \int \rho(\mathbf{r}) \cdot \epsilon_{xc}(\rho(\mathbf{r}))\ \mathrm{d}\mathbf{r} \tag{2.17}$$

where $\epsilon_{xc}(\rho)$ is the exchange-correlation energy per particle for a uniform electron gas of density ρ. The expression for the exchange energy of a uniform electron gas is known exactly. The correlation energy can be obtained from quantum monte carlo simulations [40] and has been parameterised to give a closed-form expression [41]. The two contributions are added to give $\epsilon_{xc}(\rho)$. Incorporating inhomogeneity in the density to first order leads to the generalised gradient approximations (GGA).

The most popular of these is the Perdew-Burke-Ernzerhof (PBE) functional [42]. It has long been recognised that the success of these rather simple approximations to E_{xc} is largely due to the fact that both LDA and PBE satisfy some of the properties that are known for the exact XC functional. An important example is the sum rule obeyed by the exchange-correlation hole. Since there is no systematic way to improve XC functionals, designing functionals that obey ever more exact constraints has been the guiding philosophy. An important recent development in this direction is the SCAN meta-GGA functional [43]. Meta-GGA functionals improve on GGA by using the kinetic energy density in addition to the density and its derivative. This additional flexibility allows the SCAN functional to satisfy all known exact constraints, leading to better accuracy.

Kohn-Sham DFT with local (LDA) or semilocal (GGA) functionals successfully describes the electronic structure and energetics of a wide variety of systems, including metals, semiconductors, and insulators. However, systematic errors on predictions of certain properties have been documented: LDA and GGA functionals underestimate band gaps of semiconductors and insulators, and often fail completely for transition metal compounds with strongly localised electrons. Rather than fitting the small number of exact constraints, an equally useful way to develop improved XC functionals is to fit them to correctly reproduce certain properties. Many of the most widely used functionals are based on this idea. Hybrid functionals, such as HSE [44] or PBE0 [45], modify the exchange energy to include a fraction of Hartree-Fock exchange. For example for PBE0

$$\begin{aligned} E_x[\rho, \{\phi_i\}] &= \frac{1}{4} E_x^{HF}[\{\phi_i\}] + \frac{3}{4} E_x^{PBE}[\rho] \\ E_c[\rho] &= E_c^{PBE}[\rho] \end{aligned} \tag{2.18}$$

where $E_x^{HF}[\{\phi_i\}]$ is the Hartree-Fock exchange ('exact' exchange, third term in Eqn. 2.6) evaluated with the Kohn-Sham orbitals $\{\phi_i\}$. It turns out that adding exact exchange significantly improves band gap predictions. As discussed in the previous chapter, transition metal compounds often feature strong Coulomb repulsion between electrons in d or f orbitals. DFT+U, also known as Hubbard-corrected DFT, aims to correct this by explicitly incorporating the Coulomb repulsion into the DFT energy functional, which now depends explicitly on the occupation of the d or f orbitals. The idea of fitting functionals to experimental data can be taken even further, leaving behind any physical motivations. One example of this is the B3LYP functional which achieves an accuracy comparable to quantum chemistry methods such as coupled-cluster, but is much more computationally efficient.

2.4 Practical Aspects of DFT

The technical details of KS-DFT codes vary from field to field. Physicists and materials scientists are mostly concerned with solid-state materials, and DFT implementations are tailored accordingly: they offer a natural description of periodic crystals and reciprocal space, exploit fast Fourier transforms for efficient conversion between real and reciprocal space, and use appropriate basis sets. However, a number of technical issues arise when building DFT implementations that satisfy these requirements. The root problem is that the most natural solid-state basis set (planewaves)

cannot be used to describe electronic wavefunctions close to the nucleus. One possible solution is to use a localised basis set inside spheres around each atom, and planewaves in the interstitial regions. Another is to give up on a planewave basis set and instead use atomic orbitals. The third and most popular approach is to eliminate the problematic core states from the calculation, and replace their effect with a so-called pseudopotential. The details of this planewave pseudopotential method are described in the following sections.

2.4.1 The Solid State

Within the planewave pseudopotential DFT approach, all systems are modelled as periodic solids (crystals). Three dimensional crystals are defined by a set of vectors, $\{\mathbf{a}_1, \mathbf{a}_2, \mathbf{a}_3\}$, which define the lattice and the unitcell. The unitcell is imagined to connect to itself at each of the six plane boundaries, forming a hypertorus with periodic boundary conditions. Atoms inside the unitcell are referred to as the basis. The crystal is generated by translating the unitcell by all combinations of lattice vectors $\{\mathbf{R}\} = \nu\mathbf{a}_1 + \mu\mathbf{a}_2 + \gamma\mathbf{a}_3$ for integer ν, μ, γ. Systems that are not naturally described as an assembly of unitcells (such as 2D slabs or molecules) can be treated with this approach by choosing an appropriate simulation cell.

The reciprocal lattice is defined by the set of vectors $\{\mathbf{b}_1, \mathbf{b}_2, \mathbf{b}_3\}$. The real space and reciprocal space vectors satisfy $\mathbf{a}_i \cdot \mathbf{b}_j = 2\pi\delta_{ij}$. The set of reciprocal lattice vectors $\{\mathbf{G}\}$, analogous to the real space lattice, consists of all combinations $\nu\mathbf{b}_1 + \mu\mathbf{b}_2 + \gamma\mathbf{b}_3$ for integer ν, μ, γ.

Within periodic boundary conditions Bloch's theorem [46] simplifies the description of single-particle electronic states. The single-particle Hamiltonian of KS-DFT, $\hat{H}_{KS}$, has the periodicity of the lattice. Therefore, all translation operators $\hat{T}_{\mathbf{R}}$ commute with it. This implies that the Hamiltonian and the translation operators have a complete set of common eigenstates. Without loss of generality, this is satisfied if the eigenstates can be written in the following form

$$\psi_{n\mathbf{k}}(\mathbf{r}) = e^{i\mathbf{k}\cdot\mathbf{r}} u_{n\mathbf{k}}(\mathbf{r}) \tag{2.19}$$

where $\mathbf{R}$ is a lattice vector, n labels the band and $\mathbf{k}$ is the wavevector. The functions $u_{n\mathbf{k}}(\mathbf{r})$ have the same periodicity as the lattice, i.e. $u_{n\mathbf{k}}(\mathbf{r} + \mathbf{R}) = u_{n\mathbf{k}}(\mathbf{r})$. The wavevector is confined to the first Brillouin zone.

2.4.2 Planewaves and Grids

The most natural basis set for periodic solids are planewaves $e^{i\mathbf{G}\cdot\mathbf{r}}$, where $\mathbf{G}$ is a reciprocal lattice vector. Kohn-Sham orbitals are represented as a linear combination of plane waves

$$\psi_{n\mathbf{k}}(\mathbf{r}) = \frac{1}{\sqrt{\Omega_s}} \sum_{\mathbf{G}} c_{n\mathbf{k}}(\mathbf{G})\ e^{i(\mathbf{G}+\mathbf{k})\cdot\mathbf{r}} \tag{2.20}$$

where Ω_s is the crystal volume, and the sum runs over the complete set of reciprocal lattice vectors $\{\mathbf{G}\}$. There are an infinite number of $\mathbf{G}$ vectors, but in practice the number of $\mathbf{G}$ vectors in the expansion can be converged to a manageable, finite number. One advantage of a planewave basis

set is the easily controlled convergence criterion: one simply increases the kinetic energy cutoff $E_{cut} = \frac{1}{2}|\mathbf{k}+\mathbf{G}|^2$ until the desired properties are converged to the desired precision.

In terms of the planewave coefficients, the Kohn-Sham equations become

$$\sum_{\mathbf{G}'} \left[\frac{1}{2}\,|\mathbf{k}+\mathbf{G}|^2\delta_{\mathbf{G},\mathbf{G}'} + V_{\text{eff}}(\mathbf{G}-\mathbf{G}')\right] c_{n,\mathbf{G}'}(\mathbf{k}) = \epsilon_n(\mathbf{k})c_{n,\mathbf{G}}(\mathbf{k}) \tag{2.21}$$

the first term is the kinetic energy, which is diagonal in reciprocal space, and the second term is the Fourier transform of the effective potential.

An important operation is the calculation of the density $\rho(\mathbf{r}) = \sum_{n\mathbf{k}} |\psi_{n\mathbf{k}}(\mathbf{r})|^2$ where the sum runs over occupied KS-orbitals. The most efficient way to calculate ρ is to use fast Fourier transforms to obtain real space wavefunctions, and then to square and sum them. This requires the introduction of a real space grid. While the non-zero Fourier components of the wavefunctions lie within the cut-off sphere in reciprocal space, the real space grid is a regular grid of points within the parallelepiped of the unit cell, with a number of points that can be an order of magnitude larger than the reciprocal space grid. The FFTs and grids are also used in the calculations of potentials in the solution of the KS equations. The large number of planewave basis functions does not lend itself to solutions of the KS-equations using traditional full matrix diagonalisation algorithms. The size of the basis is simply too large, and the number of desires eigenstates is usually only a small fraction of that number. Instead, iterative algorithms are employed, where the lowest-lying eigenstates are filtered out, leading to much more efficient methods.

Quantities such as the total energy are given as integrals over the first Brillouin zone. In practice, we need to choose to sample the Brillouin zone using a finite set of points. There are various methods to choose the most representative set of **k**-points. A commonly used method is that of Monkhorst and Pack [47] which uses a regular grid. For a $(q_1 \times q_2 \times q_3)$ grid, we define

$$u_{l,i} = \frac{2l - q_i - 1}{2q_i},\ l = 1, 2, ..., q_i \tag{2.22}$$

and the set of grid points is then given by

$$\mathbf{k} = u_{l,1}\mathbf{b}_1 + u_{l,2}\mathbf{b}_2 + u_{l,3}\mathbf{b}_3,\ \text{for all values of } l \tag{2.23}$$

This results in a regular grid of $q_1q_2q_3$ points in the BZ. It is often possible to achieve significant savings when the symmetry of the crystal can be exploited to reduce the number of **k**-points at which calculations have to be performed.

2.4.3 Pseudopotentials

In an atom, wavefunctions of core states are much more contracted than those of valence states. Since the valence state wavefunctions have to be orthogonal to the core states of the same (angular momentum) l-symmetry, they oscillate rapidly in the core region. Within plane wave basis sets, the representation of these oscillations requires a large number of planewaves with large $|\mathbf{G}|$. Further away from the core, valence wavefunctions are much smoother. By eliminating the core electrons

and replacing their effect by a pseudopotential, we can make the valence wavefunctions smoother in the core region, resulting in appreciable savings of computational resources.

What is a pseudopotential? In its simplest form, it is what the name implies: a potential, but not the real one. The pseudopotential is a potential term entering the Kohn-Sham Hamiltonian, which now describes a pseudo-system with a pseudo-wavefunction. To be useful, we require a relation between the pseudo-system and the real one. In practice, we make a pseudopotential $\hat{V}_{PS}$ such that the pseudo-wavefunctions agree with the real ones outside a spherical region around each atom. We also require that the pseudo-wavefunction with the pseudo-Hamiltonian have the same eigenvalue as the real wavefunction with the real Hamiltonian. Even with these two requirements, there are a large number of different ways of constructing pseudopotentials.

The pseudopotential is the extra potential term that enters the single-particle Hamiltonian for the pseudo-wavefunction, replacing the singular Coulomb potential with a smoother function. To find the pseudopotential, we need to first find the pseudo-wavefunction. There is a huge freedom in doing that, but most schemes set a cutoff radius r_c beyond which the pseudo-wavefunction is equal to the actual wavefunction, and then require that the pseudo-wavefunction is nodeless. With this, the Schrödinger equation can be inverted to find the potential term.

Because of the orthogonality to core states, each l will feel a different potential. This leads to a potential of the form

$$\hat{V}_{PS} = \sum_{l=0}^{\infty} \sum_{m=-l}^{l} v_{PS}^{l}(r) \left|lm\right\rangle \left\langle lm\right| . \tag{2.24}$$

In this form, each l-component of the wavefunction is projected out and multiplied by a separate potential $v_{PS}^{l}(r)$. Pseudopotential theory forms a field in its own right, and almost all pseudopotentials used in actual calculations are constructed by schemes which differ from the above. The fundamental ideas however are the same. Two very important considerations when choosing pseudopotentials for calculations are the hardness and the transferability. Hardness refers to the maximum kinetic energy of planewaves required to obtain converged results in a calculation. The hardness is a function of the cutoff radius; the smaller the cutoff radius, the harder the pseudopotential. The second consideration is the transferability of the pseudopotential. Pseudopotentials are usually generated from wavefunctions of isolated atoms, and one needs to ensure that the pseudopotential is also appropriate for an atom in a crystal or molecule. In general, the transferability is better the harder the pseudopotential.

2.5 Beyond DFT: Green's Function Methods

Approximate DFT is a very successful mean-field theory of electronic structure, but it has a number of shortcomings. The development of exchange-correlation functionals is an active field, but unlike other electronic structure approaches, there is no systematic route to improvement of DFT functionals. In addition, DFT is naturally a theory of ground-state properties, and as such does not offer a good description of some electronic and excited state properties. On the other

hand, wavefunction-based methods from quantum chemistry, or stochastic method like quantum monte carlo (QMC) are very accurate but do not retain any aspects of the one-electron picture, and often do not offer a natural description of reciprocal space.

Green's function methods are a good alternative to both DFT and wavefunction methods. They offer a route to systematic improvement of the approximations while retaining some aspects of the single particle picture. The single particle picture turns into the quasiparticle picture: all of the complicated interactions between particles are captured by describing their effect on the motion of a single particle. Green's functions are also naturally suited to the description of perturbations and responses of systems, and therefore easily connected to spectroscopic experiments.

The one-electron Green's function is defined as

$$G(\mathbf{r}, t; \mathbf{r}', t') = -i\langle 0|T[\hat{\psi}(\mathbf{r}, t)\hat{\psi}^\dagger(\mathbf{r}', t')]|0\rangle \tag{2.25}$$

where $|0\rangle$ is the exact ground-state wavefunction, and the field operators $\hat{\psi}^\dagger, \hat{\psi}$ create or destroy an electron at $(\mathbf{r}, t)$. The time-ordering operator T orders the operators in square brackets such that earlier times are on the right. The Green's function describes the propagation amplitude of an electron, created at $(\mathbf{r}', t')$ and destroyed at $(\mathbf{r}, t)$. For time-independent Hamiltonians G depends only on $t - t'$, and it is often convenient to work in terms of frequency rather than time. The Greens's function can be expressed in bases other than real space, so that in general it takes the form of a matrix $G_{ll'}(t) = -i\langle T[\hat{c}_l(t)\hat{c}^\dagger_{l'}(0)]\rangle$.

For a non-interacting, diagonal Hamiltonian $\hat{H} = \sum_l \epsilon_l \hat{c}^\dagger_l \hat{c}_l$, the Green's function is given by

$$G_{ll'}(\omega) = \frac{\delta_{ll'}}{\omega - \epsilon_l + i\eta \ \mathrm{sign}(\epsilon_l - \mu)} \tag{2.26}$$

where μ is the chemical potential. The poles of the Green's function are simply the energy levels of the electrons. For Hamiltonians that are not simply diagonalisable, the Green's function for the full interacting system is calculated by breaking the Hamiltonian $\hat{H}$ into two parts $\hat{H}_0$ and $\hat{H}_I$, where $\hat{H}_0$ non-interacting and diagonalisable, and $\hat{H}_I$ contains all the particle interaction terms that render the full problem difficult. With the non-interacting Green's function G_0 of $\hat{H}_0$ as a starting point, the full, interacting Green's function G is obtained using many-body perturbation theory (MBPT). In practice this can only be done approximately, but the approximation scheme is useful and systematically improvable. The full theoretical apparatus of MBPT with Feynman diagram techniques is beyond the scope of this thesis. Instead, a few key concepts will be introduced.

One important concept is the self-energy Σ, which encapsulates all of the effects of electron interactions in a single object and connects the non-interacting Greens function G_0 with the interacting Green's function G via the Dyson equation

$$G^{-1} = G_0^{-1} - \Sigma \tag{2.27}$$

where it is understood that all quantities are expressed w.r.t. some basis and contain a time or frequency dependence. Within a quasiparticle picture, the real part of Σ leads to a shift in energy of the quasiparticle relative to its unperturbed state, while the imaginary part of Σ leads

to a finite lifetime. The spectral function $A(\mathbf{k},\omega) = -1/\pi \ \mathrm{Im}[G(\mathbf{k},\omega)]$ is the equivalent of a bandstructure/DOS in the Green's function formalism. In particular, for one-electron Green's functions, the spectral function is directly related to electron emission or absorption phenomena probed by photoemission or inverse photoemission spectroscopy.

At finite temperatures, calculations are carried out in the imaginary time (Matsubara) formalism. Imaginary time calculations turn out to be much simpler for nonzero temperatures. Real time Green's functions at finite temperature can be obtained from imaginary time Green's functions via analytic continuation. The important implication here is that the DMFT as introduced below usually deals with finite T scenarios and thus uses the Matsubara formalism.

2.5.1 Dynamical Mean Field Theory

Dynamical mean-field theory (DMFT) emerged as a method to obtain approximate solutions to the Hubbard model [48, 49]. It is based on the observation that as the number of dimensions of the Hubbard model tends to infinity, the self-energy Σ loses its dependence on $\mathbf{k}$ and becomes purely local. This locality allows the construction of an exact mapping between the Hubbard model and a self-consistent quantum impurity problem. Solving the quantum impurity problem will thus yield the self-energy of the Hubbard model. Using the same idea for Hubbard models in finite dimensions leads to very good approximations.

For completeness, we reproduce the Hamiltonian of the Hubbard model that was introduced in the previous chapter

$$\hat{H} = -t \sum_{\langle ij\rangle,\sigma} (\hat{c}^{\dagger}_{i\sigma}\hat{c}_{j\sigma} + \hat{c}^{\dagger}_{j\sigma}\hat{c}_{i\sigma}) + U \sum_{i} \hat{n}_{i\uparrow}\hat{n}_{i\downarrow}. \tag{2.28}$$

The non-interacting part of $\hat{H}$ (first term) consists of a nearest-neighbour tight-binding model on a (hyper)cubic lattice, with dispersion $\epsilon(\mathbf{k}) = -2tz\cos(\mathbf{k}\cdot\mathbf{a})$ where z is the number of neighbours and $\mathbf{a}$ the vector of lattice constants. Consequently, the Green's function for the non-interacting part of the Hamiltonian takes the general form of Eqn. 2.26. To calculate the interacting Green's function, an auxiliary Anderson impurity model is introduced.

The Anderson impurity model (AIM) describes an atom with on-site interactions embedded in a bath of non-interacting electrons. The AIM Hamiltonian is

$$\hat{H} = \sum_{l,\sigma} \epsilon_l \hat{c}^{\dagger}_{l\sigma}\hat{c}_{l\sigma} + \sum_{\sigma} \epsilon_f \hat{f}^{\dagger}_{\sigma}\hat{f}_{\sigma} + U\hat{n}_{f\uparrow}\hat{n}_{f\downarrow} + \sum_{l,\sigma} \left(V_l \hat{f}^{\dagger}_{\sigma}\hat{c}_{l\sigma} + V_l^{*}\hat{c}^{\dagger}_{l\sigma}\hat{f}_{\sigma}\right) \tag{2.29}$$

where the first term represents the non-interacting medium, the second term the impurity levels, the third term the interactions on the impurity, and the fourth term the hybridisation between impurity and bath. V_l and V_l^* denote the quantum mechanical amplitudes for absorption and emission of electrons by the impurity. The individual hybridisation terms are collected together in $\Delta(\omega) = \sum_l \frac{|V_l|^2}{\omega-\epsilon_l}$. The Hamiltonian of Eqn. 2.29 contains only a single orbital on the impurity, but it may be generalised to multi-orbital impurities. The quantity of interest in the AIM is the local Green's function of the impurity, denoted $\mathcal{G}$. Since we are interested in the physics of the impurity

(the bath being non-interacting and fully solved), we care only about the Green's function of the impurity. In contrast to the Hubbard model, numerically exact solvers for the AIM exist. These impurity solvers start with one of two choices for $\mathcal{G}_0$:

1. If we let the U term in the $\hat{H}$ be the perturbation, the $\mathcal{G}_0$ of the impurity is $[\omega - \epsilon_f - \Delta(\omega)]^{-1}$. The impurity solver takes $\mathcal{G}_0$ and U and returns $\mathcal{G}$. With both $\mathcal{G}$ and $\mathcal{G}_0$, the self energy is obtained from the Dyson equation $\Sigma = \mathcal{G}_0^{-1} - \mathcal{G}^{-1}$.

2. If we let the hybridisation term be the perturbation, we can solve for the local non-interacting Green's function simply by diagonalising the Hamiltonian in the relatively small subspace corresponding to the impurity ($2^{10} = 1024$-dimensional for a d-orbital impurity). The impurity solver takes $\mathcal{G}_0$ and $\Delta(\omega)$ and returns $\mathcal{G}$, from which we can calculate Σ via the Dyson equation. The current state-of-the-art method that uses this hybridisation expansion is continuous time quantum monte carlo (CTQMC).

In mapping a Hubbard model onto an AIM, the first three terms in the AIM Hamiltonian are fully determined: the non-interacting bath term is equivalent to the tight-binding term of the Hubbard Hamiltonian, and the on-site and interaction terms of the Hubbard model are those of the impurity. Only the hybridisation is left undetermined. This is where the self-consistency condition comes in: we require that the Green function of the impurity $\mathcal{G}$ equals the local Green function of the lattice G_{loc}. The Green's function of the lattice is $G(\mathbf{k}, \omega)$

$$G(\mathbf{k}, \omega) = \frac{1}{\omega - \epsilon_{\mathbf{k}} - \Sigma(\omega)} \tag{2.30}$$

and $G_{loc}(\omega) = \frac{1}{N_{\mathbf{k}}} \sum_{\mathbf{k}} G(\mathbf{k}, \omega)$. The key point is that $\Sigma(\omega) \equiv \Sigma_{aux}(\omega)$, i.e. the self-energy of the Hubbard model is set equal to the one obtained from the AIM. The hybridisation is adjusted from one cycle to the next until the self-consistency condition $\mathcal{G} = G_{loc}$ is fulfilled.

DMFT is a mean-field theory for a quantum lattice model. Similar to how in the classical Ising model a mean-field approximation is made by requiring that the local magnetisation of a site equals the average magnetisation of the lattice, DMFT requires that the local Green's function of a site equals the averaged Green's function of the lattice.

2.5.2 DFT+DMFT

DMFT as outlined above is appropriate for lattice models. To apply the same ideas to real materials, they need to be generalised and fitted into a first-principles framework. KS-DFT is a good choice for the non-interacting part of the Hamiltonian. While Hubbard-type interactions could in principle be added for all electrons, they are most appropriate for electrons in d or f orbitals. The interactions between electrons in this correlated subspace are parameterised by Coulomb repulsions U and exchange couplings J.

How are the electrons in the correlated subspace connected to the rest of the solid? The traditional approach is to build a Hubbard-like model from the DFT solution through the use of Wannier functions. Wannier functions are constructed from the relevant d/f bands around

the Fermi energy. Each Wannier function represents a site in the Hubbard model, with hopping parameters t_{ij} between sites derived from first principles. The resulting lattice model is solved with the methods described above.

A second option to connect the correlated subspace with the rest of the solid is to construct projection and embedding operations. This is referred to as embedded DMFT. A projection operator $\hat{P}^{\mathbf{R}}$ is defined such that $G_{loc} = \hat{P}^{\mathbf{R}} G$, i.e. it projects the lattice Green's function G into the correlated subspace of the atom at site $\mathbf{R}$. The projection is usually defined in terms of a set of fixed, quasi-atomic orbitals $\phi^{\mathbf{R}}_{lm}(\mathbf{r})$ which are solutions to the atomic Schrödinger equation in the muffin-tin sphere, for the angular momentum l under consideration. In terms of these functions, the projection is

$$G^{\mathbf{R}}_{loc} = \sum_{\alpha,\beta} \langle \mathbf{r}|\phi_\alpha\rangle \langle \phi_\alpha|G|\phi_\beta\rangle \langle \phi_\beta|\mathbf{r}'\rangle = \sum_{\alpha,\beta} \langle \mathbf{r}|\phi_\alpha\rangle G_{\alpha\beta} \langle \phi_\beta|\mathbf{r}'\rangle . \tag{2.31}$$

When we have obtained the self-energy Σ in the basis of the correlated subspace via the impurity solver, it can be embedded into real space by the embedding

$$\Sigma^{\mathbf{R}}(\mathbf{r},\mathbf{r}',\omega) = \sum_{\alpha,\beta} \langle \mathbf{r}|\phi_\alpha\rangle \Sigma_{\alpha\beta} \langle \phi_\beta|\mathbf{r}'\rangle . \tag{2.32}$$

In this sense the embedding is the inverse of the projection operation. Note how embedding and projection provide a simple way to change from a real-space basis to the finite-dimensional basis of the correlated subspace.

DFT and DMFT are most easily combined into a computational scheme by defining an energy functional. The DFT+DMFT functional $\Gamma[n, G_{loc}]$ for the free energy of a system depends on both the electron density ρ and the local Green's function G_{loc} The form of this functional is

$$\Gamma[\rho(\mathbf{r}), G_{loc}] = T[\rho, G_{loc}] + \int V_{ext} \cdot \rho(\mathbf{r})\, \mathrm{d}\mathbf{r} + E_H + E_{xc}[\rho, G_{loc}] \tag{2.33}$$

Both the kinetic energy term T and the exchange-correlation term E_{xc} now explicitly depend on the local Green's function. The new E_{xc} term is a combination of DFT exchange-correlation, and DMFT correlation term involving the self-energy. However, we cannot entirely separate the part of correlation included in DFT, and the part that comes in through DMFT. We therefore need to correct for the correlation that occurs in both by subtracting a double-counting correction. The theoretically most rigorous option is the exact double-counting [50], which treats both LDA-DFT and DMFT as approximations to an exact energy functional of the Green's function.

With the definition of a free energy functional, we can find the ground state of the system by minimising the functional with respect to the Green's function. This leads to a Schrödinger-like equation that can be solved using numerical techniques very similar to those used to solve the Kohn-Sham equations. If the theoretical formalism has been defined appropriately, one can calculate energies from DFT+DMFT in a numerically robust way. Recently, it has become possible to calculate forces with DFT+DMFT (derivatives of the energy functional $\Gamma[n(\mathbf{r}), G_{loc}]$ with respect to nuclear positions $\mathbf{R}$). This interesting development can now be used to compute phonons with

DFT+DMFT, as shown in Chapter 7.

Chapter 3

Electronic Structure of Niobium Suboxides Nb_2O_{5-x}

This chapter is based on "First-Principles Study of Localised and Delocalised Electronic States in Crystallographic Shear Phases of Niobium Oxide", Can P. Koçer, Kent J. Griffith, Clare P. Grey, Andrew J. Morris, *Phys. Rev. B*, **99**, 075151 (2019). Reproduced with permission from the American Physical Society.

Abstract

Crystallographic shear phases of niobium oxide form an interesting family of compounds that have received attention both for their unusual electronic and magnetic properties, as well as their performance as intercalation electrode materials for lithium-ion batteries. Here, we present a first-principles density-functional theory study of the electronic structure and magnetism of H-Nb_2O_5, $Nb_{25}O_{62}$, $Nb_{47}O_{116}$, $Nb_{22}O_{54}$, and $Nb_{12}O_{29}$. These compounds feature blocks of niobium-oxygen octahedra as structural units, and we show that this block structure leads to a coexistence of flat and dispersive energy bands, corresponding to localised and delocalised electronic states. Electrons localise in orbitals spanning multiple niobium sites in the plane of the blocks. Localised and delocalised electronic states are both effectively one-dimensional and are partitioned between different types of niobium sites. Flat bands associated with localised electrons are present even at the GGA level, but a correct description of the localisation requires the use of GGA+U or hybrid functionals. We discuss the experimentally observed electrical and magnetic properties of niobium suboxides in light of our results, and argue that their behaviour is similar to that of n-doped semiconductors, but with a limited capacity for localised electrons. When a threshold of one electron per block is exceeded, metallic electrons are added to existing localised electrons. We propose that this behaviour of shear phases is general for any type of n-doping, and should transfer to doping by alkali metal (lithium) ions during operation of niobium oxide-based battery electrodes. Future directions for theory and experiment on mixed-metal shear phases are suggested.

3.1 Introduction

Transition metal oxides form a fascinating class of compounds with interesting electronic, magnetic, and crystallographic structures. The phase diagram of niobium oxide is especially rich, with a large number of reported phases for Nb_2O_5 [51, 52, 53], in addition to NbO and NbO_2. The high-temperature Nb_2O_5 polymorph (H-Nb_2O_5) can be regarded as the parent compound of a family known as crystallographic shear (or Wadsley–Roth) phases [17, 20]. In these phases, niobium is present in octahedral coordination, but the Nb/O ratio of Nb_2O_5 prevents the formation of purely corner-sharing octahedra. Instead, the structure must include some amount of edge-sharing connections between octahedra. The metal-oxygen octahedra in these compounds are strongly distorted due to a combination of electrostatic repulsion between transition metal ions and the second-order Jahn–Teller effect [54, 55]. Niobium sites in the center of the block are less distorted than those at the periphery. The crystallographic principles were introduced in Chapter 1. By reduction of Nb_2O_5, small amounts of Nb^{4+} can be incorporated, and a series of $Nb_2O_{5-\delta}$ compounds form. These suboxides include $Nb_{25}O_{62}$, $Nb_{47}O_{116}$, $Nb_{22}O_{54}$, and two polymorphs of $Nb_{12}O_{29}$ with different crystal symmetries (Fig. 4.1, Table 3.1).

The fully oxidised parent compound Nb_2O_5 is a wide bandgap insulator. Low concentrations of valence electrons are introduced through n-type doping to form the $Nb_2O_{5-\delta}$ phases. This reduction changes the crystal structure, but the structural motif of the blocks is retained, which makes the niobium suboxides an excellent series of phases to study the interplay between charge state and crystal structure. Magnetic susceptibility measurements show that all $Nb_2O_{5-\delta}$ phases are paramagnetic, with the number of localised moments increasing with δ [24, 26]. Spin interactions are antiferromagnetic and their strength increases with the level of reduction, as indicated by their Curie–Weiss constants. However, only the monoclinic $Nb_{12}O_{29}$ phase is found to exhibit long-range antiferromagnetic order, with an ordering temperature of 12 K [23, 56]. Electrical conductivity measurements show that all $Nb_2O_{5-\delta}$ phases show thermally-activated transport, except for $Nb_{12}O_{29}$, which is metallic down to 2 K [25, 24]. Both electrical and optical measurements indicate that the electron transport in the $Nb_2O_{5-\delta}$ phases is effectively one-dimensional along the block columns [27]. Despite the evidence for localised electrons, single crystal X-ray diffraction studies on $Nb_{22}O_{54}$ and o-$Nb_{12}O_{29}$ have not found evidence for charge ordering [57]. Additional studies have been performed on $Nb_{12}O_{29}$ indicating the presence of localised as well as delocalised electrons [25, 58, 59].

Despite their interesting physical properties, the niobium suboxides have not been investigated with first-principles methods, and the relationship between the level of reduction and the electronic and magnetic properties remains unclear. Two previous first-principles studies have examined the two polymorphs of $Nb_{12}O_{29}$, with rather different conclusions regarding the electronic structure, despite their very strong structural similarity [60, 61]. Additionally, there is new interest in crystallographic shear phases due to their excellent performance as electrode materials in batteries [13, 62], and the electronic structure of the suboxides is likely to be similar to that of other shear phases.

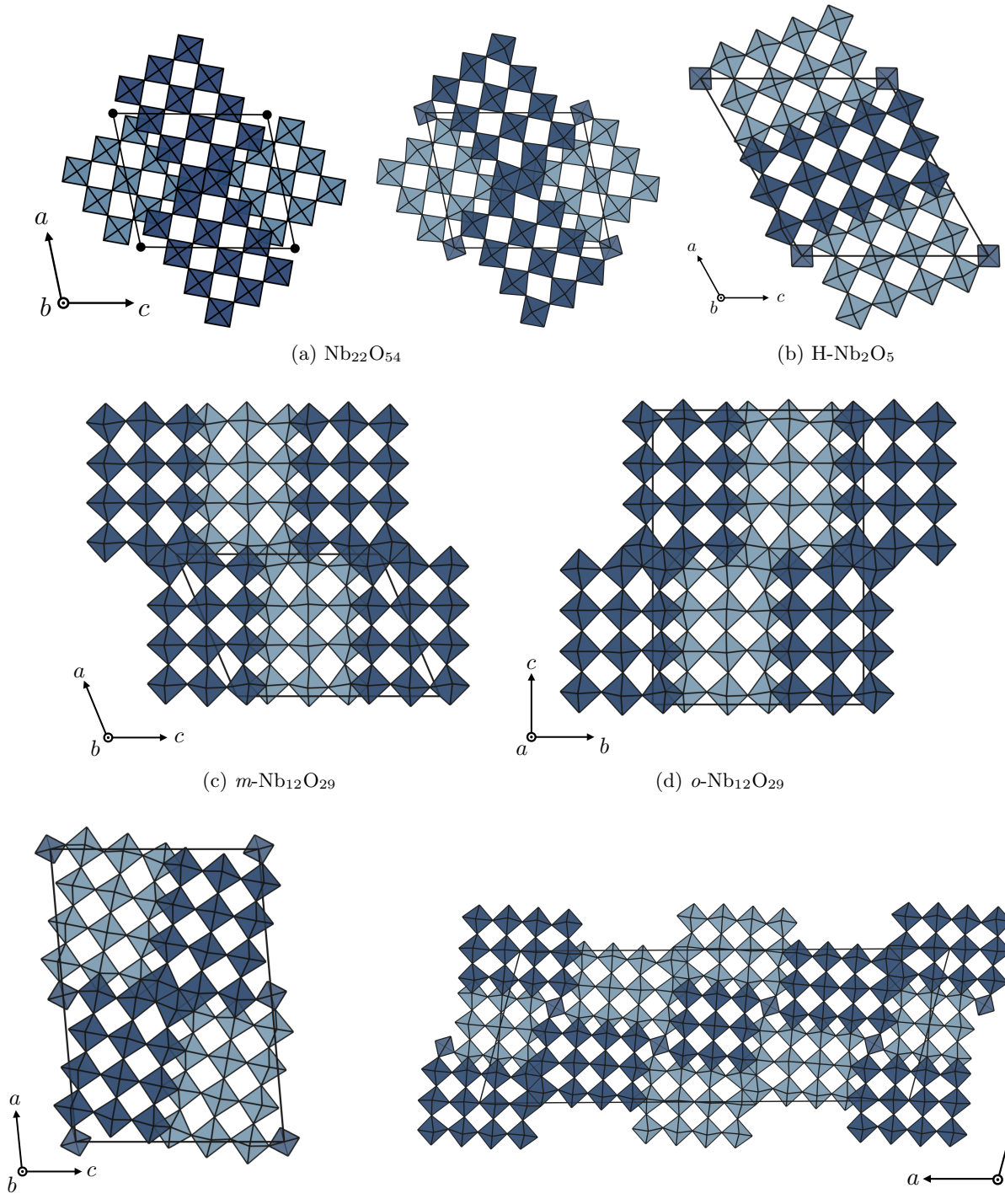

(a) $Nb_{22}O_{54}$ (b) H-Nb_2O_5

(c) *m*-$Nb_{12}O_{29}$ (d) *o*-$Nb_{12}O_{29}$

(e) $Nb_{25}O_{62}$ (f) $Nb_{47}O_{116}$

Figure 3.1: a) Idealised (left) and locally distorted (right) crystal structure of $Nb_{22}O_{54}$. The tetrahedral site is shown as a black dot in the idealised structure. Crystal structures of b) H-Nb_2O_5, c) monoclinic $Nb_{12}O_{29}$, d) orthorhombic $Nb_{12}O_{29}$, e) $Nb_{25}O_{62}$, and f) $Nb_{47}O_{116}$. Light and dark colored blocks are offset by half of the lattice parameter perpendicular to the plane of the page. Unit cells are outlined in black.

Compound	O/Nb	N_{e^-}/block	Space group	Source	a	b	c	β	Block size(s)
H-Nb_2O_5	2.500	0	$P2/m$	Expt. [52]	21.153	3.823	19.356	119.80°	$3\times4, 3\times5$
			$P2$	PBE	21.433	3.841	19.614	119.85°	
$Nb_{25}O_{62}$	2.480	$\frac{1}{2}$	$C2$	Expt. [24]	29.78	3.825	21.14	94.7°	3×4
				PBE	30.224	3.84	21.44	95.0°	
$Nb_{47}O_{116}$	2.468	$\frac{2}{3}$	$C2$	Expt. [24]	57.74	3.823	21.18	105.3°	$3\times3, 3\times4$
				PBE	58.43	3.84	21.44	105.3°	
$Nb_{22}O_{54}$	2.455	1	$P2/m$	Expt. [57]	15.749	3.824	17.852	102.029°	$3\times3, 3\times4$
			$P2$	PBE	15.931	3.842	18.036	102.06°	
			$P2$	PBE+U	15.935	3.836	18.061	101.99°	
m-$Nb_{12}O_{29}$	2.417	2	$A2/m$	Expt. [63]	15.695	3.831	20.723	113.103°	3×4
				PBE	15.903	3.832	20.967	113.1°	
				PBE+U	15.885	3.837	20.950	113.09°	
o-$Nb_{12}O_{29}$	2.417	2	$Cmcm$	Expt. [57]	3.832	20.740	28.890	-	3×4
				PBE	3.833	20.955	29.241	-	
				PBE+U	3.836	20.961	29.204	-	

Table 3.1: Structural properties of niobium (sub)oxides. Experimental and DFT optimised lattice parameters a, b and c are given in Å. Structural optimisations with DFT+U were performed with a U_{eff} value of 4.0 eV on niobium d-orbitals. N_{e^-} denotes number of electrons introduced by doping. Difference between experimental and DFT space group choices related to ordering of tetrahedral sites (see text).

In this chapter, we study six different niobium (sub)oxides using density-functional theory calculations and establish common principles governing their electronic and magnetic behaviour. As the $4d$ band in these materials is highly complex, we first examine $Nb_{22}O_{54}$ in detail, and then present results on $Nb_{12}O_{29}$, $Nb_{47}O_{116}$, $Nb_{25}O_{62}$, and H-Nb_2O_5. We show that all of these structures host flat and dispersive bands, which correspond to localised and delocalised electronic states. Each block can host a single localised state in the block plane that is spread over multiple niobium sites. Delocalised states are present along the shear planes. These results are independent of the type of n-doping, and alkali metal doped (lithiated) shear phases show similar features to the suboxides, which has implications for their use as battery electrodes. We discuss experimental studies of electrical and magnetic properties of the suboxides in terms of a consecutive filling of localised and delocalised states. Finally, based on these results, we suggest new directions for theory and experiment.

3.2 Methods

All density-functional theory calculations were performed using the planewave DFT code CASTEP [64] (version 18.1). Pseudopotentials including Nb $4s$, $4p$, $4d$ and $5s$, O $2s$ and $2p$, and Li $1s$ and $2s$ states were used for all calculations. Calculations using hybrid functionals employed norm-conserving pseudopotentials [65], all other calculations were performed using Vanderbilt ultrasoft pseudopotentials [66]. Crystal structures were obtained from the Inorganic Crystal Structure Database [67] (ICSD) when available. The structure of $Nb_{47}O_{116}$ was constructed as described in Ref. [24] as a unit cell intergrowth of $Nb_{25}O_{62}$ and $Nb_{22}O_{54}$ since no crystallographic data, other than the lattice parameters, was available. The space groups of H-Nb_2O_5 and $Nb_{22}O_{54}$ are reported as both $P2$ and $P2/m$ in the literature [52, 24, 57]. These two space group choices differ

only in the full or partial occupancy of the tetrahedral site. For modelling purposes, the ion on the tetrahedral site has to be ordered, resulting in space group $P2$. Atomic positions and lattice parameters of the structures were relaxed using the gradient-corrected Perdew–Burke–Ernzerhof (PBE) functional [42], until the maximum force on any atom was smaller than 0.01 eV/Å. The calculations used a planewave kinetic energy cutoff of 800 eV for ultrasoft pseudopotentials, and 900 eV for norm-conserving pseudopotentials, unless otherwise stated. The Brillouin zone was sampled with a Monkhorst–Pack grid [47] finer than $2\pi \times 0.03$ Å^{-1}. Lattice parameters obtained from the structural relaxations are listed in Table 3.1, and agree very well with the experimental values. Crystallographic information files (CIF) of the PBE optimised structures are available in the Supplemental Material of the published article on which this chapter is based [68]. All electronic structure calculations were performed for antiferromagnetic spin arrangements in the conventional unit cells, as antiferromagnetic spin interactions are observed experimentally [24].

Semilocal density functionals suffer from self-interaction error, which can be alleviated by the use of DFT+U. For calculations in this work, the DFT+U implementation in CASTEP [69] was used, which defines an effective U value $U_{\text{eff}} = U - J$. A value of $U_{\text{eff}} = 4.0$ eV was chosen for the Nb d orbitals, in line with other studies on niobium oxides that employed similar implementations of DFT+U within planewave codes [70]. The results presented herein are mostly insensitive to the exact value of the U_{eff} parameter if it lies in the range 3–5 eV, even though the value of the bandgap does depend on the choice of the U_{eff} parameter[1]. The structures of $Nb_{22}O_{54}$ and the $Nb_{12}O_{29}$ polymorphs were additionally optimised with PBE+U, and the results are listed in Table 3.1. PBE and PBE+U lattice parameters agree closely, and PBE+U bandstructure and density of states calculations for compounds other than $Nb_{22}O_{54}$ and $Nb_{12}O_{29}$ were performed on PBE optimised structures.

Hybrid functionals are another way to correct the self-interaction error of semilocal functionals. The range-separated HSE06 functional [44] was used to calculate the bandstructure for $Nb_{22}O_{54}$. Due to the significant additional expense incurred by the use of hybrid functionals, the computational parameters for the calculations of bandstructures at the HSE06 level are coarser. The unit cell of $Nb_{22}O_{54}$ contains 610 valence electrons, but since the cell is rather short in one particular dimension and extended in the other two, one cannot use only the Γ-point in the Brillouin zone (BZ) sampling. Instead, a $1 \times 5 \times 1$ Γ-centered **k**-point grid was used in the HSE06 self-consistent field calculations for $Nb_{22}O_{54}$.

Bandstructure calculations were performed for high-symmetry Brillouin zone directions according to those obtained from the SeeK-path package [71], which relies on spglib [72]. A spacing between **k**-points of $2\pi \times 0.025$ Å^{-1} was used. Density of states calculations were performed with a grid spacing of $2\pi \times 0.01$ Å^{-1}, and the results were postprocessed with the `OptaDOS` package [73], using the linear extrapolative scheme [74, 75]. The `c2x` [76] utility and VESTA [77] were used

[1]Regarding the appropriateness of DFT+U for calculating the electronic structure of the niobium suboxides, we note the following: (1) While DFT+U in most popular implementations is most appropriate for the correct description of atomic-like localised states, this study deals with localised states that are *not quite* localised atomic-like orbitals, (2) While the *ab initio* determination of the U parameters is possible, the complexity of the crystal structures is this case would require different U values for different types of niobium sites, (3) Our analysis of the electronic structure of the suboxides includes comparisons at GGA, GGA+U and hybrid functional levels of theory, so the "correct" U value is unlikely to yield drastically different conclusions than the ones presented herein.

for visualisation of wavefunction and density data. Data analysis and visualisation was performed with the `matador` [78] package.

3.3 Results

3.3.1 $Nb_{22}O_{54}$

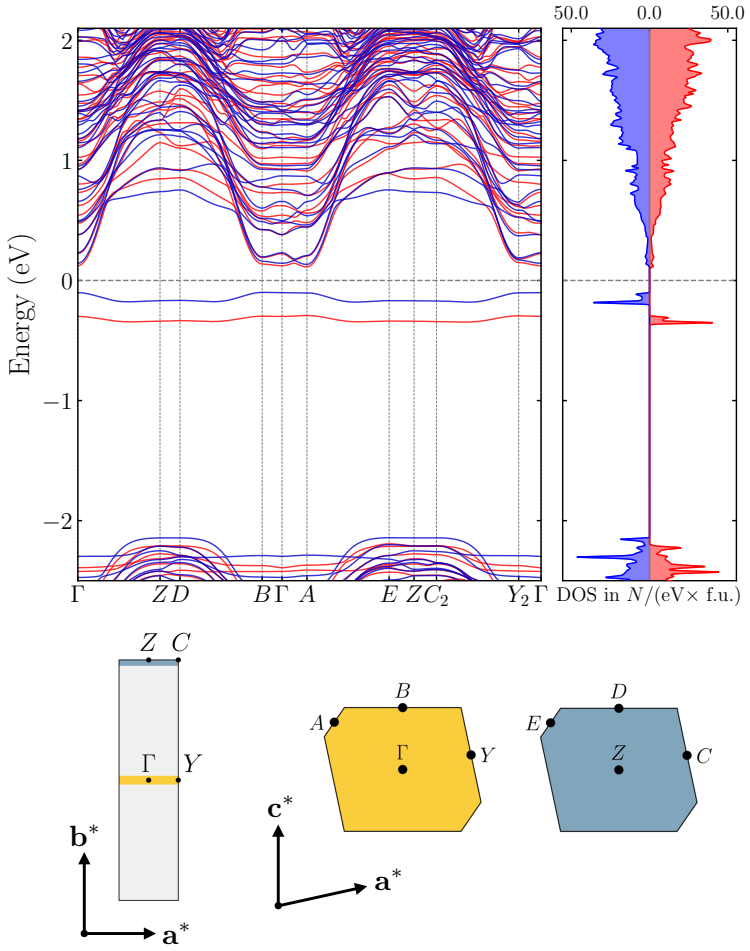

Figure 3.2: Spin-polarised bandstructure and electronic density of states of $Nb_{22}O_{54}$ (PBE+U, $U_{\text{eff}} = 4$ eV). Up and down spins colored in red and blue. High symmetry points are marked on slices through the first Brillouin zone. The flat bands below the Fermi level (dashed line) represent localised states.

$Nb_{22}O_{54}$ crystallises in space group $P2/m$ [57], and shows an ordered mixture of 3×3 and 3×4 blocks of octahedra, in addition to a tetrahedral site (Figure 4.1a). Assuming an ionic model, the compound can be described as $(Nb^{5+})_{20}(Nb^{4+})_2(O^{2-})_{54}$, with two $4d$ electrons per 22 Nb atoms (1 e^- per block, Table 3.1).

The **a** and **c** lattice vectors of $Nb_{22}O_{54}$ are longer than **b**, which is perpendicular to the block plane (Fig. 4.1, Table 3.1). The Brillouin zone (BZ) therefore has one long (along $\mathbf{b}^*$) and two short directions. The PBE+U spin-polarised bandstructure and electronic density of states (DOS) of $Nb_{22}O_{54}$ show a large gap between the valence and conduction bands, which are of oxygen $2p$ and

niobium 4*d* character, respectively (Fig. 3.2). Two fully occupied flat bands (one for each spin) lie within the band gap, leading to the peaks in the DOS below the Fermi level. The flat bands have a very small one-dimensional dispersion, as evidenced by the shapes of the corresponding peaks in the DOS, and represent localised states. In addition to the flat bands, a set of dispersive bands exists just above the Fermi level, which show the largest dispersion along $\mathbf{b}^*$. The separation between the flat bands and the rest of the conduction states is smallest at special points lying in the $\mathbf{a}^*$-$\mathbf{c}^*$ plane of Γ (Y, A, B), and largest in the parallel plane at the BZ boundary (Z, C, D, E). Due to this pattern, the dispersive bands are also effectively one-dimensional. The effective mass tensor for the lowest unoccupied bands was evaluated and diagonalised with the EMC program [79] using a stepsize of 0.0025 bohr^{-1}. The effective mass m_e^* along the high-symmetry $\mathbf{b}^*$ direction at points Γ and A is 0.47 m_e. The effective masses within the $\mathbf{a}^*$-$\mathbf{c}^*$ plane along the other eigenvectors of the effective mass tensor are 1.27 m_e and 3.15 m_e at the CBM minimum at point A. This difference in the effective masses demonstrates that the electron transport predominantly occurs along the $\mathbf{b}^*$ direction. We also note that the bands along $\mathbf{b}^*$ are the only ones that show a reasonably parabolic shape and are not interrupted by frequent band crossings and hybridisation.

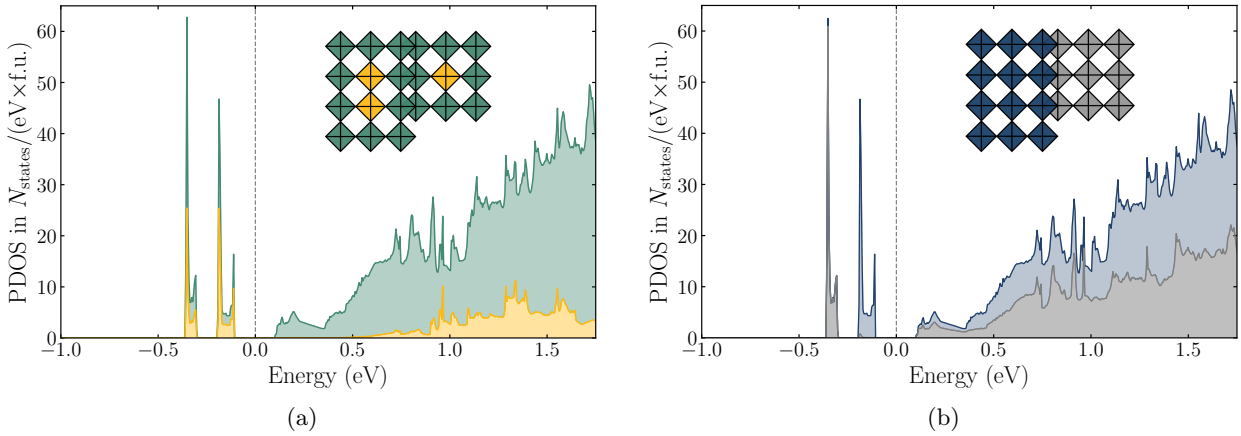

Figure 3.3: Spin-summed projected density of states (PBE+U) for $Nb_{22}O_{54}$. Fermi level is indicated by the dashed line. a) PDOS for central (gold) and peripheral (green) niobium sites. b) DOS projected for sites in different blocks, demonstrating separate localisation of electrons in 3×3 and 3×4 blocks. Contributions from sites are proportional to the shaded area.

With 12 inequivalent niobium sites in the unit cell of $Nb_{22}O_{54}$, site-resolved projected densities of states (PDOS) are complicated and difficult to interpret. More insight is gained by summing PDOS for sets of sites. Figure 3.3a shows the projection onto different types of niobium sites within the structure, which are classified as central and peripheral, depending on where they sit within the block. We note two things: (1) Both peripheral and central niobium sites contribute to the localised states, even though the contribution of the central sites is greater given the ratio of the two; and (2) only peripheral niobium sites contribute to the unoccupied density of states above the Fermi level (until 0.5 eV above), the contribution from the central sites is exactly zero. The PDOS resolved by block in Fig. 3.3b demonstrates that one localised state is contained in the 3×4 block, and the other, lower energy one, in the 3×3 block. Both blocks contribute roughly equally to the density of unoccupied conduction states.

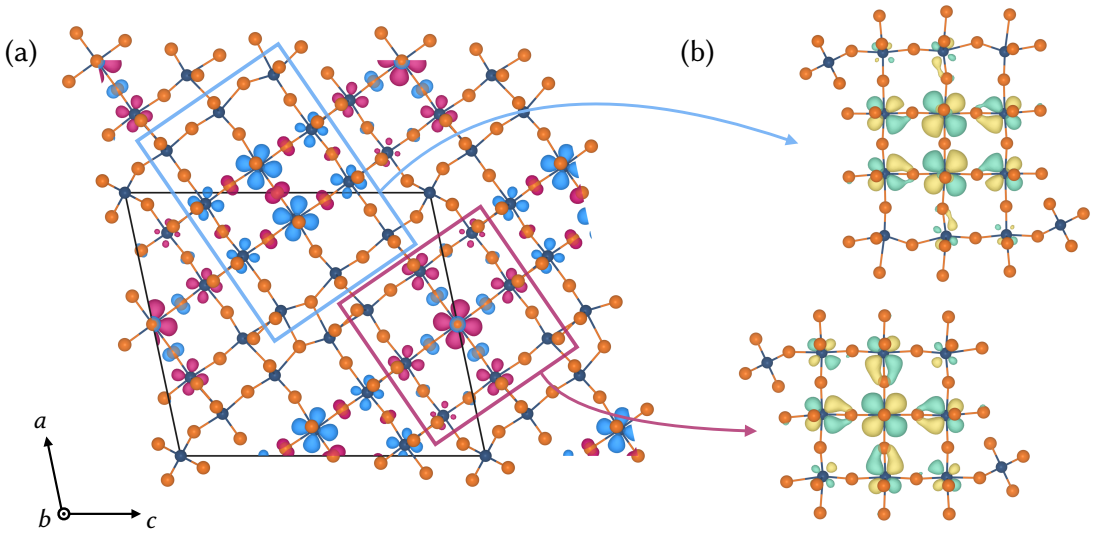

Figure 3.4: a) Spin density plot of $Nb_{22}O_{54}$. Niobium and oxygen shown in dark blue and orange, respectively. Purple and light blue represent up and down spin density, respectively. The rectangles outline the 3×4 and 3×3 blocks. Spin density isosurface drawn at a value of 0.03 $e^-/\text{Å}^3$. b) Kohn-Sham orbitals associated with localised states (flat bands in Fig. 3.2) in 3×4 and 3×3 blocks, different phases of the orbitals shown in yellow and light green.

Spin density in $Nb_{22}O_{54}$ is predominantly located on the central niobium sites (Fig. 3.4a), which also dominate the relevant states as seen from the PDOS (Fig. 3.3a). One spin is located in each block, and the spin arrangement is antiferromagnetic between the two blocks. However, the ferromagnetic arrangement is only marginally higher in energy (less than 1 meV), indicating very weak spin interactions that are likely a result of the long (nm) magnetic interaction lengths. Kohn–Sham orbitals that are occupied by these localised electrons span the entire block, but only have contribution from niobium sites in the same block (Fig. 3.4b). The flat dispersion is a result of the very weak face-on overlap (δ-overlap) between these orbitals along **b**. Both localised orbitals are similar in appearance, despite the different sizes of the blocks. This suggests that the presence of these states is a general feature of block-type structures.

The results presented above were obtained from PBE+U ($U_{\text{eff}} = 4$ eV) calculations. The $\Gamma \rightarrow Z$ segment of the $Nb_{22}O_{54}$ bandstructure computed with HSE06 and PBE is compared to the PBE+U result in Fig. 3.5. Only the up-spin component is shown, which is associated with the localised electron in the 3×3 block. The bandstructure looks similar for all functionals, and importantly, the relevant feature of localised states, i.e. the flat bands, are present even at the PBE level. However, PBE places the flat bands within the dispersive conduction bands, and both are partially occupied, while both DFT+U and the HSE06 functional place the flat bands below the other conduction bands[2]. PBE also places the opposite spin partner of the localised state in the other block much lower in energy than either PBE+U or HSE06. The precise placement of the flat bands depends on the U value, but in the tested range of 2–5 eV the flat bands are placed

[2]For the HSE06 bandstructure calculation, the **k**-point grid was coarser than for the GGA or GGA+U calculations. This was necessary to make the calculations possible. While the HSE06 bandstructure might not be fully converged, we note that the flat band localised state dropped lower in energy the finer the **k**-point grid became. The placement of the flat band state below the rest of the conduction band is therefore correct.

below the conduction bands, and the gap between them increases by approximately 200 meV per increase in U by 1 eV. The degree of electron localisation depends on the presence of a gap between flat and dispersive bands. PBE implies metallic behaviour with some amount of localised electrons, while HSE06 and PBE+U show full localisation of the electrons. A major difference between the HSE06 and PBE or PBE+U calculations is the size of the gap between valence and conduction bands, which is larger by approximately 1.2 eV for HSE06 compared to PBE+U. The spin density and Kohn-Sham orbitals were plotted from the output of PBE+U calculations, but we note that the results from PBE and HSE06 are visually indistinguishable from the PBE+U results.

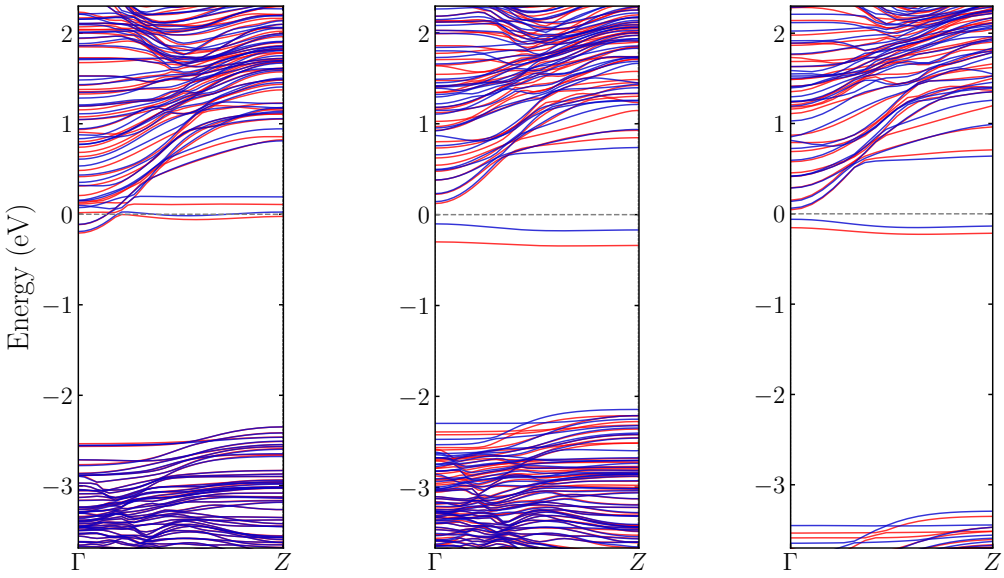

Figure 3.5: $\Gamma \rightarrow Z$ segment of the bandstructure of $Nb_{22}O_{54}$ calculated with different levels of theory. PBE, PBE+U ($U_{\text{eff}} = 4.0$ eV), and HSE06, from left to right.

3.3.2 $Nb_{12}O_{29}$

$Nb_{12}O_{29}$ is more reduced than $Nb_{22}O_{54}$ and hosts two $4d$ electrons per 12 niobium sites (i.e. 2 per block, Table 3.1). The two $Nb_{12}O_{29}$ polymorphs are structurally similar, and only differ in the long-range arrangement of the blocks; in the monoclinic polymorph the blocks form a ribbon along a, while in the orthorhombic structure the blocks zig-zag along c (Fig. 4.1).

The bandstructure of monoclinic $Nb_{12}O_{29}$ shows two flat bands (one for each spin), which lead to two peaks in the DOS (Fig. 3.6). The shape of the real-space unit cell results in a Brillouin zone with two short and one long dimension, and the bandstructure path segments are similar to those in $Nb_{22}O_{54}$. The bands for both spins lie exactly on top of each other due to the symmetry of the crystal structure, even though there is a spatial separation of spins (Fig. 3.8a). The flat bands coexist with more dispersive conduction bands, which show a dispersion which is largest in the $\mathbf{b}^*$ direction, making them effectively one-dimensional. Independent of the position of the flat bands, the larger number of electrons per block requires that some of the electrons fill dispersive conduction bands. This indicates a structural capacity for localised electrons. In $Nb_{12}O_{29}$ flat and dispersive bands are interspersed, while in $Nb_{22}O_{54}$, the flat bands lie below the rest of the

d-bands (cf. Fig. 3.2). Similar to $Nb_{22}O_{54}$, the central Nb sites contribute exclusively to the occupied density of states in a narrow region that is associated with the flat bands (Fig. 3.7). The remainder of the conduction states involve contributions from the peripheral sites.

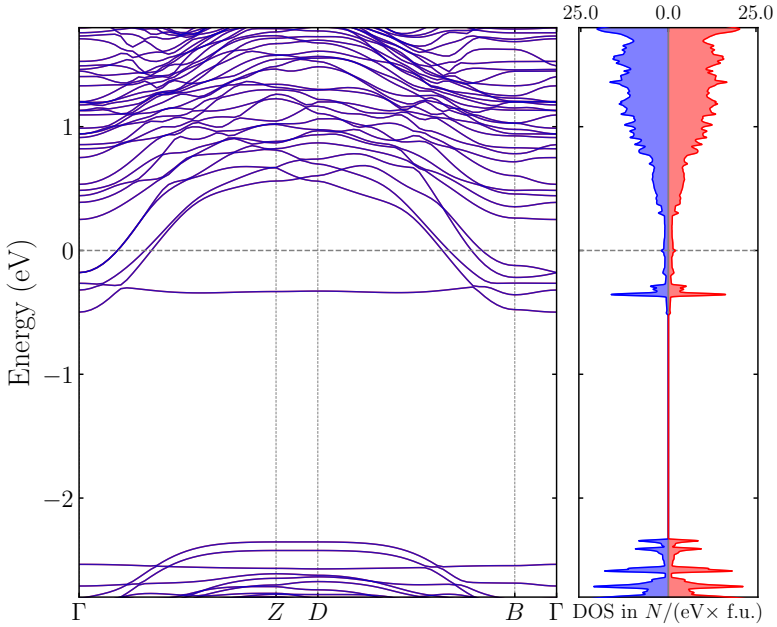

Figure 3.6: Bandstructure and density of states of monoclinic $Nb_{12}O_{29}$ (PBE+U). Fermi level indicated by a dashed line. Up and down spins colored in red and blue, respectively. Flat and dispersive bands are present, with strong similarity to those in $Nb_{22}O_{54}$.

Kohn-Sham orbitals of the localised states (Fig. 3.8c) look remarkably similar to those in $Nb_{22}O_{54}$, and are predominantly made up of Nb *d*-orbitals lying within the plane of the block. Electrons occupying these localised states are responsible for the non-zero spin density (Fig. 3.8a). Orbitals associated with dispersive bands (Fig. 3.8b,d) are made up of d_{xy} and d_{yz} atomic orbitals that are parallel to the crystallographic shear planes. The band dispersion along $\Gamma \rightarrow Z$ is explained by a reduction of in-phase overlap of the constituent atomic orbitals along the real-space **b** direction. The fact that the contributing atomic orbitals are parallel to the crystallographic shear planes and overlap face-on (Fig. 3.8b,d), rather than end-on, can be understood from a crystal field argument. For a transition metal ion in an ideal octahedral crystal field, the t_{2g} orbitals form a degenerate set. The MO_6 octahedra in shear phases, however, are far from ideal. When the degeneracy of the t_{2g} orbitals is lifted by a distortion, those *d*-orbitals that do not overlap with any σ-type ligand orbitals will be lowest in energy and contribute to the low-energy *d*-bands.

The bandstructure of the orthorhombic $Nb_{12}O_{29}$ polymorph (Fig. 3.9) looks very similar to that of the monoclinic polymorph. In fact, the results on the monoclinic polymorph presented above are transferable to the orthorhombic one. Experimentally, both polymorphs are metallic and show antiferromagnetic spin interactions, but only the monoclinic polymorph shows long-range magnetic order [56]. The magnetic susceptibility of *m*-$Nb_{12}O_{29}$ can be fit using the Bonner-Fisher form, possibly indicating one-dimensional magnetism [58]. The differences are clearly subtle, and the small energy differences (10–20 K, around 1 meV) make comparisons using density-functional theory total energy differences difficult. However, the picture of the electronic structure of $Nb_{12}O_{29}$

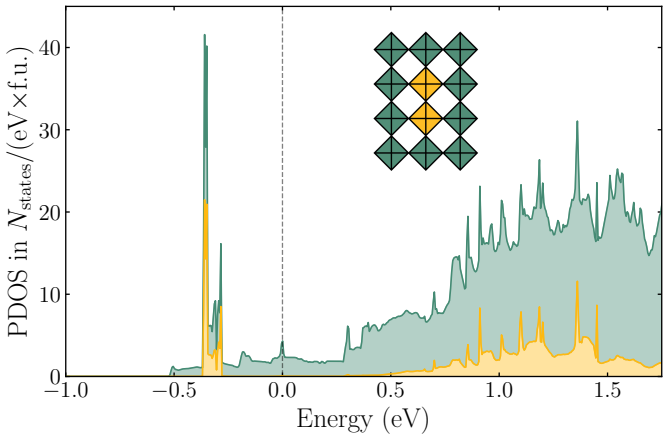

Figure 3.7: Projected density of states (PBE+U) for central (gold) and peripheral (green) niobium sites in monoclinic $Nb_{12}O_{29}$. Central niobium sites contribute to the density of occupied states only in a narrow window that is associated with the flat bands.

that emerges is clear: for both polymorphs, conductivity and local moment magnetism are provided by different sets of electrons. Our conclusions on the orthorhombic polymorph are broadly in line with the first-principles study of Lee and Pickett [61]. Those authors also found a coexistence of localised and delocalised electrons, with the localised spin residing in a large orbital dominated by the central niobium sites of the blocks, with delocalised electrons forming another subset. Our results as well as experimental studies using heat capacity measurements [59] and μSR

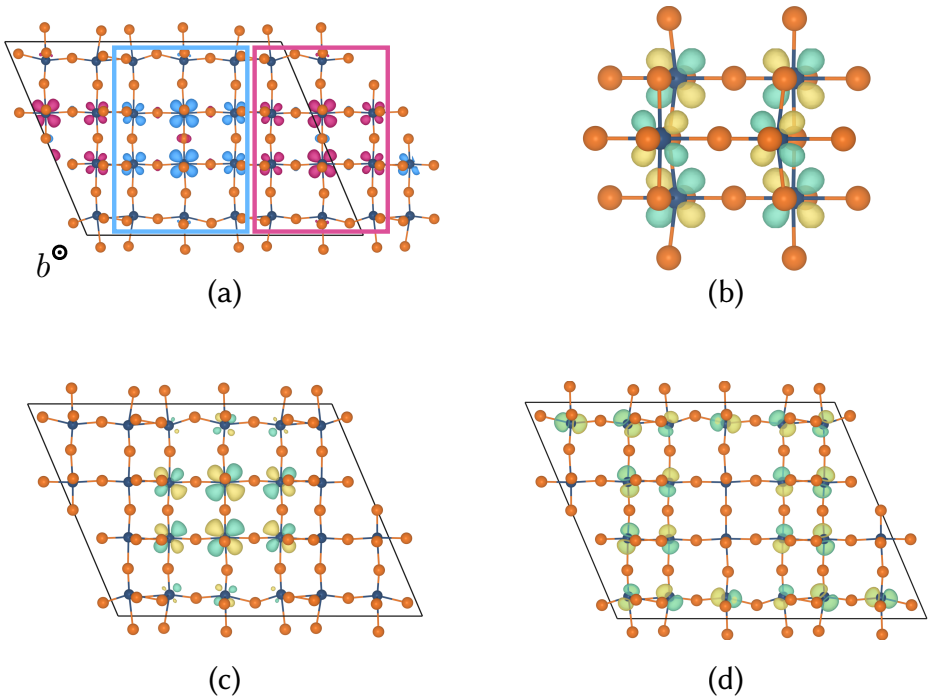

Figure 3.8: Spin density plot (a) and orbitals associated with localised (c) and delocalised (b,d) states in monoclinic $Nb_{12}O_{29}$. Spin density (a) is predominantly located on the central niobium sites, and results from the occupation of localised states (c). Delocalised states have no contribution from the central niobium sites.

spectroscopy [58] establish the presence of localised magnetic electrons in m-$Nb_{12}O_{29}$. We note that a previous study suggested the presence of itinerant moments in m-$Nb_{12}O_{29}$ on the basis of GGA calculations [60]. However, the high density of states at the Fermi level that was described to be the reason for the itinerant magnetism in fact arises from the flat band representing a localised state.

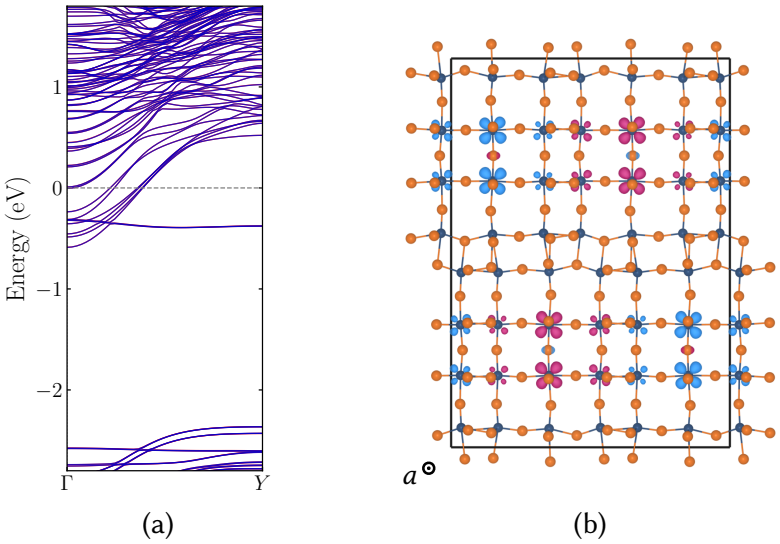

Figure 3.9: Bandstructure (PBE+U) (a) and spin density (b) of orthorhombic $Nb_{12}O_{29}$. $Y = \mathbf{a}^*/2$. The orthorhombic and monoclinic $Nb_{12}O_{29}$ polymorphs show a strong similarity in their bandstructure and spin density distribution (cf. Figs. 3.6, 3.8a).

3.3.3 $Nb_{25}O_{62}$ and $Nb_{47}O_{116}$

The compounds $Nb_{25}O_{62}$ and $Nb_{47}O_{116}$ are less reduced than $Nb_{22}O_{54}$ and host less than one electron per structural block unit (Fig. 4.1, Table 3.1). The mutually occurring localised and delocalised electronic states that were found above for $Nb_{22}O_{54}$ and monoclinic $Nb_{12}O_{29}$ are also present in $Nb_{25}O_{62}$ and $Nb_{47}O_{116}$. Localised states in blocks of the same size are nearly degenerate, and since only a fraction of the localised states is occupied (less than 1 electron per block), it is very difficult in a first-principles calculation to localise the electrons within a specific block. This could be done if the occupation of particular bands was constrained. Similarly, since the energy of the localised states depends on their occupation, judging the relative position of dispersive and localised states in these two compounds is very difficult. Charge densities for the localised states in the $Nb_{47}O_{116}$ and $Nb_{25}O_{62}$ are shown in Fig. 3.10. It seems very likely that both $Nb_{25}O_{62}$ and $Nb_{47}O_{116}$ possess only localised electrons, occupying a fraction of these localised states. Since $Nb_{47}O_{116}$ is a unit cell level intergrowth of $Nb_{22}O_{54}$ and $Nb_{25}O_{62}$, and $Nb_{22}O_{54}$ shows complete localisation of electrons, it is very likely that electrons should also fully localise in $Nb_{47}O_{116}$, at least in those parts of the structure that derive from $Nb_{22}O_{54}$.

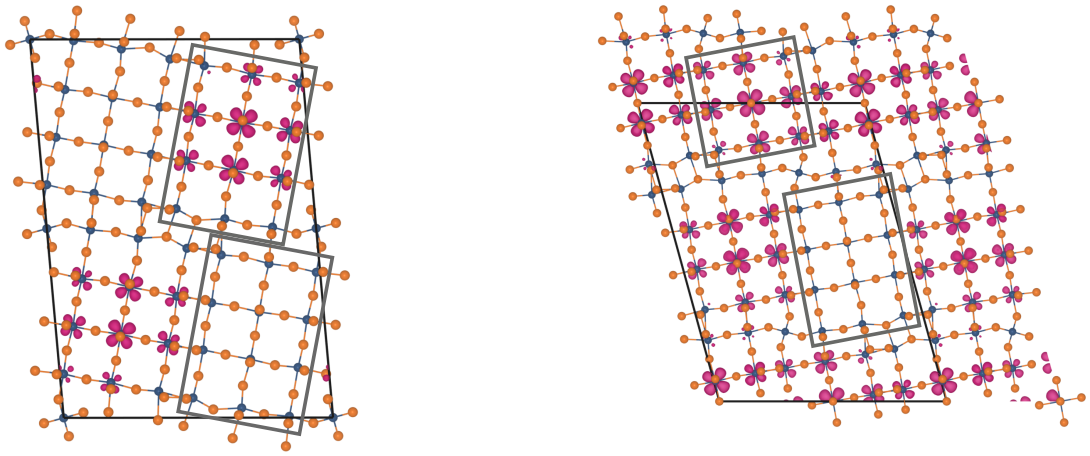

(a) $Nb_{25}O_{62}$ (b) $Nb_{47}O_{116}$

Figure 3.10: Summed charge densities from bands in (a) $Nb_{25}O_{62}$ and (b) $Nb_{47}O_{116}$. Selected empty and filled localised states within blocks are framed by rectangles. The same (conventional) unit cell as in Fig. 4.1 is shown for $Nb_{25}O_{62}$, but a smaller primitive cell for $Nb_{47}O_{116}$.

3.3.4 H-Nb_2O_5

H-Nb_2O_5 is the high-temperature phase of niobium pentoxide, and crystallises in space group $P2/m$ (Table 3.1, Fig. 4.1). As the parent compound of the crystallographic shear structures, its electronic structure provides a reference. However, since it is fully oxidised, all niobium ions have a d^0 configuration and there are no electrons occupying the conduction band.

The bandstructure of H-Nb_2O_5 shows the presence of flat and dispersive bands (Fig. 3.11a), similar to those found for the other shear phases above. However, the relative position of these bands depends on whether or not they are occupied. Doping by alkali metal ions is one way to introduce electrons into the conduction band, and in the particular case of H-Nb_2O_5 this has a practical relevance. Transition metal oxides in general, and the niobium-based oxide shear phases of this work, are used as electrodes within lithium-ion batteries. Like oxygen removal, lithium intercalation is a method to n-dope the material. Similar behaviour can often be observed from charge doping and ion insertion, for example in Na_xWO_3 [80]. The H-Nb_2O_5 phase has been studied extensively for lithium-ion battery applications and it is closely related to other shear phases that have been examined for the same purpose [81, 13]. Inserting a single lithium per unit cell into the middle of the 3×4 block results in a localised state similar to those present in the niobium suboxides (Fig. 3.11b). Note that the electron is entirely localised within the 3×4 block, with the 3×5 block remaining empty. Oxygen removal (as in the suboxides above) and lithium intercalation (examined here) clearly result in similar electronic structure features.

3.4 Discussion

Our results establish that the presence of defect-like flat bands and metallic conduction states is an innate feature of block-type structures. This coexistence arises due to the two different

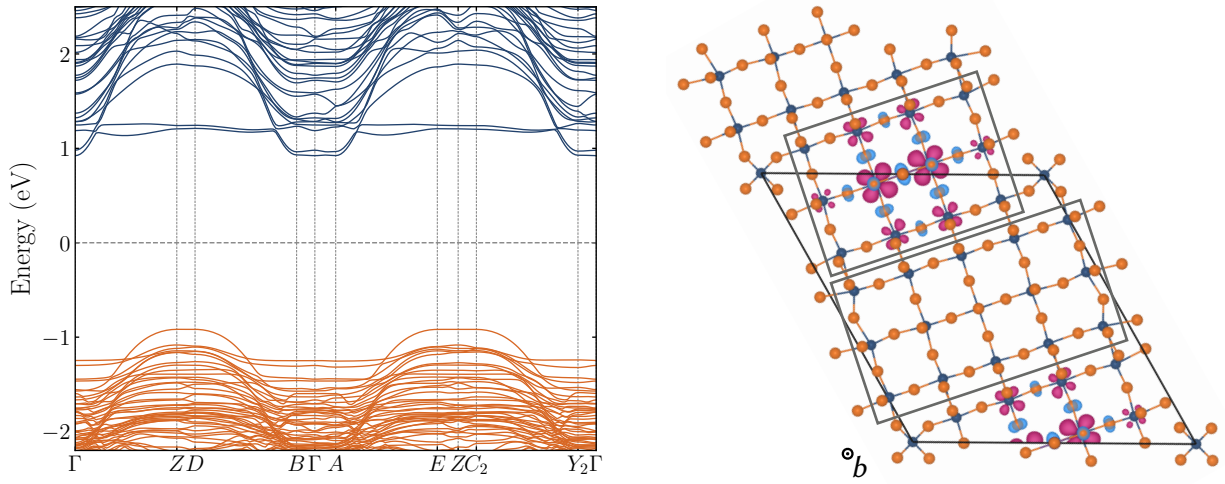

(a) (b)

Figure 3.11: (a) Bandstructure of H-Nb_2O_5 (PBE). Valence and conduction bands are colored in orange and blue, respectively. Flat and dispersive bands are present above the Fermi level (dashed line) similar to those in $Nb_{22}O_{54}$ and $Nb_{12}O_{29}$, but are unoccupied. (b) Spin density plot of lithiated H-Nb_2O_5. A single lithium is located in the middle of the smaller block, inducing a localised state.

types of niobium sites present in the crystal structures; the central NbO_6 octahedra are purely corner-shared, the distance between niobium atoms is larger and orbital overlap is reduced. This isolation results in localised electronic states, while along the crystallographic shear planes, where Nb-Nb distances are smaller and orbitals overlap more strongly, delocalised states are present. Each block can host one localised electron that is, rather unusually, spread over multiple niobium sites. This spread over multiple sites explains why single crystal X-ray diffraction studies on $Nb_{22}O_{54}$ and *o*-$Nb_{12}O_{29}$ do not show the presence of charge ordering [57], despite the detection of localised electrons by magnetic measurements [24][3]. As the electronic structure features are ultimately a result of the blocks as structural units, the same principles are likely to apply to other crystallographic shear phases in the WO_3-Nb_2O_5 and TiO_2-Nb_2O_5 phase diagrams.

Regarding possible electronic conduction mechanisms in the niobium suboxides, the relevant quantities are the filling fraction ν (number of e^- per block), and the energy gap between the flat and dispersive bands. For filling fractions of less than one, only localised states are filled ($Nb_{25}O_{62}$ and $Nb_{47}O_{116}$, Fig. 3.10) and electrons can hop from one filled block to another empty one by a polaron hopping mechanism[4]. The hopping process will have an activation energy. However, in $Nb_{22}O_{54}$ all localised states are filled and this hopping mechanism becomes impossible. With no metallic conduction electrons present, thermal excitation from the defect-like flat bands into the dispersive conduction bands might provide the dominant mechanism, as illustrated in Fig. 3.12a. This mechanism is reminiscent of doped semiconductors, and the activation energy associated with this process will depend on the separation between the flat and dispersive bands

[3] A neutron diffraction study has reported charge ordering on one of the block-central sites in *m*-$Nb_{12}O_{29}$ [82], but only below the antiferromagnetic ordering temperature. As noted previously [57], this can not explain the presence of local magnetic moments in niobium suboxides over wider temperature ranges.

[4] In this case, polaron formation occurs when an electron self-traps in the block by structure deformations. This is only strictly possible if the filling fraction is less than one.

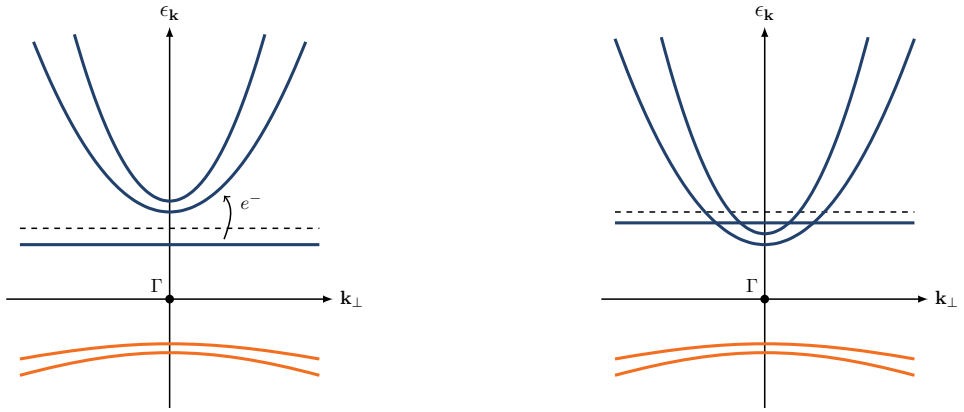

(a) $\nu \leq 1$ (b) $\nu > 1$

Figure 3.12: Schematic of bandstructure for (a) filling fraction $\nu \leq 1$ e^-/block and (b) $\nu > 1$ e^-/block. O $2p$ and Nb $4d$ dominated bands are colored in orange and blue, respectively. Fermi level is indicated by a dashed line, $\mathbf{k}_\perp$ designates reciprocal space vector associated with the real space direction perpendicular to the block plane. The relative position of flat and dispersive bands changes with the filling fraction ν.

(cf. Figs 3.5, 3.12a). Thermal excitation from flat into dispersive bands is also possible in $Nb_{25}O_{62}$ and $Nb_{47}O_{116}$, and could coexist with a polaron hopping mechanism. Finally, in the case of $Nb_{12}O_{29}$, all localised states are filled, but metallic conduction states are also partially filled (Fig. 3.12b). The result is metallic conductivity, which does not require thermal activation. Both Rüscher et al. [25] and Cava et al. [23, 24] have studied the conductivity of $Nb_2O_{5-\delta}$ compounds and observed that all phases except $Nb_{12}O_{29}$ exhibit thermally activated conductivity[5]. Rüscher et al. also noted the effectively one-dimensional electron transport properties along the block columns [27], which are consistent with the calculated band dispersions and the effective masses for $Nb_{22}O_{54}$. In addition, the experiments of Cava et al. show semiconducting electronic behaviour for $Nb_{25}O_{62}$ from 4–300 K; $Nb_{47}O_{116}$ and $Nb_{22}O_{54}$ exhibit semiconducting (thermally activated) conductivity from 0–250 K and from 0–100 K, respectively [24]. Beyond those temperatures, there is a metallic-like range of temperatures in which conductivity decreases again. Given this change in the temperature dependence of the conductivity from semiconducting to metallic, the flat bands associated with localised electrons are likely shallow donor levels (Fig. 3.12). The complex interplay between electron localisation and delocalisation in the suboxides is more similar to phenomena occurring in semiconductors on n-type doping, but distinctly different from metal-insulator transitions in transition metal oxides [83]. Our results suggest that a similar phenomenon of crossover from localised to metallic conduction could occur on lithium doping of H-Nb_2O_5, which might be observed with electrochemical, spectroscopic, or magnetic measurements. The fact that n-doping upon lithium insertion turns the wide bandgap insulating shear oxides into good conductors has important ramifications for their use as battery electrodes; both high ionic and electronic conductivity are required for a good electrode material. In the case of shear oxides, the quasi one-dimensional electron transport occurs along the block columns, which is also the

[5]The resistivity of $Nb_{12}O_{29}$ is 4×10^{-3} Ω cm at 300 K, and 2×10^{-3} Ω cm at 50 K. For $Nb_{22}O_{54}$, the values are 1.5×10^{-2} Ω cm at 300 K and 1.6×10^{-2} Ω cm at 50 K. [24].

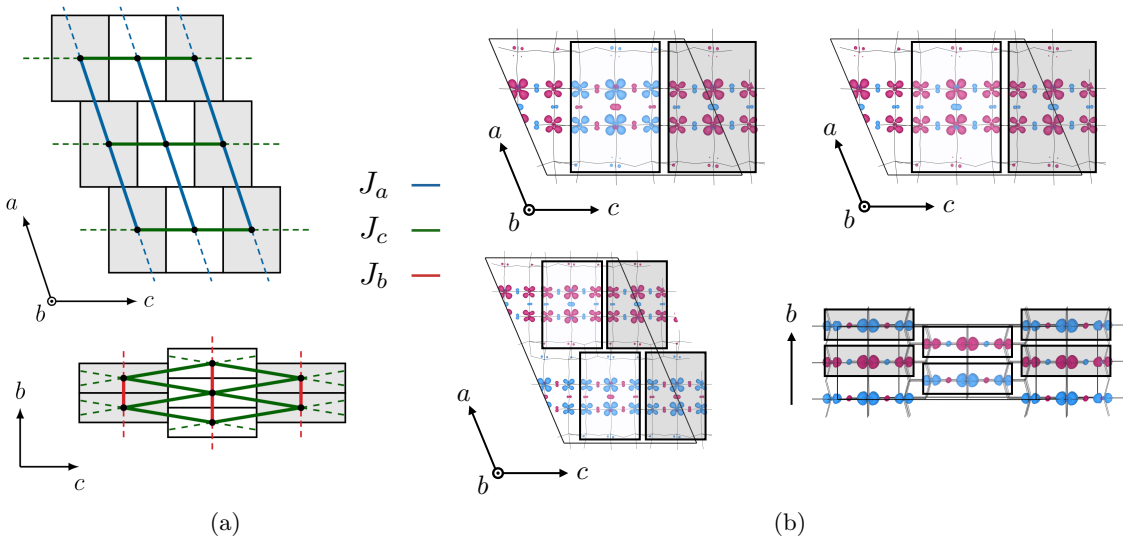

Figure 3.13: a) Possible spin-spin interactions J_i in monoclinic $Nb_{12}O_{29}$ along crystallographic a, b and c directions. b) Different spin arrangements in monoclinic $Nb_{12}O_{29}$. AFM along c (top left), fully FM (top right), AFM along a (bottom left), AFM along b (bottom right). White and grey blocks are offset by 0.5 b throughout.

dominant direction of ionic diffusion [81, 13].

Magnetic susceptibility measurements on the suboxides show that the number of localised moments increases with the degree of reduction [26, 24]. However, under the assumption that $g = 2$, the number of moments calculated from the measurements is smaller than the number of introduced electrons [26, 24]. For $Nb_{12}O_{29}$, this is consistent with one delocalised and one localised electron, but for the remaining suboxides this apparent reduction in the number of local moments is unexpected. Our first-principles results are consistent with complete localisation of electrons until a threshold is exceeded, and therefore all moments should be seen. Deviations in the g-value of the electrons might explain the discrepancy. As the electrons in these suboxides are well-localised, electron paramagnetic resonance (EPR) spectroscopy could provide some insight into the nature of the electronic states and the g-values. For $Nb_{22}O_{54}$ in particular, the different shapes of the magnetic orbitals could be used to detect electrons occupying specific blocks. Another possibility is that localised electrons contributing magnetic moments coexist with magnetically inactive electrons in all suboxides, not just $Nb_{12}O_{29}$. However, we see no evidence for this in our calculations, and the thermally activated conductivity of $Nb_{22}O_{54}$, $Nb_{47}O_{116}$ and $Nb_{25}O_{62}$ seems inconsistent with the presence of magnetically inactive (Pauli-paramagnetic) metallic electrons. Finally, we note that due to the small stoichiometric range of each suboxide, and the difficulty of synthesising these materials, defects are certainly present and could contribute to the reduced number of magnetic moments[6].

Long-range antiferromagnetic order is observed only in the monoclinic $Nb_{12}O_{29}$ phase below 12 K, all other niobium suboxides are paramagnetic [23, 24]. The Curie–Weiss constants of $Nb_2O_{5-\delta}$ are in the range of 0–24 K (0–2 meV), and indicate antiferromagnetic interactions that become stronger with increasing degree of reduction [24]. In $Nb_{25}O_{62}$ and $Nb_{47}O_{116}$, some of the

[6]For a discussion of the types of defects that can occur in these block-type structures, we refer to Refs [84, 85].

localised states are empty (cf. Fig. 3.10), and the magnetic lattice is not fully filled. Independent of the strength of interaction, if not all spins have neighbours to couple with, or there is some randomness in the distribution of the spins, long-range magnetic order is unlikely to emerge. With first-principles calculations it is very difficult to address the question of why only m-$Nb_{12}O_{29}$ orders, but $Nb_{22}O_{54}$ and o-$Nb_{12}O_{29}$ do not, since the energy differences between different magnetic states are very small. However, we can discuss the possible spin-spin interactions simply based on the shape and orientation of the magnetic orbital within the crystal structure. We will focus in particular on monoclinic $Nb_{12}O_{29}$, but similar considerations apply to the other suboxides. The magnetic orbital lies within the plane of the block. The two closest distances (two neighbours) between spins (two nearest neighbours) are along the block columns, with a separation of about 3.8 Å (J_b, Fig. 3.13a bottom). By symmetry, the interaction with spins in the four next-nearest neighbouring blocks along c, that are offset by 0.5 b, has to be the same (J_c, distance 10.6 Å, Fig. 3.13a bottom). In addition to that, each block is connected to two blocks on the same level in monoclinic $Nb_{12}O_{29}$ along the a direction (J_a, distance 15.9 Å, Fig. 3.13a top), and four others offset by 0.5 b along a (distance 15.3 Å, Fig. 3.13a top). Different spin arrangements are easily obtained from DFT calculations (spin densities are shown in Fig. 3.13b), but the energy differences between them are very small (few meV), and change significantly with the level of theory (PBE or PBE+U). Energy differences of a few meV are consistent with the interaction strengths obtained experimentally. The lowest energy magnetic ordering found in our calculations is antiferromagnetic along the c direction (Fig. 3.13b, top left).

3.5 Conclusion

We have shown that the electronic structure features common to n-doped crystallographic shear phases include (1) effectively one-dimensional flat and dispersive bands corresponding to localised and delocalised electronic states, (2) electron localisation in orbitals spanning the block planes, and (3) the partition of localised and delocalised states between central and peripheral niobium sites. Structural block units are also present in WO_3-Nb_2O_5 [86] and TiO_2-Nb_2O_5 [87, 88] phases, and many of these mixed-metal shear phases have been explored as lithium-ion battery electrodes [13, 89]. The principles laid out in this work are likely transferable to these compounds (a recent example being PNb_9O_{25} [90]), and are important for the interpretation of spectroscopic and electrochemical data.

The niobium suboxides show a transition from localised to delocalised electrons, but it is much smoother than commonly observed for metal-insulator transitions in transition metal oxides. In fact, our results portray the suboxides to be closer to n-doped semiconductors, but with a limited capacity for localised electrons. Once a filling threshold is exceeded, delocalised metallic electrons are simply added to existing localised electrons. This process is likely to occur in heavily lithium-doped shear phases during battery operation. Similarly, the experimentally observed crossover from localised to delocalised electronic behaviour in WO_{3-x} [91] might have the same underlying mechanism, as WO_{3-x} phases also exhibit some amount of crystallographic shear. More broadly, the niobium suboxides are an elegant example of the interplay between crystal and electronic

structure, and the balance between electron localisation and delocalisation in oxides of an early transition metal.

Chapter 4

Cation Disorder and Lithium Insertion Mechanism

This chapter is based on "Cation Disorder and Lithium Insertion Mechanism of Wadsley–Roth Crystallographic Shear Phases from First Principles", Can P. Koçer, Kent J. Griffith, Clare P. Grey, Andrew J. Morris, *J. Am. Chem. Soc.*, **141**, 15121–34 (2019). Reproduced with permission from the American Chemical Society.

Abstract

Wadsley–Roth crystallographic shear phases form a family of compounds that have attracted attention due to their excellent performance as lithium-ion battery electrodes. The complex crystallographic structure of these materials poses a challenge for first-principles computational modelling and hinders the understanding of their structural, electronic and dynamic properties. In this chapter, three different niobium tungsten oxide crystallographic shear phases ($Nb_{12}WO_{33}$, $Nb_{14}W_3O_{44}$, $Nb_{16}W_5O_{55}$) are studied using an enumeration-based approach and first-principles density-functional theory calculations. We report common principles governing the cation disorder, lithium insertion mechanism, and electronic structure of these materials. Tungsten preferentially occupies tetrahedral and block-central sites within the block-type crystal structures, and we find that the local structure of the materials depends on the cation configuration. The lithium insertion proceeds via a three-step mechanism, associated with an anisotropic evolution of the host lattice. Our calculations reveal an important connection between long-range and local structural changes: in the second step of the mechanism, the removal of local structural distortions leads to the contraction of the lattice along specific crystallographic directions, buffering the volume expansion of the material. Niobium tungsten oxide shear structures host small amounts of localised electrons during initial lithium insertion due to the confining effect of the blocks, but quickly become metallic upon further lithiation. The combination of local, long-range, and electronic structural evolution over the course of lithiation is beneficial to the performance of these materials as battery electrodes. The mechanistic principles arise from the compound-independent crystallographic shear structure, and therefore likely apply to Nb/Ti oxide or pure Nb oxide shear phases.

4.1 Introduction

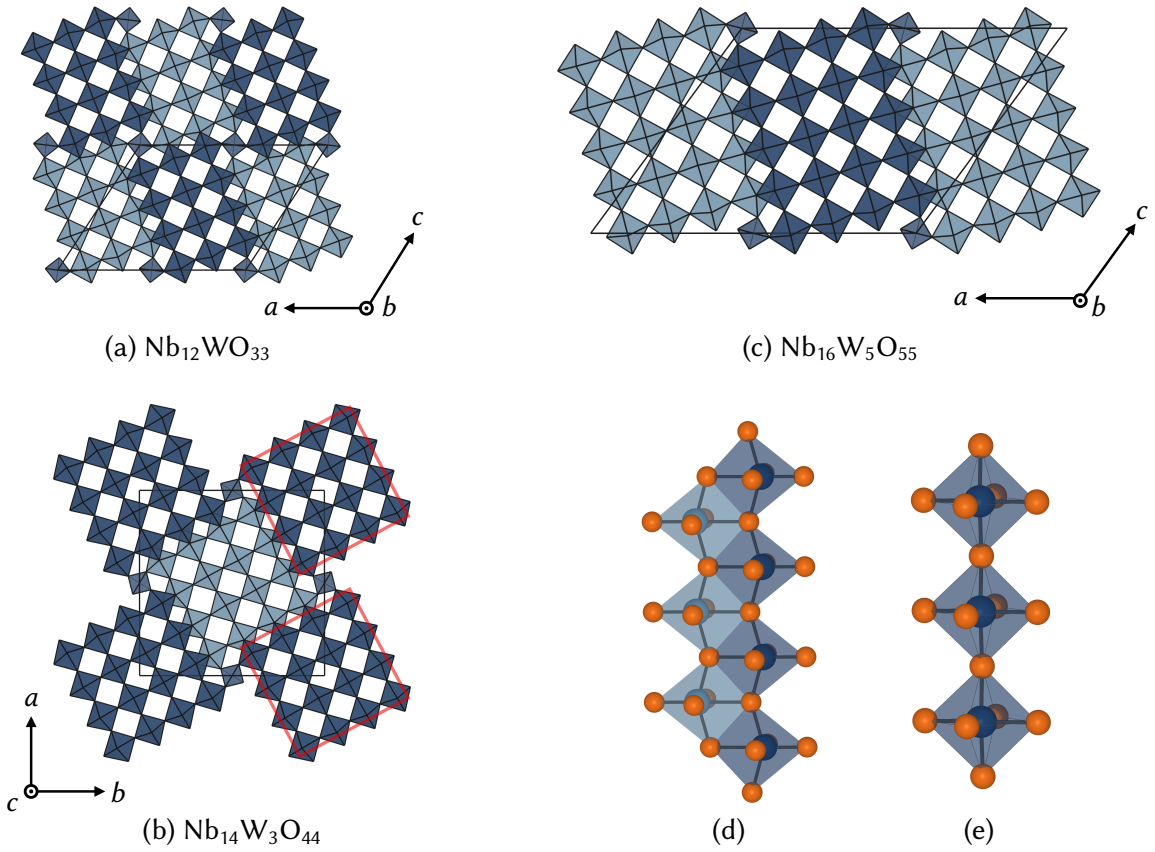

Figure 4.1: Crystal structures of Wadsley–Roth phases studied in this work: (a) $Nb_{12}WO_{33}$ (space-group $C2$), (b) $Nb_{14}W_3O_{44}$ ($I4/m$), (c) $Nb_{16}W_5O_{55}$ ($C2$). Light and dark coloured blocks are offset by half the lattice parameter perpendicular to the plane of the page. Note the increase in block size from a) $Nb_{12}WO_{33}$ (3×4) to d) $Nb_{16}W_5O_{55}$ (4×5). The blocks are framed by crystallographic shear planes (edges of red squares in (b)), along which the metal-oxygen octahedra are strongly distorted (d). The octahedra in the block centre (e) are much less distorted. Transition metal atoms shown in blue and oxygen in orange.

There is a high demand for energy storage materials with improved performance in terms of energy and power density, cycle life, and safety. High-rate electrode materials specifically are needed to accelerate the adoption of electric vehicles by increasing power density and decreasing charging times. While strategies like nanostructuring have been used extensively to improve high-rate performance in materials like LTO [92] ($Li_4Ti_5O_{12}$), this has many drawbacks, including high cost, poor stability, and poor volumetric energy density [93]. However, nanostructuring is not always necessary to obtain high rates. Recent work has shown that very high rates can be achieved in micrometre-sized particles of complex oxides of niobium (T-Nb_2O_5 [81]), ternary Nb/W oxides ($Nb_{16}W_5O_{55}$ and $Nb_{18}W_{16}O_{93}$ [13]), and ternary Ti/Nb oxides ($TiNb_{24}O_{62}$ [94] and $TiNb_2O_7$). In addition to the high-rate capability of these materials, their voltage range of +2.0 V to +1.0 V vs. Li^+/Li minimises electrolyte degradation and SEI formation, and avoids safety issues such as lithium dendrite formation.

Crystallographically, these complex oxides fall into two structural families: compounds with a tungsten bronze-type structure (T-Nb_2O_5 [51, 81] and $Nb_{18}W_{16}O_{93}$ [13]), and Wadsley–Roth phases with block-type structures. The present work is concerned with the family of Wadsley–Roth phases, which encompasses a large number of crystallographically similar compounds in the Nb_2O_5–WO_3 [17] and Nb_2O_5–TiO_2 [87] phase diagrams, in addition to pure Nb_2O_5 [52] and $Nb_2O_{5-\delta}$ [24] phases. The crystallographic principles were introduced in Chapter 1. The structures show strongly distorted octahedra due to a combination of electrostatic repulsion between cations and the second-order Jahn-Teller (SOJT) effect [54, 55]. NbO_6 octahedra at the block periphery are more strongly distorted than those in the centre, resulting in zigzag-like patterns of metal cations along the crystallographic shear planes (Fig. 4.1d). The block size depends in part on the oxygen-to-metal ratio of the compound; a higher number of oxygens per metal allows more corner-sharing connections between octahedra, and therefore larger blocks.

Lithium insertion into Wadsley–Roth phases was first studied systematically by Cava et al. in 1983 [21]. The authors examined 12 different niobium oxide-based shear structures and showed that the crystallographic shear stabilises the structures against undesirable octahedral tilt distortions of the host framework, which had previously been observed in ReO_3 [22]. The frustration of distortions allows lithium diffusion pathways to be kept open. Since the initial report by Cava et al., there have been articles detailing the electrochemical properties of many Wadsley–Roth phases, including $TiNb_2O_7$ [95, 89], $Ti_2Nb_{10}O_{29}$ [96, 97], $TiNb_{24}O_{62}$ [94], $Nb_{12}WO_{33}$ [98, 99], $Nb_{14}W_3O_{44}$ [100, 101], $Nb_{16}W_5O_{55}$ [13], $Nb_{12}O_{29}$ [62, 102], H-Nb_2O_5 [81], and PNb_9O_{25} [103]. These studies have shown good performances of Wadsley–Roth phases as Li-ion battery electrodes, with a remarkable high-rate capability [13, 89]. Ultrafast lithium diffusion was recently observed in $Nb_{16}W_5O_{55}$ with pulsed field gradient NMR spectroscopy and electrochemical techniques [13]. A strong similarity in the structural and phase evolution between different Wadsley–Roth phases has been noted [21, 13]. The phase evolution and voltage profile up to 1.5 Li/TM (Li per transition metal) can generally be divided into three regions; a first solid solution region with a sloping voltage profile is followed by a two-phase-like region where the voltage profile slope is flatter. Depending on the specific Wadsley–Roth phase, this second region of the voltage profile might be almost flat (as in H-Nb_2O_5 [81]), or have a small slope ($Nb_{16}W_5O_{55}$ [13]). Beyond the two-phase-like region, another solid solution ensues. The similarity of their electrochemistry is highlighted by the fact that most articles reporting properties of a single Wadsley–Roth phase draw comparisons to other compounds of the family [94, 13, 103, 21, 98]. Cation ordering preferences (such as in the Ti/Nb oxides [104]) and electronic structure features [24, 68] are also very similar.

Despite the rapidly growing number of experimental studies on Wadsley–Roth phases, reports of computational modelling are almost absent. First-principles modelling of Wadsley–Roth phases is both difficult and computationally expensive; the crystal structures are complex, have large unit cells with a multitude of lithium sites, and, in Nb/Ti and Nb/W oxides, feature inherent cation disorder. In this chapter, the cation disorder, lithium insertion mechanism, and electronic structure of three different Wadsley–Roth phases ($Nb_{12}WO_{33}$, $Nb_{14}W_3O_{44}$, and $Nb_{16}W_5O_{55}$) are examined using first-principles density-functional theory calculations. Their similarity in terms of both structure (cf. Fig. 4.1) and composition calls for a combined study. Building on our

previous work on the electronic structure of $Nb_2O_{5-\delta}$ crystallographic shear phases [68], this study is motivated by the recent report of structural mechanisms in $Li_xNb_{16}W_5O_{55}$ [13], which we aim to understand from first principles.

The chapter is structured as follows. We begin by studying the Nb/W cation disorder using an enumeration approach. We establish cation ordering preferences and the lowest-energy cation configurations, and discover a variability of the local structure caused by the cation disorder. Next, we present a lithium insertion mechanism for $Nb_{12}WO_{33}$ in terms of the sequence of occupied lithium sites, the voltage profile, and the local and long-range structural evolution. We show that the mechanistic principles established for $Nb_{12}WO_{33}$ are transferable to $Nb_{14}W_3O_{44}$ and $Nb_{16}W_5O_{55}$. In fact, $Nb_{12}WO_{33}$ and $Nb_{14}W_3O_{44}$ can serve as model compounds to study the more complex $Nb_{16}W_5O_{55}$. After investigating the electronic structure of the materials over the course of lithium insertion, we go on to discuss common mechanistic principles for this structural family, and their implications for battery performance. We conclude by suggesting new directions for theory and experiment on structural, dynamic, and electrochemical properties of Wadsley–Roth phases.

4.2 Methods

Structure enumeration. Symmetrically distinct cation configurations of Nb/W within the (primitive, single block) unit cells of $Nb_{14}W_3O_{44}$ and $Nb_{16}W_5O_{55}$ were enumerated with a home-made program using established techniques [105] based on a reduction of configurational space by the space group symmetry of a parent structure. Overall, 172 cation configurations were enumerated for $Nb_{14}W_3O_{44}$[1], and 45 for $Nb_{16}W_5O_{55}$[2]. Further details can be found in the Results section.

The minority cation occupancy (i.e. tungsten occupancy) P_S for site S within the crystal structure was obtained according to

$$P_S = \frac{1}{Z} \sum_i \frac{N_{S,i}}{m_S} \, g_i e^{-\frac{E_i}{k_B T}} \,, \tag{4.1}$$

where the symmetrically inequivalent cation configurations are labelled by i, and their degeneracy and energy above the ground state (per unit cell) are g_i and E_i, respectively. $N_{S,i}$ denotes the number of positions of type S that are occupied by tungsten in cation configuration i, and m_S is

[1] The space group of $Nb_{14}W_3O_{44}$ is reported as either $I\bar{4}$ or $I4/m$ [19, 106]. The $I4/m$ space group of $Nb_{14}W_3O_{44}$ requires a partial occupancy of the tetrahedral site and is therefore unsuitable for modelling purposes. In addition, the partial occupancy results in an unphysically small distance of less than 2 Å between two neighbouring tetrahedral positions. Removal of the mirror plane perpendicular to c (cf. Fig. 4.1) allows full occupancy of the tetrahedral site and changes its multiplicity, and we therefore adopt $I\bar{4}$. The only difference between these two space group choices is the full or partial occupancy of the tetrahedral site. In the space groups $I\bar{4}$ and $I4/m$, it is impossible to keep the full symmetry and distribute three tungsten atoms over 17 sites within the primitive unit cell. Instead, for $Nb_{14}W_3O_{44}$, 4 configurations in space group $C2$ and 168 configurations in space group $P1$ were generated.

[2] For $Nb_{16}W_5O_{55}$, the tetrahedral site was fixed to be occupied by tungsten, and the space group of the cation configurations was restricted to be $C2$. The first constraint was imposed because tungsten preferentially occupies the tetrahedral site (see main text). The restriction on the space group choice is necessary to reduce the complexity of the problem. This leaves 10 symmetrically independent sites in the asymmetric unit (cf. Fig. 4.2) over which two tungsten atoms are to be distributed, yielding $\frac{9\times10}{2} = 45$ different cation configurations.

the total number of positions of type S within the unit cell. The partition function is given by $Z = \sum_i g_i e^{-\frac{E_i}{k_B T}}$. Equation 4.1 can be understood as a thermodynamic average of the fraction of positions of type S occupied by tungsten. The lowest energy cation configuration of each phase was used as a starting point to generate structural models of lithiated phases.

Structures of lithiated phases were generated by enumerating all possible lithium-vacancy configurations over sets of lithium sites in $Nb_{12}WO_{33}$ and $Nb_{14}W_3O_{44}$. The crystal symmetry was kept during this enumeration. Overall, 2048 structures were enumerated for $Nb_{12}WO_{33}$, and 256 for $Nb_{14}W_3O_{44}$. Due to the much larger number of possible lithium sites in $Nb_{16}W_5O_{55}$, a full enumeration of lithium-vacancy configurations and subsequent DFT optimisation was computationally too expensive. Further details regarding the generation of lithiated structures can be found in the Results section.

Computational details. All calculations were performed using the planewave pseudopotential DFT code CASTEP [64] (version 18.1). The gradient-corrected Perdew-Burke-Ernzerhof exchange-correlation functional for solids [107] (PBEsol) was used in the calculations presented in this work, unless otherwise specified. Many of the results we report are structural, and the PBEsol functional was therefore chosen because it provides better agreeement with experimental lattice parameters than PBE or LDA [107]. However, all of the results presented in this article show the same trends if computed with PBE instead. Structural optimisations were always performed in two steps: an initial relaxation using efficient parameters, followed by re-optimisation using very high accuracy parameters. For efficient parameters, core electrons were described using Vanderbilt "ultrasoft" pseudopotentials [66], generated using the 'efficient' specifications listed in Table 4.1. These require smaller planewave kinetic energy cutoffs than the 'high accuracy' ones. The planewave basis set was truncated at an energy cutoff of 400 eV, and integration over reciprocal space was performed using a Monkhorst-Pack grid [47] with a spacing finer than $2\pi \times 0.05$ Å^{-1}. Higher accuracy was used to refine low-energy lithiated structures and all cation configurations. Harder, more transferable ultrasoft pseudopotentials were generated using the CASTEP 18.1 "on-the-fly" pseudopotential generator with the 'high accuracy' specifications listed in Table 4.1. The planewave cutoff energy was set to 800 eV, and the Monkhorst-Pack grid spacing was chosen to be $2\pi \times 0.05$ Å^{-1} for calculations on pristine $Nb_{12}WO_{33}$, $Nb_{14}W_3O_{44}$ and $Nb_{16}W_5O_{55}$ structures. For the lithiated phases, the Monkhorst-Pack grid spacing was set to $2\pi \times 0.03$ Å^{-1} due to their metallicity. Spin polarisation had a negligible effect on total energies, and structure optimisations using PBEsol were therefore performed without spin polarisation. Atomic positions and lattice parameters of all structures were optimised until the force on each atom was smaller than 0.01 eV/Å, and the maximum displacement of any atom over two consecutive optimisation steps was smaller than 10^{-3} Å.

DFT+U calculations (following the method of Ref. [69]) were performed to assess the impact of a change in the level of theory on thermodynamics and electronic structure. A value of $U = 4$ eV was chosen for the niobium and tungsten d-orbitals if not specified otherwise. This choice is in line with previous work [68] on niobium oxides. We note (and later demonstrate) that the results are mostly independent of the inclusion and exact value of the U parameter.

To further assess the impact of the DFT functional on our results, calculations using the

Element	Efficient	High accuracy
Nb	3|1.9|8|9|10|40U:50:41:42(qc=5)	3|1.5|10|12|13|40U:50:41:42(qc=6)
W	3|2.3|8|9|10|50U:60:51:52:43(qc=5)	3|2.4|9|10|11|50U:60:51:52:43(qc=6)
O	2|1.7|7|7|9|20:21(qc=5)	2|1.1|15|18|20|20:21(qc=7)
Li	1|1.3|8|9|10|10U:20(qc=5)	1|1.0|14|16|18|10U:20(qc=7)

Table 4.1: CASTEP on-the-fly pseudopotentials used in this work. All pseudopotentials are from standard internal libraries of CASTEP. The first number indicates the angular momentum channel l that is local. The second number is the core radius, r_c. q_c is an optimisation parameter. Lower q_c values result in smoother pseudopotentials, requiring smaller planewave kinetic energy cutoffs. The high accuracy pseudopotentials have a smaller core radius and are less optimised.

rSCAN functional [108] were performed with a development version of the CASTEP code (version 20.x), using ultrasoft pseudopotentials generated for rSCAN [109]. The rSCAN functional is a version of the SCAN functional, modified to provide better numerical stability. The computational parameters were the same as for the PBEsol calculations, only the `grid_scale` was changed from the default value to 2.

Thermodynamics. The thermodynamic phase stability of lithiated niobium-tungsten oxide phases was assessed by comparing the formation energy of different phases. For the pseudobinary phases considered in this work, a formation energy is defined as

$$E_f = \frac{E(\mathrm{Li}_x\mathrm{Y}) - xE(\mathrm{Li}) - E(\mathrm{Y})}{1+x} \tag{4.2}$$

for $\mathrm{Y} = \mathrm{Nb_{12}WO_{33}}$, $\mathrm{Nb_{14}W_3O_{44}}$, or $\mathrm{Nb_{16}W_5O_{55}}$. The formation energies were plotted as a function of the Li number fraction $c_{\mathrm{Li}} = \frac{x}{1+x}$. A pseudo-binary convex hull was constructed between the Y and Li end members at $(c_{\mathrm{Li}}, \mathrm{E_f}) = (0,0);(1,0)$. Thermodynamically stable phases at 0 K lie on the convex hull tieline.

Voltages for transitions between phases lying on the convex hull were calculated from the DFT total energies. For two phases on the hull, $\mathrm{Li}_{x_1}\mathrm{Y}$ and $\mathrm{Li}_{x_2}\mathrm{Y}$, with $x_2 > x_1$, the voltage V for a reaction

$$\mathrm{Li}_{x_1}\mathrm{Y} + (x_2 - x_1)\ \mathrm{Li} \rightarrow \mathrm{Li}_{x_2}\mathrm{Y} \tag{4.3}$$

is given by

$$\begin{aligned} V = & -\frac{\Delta G}{x_2 - x_1} \approx -\frac{\Delta E}{x_2 - x_1} \\ = & -\frac{E(\mathrm{Li}_{x_2}\mathrm{Y}) - E(\mathrm{Li}_{x_1}\mathrm{Y})}{x_2 - x_1} + E(\mathrm{Li})\,, \end{aligned} \tag{4.4}$$

where the Gibbs free energy is approximated by the internal energy, as the pV (pressure-volume) contributions are negligible and thermal contributions are small [110] (an assumption which we will check later).

Finite displacement phonon calculations were performed to assess the contribution of vibrational free energies to the average insertion voltage of $\mathrm{Nb_{12}WO_{33}}$. The phonon calculations used a $5 \times 5 \times 5$ supercell of the primitive Li bcc unit cell. For $\mathrm{Nb_{12}WO_{33}}$ and $\mathrm{Li_{13}Nb_{12}WO_{33}}$ both the

primitive cell and a supercell with twice the volume were used to check convergence. Free energies were computed for Li, $Nb_{12}WO_{33}$, and $Li_{13}Nb_{12}WO_{33}$, and a temperature dependent average insertion voltage was calculated as in Eqn. 4.4.

Electronic structure and postprocessing. Bandstructure calculations were performed for high-symmetry Brillouin zone directions according to those obtained from the SeeK-path package [71], which relies on spglib [72]. A spacing between **k**-points of $2\pi \times 0.025$ Å^{-1} was used for the bandstructures. Density of states calculations were performed with a grid spacing of $2\pi \times 0.01$ Å^{-1}, and the results were postprocessed with the `OptaDOS` package [73] using the linear extrapolative scheme [74, 75]. The `c2x` [76] utility and VESTA [77] were used for visualisation of crystal structures and density data. Data analysis and visualisation was performed with the `matador` [111] package.

4.3 Results

4.3.1 Cation Disorder

Neutron diffraction studies have established that the cation distribution in block-type structures is disordered but not random [104, 106, 94]. Some amount of disorder is also suggested by single crystal X-ray diffraction studies [87, 18]. Labelling conventions for the cation sites in the crystal structures are shown in Figure 4.2, and abide by literature conventions as much as possible. To derive fractional occupancies for the tungsten cations in $Nb_{14}W_3O_{44}$ and $Nb_{16}W_5O_{55}$ we apply a Boltzmann distribution (Eqn. 4.1) using the DFT total energies of the symmetrically inequivalent cation configurations. The results are listed in Tables 4.2 and A.1 for temperatures of 1050–1350 °C, which corresponds to the range of synthesis and annealing temperatures [17, 106, 13]. Cation occupancies in $Nb_{14}W_3O_{44}$ and $Nb_{16}W_5O_{55}$ at 1200 °C are presented in Fig. 4.2 using a colormap.

Site	Expt.[106]	DFT (1050 °C)	DFT (1200 °C)	DFT (1350 °C)
M1	0.39 ± 0.04	0.343	0.328	0.316
M2	0.23 ± 0.07	0.084	0.093	0.101
M3	0.00 ± 0.06	0.045	0.054	0.062
M4	0.00 ± 0.05	0.058	0.068	0.076
M5 (tet.)	0.54 ± 0.11	0.877	0.830	0.782

Table 4.2: Tungsten occupancies on cation sites in $Nb_{14}W_3O_{44}$. All sites except M5 have a multiplicity of four. Taking into account the degeneracies, the number of tungsten atoms in a single block (Fig. 4.2) is three, as required. The synthesis temperature is reported as 1350 °C [17], or 1050 °C [106]. Note that the refinement of fractional occupancies reported in Ref. [106] was performed in $I4/m$, while the DFT predictions are for $I\bar{4}$. The multiplicity of the tetrahedral site is different in these two spacegroups, and the experimental occupancy has been adjusted accordingly. The experimental data [106] includes estimated standard deviations.

If the cation distribution in $Nb_{14}W_3O_{44}$ were completely random, each site would have a tungsten occupancy of $\frac{3}{17} \approx 0.176$. Instead, tungsten is predicted to favour the M5 tetrahedral position and the M1 block-center position (Table 4.2). The preferential occupancy of tungsten on

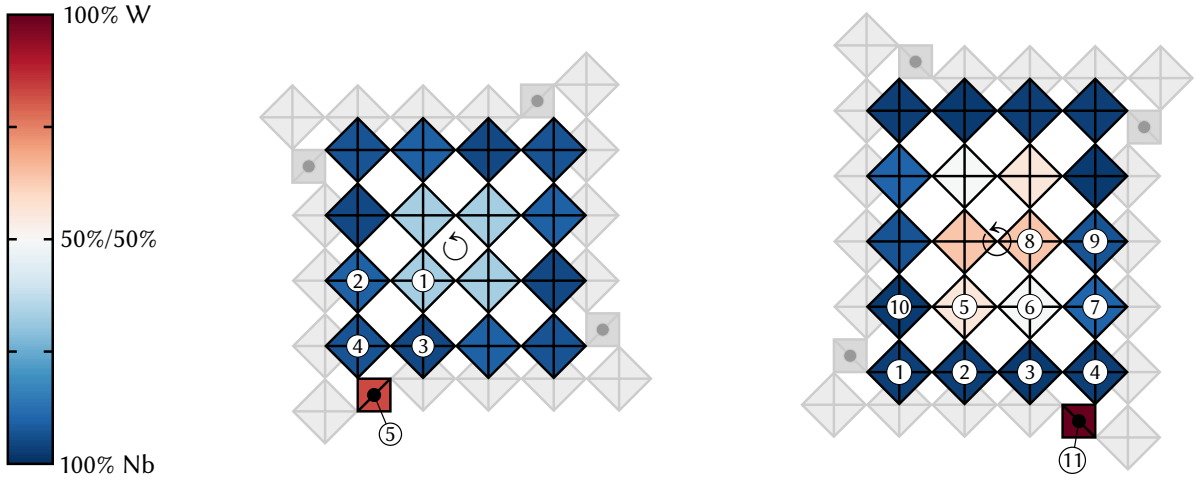

(a) $Nb_{14}W_3O_{44}$ (b) $Nb_{16}W_5O_{55}$

Figure 4.2: Symmetrically inequivalent transition metal cation sites and their occupancies in (a) $Nb_{14}W_3O_{44}$, and (b) $Nb_{16}W_5O_{55}$. The labelling follows Cheetham and von Dreele [106] for $Nb_{14}W_3O_{44}$, and Wadsley and Roth [18] for $Nb_{16}W_5O_{55}$. A temperature of 1200 °C was used to determine the cation occupancies. The positions of axes of fourfold symmetry ($Nb_{14}W_3O_{44}$) and twofold symmetry ($Nb_{16}W_5O_{55}$) are indicated by circling arrows. In both structures, tungsten preferentially occupies the tetrahedral and block-central sites.

the purely corner-shared M1 position is expected; the metal-metal distances are larger in the block center, and the occupation of these sites by the more highly charged tungsten cations (assuming W^{6+} vs. Nb^{5+}) reduces the overall electrostatic repulsion. Preferential occupation of tungsten on the tetrahedral site is due to the shorter M-O distances, which, together with the higher charge of the tungsten cations, lead to better covalency and stronger bonds. In fact, the 15 lowest energy structures generated by enumeration and DFT optimisation all have tungsten on the tetrahedral site. The two lowest energy cation configurations both have the tetrahedral site occupied by tungsten, in addition to two M1 sites. The lowest energy configuration has spacegroup $C2$, whereas the second lowest configuration has spacegroup $P1$ (+123 meV/f.u. above groundstate). The highest energy structure lies +1.29 eV/f.u. above the ground state.

The cation ordering in $Nb_{14}W_3O_{44}$ has previously been investigated by Cheetham and Allen using neutron powder diffraction [106]. DFT-derived fractional occupancies are in reasonable agreement with experiment (Table 4.2). The overall sequence of site occupancy preferences is the same. The occupancy of the tetrahedral site M5 is predicted to be larger, while the occupancy of M2 is predicted to be much smaller. Those two site occupancies also have the largest estimated experimental uncertainty (Table 4.2). Given the very similar local structures of M2, M3, and M4, the large occupancy of M2 as compared to M3 and M4 seems inconsistent. Determining occupancies in these large and complex structures is difficult, particularly when the neutron scattering lengths are not very different (7.054 and 4.86×10^{-15} m for Nb and W, respectively) [112]. We suggest that the cation distribution should be revisited, perhaps with a joint X-ray/neutron study, to help constrain the occupancies.

X-ray diffraction studies suggest that the tungsten atom in $Nb_{12}WO_{33}$ is ordered on the tetrahedral site [18]. An enumeration within the primitive unit cell of $Nb_{12}WO_{33}$ produces only 7

structures, for the 7 symmetrically inequivalent sites. Placing the tungsten atom on the tetrahedral site results in the lowest energy structure. The second lowest energy structure with tungsten in the block-center lies +364 meV/f.u. above the ground state, suggesting a strong preference for the tetrahedral site even compared to the block-center position.

Experimental data regarding the cation ordering in $Nb_{16}W_5O_{55}$ is not available. However, the structure of $Nb_{16}W_5O_{55}$ is very similar to that of $Nb_{14}W_3O_{44}$, with only one additional row of octahedra within each block. For our calculations, the tetrahedral site has been fully occupied by tungsten given the preference of tungsten for the tetrahedral site in $Nb_{14}W_3O_{44}$ and $Nb_{12}WO_{33}$. We have also constrained ourselves to configurations in space group $C2$. The more highly charged tungsten cations again prefer to occupy the purely corner-shared octahedral positions in the block middle of $Nb_{16}W_5O_{55}$; occupancies of sites M5, M6, and M8 are by far the largest (Fig. 4.2, Table A.1). The lowest energy cation configuration for $Nb_{16}W_5O_{55}$ has tungsten on sites M8 and M5, while the second and third lowest energy configurations have tungsten on sites M8 and M6 (+11 meV/f.u. vs. groundstate) and M5 and M6 (+147 meV/f.u. vs. groundstate). The highest energy cation configuration lies +2.27 eV/f.u. above the groundstate.

There are several effects that are not taken into account by the DFT prediction; (1) the modelling necessarily assumes that the material is in thermal equilibrium, but depending on synthesis temperature and annealing time, the kinetics of solid state diffusion might play a role in determining the site occupancies, (2) only single-block cation configurations were studied, limiting the length scale of interactions, (3) at the high synthesis temperature of the metal oxide, temperature effects such as volume expansion, harmonic or even anharmonic vibrations certainly play a role and the DFT energy is a good, but limited substitute for the full free energy. Nevertheless, the lowest energy single-block cation configurations are the best choice to use in modelling the lithiation mechanism. Crystallographic information files (CIF) for all PBEsol-optimised symmetrically inequivalent cation configurations of $Nb_{14}W_3O_{44}$ and $Nb_{16}W_5O_{55}$ are included in the Supporting Information of the article on which this chapter is based [113], in addition to a table of their space groups, relative energies, and degeneracies.

The individual cation configurations deviate from the idealised parent crystal structure by different amounts. For both $Nb_{14}W_3O_{44}$ and $Nb_{16}W_5O_{55}$, the distributions of lattice parameters and unit cell volumes of the cation configurations show a spread of 1-2 % around the mean. In addition to slight differences in lattice parameters, the MO_6 octahedra of both $Nb_{14}W_3O_{44}$ and $Nb_{16}W_5O_{55}$ exhibit different distortions depending on the cation configuration. To analyse these distortions, we introduce three distortion measures: a dimensionless bond angle variance $\Delta(\theta_{\mathrm{oct}})$, the quadratic elongation λ_{oct}, and an off-centering distance d_{oct}. The bond angle variance and quadratic elongation are commonly used distortion measures [114] implemented, for example, in VESTA [77]. The $\Delta(\theta_{\mathrm{oct}})$ measure is defined as the bond angle variance divided by the square of the mean to make the quantity dimensionless:

$$\Delta(\theta_{\mathrm{oct}}) = \frac{1}{12}\sum_{i=1}^{12}\left[\frac{\theta_i - \langle\theta_i\rangle}{\langle\theta_i\rangle}\right]^2, \tag{4.5}$$

where the 12 O-M-O angles are denoted by θ_i. Note that only angles which are 90° in an ideal octahedron are included. The quadratic elongation λ_{oct} is defined as

$$\lambda_{\text{oct}} = \frac{1}{6}\sum_{i}^{6}\left(\frac{l_i}{l_0}\right)^2, \tag{4.6}$$

where l_i are the M-O bond lengths, and l_0 is the M-O bond length for an octahedron with O_h symmetry whose volume is equal to that of the distorted octahedron [114]. The off-centering distance is defined as the distance between the center of the O_6 polyhedron and the metal position

$$d_{\text{oct}} = \left\| \mathbf{r}_{\text{M}} - \sum_{i=1}^{6}\frac{\mathbf{r}_{\text{O},i}}{6} \right\|, \tag{4.7}$$

where $\mathbf{r}_M$ is the metal position and $\mathbf{r}_{\text{O},i}$ are the oxygen positions. Both $\Delta(\theta_{\text{oct}})$ and d_{oct} are zero for an ideal octahedron, and λ_{oct} is one. The three distortion measures are plotted in Fig. 4.3 for the M1–M4 sites in $Nb_{14}W_3O_{44}$ for all 172 cation configurations, but we note that not all configurations will contribute equally due to their different Boltzmann weight.

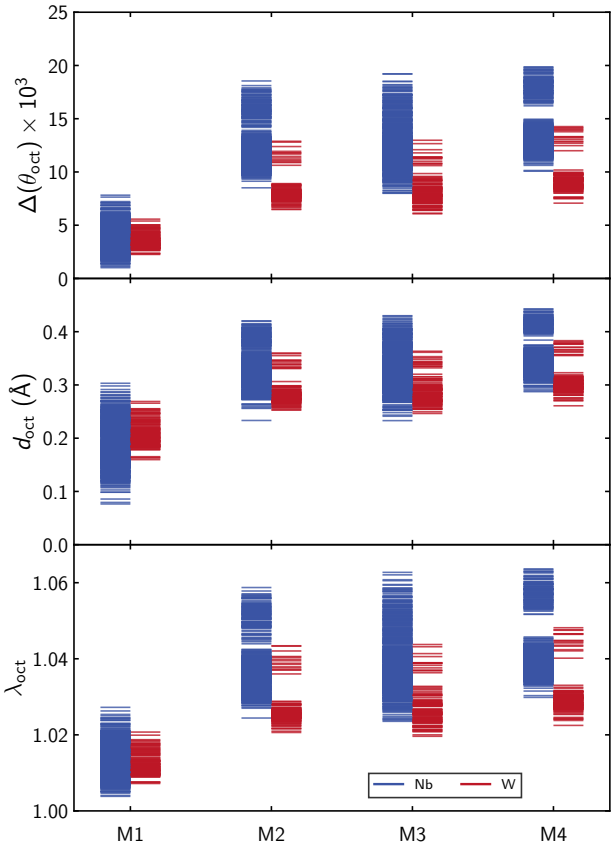

Figure 4.3: Distortion measures for octahedral positions M1–M4 (cf. Fig. 4.2) for all 172 cation configurations of $Nb_{14}W_3O_{44}$. The block-central M1 octahedra are more symmetric than the peripheral M2–M4 octahedra. All sites show a significant spread in their octahedral distortion measures.

The M1 block-center octahedron is, on average, less distorted than the the block-peripheral M2, M3, and M4 octahedra. However, all octahedral positions show a significant spread in their distortion measures, indicating a dependence of the local structure on the cation configuration. To put these results into context, we note that quadratic elongation measures for octahedra in inorganic compounds fall in the range of 1.00–1.07 [114]. $Nb_{14}W_3O_{44}$ exhibits this entire range of distortions if all transition metal sites and cation configurations are considered together. The off-center distances show a spread of approximately 0.15–0.2 Å. Given the convergence tolerance of 10^{-3} Å for the DFT geometry optimisation, this indicates a significant static disorder in the atomic positions. Similar results are obtained for $Nb_{16}W_5O_{55}$, also showing weaker distortions for the block-central sites (M5, M6, M8) and a significant spread in the distortion measures for all transition metal octahedra in the structure. Overall, these results indicate a variability of the local structure at the unit cell level in mixed-metal shear phases that is not captured by a single cation configuration. Each cation configuration has a different set of cation-cation neighbour patterns, which can cause different local distortion directions and strengths. In this study, only cation configurations within the primitive unit cell have been considered. Effects on a longer range can be important, and would lead to a more continuous variation of the local structure. For example, there are two sets within the distortion measures for tungsten on the M2 site (Fig. 4.3), separated by a gap. The more distorted set corresponds to WO_6 octahedra edge-sharing with two other WO_6 octahedra along the crystallographic shear plane, while the less distorted set corresponds to WO_6 edge-sharing with two NbO_6 octahedra. Configurations within a supercell along the c direction (cf. Fig. 4.1) would include WO_6 octahedra sharing edges with one NbO_6 and one WO_6 octahedron, and likely close the gap.

Both niobium and tungsten are generally classified as intermediate SOJT distorters within the group of d^0 cations [115]. In $Nb_{14}W_3O_{44}$, niobium and tungsten show very similar distortion strengths on the M1 positions, while the distortion for tungsten seems to be weaker for sites M2–M4. Given the local structure variability in Nb/W oxide shear structures, it is very likely that the Ti/Nb structures show the same properties, since d^0 titanium is also classified as an intermediate distorter. Stronger distortions are generally exhibited by molybdenum, while zirconium shows only very weak distortions [115]. It would be interesting to examine the effect of Mo/Zr doping on the local structure in shear phases.

4.3.2 Lithium Insertion Mechanism

$Nb_{12}WO_{33}$

Lithium sites in block-type structures divide into three sets; fivefold coordinated ‘pocket’ sites at the edge of the block, fourfold coordinated horizontal ‘window’ positions, and fourfold coordinated vertical ‘window’ positions (Fig. 4.4a). These sites have been deduced by neutron diffraction studies for lithiated block-type structures $TiNb_2O_7$ and H-Nb_2O_5 [116, 117]. We will assume and verify the presence of these sites for $Nb_{12}WO_{33}$. The lithium site energies and local structures in $Nb_{12}WO_{33}$ are shown in Fig. 4.4b. Site energies and structures were obtained by placing a single lithium atom into a $(1 \times 2 \times 1)$ supercell of $Nb_{12}WO_{33}$ (cf. Fig. 4.1) and optimising the structure.

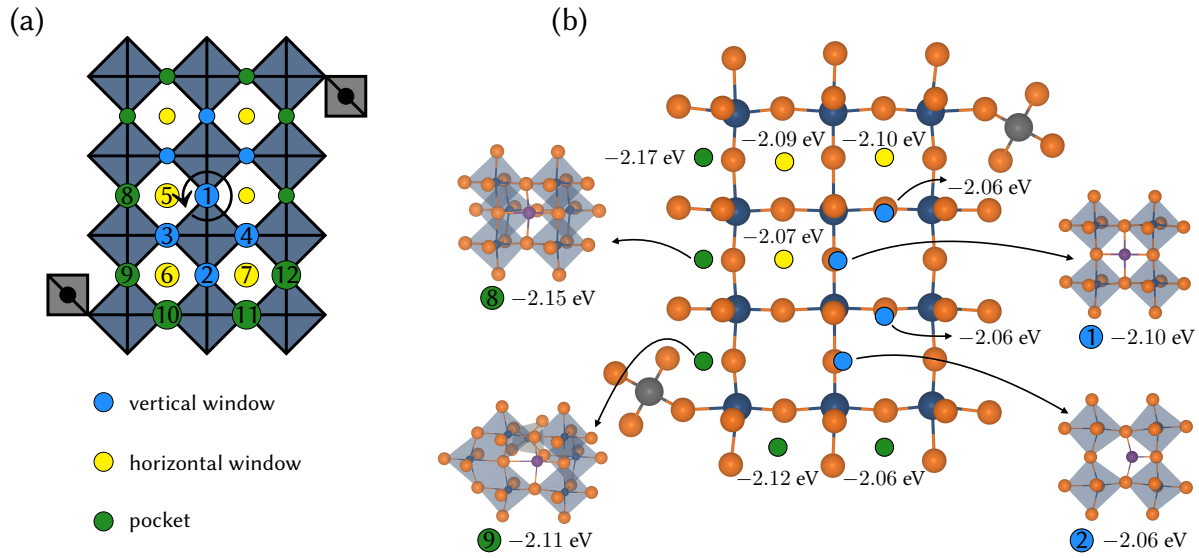

Figure 4.4: (a) Types of lithium sites present in $Nb_{12}WO_{33}$. Window positions are fourfold coordinated by oxygens, pocket positions fivefold. The circling arrow marks the twofold rotation axis of the crystal structure. This symmetry element is kept for the enumeration of lithiated structures. (b) Local structure of lithium sites and site energies in $Nb_{12}WO_{33}$. Only one of each pair of equivalent sites is shown. Insertion into fivefold coordinated sites is energetically more favourable. The vertical window positions next to the crystallographic shear planes (sites 2, 3, 4) are too large for fourfold coordination of lithium. Niobium shown in dark blue, lithium in purple, and oxygen in orange.

The site energies $E_{f,i}$ were calculated as

$$E_{f,i} = E_i - E_{\mathrm{SC}} - E(\mathrm{Li})\,, \tag{4.8}$$

where E_i is the energy of the supercell with a lithium atom placed at site i, E_{SC} is the energy of the supercell, and $E(\mathrm{Li})$ is the energy of bulk lithium. A comparison of the site energies shows that the insertion into fivefold coordinated sites is energetically more favourable. Horizontal window positions have a symmetric arrangement of oxygen atoms, while vertical window positions and some of the pocket sites are less symmetric. In the horizontal window position, the lithium ion sits slightly above the plane formed by the four oxygen atoms. The vertical window positions (sites 2, 3, and 4) are too large for fourfold coordination of lithium by the oxygen atoms, and insertion into these sites is energetically the least favourable. The resulting threefold coordinated lithium ion moves far off the plane formed by the oxygens. The single site energies of around −2.1 eV agree well with the starting point of the voltage profile at 2 V vs. Li^+/Li [99].

In order to simulate the lithium insertion into $Nb_{12}WO_{33}$ over the entire range of lithium content, lithiated structures $Li_xNb_{12}WO_{33}$ were generated by enumerating all possible lithium-vacancy configurations for the sites shown in Fig. 4.4. The special position in the center of the block (site 1) was fixed to be occupied. Using the remaining 11 independent sites for $Nb_{12}WO_{33}$, $2^{11} = 2048$ lithiated structures result, for stoichiometries of $Li_xNb_{12}WO_{33}$ with x ranging from 1 to 23 in steps of 2. This enumeration produces 'snapshots' of the structure and energetics of $Li_xNb_{12}WO_{33}$ at specific stoichiometries. The convex hull of the lowest energy $Li_xNb_{12}WO_{33}$

structures (Fig. A.1a) shows stable or nearly stable phases for each of the stoichiometries examined, indicating that no extended two-phase regions occur. To reliably capture the lithium insertion mechanism, it is useful to include metastable structures (i.e. up to a certain cutoff energy above the convex hull tieline) in the analysis. These metastable structures could be accessed at finite temperatures. If only thermodynamically stable structures are considered, there is no simple sequence of occupation of lithium sites (Fig. 4.5), although there is a slight initial preference for occupation of fivefold coordinated sites and undistorted fourfold sites, especially if metastable structures are included. Both site energies (Fig. 4.4) and Li-Li interactions are important for determining the lithium insertion sequence.

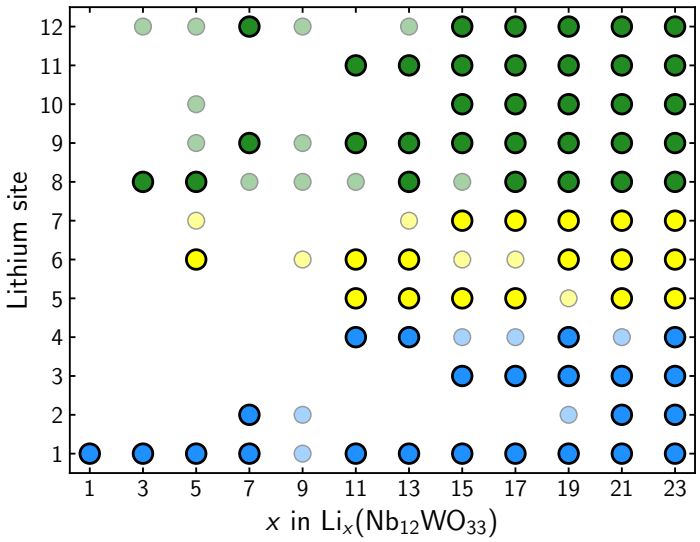

Figure 4.5: Occupation of lithium sites for each sampled stoichiometry. Lithium sites labelled and coloured according to Fig. 4.4. Bold dots correspond to sites occupied in the structure on the convex hull tieline, smaller dots mark sites that are occupied in structures up to 200 meV/f.u. above the convex hull tieline. There is no simple sequence of lithium site occupation.

A comparison of the experimental [99] and DFT-predicted voltage profiles (calculated with Eqn. 4.4) at the GGA and GGA+U levels of theory is shown in Figure 4.6. The DFT-predicted voltage profiles are necessarily composed of abrupt step changes due to the discrete number of stoichiometries, and only qualitative comparisons between experimental and DFT-predicted voltage profiles should be made. We also note that the experimental voltage profile has not explicitly been recorded under equilibrium conditions.

Compared to the experiment, PBEsol slightly underestimates the average insertion voltage; the average experimental voltage up to 1 Li/TM is 1.65 V, whereas PBEsol predicts 1.44 V. The average insertion voltages evaluated with PBE and LDA are 1.30 V and 1.70 V, respectively. We note that the inclusion of a U value for the niobium $4d$ orbitals has a minor effect on the average insertion voltage; for both $U = 3$ eV and $U = 4$ eV, the average insertion voltage up to 1 Li/TM is 1.45 V. It is well known that GGA functionals underestimate lithium insertion voltages of transition metal oxides, but this can be corrected for late first-row elements (Fe/Mn/Co/Ni) by DFT+U methods [3]. The case of niobium oxides seems to be closer to that of d^0 titanium

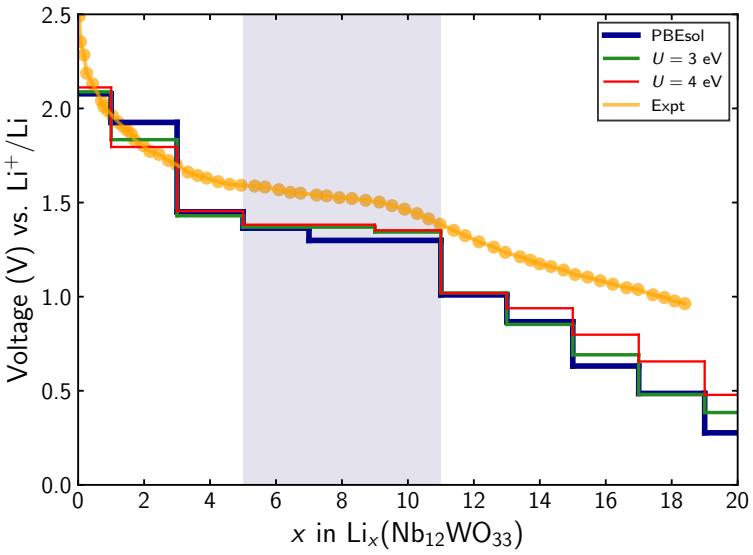

Figure 4.6: Experimental voltage profile (orange, digitised from Ref. [99]) compared to DFT predictions: PBEsol (blue), PBEsol+U for $U = 3$ eV (green), and $U = 4$ eV (red). The predicted voltage profiles are composed of steps due to the discrete sampling of stoichiometries, and are in qualitative agreement with the experimental profile.

oxides, in that the use of DFT+U is ineffective [118]. In addition it is unclear what the value of U should be for this case; the electronic structure and chemical bonding will change as a function of lithium concentrations, possibly requiring different U values at different points to be described accurately. However, total energies (and therefore phase stability) for sets of structures with different U values cannot be compared. Since the difference between GGA and GGA+U results is small, we will continue with a GGA treatment and defer discussion of the electronic structure to a later section. We note that while hybrid functionals like HSE06 are able to provide better agreement with experimental voltages, their use is computationally more expensive and errors of ± 0.2 V are still common [3]. The voltage profile was also computed with the rSCAN functional, which provided almost identical results to PBEsol.

Finite temperature effects, such as configurational entropy and vibrational free energy, were neglected for the calculation of the voltage profiles shown in Fig. 4.6. The vibrational free energy contribution to the average insertion voltage of $Li_xNb_{12}WO_{33}$ up to 1.0 Li/TM was computed as a function of temperature and is shown in Fig. 4.7. Surprisingly, the inclusion of the vibrational free energy gives a room temperature average insertion voltage of 1.36 V, which is 0.1 V lower than the estimate without vibrational contribution. This increases the discrepancy between experiment and theory. Inspecting the phonon density-of-states of Li, $Nb_{12}WO_{33}$, and $Li_{13}Nb_{12}WO_{33}$, it is clear that the combination of Li and $Nb_{12}WO_{33}$ has more phonon modes of lower frequencies compared to $Li_{13}Nb_{12}WO_{33}$, which explains the trend in the average insertion voltage as a function of temperature. The second finite temperature contribution to the insertion voltage, the configurational entropy, can not be estimated easily for $Li_xNb_{12}WO_{33}$, since we only have a set of configurations that were generated by a constrained enumeration. However, a simple lattice gas model [9] shows that the configurational entropy always shifts the average insertion voltage up:

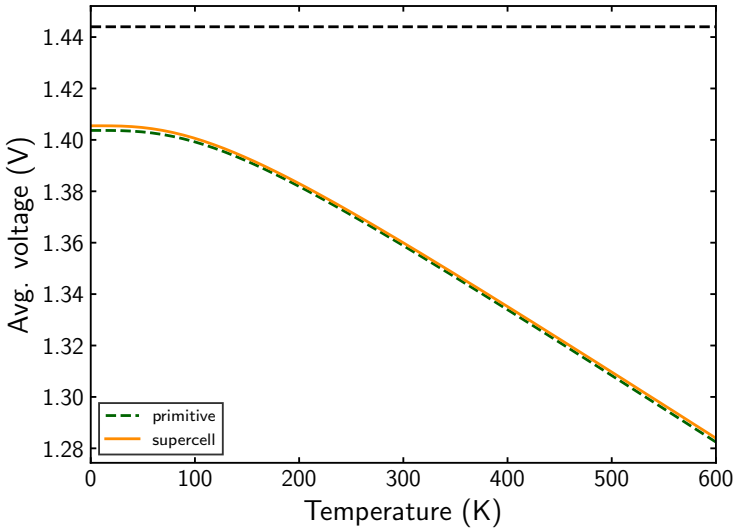

Figure 4.7: Average insertion voltage (PBEsol) up to 1.0 Li/TM with inclusion of vibrational free energy effects. The average voltage was computed as in Eqn. 4.4 without neglecting the vibrational free energy contributions for $Nb_{12}WO_{33}$, Li, and $Li_{13}Nb_{12}WO_{33}$. The black dashed line represent the average insertion voltage without inclusion of vibrational effects, and the green and gold lines represent the same calculation for different supercell sizes.

at 1.0 Li/TM, not all Li sites in $Li_{13}Nb_{12}WO_{33}$ are filled, but Li and $Nb_{12}WO_{33}$ are fully ordered compounds. Thus, the configurational entropy will only lower the free energy of $Li_{13}Nb_{12}WO_{33}$, having no effect on Li or $Nb_{12}WO_{33}$. Therefore, the average insertion voltage will increase. We note that both vibrational and configurational contributions are small compared to the impact of the exchange-correlation functional.

While the average insertion voltage is underestimated, the DFT-predicted profiles in Fig. 4.6 look similar to the experimental one; there seems to be a region with rather flat slope between $x = 3$ and $x = 11$, which matches the flatter second region of the experimental profile. Despite the shallow gradient of the electrochemical profile, this region does not correspond to a true two-phase region. The similarity between the experiment and DFT prediction is present for both the PBEsol and PBEsol+U results, and becomes clearer if the predicted profiles are shifted upwards by the difference in the average insertion voltage, corresponding to an adjustment of the Li chemical potential (Fig. A.1b).

The evolution of the lattice parameters of $Nb_{12}WO_{33}$ as a function of lithium content is anisotropic (Fig. 4.8a). Lattice parameter b, which is perpendicular to the plane of the block, expands, and most of the expansion takes place between $x = 5$ and $x = 11$. Lattice parameters a and c first expand until $x = 5$, and then contract to a minimum at $x = 11$ that lies almost 0.3 Å below the lattice parameters of the pristine structure. For $x > 11$, a and c expand again. The lattice contraction occurs in the same region as the flatter part of the voltage profile (shaded blue in Figs. 4.6, 4.8a). The same evolution of the lattice parameters is also observed when phases up to 200 meV/f.u. above the convex hull tieline are included in the analysis. These metastable structures might be formed during cycling, or be partially accessible due to finite temperature effects. However, the same lattice evolution would result.

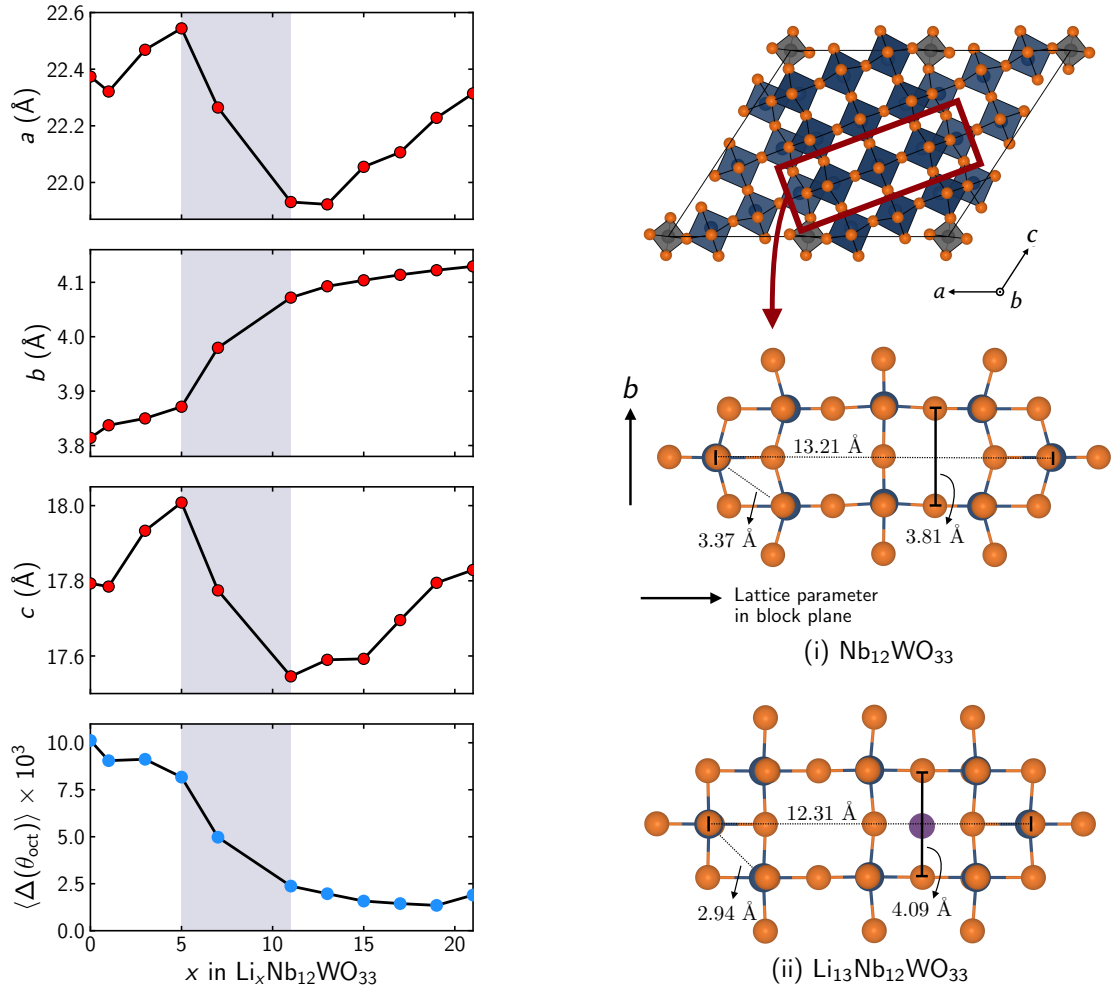

(a) (b)

Figure 4.8: Structural evolution of $Li_xNb_{12}WO_{33}$ as a function of lithium content x. (a) The lattice parameters evolve anisotropically; b expands over the entire x range, while a and c first expand until $x = 5$, contract, and then expand again beyond $x = 13$. The average octahedral distortion $\langle\Delta(\theta_{oct})\rangle$ decreases, with most of the decrease between $x = 5$ and $x = 11$. (b) The local structure in (i) $Nb_{12}WO_{33}$ and (ii) $Li_{13}Nb_{12}WO_{33}$ along the second row of octahedra in the 3×4 block. Niobium in dark blue, oxygen in orange, and lithium in purple. The interatomic distances demonstrate 1) an expansion perpendicular to the block plane, 2) a contraction within the block plane, and 3) a decrease of Nb-Nb distances along the shear planes. Compared to $Nb_{12}WO_{33}$, the NbO_6 octahedra in $Li_{13}Nb_{12}WO_{33}$ are more symmetric, corresponding to a smaller distortion measure $\langle\Delta(\theta_{oct})\rangle$.

Over the course of lithium insertion, the transition-metal oxygen octahedra become progressively more symmetric, as shown by the evolution of the average distortion measure $\langle\Delta(\theta_{oct})\rangle$ (Fig. 4.8a), obtained according to

$$\langle\Delta(\theta_{oct})\rangle = \frac{1}{N_{oct}} \sum_{j=1}^{N_{oct}} \Delta_j(\theta_{oct})\,. \tag{4.9}$$

Compared to the pristine $Nb_{12}WO_{33}$, the distortions in both the MO_6 octahedra and the lithium sites are largely removed in $Li_{13}Nb_{12}WO_{33}$ (Fig. 4.8b). The evolution in the lattice parameters and

the local structure is closely linked. Over the course of lithium insertion, the blocks of octahedra in $Nb_{12}WO_{33}$ first expand and then contract within the *ac* plane (Fig. 4.8). Perpendicular to the *ac* plane, they expand monotonically. An expansion is expected for lithium insertion, as an increase of the number of atoms within the same volume should lead to an increase thereof. The decrease in the lattice parameters within the block is associated with the MO_6 octahedra symmetrisation. As the apical oxygens of the octahedra along the shear planes are pulled towards the block center, the lattice shrinks within the block plane (Fig. 4.8b). The block height expands from 3.81 Å to 4.09 Å, and the Nb-Nb distance along the shear plane decreases by over 0.4 Å.

The structural changes are closely connected to the occupation of specific lithium sites; the thermodynamically stable phases of $Li_xNb_{12}WO_{33}$ (Fig. 4.5) show occupation of undistorted sites (1, 6, and 8) for $x \leq 5$. For $x \geq 7$, vertical window positions that were previously highly distorted are occupied, and the distortions in both lithium sites and octahedra start to be removed.

Based on the predicted voltage profile, lattice evolution, and local structure changes, the overall phase evolution of $Nb_{12}WO_{33}$ through three regions can be rationalised. Taken together, and compared to previous experiments, these results suggest two solid solution regions, with a two-phase-like region in between. The two-phase-like region is marked by a block-plane contraction and a removal of distortions in the transition metal-oxygen octahedra.

$Nb_{14}W_3O_{44}$ and $Nb_{16}W_5O_{55}$

Following on from $Nb_{12}WO_{33}$, we now demonstrate that very similar lithium insertion mechanisms apply to $Nb_{14}W_3O_{44}$ and $Nb_{16}W_5O_{55}$.

The crystal structures of $Nb_{12}WO_{33}$, $Nb_{14}W_3O_{44}$, and $Nb_{16}W_5O_{55}$ are all are based on the block principle and feature the same local structural distortions (cf. Fig. 4.1). This similarity leads to the presence of the same types of lithium environments in all three structures. The classification into pocket and window sites in $Nb_{14}W_3O_{44}$ and $Nb_{16}W_5O_{55}$ follows the same principles as for $Nb_{12}WO_{33}$ (Fig. A.2). Notably, the vertical window positions next to the crystallographic shear planes (sites 3 and 5 in $Nb_{14}W_3O_{44}$, and sites G, H, K in $Nb_{16}W_5O_{55}$, Fig. A.3) are strongly distorted due to the zigzag patterns of the octahedra (cf. Fig. 4.1). Lithium site energies for $Nb_{14}W_3O_{44}$ are in the range of -2.0 eV to -2.2 eV, while the site energies for $Nb_{16}W_5O_{55}$ are slightly lower (-2.2 eV to -2.4 eV), due to the higher concentration of tungsten (cf. Table A.2). Insertion into fivefold coordinated sites is energetically favoured.

The enumeration for $Li_xNb_{14}W_3O_{44}$ was performed in the same way as for $Li_xNb_{12}WO_{33}$. The special position in the center of the block was fixed to be unoccupied. Given the remaining 8 lithium sites, $2^8 = 256$ structures were enumerated. The number of lithiated structures generated by enumeration for $Nb_{14}W_3O_{44}$ is much smaller compared to $Nb_{12}WO_{33}$. Structures with lithium content between those covered by enumeration were 'interpolated' by using the low-energy enumerated structures as a starting point. For example, candidate structures of $Li_6Nb_{14}W_3O_{44}$ were generated by filling half of the lithium sites occupied in $Li_4Nb_{14}W_3O_{44}$ and $Li_8Nb_{14}W_3O_{44}$. Overall, the sampling of lithiated structures for $Nb_{14}W_3O_{44}$ is coarser than for $Nb_{12}WO_{33}$, due to the higher computational cost of optimising the lithium configurations in a larger unit cell. A convex

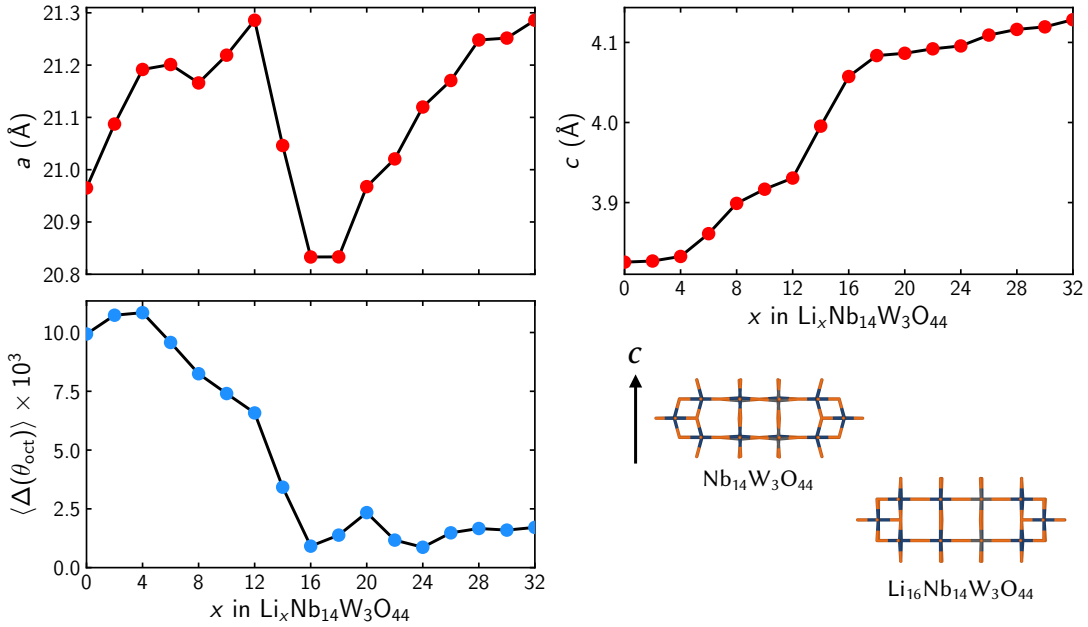

Figure 4.9: Local and long-range structural evolution of $Nb_{14}W_3O_{44}$ during lithium insertion. The anisotropic lattice evolution and the removal of the octahedral distortions ($\langle\Delta(\theta_{oct})\rangle$) strongly resembles $Nb_{12}WO_{33}$. (cf. Fig. 4.8). Compared to $Nb_{14}W_3O_{44}$, the transition metal-oxygen framework (bottom) for the fully lithiated $Li_{16}Nb_{14}W_3O_{44}$ structure shows significantly weaker octahedral distortions. Lithium ions have been omitted in $Li_{16}Nb_{14}W_3O_{44}$ for clarity. The removal of the distortions leads to a contraction of the lattice parameters within the block plane (perpendicular to c).

hull of the lowest energy $Li_xNb_{14}W_3O_{44}$ phases shows thermodynamically stable phases at every sampled stoichiometry. A full enumeration of lithium-vacancy configurations in $Nb_{16}W_5O_{55}$ is not possible. The primitive unit cell contains 22 independent lithium sites, resulting in $2^{22} = 4194304$ possible lithium-vacancy configurations.

The structural evolution of $Nb_{14}W_3O_{44}$ over the course of lithium insertion (Fig. 4.9) bears a strong resemblance to that of $Nb_{12}WO_{33}$ (cf. Fig. 4.8). Lattice parameter c, perpendicular to the block plane, expands monotonically, with most of the expansion taking place between $x = 12$ and $x = 16$ (Fig. 4.9). The parameter a first increases, then shrinks below its initial value with a minimum at $x = 16$. Another expansion for $x > 18$ follows. Note that lattice parameter a (which is equal to b in the $I\bar{4}$ spacegroup of $Nb_{14}W_3O_{44}$) was extracted as $a = \sqrt{V/c}$ (cf. Fig. 4.1). The same trend in the evolution of the lattice parameters is also observed when phases up to 100 meV/f.u. above the convex hull tieline are included in the analysis. The distortions of the MO_6 octahedra are removed as demonstrated by the decrease in the $\langle\Delta(\theta_{oct})\rangle$ measure (Eqn. 4.9). The contraction and distortion removal is associated with occupation of the distorted vertical window positions, in direct analogy to $Nb_{12}WO_{33}$. However, the extent of the structural regions differs between $Nb_{12}WO_{33}$ and $Nb_{14}W_3O_{44}$. In $Nb_{12}WO_{33}$, the maximum expansion of the a and c parameters occurs at 0.4 Li/TM, while in $Nb_{14}W_3O_{44}$ it occurs at 0.71 Li/TM. The contraction region is also wider in $Nb_{12}WO_{33}$; it spans from 0.38 Li/TM to 1.0 Li/TM, while in $Nb_{14}W_3O_{44}$, the contraction occurs from 0.71 Li/TM to 1.06 Li/TM. It is difficult to decide whether this is a physically significant difference, or simply due to the smaller number of lithium configurations

that were sampled for $Nb_{14}W_3O_{44}$ as compared to $Nb_{12}WO_{33}$.

Lithium insertion into $Nb_{14}W_3O_{44}$ initially proceeds via occupation of sites 1, 4, and 8 (cf. Fig. S8), but overall there is no simple sequence for the filling of lithium sites. The lowest energy structures for each stoichiometry are available as crystallographic information files (CIF) in the Supporting Information of the article on which this chapter is based [113].

In complete analogy to $Nb_{12}WO_{33}$, the local and long-range structural changes in $Nb_{14}W_3O_{44}$ are linked. The removal of the distortions of the MO_6 octahedra along the shear planes pulls the blocks closer together (Fig. 4.9). As a result, the lattice parameter in the block plane, a, decreases.

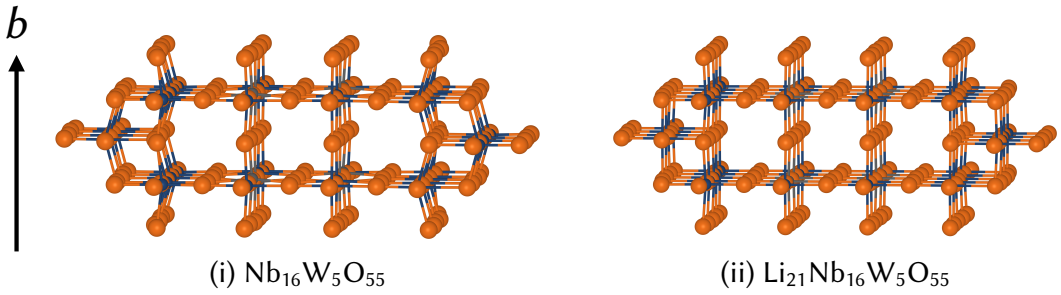

Figure 4.10: Structure of the transition-metal oxygen framework in pristine and fully lithiated $Nb_{16}W_5O_{55}$. Lithium ions have been omitted in the lithiated structure for clarity. The transition metal-oxygen framework in $Li_{21}Nb_{16}W_5O_{55}$ shows significantly more symmetric MO_6 octahedra. The removal of the distortions leads to a contraction of the lattice parameters within the block plane (perpendicular to b).

While we cannot perform a thorough sampling of lithium-vacancy configurations for $Nb_{16}W_5O_{55}$, the strong structural similarity between these three niobium-tungsten oxides suggests that the same trend of lattice and local structural evolution will apply to $Nb_{16}W_5O_{55}$. As a proof-of-principle, we have produced a structural model for $Li_{21}Nb_{16}W_5O_{55}$ by occupying sites E, I, J, L, N, M, and G (cf. Fig. S8), which is shown in Fig. 4.10. Compared to the pristine structure, the lithiated structure shows a contraction in the block plane (a = 29.54 Å vs. a = 29.34 Å, c = 23.10 Å vs. c = 22.95 Å, for $Nb_{16}W_5O_{55}$ and $Li_{21}Nb_{16}W_5O_{55}$ respectively), and an expansion perpendicular to the block plane (b = 3.81 Å vs. b = 4.06 Å), in good quantitative agreement with experimental findings [13]. The octahedral distortion measure $\langle\Delta(\theta_{oct})\rangle$ decreases from 10.25×10^{-3} for $Nb_{16}W_5O_{55}$ to 0.86×10^{-3} for $Li_{21}Nb_{16}W_5O_{55}$. Clearly, lithium insertion causes the same overall structural changes in all three niobium-tungsten oxides $Nb_{12}WO_{33}$, $Nb_{14}W_3O_{44}$, and $Nb_{16}W_5O_{55}$.

4.3.3 Electronic Structure of Lithiated Phases

In this section, we briefly present key electronic structure features of niobium-tungsten oxide shear phases. The electronic structure of the shear structures determines their electronic conductivity, which is important for high-rate battery performance. Additionally, the results presented here serve to explain the mixed-metal redox process and to justify the level of theory used in this study. We will focus on $Nb_{14}W_3O_{44}$, but the results are transferable to $Nb_{12}WO_{33}$ and $Nb_{16}W_5O_{55}$.

The pristine shear phases are wide bandgap insulators (Fig. 4.11). The metal cations are fully oxidised and formally have a d^0 configuration. The valence and conduction bands (Fig. 4.11) are

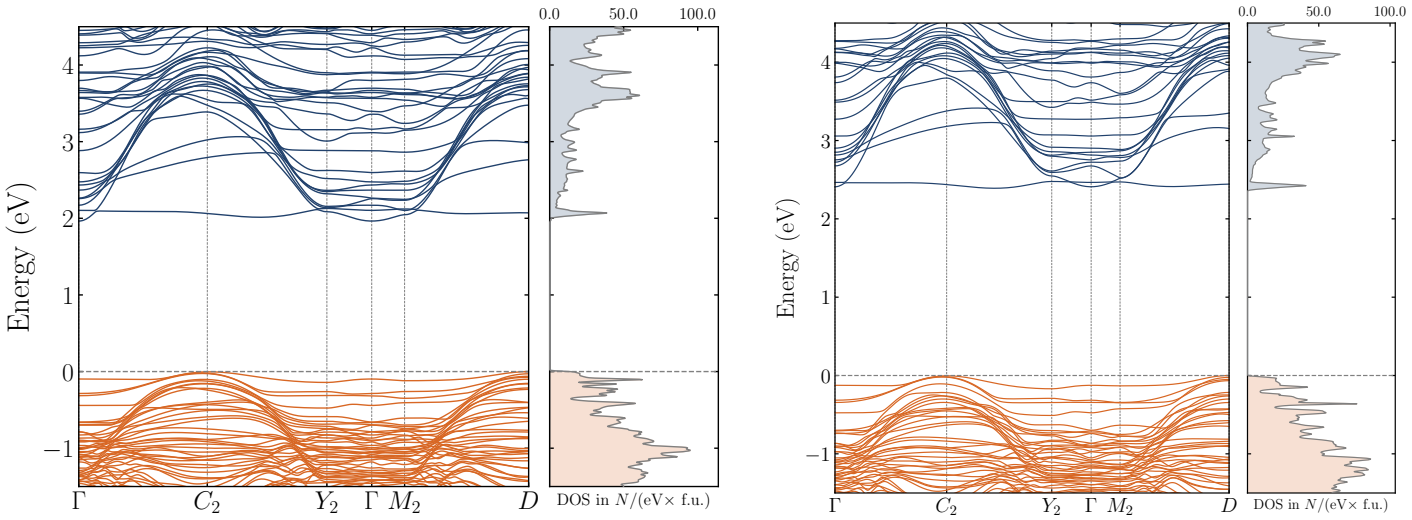

(a) PBEsol (b) rSCAN

Figure 4.11: Bandstructure and electronic densities of states for $Nb_{14}W_3O_{44}$, calculated with (a) PBEsol and (b) rSCAN. Oxygen $2p$ dominated valence band is coloured in orange, while the Nb $4d$/W $5d$ conduction band is shown in blue. Both flat and dispersive conduction bands are present. The long band structure path segments involve changes in wavevector $\mathbf{k}$ along the direction reciprocal to the lattice parameter perpendicular to the block plane ($\mathbf{c}^*$ for $Nb_{14}W_3O_{44}$). The Fermi level (dashed line) sits on top of the valence band. The PBEsol bandgap is 2.0 eV, and the rSCAN bandgap is 2.4 eV. Except for the difference in the bandgap, the two functional give very similar results.

of O $2p$ and Nb $4d$/W $5d$ character, respectively. The experimental bandgap value has not been reported; PBEsol and rSCAN give values of 2.0 eV and 2.4 eV for the bandgap of $Nb_{14}W_3O_{44}$, respectively. As expected, the bandgap for the rSCAN functional is larger [119], and likely closer to the true value. Lithium intercalation leads to n-type doping of the material, introducing electrons into the previously empty conduction band. To understand the electronic structure of the mixed-metal shear phases, it is useful to draw comparisons to the niobium suboxides $Nb_2O_{5-\delta}$, which also feature block-type crystal structures [24]. These compounds are formed by n-type doping of H-Nb_2O_5, and show interesting properties: magnetism, which is rare in niobium oxides, flat bands around the Fermi energy, and an ability to host both localised and delocalised electrons [26, 24, 61, 68]. We have previously shown that these features are fundamentally associated with the block-type crystal structure [68] and therefore also occur in $Nb_{12}WO_{33}$, $Nb_{14}W_3O_{44}$, and $Nb_{16}W_5O_{55}$ on n-doping. In fact, the bandstructures of the niobium-tungsten oxides show a strong similarity to those of the suboxides and H-Nb_2O_5 [68], with both flat and dispersive conduction bands present (Fig. 4.11).

Insertion of a single lithium into the block of $Nb_{14}W_3O_{44}$ leads to the formation of a localised electronic state (Fig. 4.12). This localised state is spread over multiple (predominantly block-central) sites and lies in the plane of the block. The localised state forms as the Fermi level is moved into the conduction band by n-doping, specifically by the occupation of the flat band (corresponding to the peak in the DOS, cf. Fig. 4.11). A small gap is opened up between the localised state and the remainder of the conduction bands (cf. Fig. 4.12a,b). Remarkably, this localisation is independent of the inclusion of a U value on the Nb or W d-orbitals. The localisation

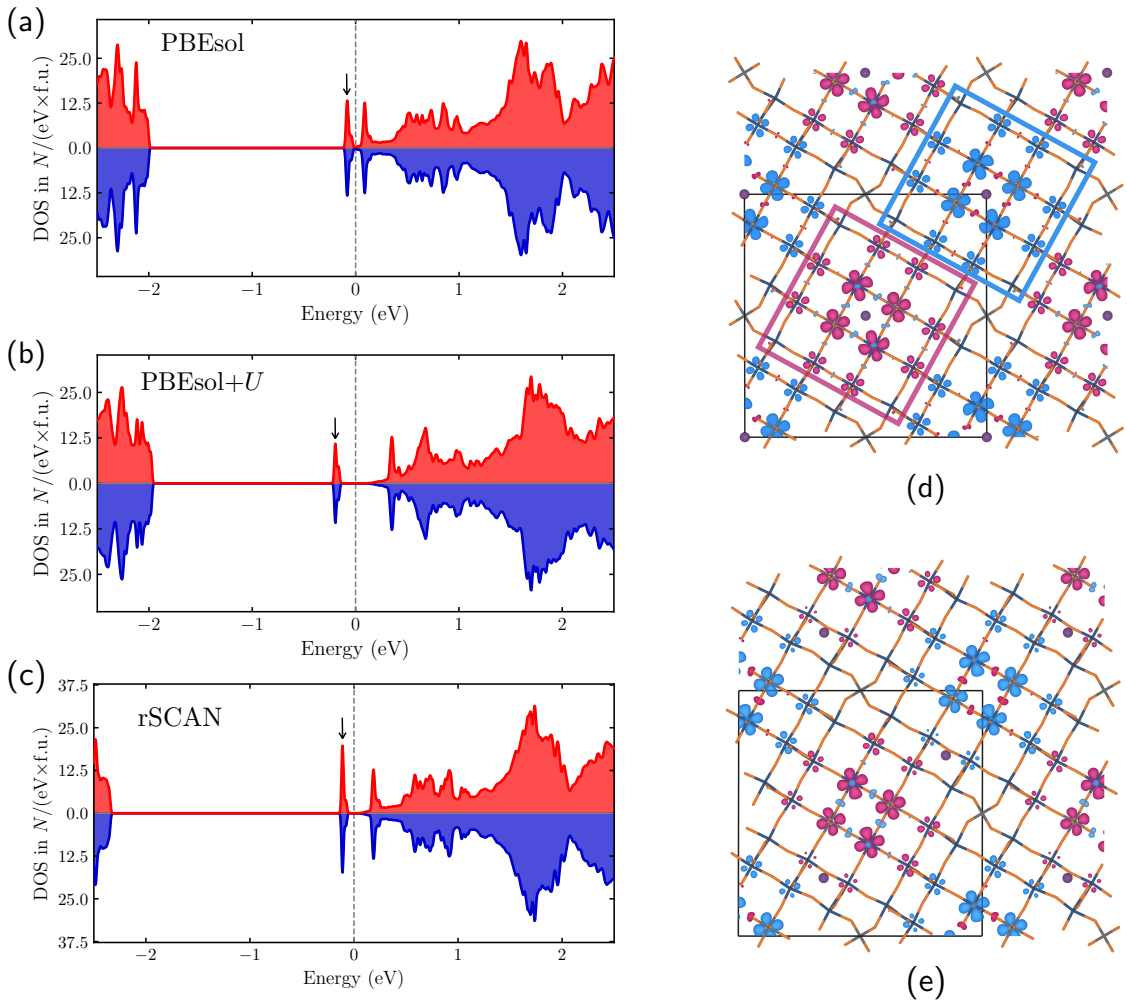

Figure 4.12: $Li_1Nb_{14}W_3O_{44}$ density of states of an antiferromagnetic spin arrangement between blocks computed with (a) PBEsol, (b) PBEsol+U (U = 4 eV), and (c) rSCAN. A localised state (marked by the arrow) is present in all three. Spin density plots (isosurface value 0.012 $e^-/Å^3$) for structures with lithium positioned (d) in the center of the block, and (e) at the edge of the block . The spin density distribution is due to the localised state, and is independent of the lithium position.

is shown even at the GGA level, even though the gap is very small (35 meV), and increases with the introduction of a U value for the metal d-orbitals (270 meV for U = 4 eV). The same localisation is also shown by the rSCAN results, with a gap value of approx. 100 meV. The spin and charge density distribution is the same for all three functionals. Additionally, the spin and charge distribution is also independent of whether the lithium ion is positioned in the block center or periphery (cf. Fig. 4.12c,d). This indicates that there is no strong coupling between the lithium ion and electron. A similar formation of localised electrons is also observed in $Nb_{12}WO_{33}$ and $Nb_{16}W_5O_{55}$. It would be interesting to determine experimentally the position of the localised dopant state relative to the bottom of the conduction band. Given that the charge associated with the localised electronic state resides predominantly on block-central sites (M1 in $Nb_{14}W_3O_{44}$, cf. Fig. 4.2), the block interiors are reduced first upon lithium insertion into niobium-tungsten shear oxides. Since the metal positions in the block center are mostly occupied by tungsten in $Nb_{14}W_3O_{44}$ and $Nb_{16}W_5O_{55}$, tungsten reduction is slightly favoured initially. In fact, this preference has been observed in $Nb_{16}W_5O_{55}$

by X-ray absorption spectroscopy [13].

Further n-doping/lithium insertion up to $Li_3Nb_{14}W_3O_{44}$ fully fills the flat band, but also partially fills the remaining dispersive conduction bands, resulting in metallicity (Fig. 4.13). In contrast to the flat band, the dispersive conduction bands are predominantly hosted on block edge sites [68] (M2-M4 in $Nb_{14}W_3O_{44}$, cf. Fig. 4.13). Reduction of the block edge sites takes place by filling these dispersive conduction bands. For even larger lithium concentrations, the structures are strongly metallic (cf. Fig. A.4 for $Li_{16}Nb_{14}W_3O_{44}$). At the GGA level, we observe no spin polarisation for either $Li_3Nb_{14}W_3O_{44}$ or $Li_{16}Nb_{14}W_3O_{44}$. We do not observe the opening of a band gap by the introduction of U value ($U = 4$ eV) for either stoichiometry, and the compounds remain strongly metallic (Fig. S16). The same is true for fully lithiated $Nb_{12}WO_{33}$ and $Nb_{16}W_5O_{55}$. Besides the slight initial preference for tungsten reduction, niobium and tungsten show similar redox activity in $Nb_{16}W_5O_{55}$ (Nb^{5+}/Nb^{4+} and W^{6+}/W^{5+}, with multielectron reduction possible beyond 1.0 Li/TM) [13].

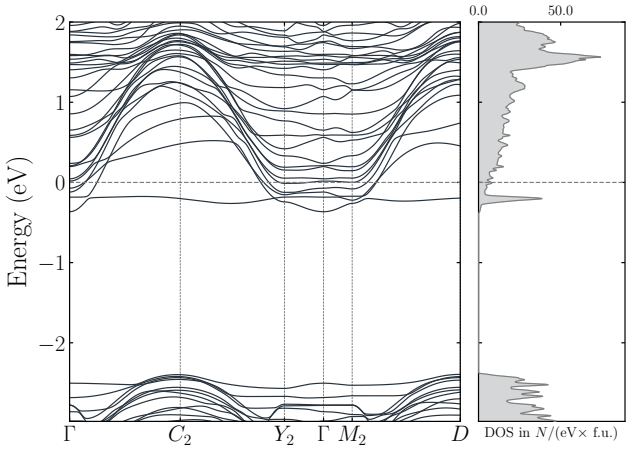

Figure 4.13: Bandstructure and density of states of $Li_3Nb_{14}W_3O_{44}$. Relative to $Nb_{14}W_3O_{44}$ (Fig. 4.11), the n-doping by lithium insertion has moved the Fermi level (dashed line) into the conduction band.

Overall, we conclude that while lithiated shear phases can show electron localisation, it is of a different type than for typical transition metal oxides. The block-structure with its orthogonal crystallographic shear planes seems to have a confinement effect such that the electron localises within the block plane, but is not confined to a single d-orbital on a single transition metal site. These electronic structure features are exactly the same as those observed in $Nb_2O_{5-\delta}$ [68]. Compared to the strong localisation of small polarons in systems like Li_xTiO_2 [120, 121] and Li_xFePO_4 [122], the localisation in shear oxides is weaker, and easily overcome by further doping; the materials quickly become metallic on lithium insertion. The strong d-orbital overlap along the shear planes gives rise to large bandwidths, and in fact, the delocalised states are hosted on transition metal sites at the block periphery [68]. The preferred electron transport direction is expected to be perpendicular to the block plane, based both on experimental results on similar compounds and the calculated band dispersions [27, 68]. The good electronic conductivity suggested by these calculations is beneficial for high-rate battery performance. In addition to a good conductivity upon lithium insertion, there will be a change in the colour of the materials from white-ish to

blue/black [62, 24]. Given the facile lithiation and high-rate performance, this naturally opens up the possibility of electrochromic applications of niobium-tungsten oxides.

4.4 Discussion

4.4.1 Common Mechanistic Principles

The three niobium-tungsten oxides $Nb_{12}WO_{33}$, $Nb_{14}W_3O_{44}$, and $Nb_{16}W_5O_{55}$ are strikingly similar in their cation ordering preferences, lithium insertion mechanisms, and electronic structure. This is expected given their close chemical and structural relationship. Regarding the lithium insertion mechanism, a set of common mechanistic principles emerge from our DFT results:

- Lithium is initially inserted into fivefold coordinated sites and undistorted fourfold coordinated sites
- Between 0–1.5 Li/TM, the lattice evolves through three regions; the lattice parameter perpendicular to the plane of the block expands monotonically, while in the block plane, the lattice parameters expand, contract, and then expand again
- Distortions of the MO_6 octahedra are removed over the course of lithium insertion; this symmetrisation makes previously highly distorted sites available for lithium occupation
- A DFT-predicted voltage profile of $Nb_{12}WO_{33}$ suggests that the lattice changes are associated with different regions of the voltage profile; during the block-plane contraction the voltage is almost constant
- Local and long-range structural evolution are closely linked; removal of octahedral distortions along the shear planes allows neighbouring blocks to slide closer together, causing the lattice contraction

Experimentally, the three-region voltage profile and phase evolution is the most well-established feature of the lithiation mechanism [98, 99, 21, 89, 101, 100, 94, 13]. The three-stage anisotropic host-lattice response has been observed in $Nb_{16}W_5O_{55}$ by Griffith et al. [13] using *operando* synchrotron XRD, and correlates with the regions of the electrochemical profile. Lattice parameters of $Li_xNb_{12}WO_{33}$ phases have been reported by Cava et al. [21] and Yan et al. [99]. Both authors observed an anisotropic lattice change after full lithiation ($Li_{10.7}Nb_{12}WO_{33}$ and $Li_{13}Nb_{12}WO_{33}$, respectively), with an *a*-*c* plane contraction and expansion along *b*. However, the lattice changes between the two studies are not consistent, with Cava et al. reporting an expansion of +8.2 % along *b*, while Yan et al. report +3.5 %. The study of Yan et al. was performed on nanosized material, making it not directly comparable to previous reports or DFT results.

Lattice parameters of $Li_xNb_{14}W_3O_{44}$ phases have been reported by Cava et al. [21], Fuentes et al. [100], and Yan et al. [101] While the results of Cava et al. again agree with our DFT prediction, and suggest an anisotropic evolution of the lattice parameters, the results obtained by Fuentes et al. (chemically lithiated material) and Yan et al. (nanosized material) are at variance with the

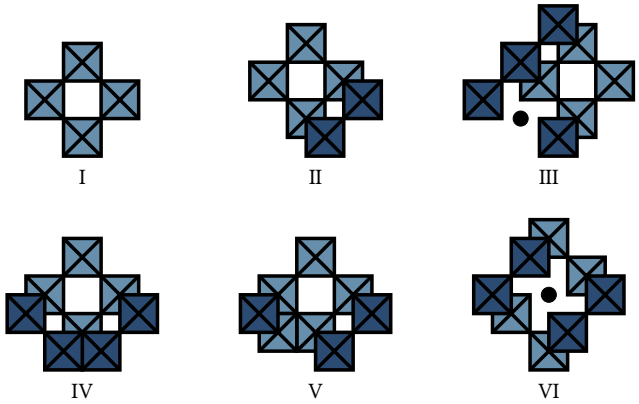

Figure 4.14: Cavity types found in Wadsley–Roth phases according to Cava et al. [21]. The tetrahedral site is denoted by a black dot.

DFT prediction and differ strongly from the structural evolution of the related oxides $Nb_{12}WO_{33}$ and $Nb_{16}W_5O_{55}$. We suggest that the structural evolution of $Nb_{12}WO_{33}$ and $Nb_{14}W_3O_{44}$ is closer to that of $Nb_{16}W_5O_{55}$ and should be re-examined. There is strong reason to believe that the similar three-region voltage profiles of $Nb_{12}WO_{33}$, $Nb_{14}W_3O_{44}$ and $Nb_{16}W_5O_{55}$ are associated with a similar lattice evolution.

Regarding the local structure evolution, only results on $Nb_{16}W_5O_{55}$ are available, which clearly show that the MO_6 octahedra become progressively more symmetric as lithium is inserted [13]. The local structure evolution was observed through X-ray absorption spectrocopy (XAS) measurements at the Nb K-edge and W L_I-edge, which show a decrease of pre-edge intensity over the course of lithium insertion. Pristine block-type crystal structures always feature strongly distorted metal-oxygen octahedra. The pre-edge arises from the dipole-forbidden $s \rightarrow d$ transition, which is absent for a metal in perfectly octahedral coordination. Removal of octahedral distortions therefore results in a decrease of intensity in this transition. Based on the DFT results, this is expected to be a universal feature of the lithium insertion mechanism of shear structures. XAS experiments on shear phase $TiNb_2O_7$ also observe such a symmetrisation in the transition metal–oxygen octahedra [89], suggesting that our results are transferable to the Ti/Nb shear oxides. The reduction of d^0 cations prone to second-order Jahn-Teller (SOJT) distortions usually leads to a removal of the distortion (e.g. Li_xWO_3 and Na_xWO_3 phases [123, 80]). In shear oxides, the reduction can alleviate both the SOJT distortions as well as the electrostatic repulsion between cations along the shear planes, inducing symmetrisation.

Most previous attempts to explain the lithium insertion mechanism of block-type phases have referred to the types of cavities that are found in shear structures, which were first identified by Cava et al [21]. For example, the insertion mechanism for $Nb_{12}WO_{33}$ has been proposed to proceed via insertion into type II, type III, and then type IV cavities [99, 98] (Figure 4.14). Similar mechanisms have been proposed for other block-type structures [103, 100]. Our DFT calculations do not support this kind of mechanism; each cavity contains multiple lithium sites of different types (window, pocket). Instead of resorting to cavity types, it is more accurate to describe the lithium insertion mechanism by the type of site that is being filled, and what structural changes this lithium occupation causes. The cavity types are very useful, however, for the structural understanding of

pristine shear oxide phases.

4.4.2 Implications for Battery Performance

We have shown that cation disorder has a significant effect on the local structure in niobium-tungsten oxide shear phases. Compared to a hypothetical ordered structure, a lithium ion within a disordered niobium tungsten oxide shear structure experiences different local environments from one unit cell to the next. The same type of lithium site will be framed by different patterns of niobium and tungsten ions, with different octahedral distortions, and different local electronic structures. This randomness in the potential energy landscape of the lithium ions in a disordered structure suppresses lithium ordering and makes a larger number of sites available for occupation. While an examination of the strength of coupling between the configurations of cations and lithium ions is beyond the scope of this study, it is expected to have a beneficial effect on performance.

Given that cation disorder can be a favourable attribute to enhance electrochemical performance [13, 124], it is important to be able to control the degree of disorder. Our results suggest that tungsten energetically strongly prefers the tetrahedral site. Due to the site multiplicity and composition, $Nb_{12}WO_{33}$ can fully order with tungsten on the tetrahedral site and niobium on the block sites. However, it could be advantageous to quench from high temperatures during synthesis to lock in some degree of disorder. $Nb_{14}W_3O_{44}$ and $Nb_{16}W_5O_{55}$ have far more tungsten atoms than tetrahedral sites, but octahedral tungsten prefers the centre of the blocks. It would be interesting to examine the electrochemical behaviour as a function of cation disorder, controlled by the cooling rate during the synthesis of the material. Another way to increase the degree of disorder would be to introduce a third cation into the material. Within the group of d^0 cations titanium would be the obvious choice, since it is present in Ti/Nb crystallographic shear structures (such as $TiNb_2O_7$). Molybdenum and zirconium would be other interesting choices.

The correlation between local and long-range structure evolution in the crystallographic shear phases directly affects the battery performance. As lithium intercalates, the total volume expansion is mitigated by the contraction within the block plane. The presence and subsequent relaxation of the octahedral distortions provides a mechanism to realise smaller volume changes in this structural family. Volume changes have an impact on long-term cycling stability; large expansion and contraction are associated with microstructural fracture, loss of particle contact within the electrode, and SEI degradation/reformation as fresh surfaces are exposed. The tempered volume changes in shear oxides thus likely contribute to their observed stability over 1000 cycles [13], even with micrometer-dimension particles that are generally more susceptible to cracking than nanoparticles.

Many of the performance-critical properties of the niobium-tungsten oxides are intimately related to the crystal structure; the simultaneous presence of crystallographic shear planes and the ReO_3-like block interiors is key to the electrochemical performance. As previously described by other authors [21, 13], the shear planes frustrate octahedral unit modes that clamp up diffusion pathways. In addition, the shear planes serve at least two other purposes: removal of local structural distortions along the shear planes buffers volume expansion, and the smaller metal-metal distances of edge-shared octahedra provide good orbital overlap and therefore enhanced electronic

conductivity. The ReO_3-like block interiors, on the other hand, feature open tunnels allowing rapid lithium-ion diffusion. It seems that only when the crystal structure reaches a certain level of complexity can all of these elements be present simultaneously. The structural motifs providing each different function require structural complexity and a large unit cell size.

4.5 Conclusion

In this work, we have used an enumeration-based approach in combination with density-functional theory calculations to reveal common principles governing the cation disorder, lithium insertion mechanism, and electronic structure of the niobium-tungsten oxides $Nb_{12}WO_{33}$, $Nb_{14}W_3O_{44}$, and $Nb_{16}W_5O_{55}$. The cross-compound transferability of our results is due to the crystallographic shear structure common to all three materials. Our results shed light on the experimentally observed three-stage lithium insertion mechanism, and reveal an important connection between the long-range and local structural changes: the removal of octahedral distortions provides a mechanism to contract the lattice in the block plane during the second stage of lithium insertion, thereby buffering the overall volume expansion. Regarding the cation disorder, we find that there is a strong preference for tungsten occupation on the tetrahedral and block-central sites of the structures. The cation disorder also has a strong influence on the local structure of the materials; different Nb/W cation arrangements produce different local octahedral distortions. Electronic structure calculations of *n*-doped/lithiated structures suggest only weak localisation of electrons upon initial lithium insertion, and the materials quickly become metallic on further lithium intercalation. Overall, our calculations suggest that the changes in local, long-range, and electronic structure on lithiation are beneficial to the battery electrode performance of the niobium-tungsten shear oxides.

Our approach of studying multiple members of one structural family has allowed us to draw compound-independent conclusions, and to use smaller model structures to represent more complex ones. The principles we have established for the niobium-tungsten shear oxides likely apply in a similar fashion to Ti/Nb oxide shear structures as well. Future computational work will focus on the extension of the mechanistic principles described here to the Ti/Nb oxide shear structures, and on modelling the diffusion process within niobium-tungsten oxide shear structures.

Chapter 5

Lithium Diffusion in Niobium Tungsten Oxide Shear Structures

This chapter is based on "Lithium Diffusion in Niobium Tungsten Oxide Shear Structures", Can P. Koçer, Kent J. Griffith, Clare P. Grey, Andrew J. Morris, *Chemistry of Materials*, **32**, 3980–3989 (2020). Reproduced with permission from the American Chemical Society.

Abstract

Niobium tungsten oxides with crystallographic shear structures are a promising class of high-rate lithium-ion anode materials. Lithium diffusion within these materials is studied in this chapter using density-functional theory calculations, specifically nudged elastic band (NEB) calculations and *ab initio* molecular dynamics (AIMD) simulations. Lithium diffusion is found to occur through jumps between fourfold coordinated window sites with low activation barriers (80–300 meV), and is constrained to be effectively one-dimensional by the crystallographic shear planes of the structures. A number of other processes are identified, including rattling motions with barriers on the order of the thermal energy at room temperature, and intermediate barrier hops between fourfold and fivefold coordinated lithium sites. We demonstrate that cavities of distinct types host different diffusion pathways; within the ReO_3-like block units of the structures, cavities at the corners and edges host more isolated diffusion tunnels than those in the interior. Diffusion coefficients are found to be in the range of 10^{-12}–10^{-11} m^2s^{-1} for lithium concentrations of 0.5 Li/TM. Overall, the results provide a complete picture of the diffusion mechanism in niobium tungsten oxide shear structures, and the structure–property relationships identified in this work can be generalised to the entire family of crystallographic shear phases.

5.1 Introduction

Lithium-ion batteries with short charge times and high power density are required to accelerate consumer adoption of electric vehicles and relieve intermittency of renewable energy resources [125,

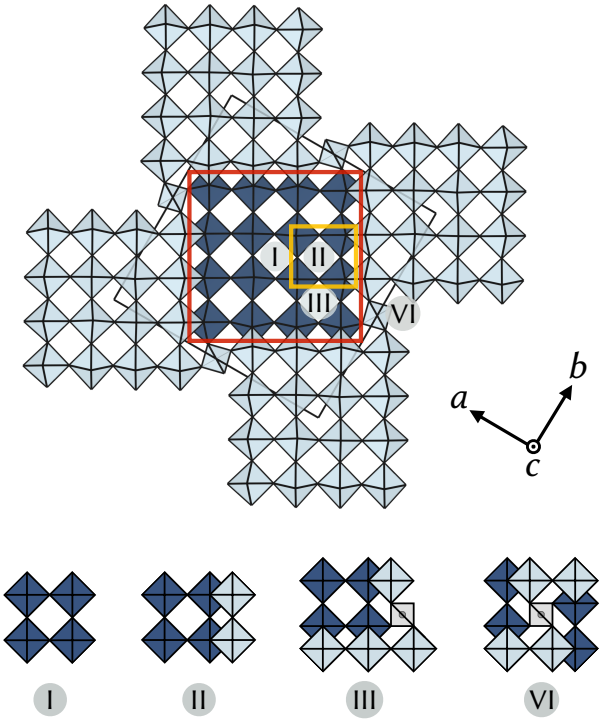

Figure 5.1: Crystal structure of $Nb_{14}W_3O_{44}$ (space group $I4/m$). Light and dark blocks are offset by $\frac{1}{2}c$. The 4×4 block is framed by crystallographic shear planes (edges of red square). Four types of cavities (Cava classification [21], bottom, view along c) occur in $Nb_{14}W_3O_{44}$, and a single type II cavity is framed by the yellow square.

126]. While there are many factors determining the charge/discharge rate of a device [125], and not all materials with high-rate capability are suited for each application, the ionic and electronic conduction within the active materials represent fundamental limits to the achievable rate. Lithium diffusion in electrode materials, quantified by a diffusion coefficient D, is usually much slower than in the electrolyte (liquid or solid). To achieve high rates, the slower diffusion can be compensated by nanostructuring the electrode material, decreasing the diffusion length L, and thereby reducing the time $\tau = L^2/D$ required to lithiate a particle. However, nanostructuring, as commonly applied to $Li_4Ti_5O_{12}$ and TiO_2, has disadvantages in terms of cost and stability, and can be avoided if the electrode material has intrinsically fast lithium diffusion.

A number of niobium-based complex oxides with open framework structures show very fast lithium diffusion, and are promising for applications as high-rate, high-voltage anodes. These include T-Nb_2O_5 [81], $TiNb_2O_7$ [29], and the recently discovered niobium tungsten oxides $Nb_{16}W_5O_{55}$ and $Nb_{18}W_{16}O_{93}$ [13], among others. This chapter focuses on niobium tungsten oxides with Wadsley–Roth crystallographic shear structures, specifically $Nb_{12}WO_{33}$, $Nb_{14}W_3O_{44}$, $Nb_{16}W_5O_{55}$, and $Nb_{18}W_8O_{69}$. These materials feature crystal structures comprised of ReO_3-like blocks of $n \times m$ corner-sharing octahedra (light and dark blue in Fig. 5.1). Blocks are connected to each other along crystallographic shear planes (Fig. 5.1, red square), and tetrahedral sites are present at the corners of the blocks to fill voids. Along the direction perpendicular to the plane of the block, the blocks connect to form columns (c direction in Fig. 5.1). The niobium tungsten oxides differ in the size of the blocks; $Nb_{12}WO_{33}$ features blocks of size 3×4, $Nb_{14}W_3O_{44}$ size 4×4 (Fig. 5.1), $Nb_{16}W_5O_{55}$ size

4×5, and $Nb_{18}W_8O_{69}$ size 5×5. The blocks feature different types of cavities/tunnels (Fig. 5.1), first categorised by Cava et al. [21]. Niobium tungsten oxide shear structures feature cavities of types I, II, III and VI, except for $Nb_{12}WO_{33}$ which does not contain a type I cavity due to its smaller block size. Cavities of type IV and V are present in other shear structures (e.g. $TiNb_2O_7$), but not in the materials studied here. The type VI cavity is special because in comparison to the others, the open space within it is blocked by the tetrahedral site.

Lithium intercalation into niobium tungsten oxides has been studied both experimentally [13, 98, 99, 100, 101] and computationally [113]. Recent mechanistic studies have highlighted the role of local and long-range structural changes during lithium insertion. Experimental [24] and computational [68, 113] studies on shear structures observe good electronic conductivity, suggesting that electronic conduction is not rate-limiting. Lithium diffusion in $Nb_{16}W_5O_{55}$ has been studied by pulsed-field-gradient NMR spectroscopy, observing large diffusion coefficients of 10^{-12}–10^{-13} m^2s^{-1} at room temperature, and low activation energies of 0.1–0.2 eV [13]. Diffusivities for $Nb_{18}W_8O_{69}$, measured using the same technique, are slightly larger [127]. Measurements of diffusion coefficients and activation energies for lithium diffusion in $Nb_{12}WO_{33}$ and $Nb_{14}W_3O_{44}$ are currently not available but are expected to be in the same range. Regarding the mechanism, bond valence sum maps [13, 127] and computational results for structurally similar compounds (e.g. $TiNb_2O_7$, Ref. [128]) suggest one-dimensional diffusion down the block tunnels.

In this chapter, lithium diffusion within the niobium tungsten oxide shear structures $Nb_{12}WO_{33}$ and $Nb_{14}W_3O_{44}$ is studied using first-principles density-functional theory calculations. Building on the results regarding the lithium insertion mechanism of these materials [113], the aim of this chapter is to understand the lithium diffusion mechanism of niobium tungsten oxides. In keeping with the approach from the previous chapter, structures with smaller block sizes are studied explicitly, and the results are extrapolated to the whole family. Due to their use as electrode materials, the lithium concentration in the niobium tungsten oxides varies as the battery operates, and this requires an analysis of the diffusion as a function of lithium concentration. To piece together the diffusion mechanism of niobium tungsten oxide shear structures over a range of lithium concentrations, this work uses two different methods: nudged elastic band (NEB) calculations, and *ab initio* molecular dynamics (AIMD) simulations.

NEB calculations [129] are used to find minimum energy paths over the potential energy surface connecting local minima of lithium sites, and to provide the activation energy for hopping between them. Activation energies can be related to hopping rates via transition state theory. NEB calculations are computationally more efficient than AIMD simulations and provide insight into lithium diffusion at low lithium concentrations. At higher lithium concentrations, the dependence of the activation energy on the local lithium arrangement becomes important. For the niobium tungsten oxides, the complexity of the crystal structures and the structural changes during lithium intercalation make it cumbersome to probe all barriers at all states of charge, so another method is required. AIMD simulations probe the lithium dynamics at a given temperature directly, and take into account both temperature effects and Li–Li interactions. Diffusion coefficients and lithium probability distributions at any concentration can be determined, and AIMD simulations are thus the method of choice for higher lithium concentrations.

The chapter is structured as follows. We begin by studying lithium diffusion in the dilute limit in $Nb_{12}WO_{33}$ and $Nb_{14}W_3O_{44}$ using NEB calculations, establishing activation barriers, diffusion dimensionality, and the impact of structural features on diffusion. AIMD simulation results are presented next, providing a clear picture of diffusion pathways and estimates of diffusivities. We then discuss how these results extrapolate to the other niobium tungsten oxide structures and how they relate to experimental measurements. Conclusions and directions for future work are presented in the final section.

5.2 Methods

DFT calculations were performed with the VASP code [130], using projector augmented-wave potentials [131] to describe the interaction between core and valence electrons. The following atomic states were treated as valence: Li 1s and 2s, O 2s, and 2p, Nb 4s, 4p, 4d, 5s, and 5p, W 5s, 5p, 5d, 6s, and 6p. The PBEsol [107] functional was used for all calculations. Previous work has demonstrated that magnetism and electron localisation in n-doped crystallographic shear phases is weak, and that the materials quickly become metallic or very good semiconductors during lithium intercalation [68, 24, 113, 128]. All calculations were therefore performed without spin-polarisation or Hubbard U corrections for the transition metal d-orbitals.

Structure models for $Nb_{12}WO_{33}$ and $Nb_{14}W_3O_{44}$ were obtained from the work presented in Chapter 4, published in Ref. [113]. For each structure, the lowest energy cation configuration was used. Lattice parameters and atomic positions of $Nb_{12}WO_{33}$ and $Nb_{14}W_3O_{44}$ were optimised using a planewave kinetic energy cutoff of 700 eV and a **k**-point grid spacing of 0.2 Å^{-1}, until the force on each atom was smaller than 0.01 eV/Å. Input structures for AIMD simulations were optimised using the same parameters. In the case of input structures for NEB calculations, only the atomic positions were optimised to keep the cell fixed during the transition state search.

Supercell construction. For the NEB and AIMD calculations, nondiagonal supercells of the conventional unit cells were constructed according to

$$\begin{pmatrix} \mathbf{a}' \\ \mathbf{b}' \\ \mathbf{c}' \end{pmatrix} = S \begin{pmatrix} \mathbf{a} \\ \mathbf{b} \\ \mathbf{c} \end{pmatrix}$$

with the following supercell matrices for $Nb_{12}WO_{33}$:

$$S_{\mathrm{NEB}} = \begin{pmatrix} \frac{1}{2} & \frac{1}{2} & 0 \\ 0 & 2 & 0 \\ \frac{1}{2} & \frac{1}{2} & 1 \end{pmatrix}, \quad S_{\mathrm{AIMD}} = \begin{pmatrix} \frac{1}{2} & \frac{1}{2} & 0 \\ 0 & 3 & 0 \\ \frac{1}{2} & \frac{1}{2} & 1 \end{pmatrix}$$

and similarly for $Nb_{14}W_3O_{44}$. The transformation matrices include a reduction to the primitive cell (hence the fractions), a basis change, and a diagonal supercell construction. These supercells are close to orthorhombic and reduce periodic image effects more than the conventional cells, which

are rather short along one direction and extended in the other two. The NEB cells contain two blocks stacked along the direction perpendicular to the block plane, while the AIMD cells contain three stacked blocks. Structure files are available in supporting datasets at [132].

Nudged Elastic Band Calculations. Nudged elastic band [129] calculations were performed in supercells of $Nb_{12}WO_{33}$ and $Nb_{14}W_3O_{44}$, containing 92 and 122 non-Li atoms, respectively. All NEB calculations were performed using the VTST tools code plugin (Ref. [133]), with a planewave kinetic energy cutoff of 700 eV and a **k**-point grid spacing of 0.2 $Å^{-1}$ to sample the Brillouin zone. Initial Li positions were obtained from the results in Chapter 4 [113]. A single Li atom was inserted into the supercell at each position and the structure was optimised with a fixed lattice until the force on each atom was smaller than 0.01 eV/Å. Sites in close proximity were used as initial guesses for endpoints of minimum energy paths. Between 5–9 images were used to resolve the paths. In cases where an intermediate minimum was found between two endpoints, the intermediate was optimised and added as a new endpoint. The NEB calculations were stopped once the force on each image was smaller than 0.01 eV/Å. For very low-energy barriers ($E_a < 0.1$ eV), the convergence of the barrier value was verified with a smaller force tolerance of 0.005 eV/Å.

As the energies of the states before and after a lithium-ion hop may differ, kinetically-resolved activation barriers [15] ΔE_{KRA} are reported throughout:

$$\Delta E_{\mathrm{KRA}} = E_{\mathrm{TS}} - \frac{1}{2}(E_i + E_f) \tag{5.1}$$

where E_i and E_f are the energies of the initial and final states, and E_{TS} is the energy of the transition state (obtained from a spline interpolation of the energy profile). This removes the direction dependence of the activation barrier.

***Ab initio* molecular dynamics.** Structure models for lithiated phases were obtained from Ref. [113] and optimised as described above. Supercells of $Li_xNb_{12}WO_{33}$ ($x = 5, 8, 17$) and $Li_8Nb_{14}W_3O_{44}$, containing 138 and 183 non-Li atoms, respectively, were constructed (also described above). To ensure a reasonable computational cost for the MD simulations, the planewave kinetic energy cutoff was reduced to 450 eV, **k**-point grids of $2 \times 2 \times 1$ and $2 \times 1 \times 1$ were used for the supercells of $Nb_{12}WO_{33}$ and $Nb_{14}W_3O_{44}$.

The parameters used for AIMD were validated as follows. The barriers obtained from NEB calculations with fully converged parameters were recalculated with the coarser AIMD parameters. Three different barriers for lithium hopping were recalculated for the $Nb_{12}WO_{33}$ structure: A→B, B→C, and C→D. These hopping processes are described in detail later. The results are shown in Figure 5.2. The differences between the kinetically resolved activation energies computed with the two different parameter sets are small (within 0.01 eV), and it is therefore reasonable to conclude that the potential energy surface is sufficiently well-described with the coarser parameter set to perform molecular dynamics calculations. However, the relative energies of the lithium sites change slightly. For example, for the converged parameters (Fig. 5.2a), site A is the most stable site, while for the coarser parameters (Fig. 5.2b), site D is most stable. In addition to the validation of the energy barriers, an MD simulation in the *NVE* ensemble was performed for an average temperature of 924 K over 4 ps and energy conservation was monitored. As shown in Figure 5.3, both short-

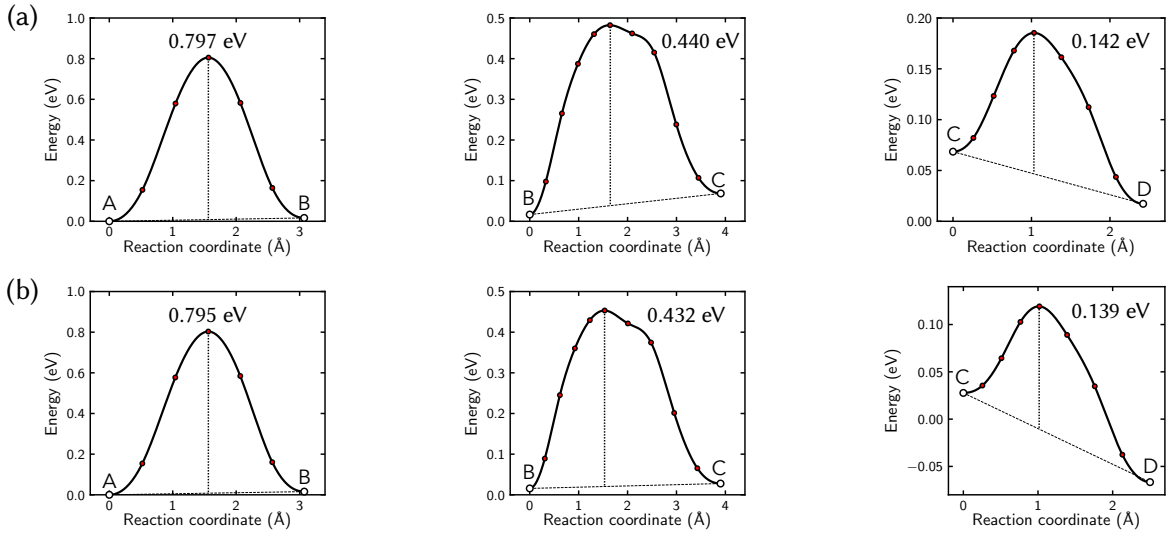

Figure 5.2: Comparison of NEB energy profiles for (a) fully converged parameters, (b) coarser parameter set used for AIMD. Energies are referenced against the energy of site A. Parameters are described in detail in the main text. Kinetically resolved activation barriers differ by less than 10 meV for the two parameter sets. There are, however, small changes in the lithium site energies.

term and long-term energy conservation is excellent. Based on these tests, the coarser parameter set is sufficient to perform meaningful AIMD simulations.

Production runs were performed in the NVT ensemble, using a Nosé–Hoover thermostat. The timestep was set to 1.5 fs. Simulations were performed for temperatures of 600–1500 K, depending on the stoichiometry. Elevated temperatures are needed to be able to observe diffusion events within the system size and time constraints of AIMD simulations [3, 4]. The systems were heated to the final temperature over a period of 2 ps, with velocity scaling at each timestep. After an equilibration time of 6 ps, the simulations were run for at least 150 ps. Final configurations of AIMD runs were optimised and inspected to verify that the host framework had not changed. Simulations were performed for stoichiometries $Li_5Nb_{12}WO_{33}$, $Li_8Nb_{12}WO_{33}$, $Li_{17}Nb_{12}WO_{33}$, and $Li_8Nb_{14}W_3O_{44}$, but various problems were encountered during the AIMD simulations, and a detailed description is given in the Results section.

The tracer (or self-) diffusion coefficient D^* is defined as

$$D^* = \frac{1}{2d} \lim_{t\to\infty} \frac{d}{dt} \frac{1}{N} \sum_{i=1}^{N} \langle |\mathbf{r}_i(t+t_0) - \mathbf{r}_i(t_0)|^2 \rangle_{t_0} \tag{5.2}$$

$$= \frac{1}{2d} \lim_{t\to\infty} \frac{d}{dt} \langle \Delta\mathbf{r}^2(t) \rangle \tag{5.3}$$

where N is the number of diffusing particles, and d is the dimensionality of the diffusion ($d = 1$ for the Nb/W oxides, see below). Averaging over initial times t_0 is essential to obtain well-converged results. The tracer diffusion coefficient was determined by a linear regression of $2dt$ against $\langle \Delta\mathbf{r}^2(t) \rangle$. Plots of the mean squared displacement as a function of time are available in the Supporting Information of Ref. [132] Assuming a temperature dependence of the diffusion coefficient of $D^*(T) = D_0\ e^{-\frac{E_a}{k_B T}}$, Arrhenius plots were constructed to determine the activation

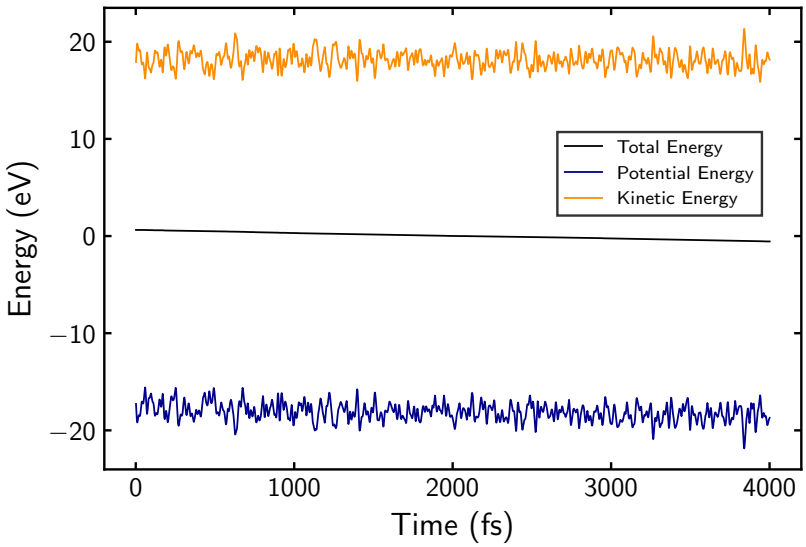

Figure 5.3: AIMD simulation of $Li_5Nb_{12}WO_{33}$ (3 f.u. supercell), in the *NVE* ensemble with an average temperature of 924 K, using the AIMD parameters described in the main text. The total and potential energy are shifted such that the average total energy is zero. The total energy is conserved well, exhibiting only very small oscillation on a short time scale and little drift (−0.3 eV/ps = −2 meV/(atom·ps)) over longer times.

energy E_a. The diffusion coefficients at room temperature were obtained by extrapolating the Arrhenius expression, as AIMD simulations at room temperature are not feasible [3, 4].

The probability density distribution [134] of lithium ions in the structure, $P(\mathbf{r})$, was extracted from simulations at 900 K for all stoichiometries. $P(\mathbf{r})$ was obtained by counting the number of Li ions at each point on a uniform grid over the unit cell, and averaging over the simulation time. Resulting structures were visualised with VESTA [77].

5.3 Results

5.3.1 Lithium Hopping in $Nb_{12}WO_{33}$

Due to the large unit cell and low symmetry (space group $C2$) of $Nb_{12}WO_{33}$, there are many inequivalent lithium positions. Each cavity contains multiple lithium positions, e.g. cavity II contains positions A, B, C, and D. These positions were previously described in Ref. [113], and are relabelled as compared to previous work for ease of presentation (Fig. 5.4a). Despite the fact that they are symmetrically inequivalent, they can be clustered based on their local structure. Fivefold coordinated 'pocket' sites (A, B, H, I) are found along the shear planes at the periphery of the block (red rectangle, Fig. 5.4). The other sites (C, D, E, F, G) are fourfold coordinated 'windows', described as 'horizontal' or 'vertical' depending on the orientation of the window relative to the plane of the block [113]. We note two subtleties about their local structure: (1) the vertical window positions next to the shear planes (F, F') more strongly resemble threefold coordinated sites, and (2) in all window positions, the lithium ions sit above the plane formed by the oxygen atoms. A split position is present on the other side of the window. For example, Li ions in D and D'

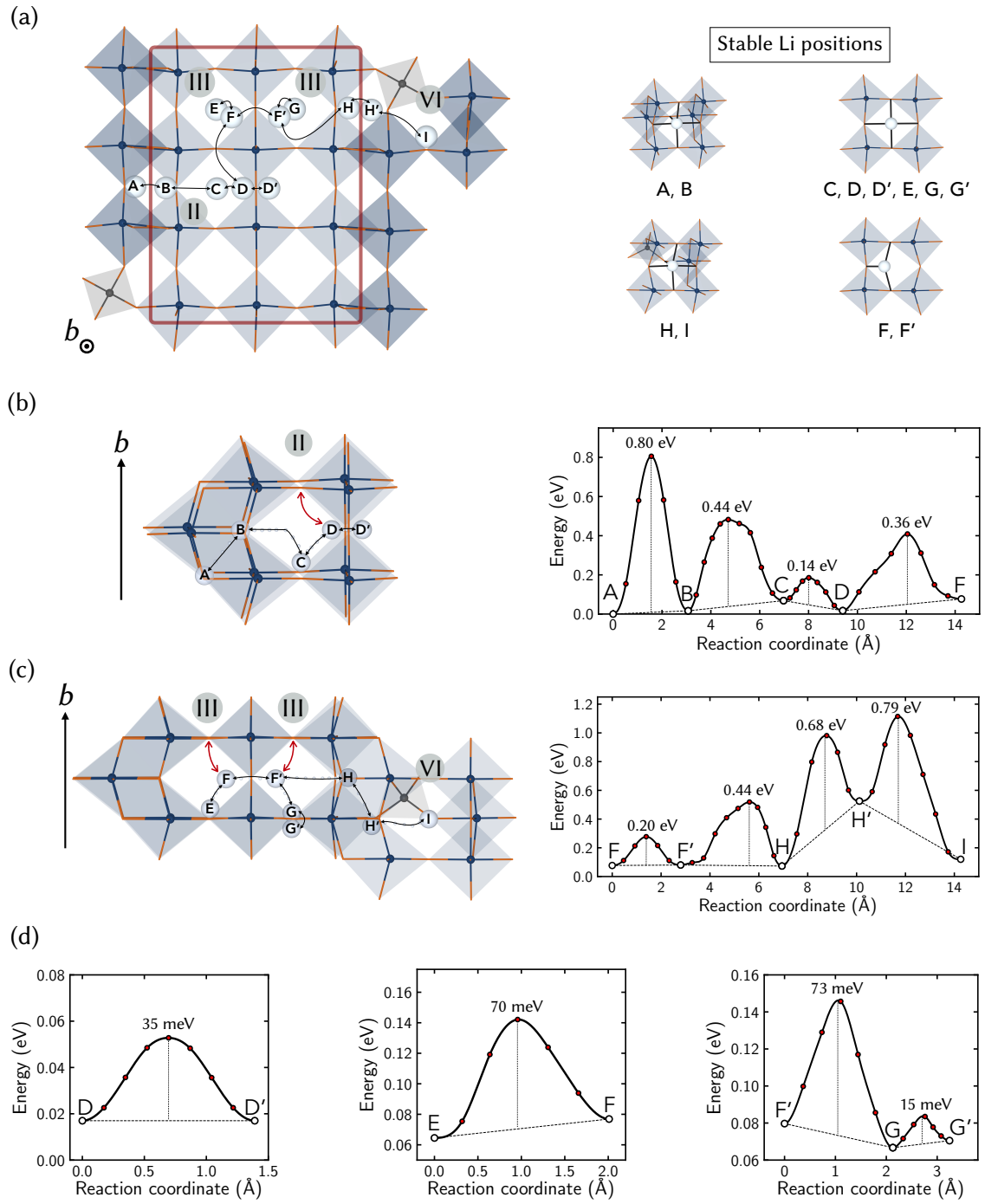

Figure 5.4: Minimum energy paths and activation barriers (NEB) for lithium ion motion in $Nb_{12}WO_{33}$. (a) Lithium sites (A-I) and hops between them. A 3×4 block is framed by the red rectangle representing the shear planes. Cavities are labelled by type. (b) Hops and energy profiles/activation barriers in Cavity II (c) Cavities III and VI. (d) Energy profile along the paths with very low barriers. Local rattling processes (D↔D', G↔G') show the lowest activation barriers (15–35 meV), followed by hops faciliating long-range diffusion down the *b* axis (C↔D, E↔F, G↔F', 70–140 meV). These *b*-axis hops percolate the structure through a chain of effectively equivalent jumps shown by the red arrows in (b) and (c). Cross-block motion (A↔B, H↔I) has very high activation barriers and is therefore slow. Niobium shown in dark blue, oxygen in orange, lithium in off-white, and tungsten in grey.

(Fig. 5.4a) are 0.5 Å above the plane formed by the four oxygens.

A continuous path (with a few branches) through the cavities in $Nb_{12}WO_{33}$ is shown in Fig. 5.4. This path does not include all possible barriers, even in the dilute limit, but all transitions between the different types of sites. Note that there is a twofold rotation axis running through the center of the block, so that the unlabelled part is equivalent by symmetry. The two type III cavities in Fig. 5.4 are structurally very similar but not equivalent by symmetry, and are therefore both included in the path.

Results presented in Figure 5.4 show a clear hierarchy of activation barriers, and therefore lithium motion, in $Nb_{12}WO_{33}$. Very high barriers are found for motion from one block to another, either by crossing the shear plane (hop A↔B, $\Delta E_{\mathrm{KRA}} = 0.80$ eV, Fig. 5.4b), or by moving through cavity VI (H↔H'↔I, Fig. 5.4c) next to the tetrahedral site occupied by tungsten. The motion through cavity VI goes via a high energy intermediate H' site with an energy 0.6 eV above the most stable lithium site. The sequence of hops H↔H'↔I encounters a barrier of at least 1.0 eV. Due to the high activation barriers, lithium motion from one block to another in the *ac* plane will be very slow.

Hops from fivefold coordinated pocket sites at the block edges into the block center (B↔C, H↔F', Fig. 5.4b,c) present the next-largest barriers with values of 0.44 eV. This value is rather large compared to the barriers of other processes within the structure (see below). It suggests that hopping between the sites at the block edges and the sites in the block interior is slow, and the block-peripheral pocket sites are therefore somewhat isolated. The oxygen atoms that coordinate the lithium ions in the pocket sites are rigid because they belong to edges shared between octahedra. While moving out of the pocket site, the Li ion loses the local bonding interaction with the oxygens, which cannot bend towards the Li to support it. This leads to the relatively high activation barriers. The resulting minimum energy paths for B↔C and H↔F' hops involve Li almost 'floating' through the cavity (Fig. 5.4b,c). Note that there is no direct G↔H hop; an attempted NEB calculation for this hop goes via an intermediate F site.

Within the *ac* plane, Li can jump between cavities that belong to the same block with intermediate activation barriers (D↔F $E_a = 0.36$ eV, F↔F' $E_a = 0.2$ eV, Fig. 5.4b,c). Most of the hops within or out of cavity III are faciliated by the interstitial-like F and F' sites. As shown in Ref. [113] and by the AIMD simulations (see below), these F and F' sites disappear at higher lithium concentrations as the distortions of the framing octahedra are removed.

The most important hops are those that facilitate long-range diffusion along the *b* axis, specifically C↔D in cavity II, and E↔F and F'↔G in cavities III. These processes have low barriers of 70–140 meV, and cover jump distances of 1.9 Å, half the *b* lattice parameter. Note that these hops form percolating chains along the *b* axis, shown by the red arrows in Fig. 5.4b,c.

In addition, there are processes with ultra-low barriers that are associated with 'rattling' in the fourfold coordinated window positions (D↔D', G↔G'). As described above, the Li ion sits slightly above the plane formed by the four coordinating oxygen atoms of the window. An equivalent position is found on the other side of the plane. Barriers for these local rattling processes are in the range of 15–35 meV, on the order of the thermal energy at room temperature ($k_BT = 25$ meV). For

these ultra-low barrier processes, the coordination of the Li ion barely changes during the motion, explaining the very low activation energies. The transition states are also fourfold coordinated Li ions, sitting within the window formed by the framing oxygen atoms, rather than slightly above or below. Due to the low barriers and small distances it is more accurate to describe this motion as an anharmonic vibration, rather than a Li ion jump.

5.3.2 Lithium Hopping in $Nb_{14}W_3O_{44}$

The 4×4 blocks of $Nb_{14}W_3O_{44}$ feature a type I cavity in the middle of the block, which is not present in $Nb_{12}WO_{33}$. In our structure model tungsten occupies the tetrahedral site and two of the block-central transition metal sites (Fig. 5.5). The parent structure has a fourfold rotation axis through the middle of the block. Note that $Nb_{14}W_3O_{44}$ has a different axis system than $Nb_{12}WO_{33}$; the blocks lie in the *ac* plane in $Nb_{12}WO_{33}$, but in the *ab* plane in $Nb_{14}W_3O_{44}$, due to the different space group.

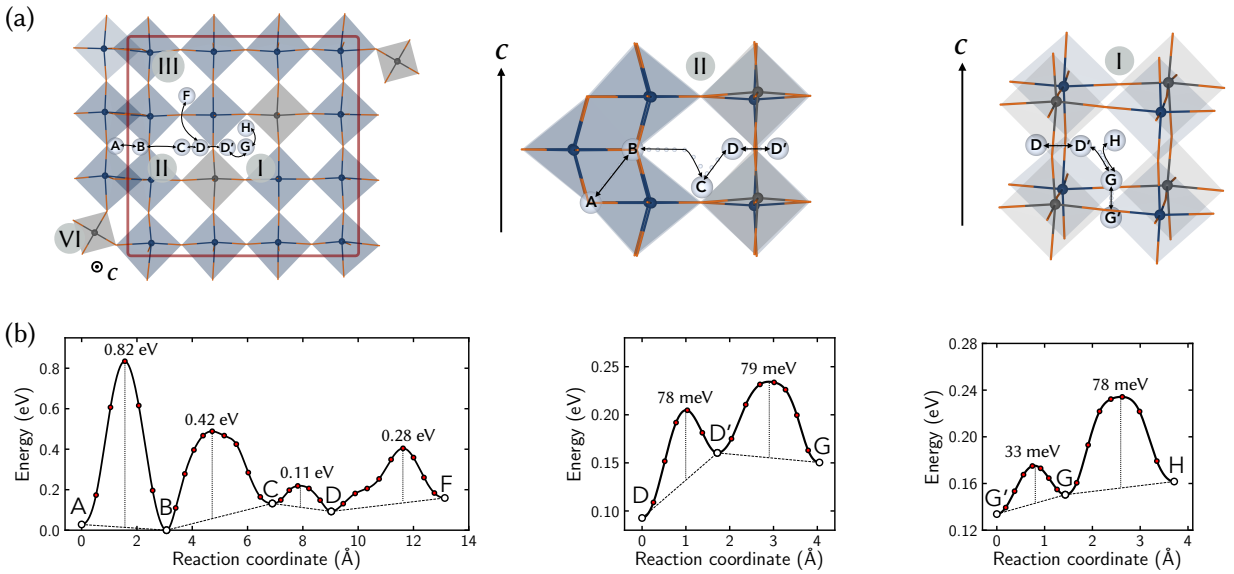

Figure 5.5: Minimum energy paths and activation barriers (NEB) for lithium ion motion in $Nb_{14}W_3O_{44}$. (a) View of the hopping pathways within the block and within individual cavities. (b) Activation barriers for lithium motion. Barriers are especially low for motion within cavity I. Long-range diffusion occurs almost exclusively along the *c* axis, but Li ion motion in the *ab* plane is possible within a single block (red rectangle). Niobium shown in dark blue, oxygen in orange, lithium in off-white, and tungsten in grey.

The lithium diffusion paths and associated activation barriers for $Nb_{12}WO_{33}$ and $Nb_{14}W_3O_{44}$ are very similar: the barrier for crossing from one block to another through the crystallographic shear plane is again very high (A↔B, ΔE_{KRA} = 0.82 eV). The hop from the pocket site at the edge of the block to a window site (B↔C) has the next-largest activation barrier of 0.42 eV.

The cross-cavity motion from type II to III has a high barrier (D↔F, 0.28 eV) compared to the II to I motion (C↔D↔D'↔G, max. barrier 0.11 eV). The D→F hop takes place next to octahedra at the shear plane, which share edges and are strongly distorted. The octahedra framing the path from cavity II to I on the other hand are exclusively corner-sharing and do not show these strong

distortions. One of the oxygen atoms of the window next to the shear plane is part of a shared edge, therefore less flexible and less effective at supporting the Li ion during the D↔F hop, which leads to the higher activation barrier. This rigidity of the oxygen atoms that are part of shared edges between octahedra is also responsible for the absence of stable lithium positions within the distorted windows (cf. F sites), and the high barrier for hops between pocket sites and the block interior (see above). A similar pattern is also found in $Nb_{12}WO_{33}$ (Fig. 5.4), where the motion between the type II cavities through the central window shows a much lower activation barrier than the hops next to the shear planes. AIMD simulations (see below) confirm this pattern.

Cavities of type I are approximately cubic and show the least distorted octahedra in the structure (Fig. 5.5a,b). Li motion within cavity I is facile with low activation barriers for hopping between the window sites (80 meV, Fig. 5.5b), and even lower barriers for the rattling process within window sites (e.g. G↔G', 30 meV). Cavity I is connected to four type II cavities via low barrier hops, which suggests that it facilitates Li motion within the block plane to a much greater extent than the cavities next to the shear planes.

The lowest energy barriers are found for motion along the c axis in $Nb_{14}W_3O_{44}$ (C↔D in cavity II, G↔D', G↔H in cavity I), with values between 80–110 meV. These hops can occur in Cavities I, II and III, even though hops within III were not explicitly calculated for $Nb_{14}W_3O_{44}$. The dominant diffusion pathway will therefore be along the c axis (cf. b axis in $Nb_{12}WO_{33}$).

There are a number of subtleties regarding the interpretation of the NEB results for both $Nb_{12}WO_{33}$ and $Nb_{14}W_3O_{44}$ that are worth mentioning. The barriers are reported as kinetically resolved barriers (cf. Methods) to remove the direction dependence for hops that have endpoints with different energies. In terms of the activation barrier for diffusion, it is the larger of the two barriers that will be relevant (e.g. the D→C hop has a larger barrier than C→D for $Nb_{12}WO_{33}$, Fig. 5.4). Another point to note is that not all lithium sites have the same energy, and the first lithium ions that are inserted into the structure will predominantly occupy the lower energy pocket sites at the block edges. However, the other lithium sites in the block interior are well within an accessible energy range of less than 100 meV for $Nb_{12}WO_{33}$, and are entropically favoured due to the fact that the potential energy landscape is inherently flatter in the block interior than at the block edges, resulting in softer vibrational modes. Furthermore, lithium ions in the lower energy sites do not inhibit transport as they are tucked away in pockets at the block periphery. For $Nb_{14}W_3O_{44}$, there is the additional complication of appreciable Nb/W cation disorder, which will modify both the site energies and activation barriers for lithium motion. All of these considerations suggest that even at very dilute lithium concentrations, there is a population of lithium ions within the block interior that can diffuse with activation barriers of 0.1–0.2 eV.

5.3.3 Li Probability Density

AIMD simulations were performed to study the lithium dynamics explicitly over a range of lithium concentrations. Isosurfaces of the lithium ion probability density of $Li_5Nb_{12}WO_{33}$ are shown in Fig. 5.6. The lithium probability density $P(\mathbf{r})$ (sampled through AIMD) is related to an effective free energy landscape for lithium ions, $E(\mathbf{r})$, via $P(\mathbf{r}) \propto e^{-\frac{E(\mathbf{r})}{k_B T}}$. Stable sites (purple isosurface

in Fig. 5.6) are in agreement with those seen in the NEB calculations. The dominant diffusion paths run along the b axis in one-dimensional channels within each cavity (light blue isosurface in Fig. 5.6). Interestingly, the movement in the ac plane is dominated by hops between the two type II cavities in the center, which are connected by a bridge. Movement between the remaining diffusion channels in type III cavities, and hops between the fivefold coordinated sites and the 1D channels, is much less probable. This is consistent with the results obtained from nudged elastic band calculations: hops through the windows next to the shear planes, and hops between fivefold coordinated sites and those in the block centre, have much higher activation energies than the movement down the tunnels, or the rattling within the central window.

The Li probability density isosurface for $Li_8Nb_{14}W_3O_{44}$ (Fig. 5.7) shows the same patterns: a connected diffusion network between cavities of type I and II, which is not connected to channels in cavities III. $Li_8Nb_{12}WO_{33}$ and $Li_8Nb_{14}W_3O_{44}$ share these patterns because cavities of the same type are structurally very similar, even if they are found in blocks of different sizes.

At higher lithium concentrations, the transition metal–oxygen framework of the structure changes; distortions of octahedra next to the crystallographic shear planes are removed and the window sites next to the shear planes become stable sites for lithium occupation. This is linked to

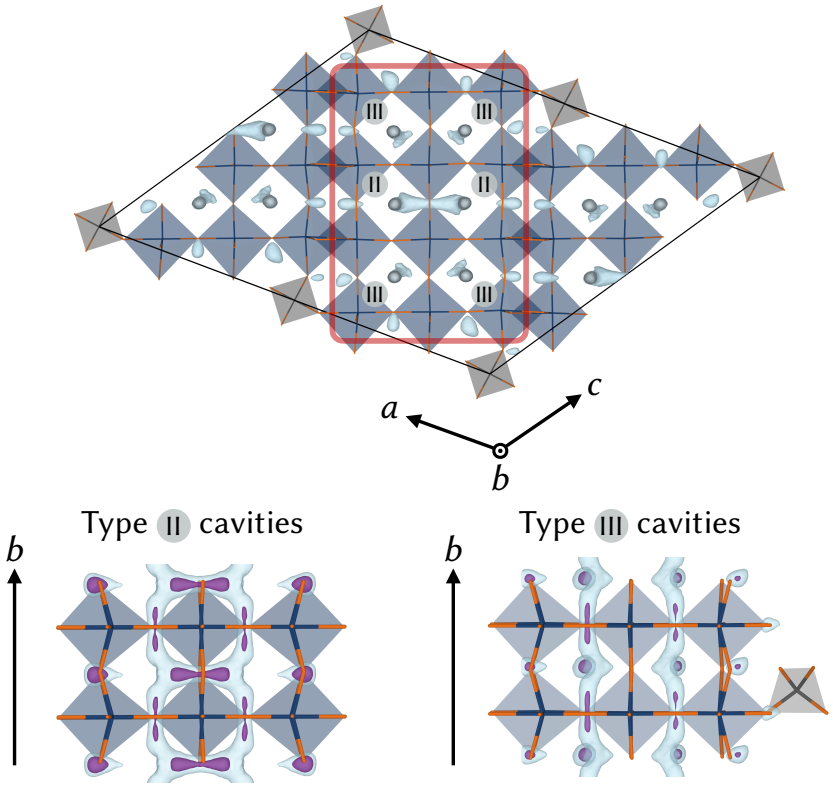

Figure 5.6: Li-ion probability density distribution within $Li_5Nb_{12}WO_{33}$, obtained from AIMD simulations. Views parallel to the b axis (top) and perpendicular to the b axis (bottom). Isosurface values are $P = P_{max}/30$ (light blue) and $P = P_{max}/5$ (purple). The network of connected sites participating in diffusion along the b axis is restricted to the block interior. While the tunnels in cavities II (bottom left) are connected to each other via a bridge, the tunnels in cavities of type III (bottom right) are isolated. Diffusion channels and stable lithium sites are in very good agreement with NEB results (cf. Fig. 5.4b,c and Fig. S5).

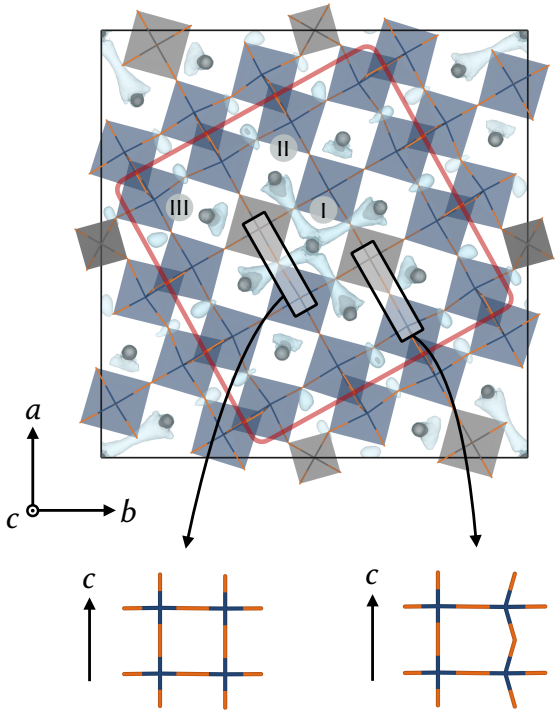

Figure 5.7: Li-ion probability density isosurface ($P = P_{\max}/30$) for $Li_8Nb_{14}W_3O_{44}$. The red square outlines a block, and specific cavities of types I, II and III are marked. The single block features nine parallel tunnels, but only tunnels in cavities of type I and II are connected to each other. Cavities of types I and II share undistorted windows (bottom left), through which diffusion is easier than through the distorted windows (bottom right).

a contraction of the lattice parameters in the block plane [113]. The structural change is a function of lithium concentration, and is not present in $Li_5Nb_{12}WO_{33}$, partly in $Li_8Nb_{12}WO_{33}$, and fully in $Li_{17}Nb_{12}WO_{33}$. Stable lithium positions appear in the previously unstable distorted window sites forming bridges between type III cavities in $Li_8Nb_{12}WO_{33}$ (Fig. S7). The diffusion remains one-dimensional within tunnels running along the b axis.

5.3.4 AIMD - Quantitative Analysis

Various problems were encountered during the AIMD simulations. The temperatures of AIMD simulations have to be high enough to see lithium motion on the timescale that is accessible, but above 900 K, defect formation was observed in the host structure (see below). This limited the available temperature range to 600–900 K. In terms of the stoichiometries, a large number of lithium ions are required for sufficient statistics. However, if the concentration of Li ions is too large, the dynamics becomes very sluggish. These problems led to only two stoichiometries ($Li_8Nb_{12}WO_{33}$ and $Li_8Nb_{14}W_3O_{44}$) having enough data to do a quantitative analysis of the diffusion coefficients. The analysis of the lithium probability density distributions above was performed for AIMD simulations at a single temperature, for which sufficient data was available for all stoichiometries.

Diffusion coefficients over the temperature range 600–900 K for $Li_8Nb_{12}WO_{33}$ and $Li_8Nb_{14}W_3O_{44}$ are plotted in Fig. 5.8 together with an Arrhenius fit. The resulting room temperature diffusion coefficients and activation energies are listed in Table 5.1. Only the component of the MSD per-

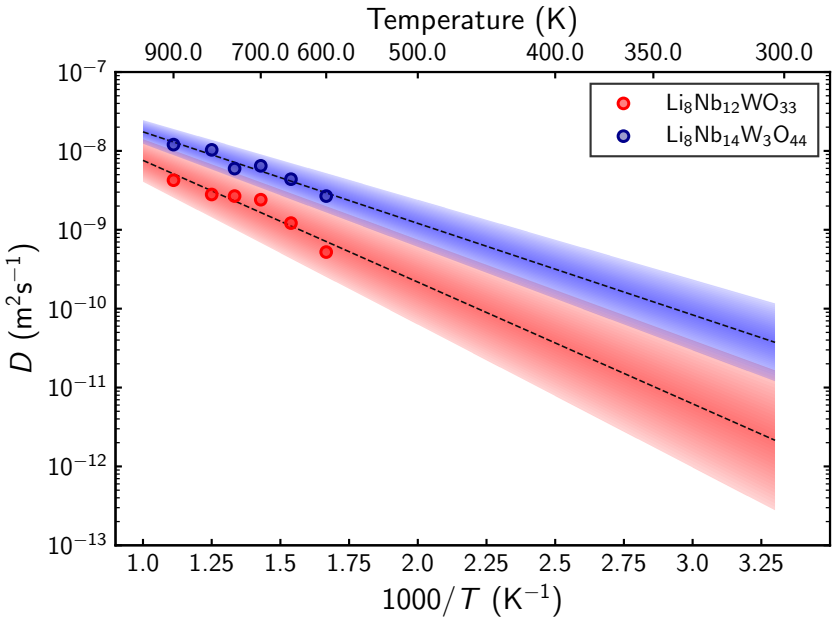

Figure 5.8: Arrhenius plot of AIMD simulation results for $Li_8Nb_{12}WO_{33}$ (red) and $Li_8Nb_{14}W_3O_{44}$ (blue). The shaded region corresponds to extrapolation including standard errors of the activation energies.

pendicular to the block plane is used in the fit, which corresponds to the b axis in $Nb_{12}WO_{33}$, and to the c axis in $Nb_{14}W_3O_{44}$. The diffusion coefficients are denoted $D^{\perp}$ to make this clear. Within the block plane the MSD is not even linear due to the hard boundary formed by the shear planes. $Li_8Nb_{14}W_3O_{44}$ shows faster diffusion than $Li_8Nb_{12}WO_{33}$ and the data for this compound is a better fit to the Arrhenius expression, with a lower error on the estimate of the activation energy.

Stoichiometry	Li/TM	$D^{\perp,*}_{298\mathrm{K}}$ (m^2s^{-1})	E_a (eV)
$Li_8Nb_{12}WO_{33}$	0.615	$1.8 \cdot 10^{-12}$	0.31 ± 0.05
$Li_8Nb_{14}W_3O_{44}$	0.471	$3.2 \cdot 10^{-11}$	0.23 ± 0.03

Table 5.1: Diffusion coefficients and activation energies obtained from AIMD simulations. The diffusion is highly anisotropic and only the value along the direction perpendicular to the block plane $D^{\perp}$ is reported (b axis in $Nb_{12}WO_{33}$, c axis in $Nb_{14}W_3O_{44}$).

The activation energies for $Li_8Nb_{12}WO_{33}$ and $Li_8Nb_{14}W_3O_{44}$ are between 0.2–0.3 eV, slightly larger than those obtained from NEB results (0.1–0.2 eV). The increase in the activation energy is attributed to the much larger lithium concentrations that are probed in the AIMD simulations (roughly 0.5 Li/TM), which result in repulsive Li–Li interactions, increasing the activation energies for Li-ion hops. The extrapolated room temperature diffusion coefficients are high (10^{-12}–10^{-11} m^2s^{-1}), comparable with values for solid electrolytes [135, 13]. The activation barrier is lower, and the diffusion coefficient higher, for $Li_8Nb_{14}W_3O_{44}$ than for $Li_8Nb_{12}WO_{33}$. Both the lower lithium content and the structural framework with more and better connected tunnels likely are responsible for this.

5.3.5 Tungsten Interstitial Defects

For AIMD simulations above 900 K, tetrahedrally coordinated tungsten atoms within the type VI cavities were observed to migrate into adjacent octahedral positions (Fig. 5.9). These interstitial defects were observed for both $Li_8Nb_{12}WO_{33}$ and $Li_{17}Nb_{12}WO_{33}$, and occurred more frequently with increasing temperature and lithium content. This indicates that the activation barrier for the migration of tungsten decreases with increasing lithium concentration. The decrease in the activation barrier might be due to the reduction of the transition metal ions and the removal of distortions within transition metal–oxygen octahedra, both of which are known to occur as the lithium concentration increases [113, 13]. Activation barriers for this tungsten migration cannot be obtained directly from the AIMD simulations. However, given that the formation of the defects occurred only above 900 K, and Li-ions are already observed to be mobile below that temperature, we can conclude that the tungsten migration barrier is significantly larger than that for Li-ion migration. Meaningful lithium diffusion coefficients were not extracted from simulations exhibiting these defects because the host framework had changed, with new lithium positions and diffusion pathways within the type VI cavities. This limited the temperature range for AIMD simulations to 600–900 K. Interstitial defects of this type were previously observed experimentally, and were suggested to explain off-stoichiometry in block-type niobium oxide structures [85]. It could also be present in small concentrations in the niobium tungsten oxides after synthesis. A detailed investigation of these defects is left to future work.

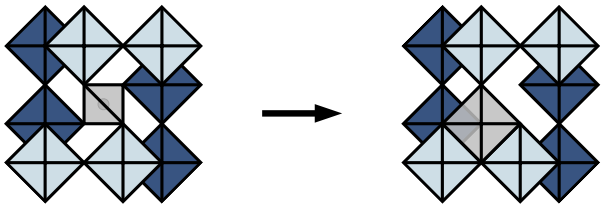

Figure 5.9: Interstitial defect observed to form in type VI cavities by migration of tungsten from a tetrahedral site into an adjacent octahedral site.

5.4 Discussion

Overall, the diffusion mechanism in niobium tungsten oxides with crystallographic shear structures is strongly anisotropic, effectively one-dimensional down the tunnels, in agreement with previous suggestions [13, 128, 127]. Hops within the block plane are facile but eventually hit the shear plane boundaries which prevent long-range motion perpendicular to the tunnels. The Li-ion dynamics within the structures is constrained to occur within blocks. NEB calculations show activation barriers of 0.1–0.2 eV in the dilute limit, and AIMD simulations suggest activation barriers of 0.2–0.3 eV at concentrations around 0.5 Li/TM. At those concentrations, AIMD simulations predict room temperature diffusion coefficients in the range of 10^{-12}–10^{-11} m^2s^{-1}, on par with the best known solid electrolytes.

In addition to the overall mechanism, a number of structure-specific details are worth dis-

cussing. The diffusion of lithium ions in the structure occurs mostly through hops between fourfold coordinated window sites, which are located in the block interior. Hops into or out of fivefold coordinated pocket sites occur much less frequently, because these hops have large activation barriers. The pocket sites are also connected to fewer neighbouring Li positions than the window sites. If the parallel 1D diffusion channels are a 'multi-lane highway' [13], the pocket sites are essentially parking spots.

We can expand on the role of the pocket sites at the block edges a little more: at dilute lithium concentrations, there is a question as to whether lithium ions are trapped in those sites or not. There is a notable asymmetry between lithium intercalation and deintercalation here: starting with an empty Nb/W oxide structure, the lithium ions have to enter the structure through one of the channels, which will be exposed at surfaces of the particles. In contrast, there is no direct way to enter one of the pocket sites.

Once in the channels, ions are much more likely to diffuse down the channels than move into the fivefold coordinated pocket sites, due to the difference in the activation energies. The relative probability can be estimated by the ratio of the rates. Assuming activation energies of 0.14 eV for down-tunnel motion (cf. Fig. 5.4, C↔D), 0.44 eV for a transition into a pocket site (cf. Fig. 5.4, B↔C), and a rate expression $\Gamma \propto e^{-\frac{E_a}{k_B T}}$, the down-tunnel motion is faster by a factor of

$$\frac{\Gamma_{\mathrm{in-tunnel}}}{\Gamma_{\mathrm{tunnel}\rightarrow\mathrm{pocket}}} = \frac{e^{-0.14\mathrm{eV}/k_B T}}{e^{-0.44\mathrm{eV}/k_B T}} \approx 1.6 \cdot 10^5$$

for $T = 293$ K. Hence, once an ion is in the channel, down-tunnel transport is overwhelmingly likely, and lithium ions therefore move down the tunnels rapidly before finally making a transition into a pocket site. Now consider the reverse process of deintercalation: to pull lithium ions in pocket sites out, they first have to make a transition into the channels. But this is a slow process, and lithium ions in the pocket sites could remain trapped during high-rate deintercalation. Based on these considerations, and the fact that there will likely be partial occupation of many sites at low lithium concentrations (cf. Results), the pocket sites only significantly inhibit fast lithium ion motion during high-rate deintercalation. The practical implication for full battery cells with niobium tungsten oxide anodes is that the charging process may be faster than discharge, which is compatible with most applications such as regenerative braking, fast charging electronics, and others, that can utilise high input power densities.

The different types of cavities contain different stable lithium positions and diffusion channels, but these are remarkably transferable between different compounds (i.e. $Nb_{12}WO_{33}$ and $Nb_{14}W_3O_{44}$). Most notably, the type III cavities at the block corners present more isolated diffusion channels compared to the type I and II cavities. As mentioned previously, this is due to the fact that motion from a type III cavity into any neighbouring cavity in the block plane must proceed via a distorted window, which does not feature a stable intermediate lithium position. On the other hand, moving out of type I or II cavities through an undistorted window is easier due to an intermediate stable Li position and hence a lower overall activation energy. Given the cross-compound transferability of the properties of the different cavity types, one can easily extrapolate what the lithium motion will look like in shear structures $Nb_{16}W_5O_{55}$ and $Nb_{18}W_8O_{69}$,

even though they were not studied explicitly in this work. Overall, the shear structures of niobium tungsten oxides present a complex energy landscape for lithium motion, with very different barrier sizes: a flat landscape in the interior giving rise to fast lithium diffusion, high barriers for pocket sites, and very high barriers for moving between blocks.

Due to these differences between cavity types, it seems that structures with the maximum number of type I and II cavities show the most interconnected diffusion network and the fastest lithium diffusion. These would also be the structures with the largest block sizes. Considering the four known niobium tungsten oxide single block structures ($Nb_{12}WO_{33}$, $Nb_{14}W_3O_{44}$, $Nb_{16}W_5O_{55}$, and $Nb_{18}W_8O_{69}$), it is therefore likely that the diffusion is fastest in $Nb_{18}W_8O_{69}$, although it is questionable whether these differences can be accurately measured. Of course, this argument is based on structural considerations and neglects the impact of a changing ratio between niobium and tungsten. The niobium tungsten oxides are also partially disordered [113, 106], and while we have not explored the effect of the cation disorder on the diffusion, it could be important.

True one-dimensional diffusion is special because the diffusing particles cannot pass each other. In fact, the tracer diffusion coefficient for pure 1D diffusion is zero, due to the fact that the mean-square displacement grows as the square root of the time, rather than linearly [16]. In the niobium tungsten oxides, jumps between the one-dimensional channels are therefore required to obtain a non-zero tracer diffusion coefficient. It would be interesting to examine to what extent the constrained, effectively one-dimensional ionic motion is correlated, especially within the more isolated tunnels at the block corners. We stress that this applies only to *tracer* diffusion, not to *chemical* diffusion in 1D, which is still well defined. The tracer diffusion coefficient describes motion of a single (tagged) particle, whereas the chemical diffusion coefficient is related to collective (mass) transport [16, 4]. While the transport coefficient is relevant for rate performance, it is the tracer diffusion coefficient that has been measured by pulsed-field-gradient (PFG) NMR spectroscopy measurements on lithiated niobium tungsten oxide phases. The PFG NMR experiments should therefore be sensitive to the correlation effects, especially in shear phases with smaller blocks.

The PFG NMR measurements on $Li_xNb_{16}W_5O_{55}$ show room temperature diffusivities of 10^{-13}–10^{-12} m^2s^{-1} and activation energies of 0.1–0.2 eV [13], while $Li_xNb_{18}W_8O_{69}$ shows even higher diffusivities of 10^{-12}–10^{-10} m^2s^{-1} [127]. These measurements were performed for lithium concentrations up to 0.4 Li/TM, and probe long-range lithium transport. Measurements on the two phases studied in this work, $Nb_{12}WO_{33}$ and $Nb_{14}W_3O_{44}$, are not currently available. However, given the cross-compound transferability demonstrated in this work, we can tentatively compare values: both activation energies and the magnitude of the diffusion coefficients are comparable, although lithium concentrations in this work are either much lower (NEB) or higher (AIMD) than in the experiments. The results presented in this work place the experimentally derived values into context and offer a detailed structural understanding of the mechanism. PFG NMR experiments only measure long-range lithium motion that contributes to diffusion. NMR relaxometry experiments, on the other hand, probe all types of lithium motion (including local motion) and provide estimates of barriers. Relaxometry experiments would therefore be very useful to understand the hopping motion and associated barriers in more detail. It is unfortunate that the high computational cost of AIMD simulations prevents a more detailed study of the diffusion coeffi-

cients and activation barriers as a function of concentration at this time. Classical MD studies with appropriate potentials would be very useful as an avenue for future work in this direction.

5.5 Conclusion

In this chapter, the lithium diffusion mechanism in niobium tungsten oxide shear structures was studied using density-functional theory. Lithium diffusion takes place in parallel tunnels, but is constrained to be effectively one-dimensional by the crystallographic shear planes. The Li-ion jumps that contribute to long-range diffusion have activation energies of 0.1–0.2 eV in the dilute limit, and slightly larger barriers at higher lithium concentrations (around 0.5 Li/TM). The low activation barriers lead to high room temperature diffusivities (10^{-12}–10^{-11} m^2s^{-1} for stoichiometries probed in this work), and are responsible for the excellent high-rate capability of the niobium tungsten oxides in lithium ion batteries.

While the Li-ion motion that contributes to long range diffusion takes place by jumps between window sites in the block interior, there are a number of other processes occuring within the structure: local rattling motions, and jumps between window and pocket sites. In addition, the lithium motion is different depending on the cavity type. The activation barriers for jumps between different types of sites are transferable between different niobium tungsten oxides, due to their strong structural similarity. Overall, these results paint a clear picture of the diffusion mechanism in niobium tungsten oxide shear structures, and illustrate the relationship between the diffusion mechanism and the atomic structure of the materials. The same relationships should hold in other crystallographic shear phases as well.

Chapter 6

Lattice Dynamics Calculations with DFT+DMFT

This chapter is based on "Efficient lattice dynamics calculations for correlated materials using DFT+DMFT", Can P. Koçer, Kristjan Haule, G. Lucian Pascut, Bartomeu Monserrat, *Phys. Rev. B*, **102**, 245104 (2020). Reproduced with permission from the American Physical Society.

Abstract

Phonons are fundamentally important for many materials properties, including thermal and electronic transport, superconductivity, and structural stability. This chapter describes a method to compute phonons in correlated materials using state-of-the-art DFT+DMFT calculations. The approach combines a robust DFT+DMFT implementation to calculate forces with the direct method for lattice dynamics using non-diagonal supercells. The use of non-diagonal instead of diagonal supercells drastically reduces the computational expense associated with the DFT+DMFT calculations. The method is benchmarked for typical correlated systems (Fe, NiO, MnO, $SrVO_3$), including tests for **q**-point grid convergence and different computational parameters of the DFT+DMFT calculations. The efficiency of the non-diagonal supercell method allows us to access **q**-point grids of up to $6 \times 6 \times 6$. In addition, we discover that for the small displacements that atoms are subject to in the lattice dynamics calculation, fixing the self-energy to that of the equilibrium configuration is in many cases an excellent approximation that further reduces the cost of the DFT+DMFT calculations. This fixed self-energy approximation is expected to hold for materials that are not close to a phase transition. By providing an efficient and general method for the calculation of phonons using DFT+DMFT, this work opens up many possibilities for the study of lattice dynamics and associated phenomena in correlated materials.

6.1 Introduction

First-principles calculations of phonons in real materials play an important role in explaining experimental observations and in predicting novel materials phenomena. Apart from standalone calculations, lattice dynamics often form the input for a wide variety of follow-up calculations of materials properties, including thermodynamics, superconductivity, thermal and electronic transport, and finite temperature optical response.

The overwhelming majority of lattice dynamics calculations of materials employ density functional theory (DFT). However, commonly employed exchange-correlation functionals such as LDA and PBE have severe shortcomings when applied to materials with strongly correlated d or f electrons. While these problems can be partially remedied by DFT+U methods or hybrid functionals, dynamical mean field theory (DMFT) in combination with DFT generally leads to a better description of the electronic structure of correlated materials [136]. It is therefore desirable to extend the range of applicability of DFT+DMFT calculations to study structural and vibrational properties of correlated materials. To this end, DFT+DMFT implementations for total energies and forces have been developed recently [137, 138, 139, 140].

Phonon calculations are usually performed by one of three methods: linear response, frozen phonons, or the direct method. In the context of DMFT, early work by Savrasov and Kotliar [141] described a linear response method to calculate phonon spectra of MnO and NiO. The authors used the simple Hubbard-I solver and neglected the change of the self-energy with displacement, a term that involves the derivative of the self-energy Σ with respect to the Green's function G, $\delta\Sigma/\delta G$. This term is very difficult to compute by the current generation of impurity solvers. The frozen phonon method was used in the work of Leonov *et al.* [142] to calculate lattice dynamics of paramagnetic iron and more recently by Appelt *et al.* to compute the phonons of palladium [143]. Frozen phonon calculations rely on *a priori* knowledge of the phonon eigenvectors so that phonon frequencies are easily calculated from total energy differences without the need to evaluate forces. As such, the method only applies to simple, highly symmetric structures. The direct method is both simple and general, requiring only the forces on atoms, and given the recent advances in force implementations of DFT+DMFT, should be the method of choice. A recent example of this is the study of phonons in iron by Han *et al.* [144]. However, as it relies on the construction of supercells to access phonons at points other than Γ, the computational cost can quickly become unmanageable for an already expensive electronic structure method such as DMFT.

In this chapter, a method to compute vibrational properties of correlated materials from DFT+DMFT is described and benchmarked. The method combines two ingredients: (1) Forces from DFT+DMFT, efficiently obtained from a robust implementation based on the free-energy Luttinger-Ward functional [138], and (2) the direct method for phonon calculations, using non-diagonal rather than diagonal supercells for significant savings in computational expense [145]. In addition, we discover that using a fixed self-energy obtained from the equilibrium configuration for the configurations with atomic displacements is an excellent approximation. Since the solution of the impurity problems is the most expensive step of the calculations, this approximation results in additional large savings of computing time.

The chapter is organised as follows: The next section describes the background theory and implementation of the DFT+DMFT method, and lattice dynamics calculations with non-diagonal supercells. In Sec. 6.3, results of the calculations for Fe, NiO, MnO and $SrVO_3$ are described and discussed in turn, including tests for **q**-point grid convergence, use of fixed self-energies, and other computational parameters. We draw conclusions and outline future work in Sec. 6.4.

6.2 Methods

6.2.1 DFT+DMFT

The DFT+DMFT calculations are based on the method and implementation of Haule *et al.* [146, 147, 137, 35], often referred to as DFT + embedded DMFT (DFT+eDMFT). In this method, the DFT+DMFT free energy is expressed in the form of a Luttinger-Ward functional, which is stationary. Stationarity in this context means that when the DFT+DMFT Dyson equation for the Green's function is satisfied, the solution is a stationary point of the Luttinger-Ward functional. This is important as it allows reliable evaluation of free energies and forces [138]. To connect the correlated subspaces to the rest of the solid, projection operators $\hat{P}^{\mathbf{R}}$ are defined such that $G^{\mathbf{R}}_{\mathrm{loc}} = \hat{P}^{\mathbf{R}} G$, where G and $G^{\mathbf{R}}_{\mathrm{loc}}$ are the Green's function of the solid and the local Green's function of the correlated atom at site $\mathbf{R}$, respectively. On-site correlations of d or f orbitals are treated exactly while more itinerant degrees of freedom are treated on the DFT level. The projectors are fixed and consist of a set of quasi-atomic orbitals $\phi^{\mathbf{R}}_{lm}(\mathbf{r})$ that are solution to the Schrödinger equation inside the muffin-tin sphere. The projection and embedding with fixed projectors is required to preserve the stationary nature of the functional. The DFT+DMFT calculation proceeds as follows: (1) the Green's function of the lattice G is projected onto the local orbital basis (d or f orbitals) to calculate the local Green's functions $G^{\mathbf{R}}_{\mathrm{loc}}$ for each independent correlated atom at sites $\{\mathbf{R}\}$, (2) the impurity problem for each independent correlated atom is solved using the continuous time quantum monte carlo [148, 149] (CTQMC) solver to obtain the self-energy in the local orbital basis $\Sigma_{\alpha\beta}(\omega)$, (3) the self-energy is embedded into real space according to

$$\Sigma^{\mathbf{R}}(\mathbf{r}, \mathbf{r}', \omega) = \sum_{\alpha,\beta} \langle \mathbf{r}|\phi_\alpha\rangle \Sigma_{\alpha\beta}(\omega) \langle \phi_\beta|\mathbf{r}'\rangle \tag{6.1}$$

and is nonzero only within the muffin-tin spheres of the correlated atoms. The self energy then enters the Dyson equation of the solid to obtain the lattice Green's function. Self-consistency is achieved when the local Green's functions obtained from lattice and impurity match.

The forces on atoms are defined as the derivatives of the Luttinger-Ward free energy functional with respect to the atomic positions, which includes the effects of electronic and magnetic entropy [138]. Importantly, they are easily and reliably evaluated in this implementation, being even more numerically precise to compute than the free energy. Accurate forces are essential for calculating phonons from finite differences. Other implementations of forces within DFT+DMFT exist; for example the work of Leonov *et al.* (Ref. [140]). In contrast to the force implementation used in this work, the method in Ref. [140] uses a Wannier function basis and does not define

the force as the derivative of a stationary free energy functional. Despite these difference, the implementation of Ref. [140] should in principle also be suited for lattice dynamics calculations with the direct method.

All DFT+DMFT calculations were performed using the code available at [147]. The DFT part of the calculation is based on the `WIEN2K` code [150], using an all-electron LAPW basis set. The LDA is used throughout as the exchange-correlation functional for the DFT part. A window of 20 eV around the Fermi level is used for the hybridisation. The DMFT calculations were performed using the exact double counting [50]. Experimental lattice parameters were obtained from Ref. [151] for Fe, Ref. [152] for MnO and NiO, and Ref. [153] for $SrVO_3$. The interaction parameters for Fe were obtained from a previous study that performed constrained DMFT calculations ($U = 5.5$ eV, $J = 0.84$ eV) [144]. For both MnO and NiO, $U = 9.0$ eV was chosen for the correlated d-orbitals with $J_{\mathrm{Mn}} = 1.14$ eV and $J_{\mathrm{Ni}} = 1.3$ eV. For $SrVO_3$, $U = 6.0$ eV and $J = 1.0$ eV were used. Fine tuning of the parameters is avoided in this study. Calculations for the primitive cells of Fe, MnO, and NiO used $\mathbf{k}$-point grids of size $12 \times 12 \times 12$, and for $SrVO_3$ a $10 \times 10 \times 10$ grid was used. Equally dense grids were used for all supercell calculations.

6.2.2 Lattice Dynamics

The objective of lattice dynamics calculations in the harmonic approximation is to determine the dynamical matrix at a given $\mathbf{q}$-point in the irreducible Brilouin zone. For a crystal with a primitive cell of $i = 1, ..., N$ atoms at positions $\{\boldsymbol{\tau}_i\}$, the dynamical matrix at point $\mathbf{q}$ is defined as

$$D_{i\alpha,j\beta}(\mathbf{q}) = \frac{1}{\sqrt{m_i m_j}} \sum_{\mathbf{R}} \Phi_{i\alpha,j\beta}(\mathbf{R}) e^{i\mathbf{q}\cdot(\mathbf{R}+\boldsymbol{\tau}_j-\boldsymbol{\tau}_i)} \tag{6.2}$$

where α, β label cartesian coordinates and i, j label the atoms within a primitive cell. The masses of the atoms are given by m_i and m_j, and

$$\Phi_{i\alpha,j\beta}(\mathbf{R}-\mathbf{R}') = \frac{\partial^2 E}{\partial u_{i\alpha\mathbf{R}'} \partial u_{j\beta\mathbf{R}}} = -\frac{\partial F_{j\beta\mathbf{R}}}{\partial u_{i\alpha\mathbf{R}'}} \tag{6.3}$$

is the matrix of interatomic force constants, which is a function of $\mathbf{R} - \mathbf{R}'$ only, due to the translational invariance of the solid. The Born-Oppenheimer potential energy surface E is in this case given by the free energy as obtained from the Luttinger-Ward functional of DFT+DMFT, while $u_{i\alpha\mathbf{R}'}$ corresponds to the displacement of atom i in the primitive cell at positions $\mathbf{R}'$ along cartesian direction α. In practice $\Phi_{i\alpha,j\beta}$ is computed row by row through the derivatives of the forces $F_{j\beta\mathbf{R}}$. The phonon frequencies and eigenvectors are found by diagonalising the dynamical matrix. We have used atomic displacements of 0.02 Bohr throughout, but tests with 0.01–0.04 Bohr show almost identical results for Fe and NiO.

In the direct method of lattice dynamics calculations, the force constant matrix is determined by constructing a supercell. Conventionally, to determine phonon frequencies and eigenvectors on a $N_1 \times N_2 \times N_3$ $\mathbf{q}$-point grid, a supercell of dimensions $N_1 \times N_2 \times N_3$ would be constructed. In this work, the non-diagonal supercell method of Monserrat *et al.* [145] is used, which allows a more

efficient determination of the force constant and dynamical matrices than the use of a diagonal supercell. The method relies on the fact that a perturbation of the atomic positions that has a wavevector $\mathbf{q}$ is commensurate with a supercell for which $\mathbf{q}$ is a reciprocal lattice vector. It can then be shown that for a $N_1 \times N_2 \times N_3$ $\mathbf{q}$-point grid, a set of supercells, each of which contains at most a number of primitive cells equal to the least common multiple of N_1, N_2, and N_3, are sufficient to determine the dynamical matrix at every $\mathbf{q}$-point in the grid. In particular, the method allows the sampling of vibrational Brillouin zones with a uniform grid of size $N \times N \times N$ using supercells that contain at most N primitive cells. In contrast, using only diagonal supercells, the largest of these contains N^3 primitive cells. Non-diagonal supercells are solutions to the "minimum supercell problem" for computing phonons as recently described by Fu *et al.* [154], and are the most efficient method (in terms of system size) to compute phonons at a given $\mathbf{q}$-point. The ideas can be generalised to interactions between phonons, as described in Ref. [154].

The true force constant matrix satisfies certain sum rules [155]. In particular, Newton's third law requires that the sum of the forces on the atoms is zero for every calculation ($\sum_i \mathbf{F}_i = \mathbf{0}$). In terms of the force constant matrix, this means that every row and column must sum to zero:

$$\sum_j \Phi_{i\alpha,j\beta} = 0. \tag{6.4}$$

Stated differently, $\Phi_{i\alpha,i\beta}$ must be given by

$$\Phi_{i\alpha,i\beta} = -\sum_{j\neq i} \Phi_{i\alpha,j\beta} \tag{6.5}$$

The difference between $\Phi_{i\alpha,i\beta}$ as obtained from the calculation, and calculated by Eq. 6.5 can be used as a measure to judge the accuracy or numerical precision of the force evaluations in the *ab initio* calculation [156]. This is particularly relevant for DFT+DMFT calculations as the forces are affected by statistical noise. We have also observed that the sum rule and symmetry violations tend to be larger with DFT+DMFT derived forces than for pure DFT calculations. The sum rule and the point group symmetry are therefore applied to the force constant matrices.

In polar insulators, the longitudinal optical (LO) and transverse optical (TO) phonon modes are split close to the Γ point due to the interaction between LO phonons and macroscopic electric fields. This LO-TO splitting needs to be taken into account to accurately model the phonon spectra of MnO and NiO. In DFT calculations, LO-TO splitting is included by separately calculating the Born effective charge tensors Z_i^* and the macroscopic dielectric tensor ϵ_∞, and adding a non-analytic correction to the dynamical matrix [157]. Unfortunately, for Green's function based methods like DMFT, the calculations of polarisation (and hence Born effective charges) is still an unsolved theoretical problem. In the limit $\mathbf{q} \to 0$, the frequencies of the LO and TO phonon modes ω_{LO} and ω_{TO} are related to Z^* and ϵ_∞ according to

$$\omega_{\mathrm{LO}}^2 - \omega_{\mathrm{TO}}^2 = \frac{e^2}{\epsilon_0 \mu \Omega} \frac{|Z^*|^2}{\epsilon_\infty} \tag{6.6}$$

where e is the elementary charge, Ω is the volume of the primitive unit cell, ϵ_0 is the vacuum

permittivity, and μ is the reduced mass of the two atoms in the unit cell. The phonon frequencies ω_{LO} and ω_{TO} can be obtained from a non-diagonal supercell representing a $\mathbf{q}$-point close to Γ, and the resulting value of $|Z^*|^2/\epsilon_\infty$ is used for the non-analytic correction to the dynamical matrix.

6.3 Results and Discussion

6.3.1 Fe

At ambient pressure, iron crystallises in three different polymorphs: the bcc-α phase (stable below 1185 K), the fcc-γ phase (stable between 1185–1670 K), and the bcc-δ phase (stable up to the melting point of 1811 K). The bcc-α phase is ferromagnetic below the Curie temperature of 1043 K. DFT+DMFT calculations are well suited for the *ab initio* simulation of the interplay between metallicity and local moments in iron [158]. Importantly, DFT+DMFT is able to capture both the paramagnetic regime and the temperature-dependent change in the local moment. Within DFT, describing these temperature effects requires much additional work starting from the actual first-principles calculations [159, 160, 161].

The temperature dependence of the phonon spectra of elemental iron has been studied previously both experimentally [162, 163] and computationally [144, 142]. In the ferromagnetic bcc α-phase, a pronounced softening of the phonon modes is observed as the temperature increases. The phonon softening can be captured with a number of different simulation methods [159, 160, 161]. A recent DFT+DMFT study by Han *et al.* clearly attributed the phonon softening to the melting of the ferromagnetic order [144].

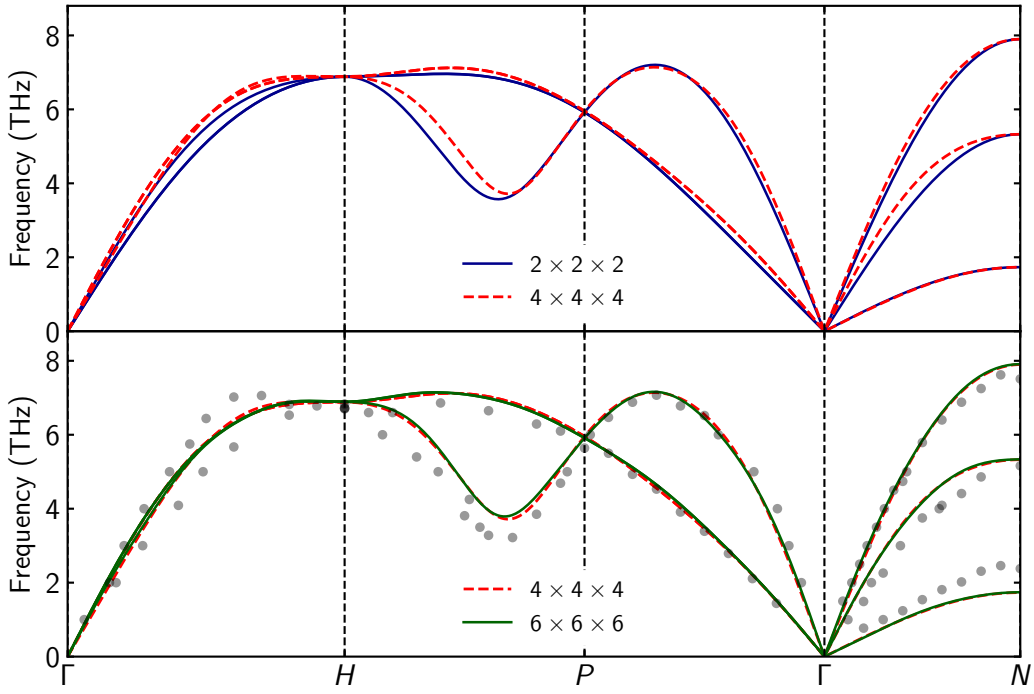

Figure 6.1: Convergence of the phonon dispersion of paramagnetic bcc δ-Fe (T = 1740 K) with $\mathbf{q}$-point grid size. The grey dots correspond to the experimental data from Ref. [163].

Here we compute the phonons for iron at temperatures of 1160 K and 1740 K at the experimental equilibrium volumes. The convergence of the phonon dispersion of paramagnetic δ-Fe ($T = 1740$ K) is shown in Fig. 6.1. While previous work used a minimal $2\times2\times2$ **q**-point grid [144], there are small but visible differences between the results of a $2 \times 2 \times 2$ and a $4 \times 4 \times 4$ grid. The phonon dispersion is effectively converged with a $4 \times 4 \times 4$ grid, because the differences with the $6 \times 6 \times 6$ result are small. The advantage of non-diagonal supercells is clear with the largest grid; while for non-diagonal supercells, only supercells of up to six atoms are needed (scaling linearly with grid size N), the diagonal supercell would contain 216 atoms (scaling as N^3). For the case of iron the DFT+DMFT force calculations are remarkably robust; the difference between the force computed directly by DFT+DMFT ($\mathbf{F}_i$) and that required by the acoustic sum rule ($-\sum_{j\neq i}\mathbf{F}_j$) is smaller than 0.1% (cf. Methods).

The agreement between the experimental data (grey dots in Fig. 6.1, Ref. [163]) and the calculations is very good, although there are small differences in the frequencies at certain **q**-points, and the splitting of the branches along $\Gamma \rightarrow H$ is much smaller than in the experiment.

The phonon dispersion of the ferromagnetic α-phase is shown in Fig. 6.2 for a temperature of 1160 K. While the experimental Curie temperature T_C is 1043 K, it is overestimated by DFT+DMFT calculations. This due to the fact that DMFT is a mean field theory and as such overestimates phase transition temperatures. Within DFT+DMFT, the transition temperature depends on the choice of Coulomb interaction in the impurity solver [164, 165]. The two options are the density-density only ('Ising') and rotationally invariant ('Full') Coulomb interaction. In the case of Fe, the choice of Coulomb interaction has an effect on the magnetic properties; while the Curie temperature with the Ising Coulomb interaction is 2500 K, using the Full interaction, the T_C is 1550 K [144]. As a consequence, the magnetic moment for the same physical temperature of 1160 K is larger for Ising (2.38 μ_B) than for Full (1.7 μ_B). A comparison of the phonon dispersions at 1160 K calculated with Ising and Full Coulomb interactions demonstrates that the phonon frequencies with Ising are larger (Fig. 6.2). This difference is expected given the larger magnetic moment with Ising and the fact that the phonons in Fe soften with decreasing ferromagnetic order, as observed previously [144, 163]. For the paramagnetic case, no such difference between Ising and Full is observed and the phonon dispersions computed with the two methods are identical (not shown). This illustrates two important points: (1) it is consistent with the interpretation that the phonon softening is largely due to melting of the ferromagnetic order [144], and (2) it suggests that phonons can be sensitive to the choice of Coulomb interaction. If this is the case, the approach used in Ref. [144] of scaling the physical temperature with respect to T_C is appropriate.

While the use of non-diagonal supercells significantly speeds up the DFT+DMFT lattice dynamics calculations, it is still very expensive compared with DFT. The cost of the DFT+DMFT calculations increases with the number of atoms N_{at} in the unit cell as $aN_{\mathrm{at}} + bN_{\mathrm{at}}^3$. The linear term is due to the solution of the quantum impurity problems, which dominates the cost of the DFT calculation (cubic term, small b) for reasonably sized systems [166]. The lattice dynamics calculations use very small atomic displacements (0.02 bohr) and it is worth checking how much the solution of the impurity problem is affected by the small changes in atomic positions. Fig. 6.3 shows the difference between phonon dispersions obtained by (1) solving the impurity problem

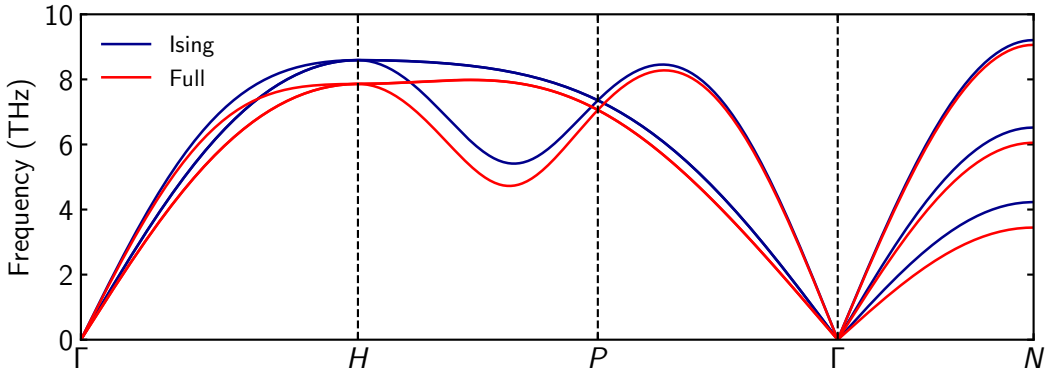

Figure 6.2: Phonon dispersion of ferromagnetic bcc α-Fe ($T = 1160$ K) computed with a $2 \times 2 \times 2$ **q**-point grid. The phonon dispersion shows clear differences between density-density ('Ising') and rotationally invariant ('Full') Coulomb interactions used in the impurity solver. With 'Ising', the magnetic moment is larger than with 'Full', and the phonons are consequently harder.

separately for each correlated atom in the unit cell [variable $\Sigma(\omega)$], and 2) a calculation in which the self-energy for each correlated Fe atom is fixed to be equal to that of an Fe atom in the undisplaced equilibrium configuration [fixed $\Sigma(\omega)$]. The differences are very small; for example, at the N point the phonon frequencies differ by at most 0.1 THz. Based on these results, it seems that fixing the self-energy is an excellent approximation for the case of iron. These differences are of the same magnitude as those that would be deemed acceptable when carrying out a convergence test of the phonon frequencies with respect to the basis set size (RK_{max}), or the number of **k**-points in the calculation. This suggests that the hybridisation and the impurity levels are not sensitive to the small displacements that are involved in the lattice dynamics calculation, and the impurity problem is hardly affected. Performing the calculations with a fixed self-energy offers a massive benefit: a single DFT+DMFT calculation in the high-symmetry equilibrium configuration is sufficient to obtain $\Sigma(\omega)$. After that, the forces for structures with various displacements of atoms can be calculated at the cost of a DFT calculation, since all that is required is the calculation of the lattice Green's function with a fixed $\Sigma(\omega)$. Timing information shows that for the calculation of the $2 \times 2 \times 2$ **q**-point grid shown in Fig. 6.3, performing the calculations with a fixed self-energy is ten times faster. In general, the speedup depends on the ratio of the amount of time spent in the impurity solver to the time spent in other steps of the calculation.

It is important to examine the validity of fixing the self-energy in each individual case. As shown in the following sections, for the materials studied in this work, a fixed self-energy is an excellent approximation. Put differently, this means that the change in the self-energy with respect to position is small and therefore the two-particle vertex function is not important for computing forces. However, one might expect that this approximation breaks down when the material is close to a phase transition. At present, we recommend testing this approximation in particular cases that are under consideration. In the following, we have tested it by comparing at least the Γ-point phonon frequencies with a fixed self-energy to those of a non-approximated calculation.

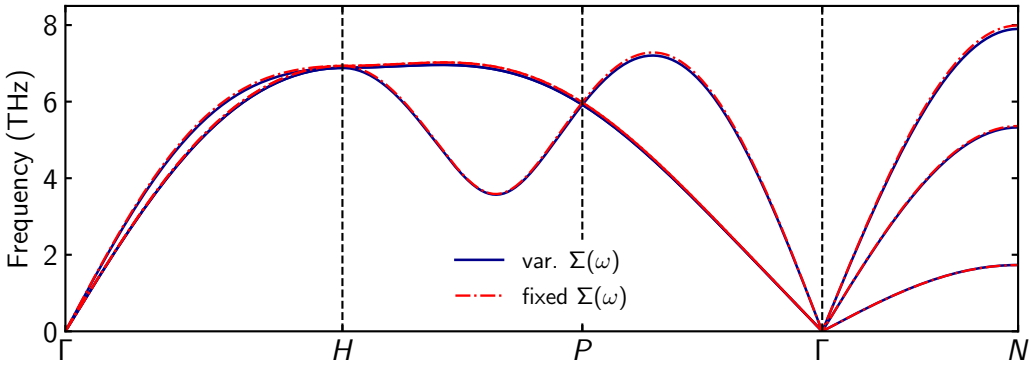

Figure 6.3: Phonon dispersion of paramagnetic bcc δ-Fe ($T = 1740$ K, $2 \times 2 \times 2$ **q**-point grid) with fixed and variable self-energy (see text). The results match to within 0.1 THz.

6.3.2 NiO and MnO

NiO and MnO are antiferromagnetic insulators with Neel temperatures T_N of 525 K and 116 K respectively. Above T_N, the compounds are paramagnetic insulators. Magnetic ordering in NiO and MnO induces a change in crystal symmetry; while the high temperature phases are cubic, the low temperature AFM phases are rhombohedral. The phonon spectra of both NiO and MnO do not depend sensitively on the presence of long-range magnetic order [167], but the change in crystal symmetry leads to small changes in the phonon frequencies due to magnetic anisotropy [168, 169, 170]. One of the advantages of using DFT+DMFT over DFT for lattice dynamics calculations of NiO and MnO is the ability to simulate the paramagnetic regime directly. We therefore chose to perform the calculations for the paramagnetic regime at room temperature. MnO is in fact paramagnetic at room temperature, and for NiO this is a commonly used simplification.

The cubic phase is also convenient because it simplifies including LO-TO splitting for MnO and NiO. Since it is currently not possible to calculate Born effective charge tensors with DFT+DMFT, the LO-TO splitting has to be calculated using elongated supercells that represent **q**-points close to Γ. It is much easier to do this for the cubic paramagnetic phases than for the AFM phases. Unfortunately, elongated supercells [e.g. corresponding to $\mathbf{q} = (0, 0, \frac{1}{8})$] led to problems with the DFT+DMFT force calculations. Specifically for the binary crystal structures NiO and MnO, the non-diagonal supercells showed non-zero forces on atoms even in the high-symmetry equilibrium configuration. The problems became more severe with larger cell sizes, increasingly unequal lattice parameters, and large deviations of unit cell angles from 90°. While the computational expense of a $6 \times 6 \times 6$ or $8 \times 8 \times 8$ **q**-point grid would have been manageable, the systematic issues with the forces prevented the use of larger grids. We note that these issues were not due to statistical noise in the impurity solver and seem to leave room for improvement of the implementation. These problems were not encountered in the case of Fe, and therefore seem to be related to having two atomic species present in the cell, one of which is being treated as correlated while the other is not. While these issues affect the lattice dynamics calculations, which involve small atomic displacements, the force implementation works very well for structural optimisation of correlated materials [139, 172, 173]. Since we were unable to extract the LO and TO mode frequencies, we

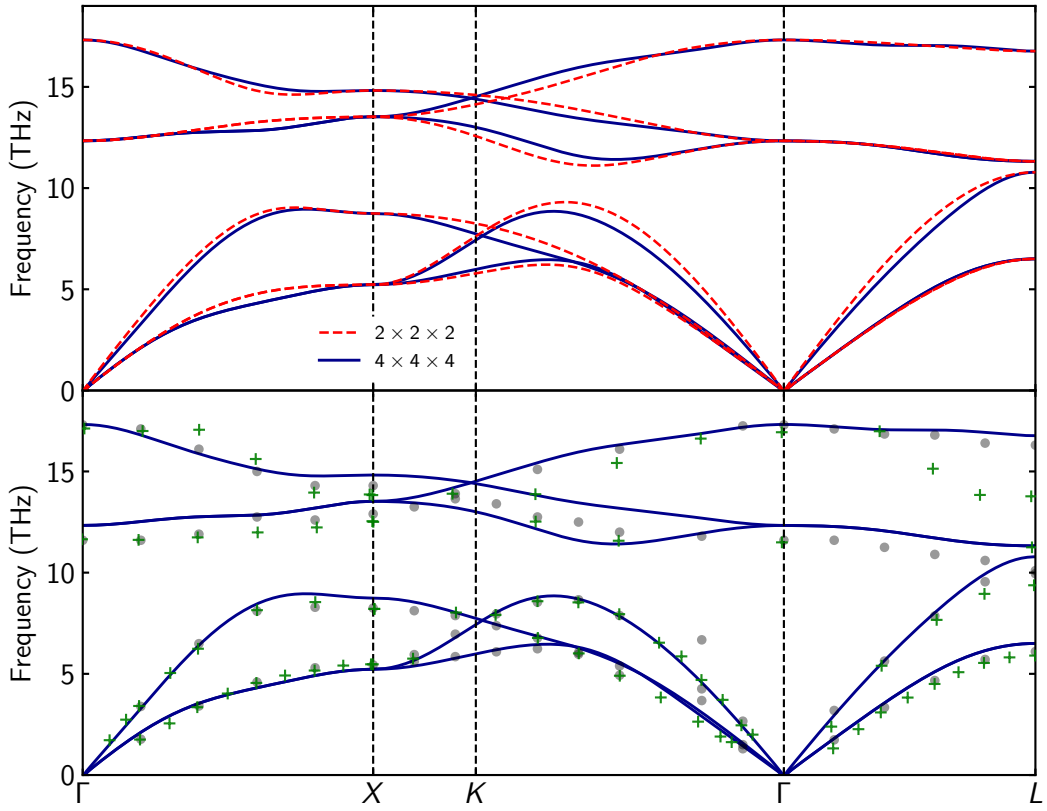

Figure 6.4: Convergence of the phonon dispersion of NiO with the size of the **q**-point grid. The grey dots correspond to the data of Reichardt *et al.* [167], and the green crosses to the data of Coy *et al.* [171].

instead use values of Z^* and ϵ_∞ from Ref. [141] or experiment [174, 175] for the LO-TO splitting. While unsatisfactory, there is currently no other method of including the LO-TO splitting using finite differences.

Phonon dispersions for NiO with different **q**-point grid sizes are compared in Fig. 6.4. The differences between the $2 \times 2 \times 2$ and $4 \times 4 \times 4$ **q**-point grids are larger than for the case of Fe, which can be attributed to the stronger screening in the metal. For NiO, non-diagonal supercells allow us to access a grid of $4 \times 4 \times 4$ with supercells that contain at most 4 primitive cells (8 atoms). A diagonal supercell would contain 64 primitive cells (128 atoms), which would be much more computationally expensive. The DFT+DMFT phonon dispersions are compared to two sets of experimental data from Refs. [167, 171] in Fig. 6.4. The agreement between experiment and calculation is good, especially given the differences between the two sets of experimental data. The acoustic branches show a better agreement with the experimental data than the optical branches. Using the self-energy of the equilibrium configuration for the lattice dynamics calculation is also an excellent approximation for NiO; for example, the TO mode frequency at Γ changes by less than 0.01 THz. Depending on the shape of the non-diagonal supercell the differences between the results obtained from a fixed vs variable self-energy can be larger, but this is likely due to the issues with the DFT+DMFT force calculations discussed above.

Phonon dispersions for MnO with grids of sizes $2 \times 2 \times 2$ and $4 \times 4 \times 4$ are shown in Fig. 6.5. As

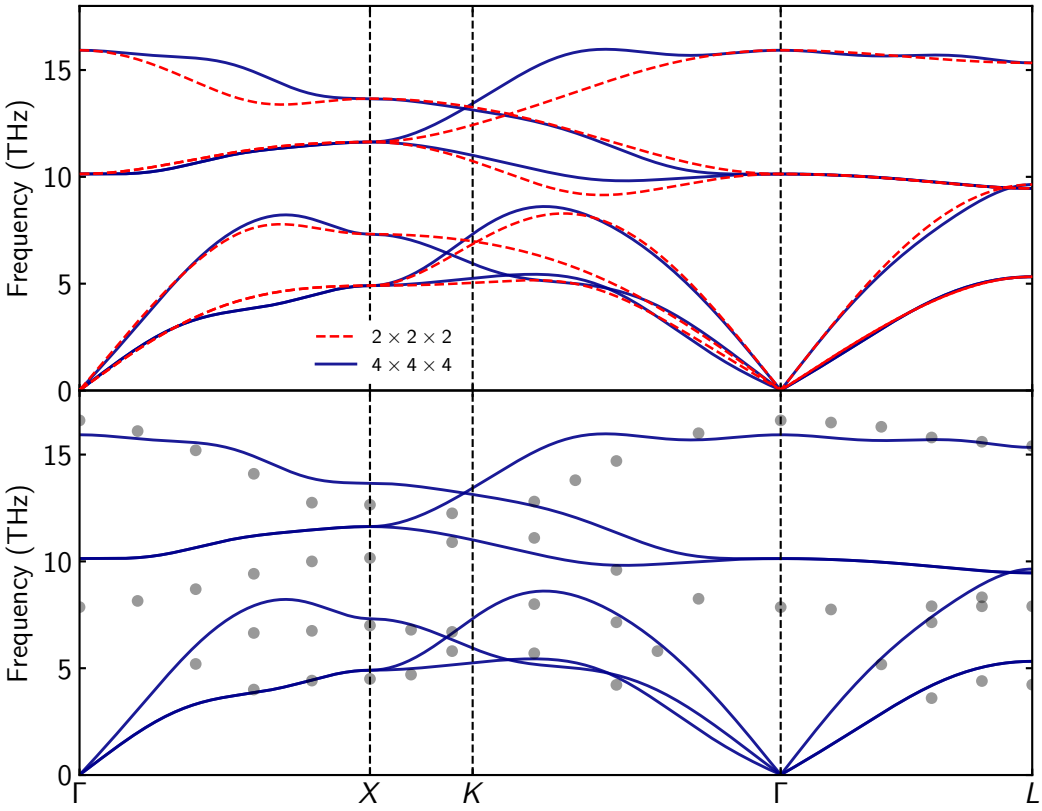

Figure 6.5: Convergence of the phonon dispersion of MnO with the size of the **q**-point grid. The grey dots correspond to the data of Wagner *et al.* [176].

for NiO, there are significant differences in the phonon dispersions obtained with a larger **q**-point grid. The DFT+DMFT results for the $4 \times 4 \times 4$ grid are compared to the experimental data of Wagner *et al.* [176]. For MnO, the agreement with experiment is not as good as for NiO. This is mostly due to a difference of 2.3 THz between the experimental and calculated TO phonon mode frequency at Γ.

The vibrational properties of MnO and NiO have been studied previously by DFT with different functionals, including DFT+U and hybrid functionals [177, 178, 179]. The study by Linnera *et al.* [179] used hybrid functionals and obtained good agreement with the experimental phonon spectrum of NiO, but a strong underestimation of the optical phonons at Γ for MnO. DFT+U was used in Refs. [177, 178], obtaining good agreement with experimental phonon frequencies for MnO when choosing an appropriate U value. We have tested U values in the range 8–10 eV in DFT+DMFT calculations for MnO, but this did not improve agreement with the experimental phonon frequencies (although tuning to much lower U values might). Given the charge-transfer insulating nature of MnO an insensitivity to the precise U value is expected.

6.3.3 $SrVO_3$

The perovskite $SrVO_3$ is often cited as a textbook example of a strongly correlated metal. The vanadium atom nominally has a d^1 configuration with a single electron in its t_{2g} subshell. The

$SrVO_3$ spectral function shows a well-established three-peak structure, with a quasiparticle peak around the Fermi level, and pronounced lower and upper Hubbard bands below and above [180, 181]. We have calculated the phonons of $SrVO_3$ at $T = 293$ K with DFT+DMFT to assess the effect of strong correlations on the vibrational properties of the material. Note that due to the metallic nature of the material there is no LO-TO splitting.

For $SrVO_3$, the violation of the acoustic sum rule is much more severe than for Fe, NiO, or MnO. The condition of Eqn. 6.5 is satisfied only to within 5–7% in the worst cases, which is a significantly larger violation than for the previous materials. For displacements that involve the correlated vanadium atom and its nearest neighbours the violation of the acoustic sum rule is worse than for displacements that only involve Sr. This issue likely arises due to contributions to the forces from terms that depend on the correlated subspace. In the case of Fe, all atoms are equivalent and this term cancels, while for NiO, MnO, and $SrVO_3$ these terms cannot cancel because of the presence of different atomic species. Enforcing the sum rule is essential to obtain useful results.

As for the other materials, reusing the self-energy of the equilibrium configuration for the lattice dynamics calculation is an excellent approximation. For the modes at Γ, the frequencies computed with a fixed vs variable self-energy differ by less than 0.01 THz. We therefore performed the calculations of a 2×2×2 **q**-point grid for $SrVO_3$ with a fixed self-energy. The resulting LDA+DMFT phonon dispersion is shown in Fig. 6.6 and compared to the LDA Γ-point phonon frequencies, since experimental data for the vibrational properties of $SrVO_3$ is not available. The results confirm

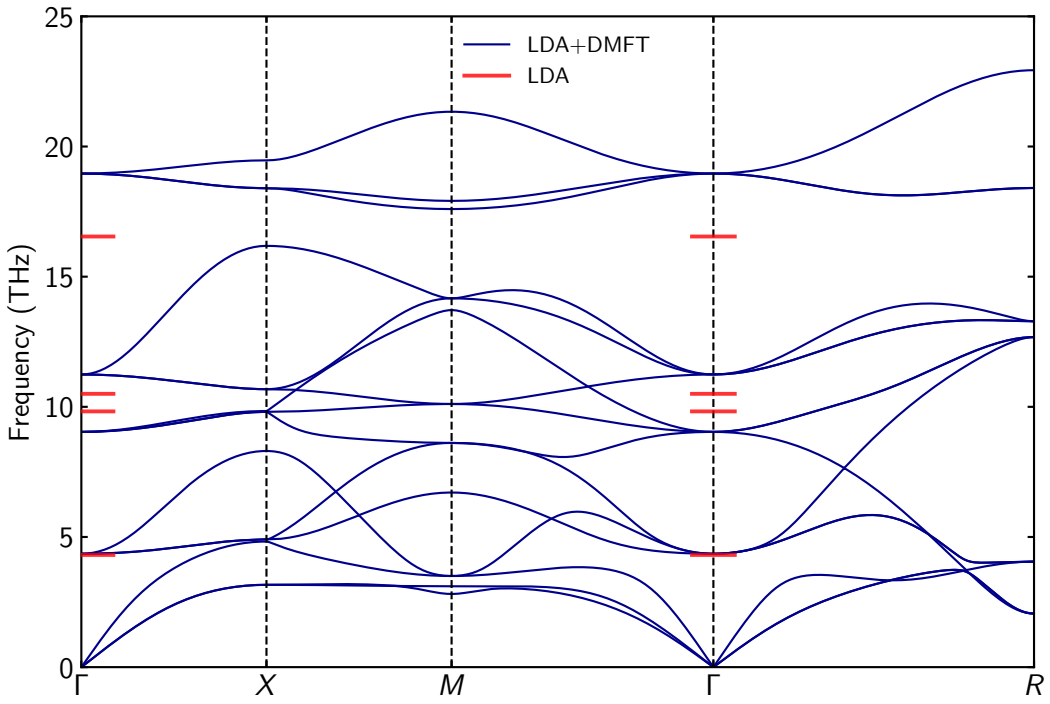

Figure 6.6: Phonon dispersion of $SrVO_3$ ($T = 293$ K) computed with a $2 \times 2 \times 2$ **q**-point grid, at the LDA+DMFT level of theory. Frequencies of Γ point phonons calculated with LDA are marked in red.

the dynamical stability of the $SrVO_3$ perovskite structure at the LDA+DMFT level of theory. Focusing on the Γ point, there are five threefold degenerate phonon modes. The frequencies of the modes are renormalised by correlation effects by different amounts. The frequency of the highest mode changes the most, while the frequency of the lowest mode, dominated by Sr moving against an almost rigid VO_6 octahedron, is the same for LDA and LDA+DMFT. This is expected since the correlated atom and its nearest neighbours do not change their relative positions, and confirms the internal consistency of the LDA+DMFT phonon calculations; if a phonon mode does not involve the motion of the correlated atoms or their direct neighbors, the frequency should be unchanged from the DFT value. On the other hand, if a mode features large changes in the relative positions of a correlated atom and its nearest neighbors, correlation effects can be expected to strongly impact the frequency of that mode. This is the case for the highest frequency Γ-point phonon, which is more strongly affected by correlation effects because the vanadium and oxygen atoms move relative to each other. These observations indicate the most useful applications of DMFT phonon calculations: phonon effects that depend on correlations and temperature due to the involvement of correlated atoms in the atomic motion.

6.4 Conclusion

This chapter described a method to efficiently compute phonons in correlated materials using a DFT+DMFT approach. The method combines a robust DFT+DMFT force implementation with the use of non-diagonal supercells for finite difference lattice dynamics calculations. We have calculated phonons of multiple different correlated materials, including metals and insulators, elemental, binary and ternary crystals. The efficiency of the method allowed us to access **q**-point grids of very large size. The agreement between the calculations and available experimental data is generally good. Based on our tests, the self-energy obtained from a DFT+DMFT calculation of the equilibrium configuration is accurate enough for lattice dynamics calculations, which eliminates the need to solve a large number of impurities for configurations with displaced atoms. Finally, we have discussed some issues with the DFT+DMFT force implementation that should be solved to make the calculation of phonons using finite differences more robust.

There are many problems in condensed matter physics involving strongly correlated materials that would benefit from an elucidation of the phonons with DFT+DMFT. Cases that come to mind are the phase diagram of f-elements such as cerium and uranium, and the metal-insulator transitions in vanadate materials. The method should be especially useful for evaluating phonons close to phase transitions to clarify the role they play in correlated materials and for the interpretation of temperature dependent diffuse scattering across structural phase transitions [182, 183]. More generally, finite difference approaches for lattice dynamics will also be useful for calculations of electron-phonon coupling and a variety of other phenomena in strongly correlated materials that depend on atomic vibrations.

Chapter 7

Conclusion and Outlook

In this thesis, a range of first-principles methods have been used to study complex phenomena in oxide materials. The first part of the thesis was concerned with the Wadsley–Roth phases. Compounds in this family of niobium-based oxides share a distinct "block-type" crystal structure, giving rise to similar properties across the family. Different aspects of the Wadsley–Roth phases were studied carefully to understand their fundamental properties and their excellent performance as lithium-ion battery electrode materials. The second part of the thesis left the Wadsley–Roth phases behind to develop a method to calculate vibrational properties of correlated materials with DFT+DMFT, and apply it to a selection of typical correlated materials.

In Chapter 3, the electronic structure and magnetic properties of the niobium suboxides Nb_2O_{5-x} were investigated using first-principles calculations at different levels of theory. The motivation for this study was twofold: 1) the niobium suboxides form an interesting group of compounds on their own, and 2) establishing an understanding of the electronic structure of Wadsley–Roth phases and the appropriate level of theory was crucial for the work in the following two chapters. By investigating the electronic bandstructures and density-of-states of five different compounds we conclusively established the coexistence of flat and dispersive energy bands, corresponding to localised and delocalised electronic states. Localised electrons occupy large orbitals that span multiple niobium sites in the plane of the blocks. Localised and delocalised electronic states were both found to be effectively one-dimensional and were partitioned between different types of niobium sites. Flat bands associated with localised electrons were present even at the GGA level, but a correct description of the localisation requires the use of GGA+U or hybrid functionals. Our computational results allowed us to explain the experimentally observed electrical and magnetic properties of niobium suboxides, whose behaviour turns out to be similar to n-doped semiconductors. However, there is a limited capacity for localised electrons: when a threshold of one electron per block is exceeded, metallic electrons are added to existing localised electrons. This behaviour was found to be general for any type of n-doping, and also occurs when these materials are n-doped by alkali metal (lithium) ions during operation of niobium oxide-based battery electrodes.

Following this, the cation disorder and lithium insertion mechanism of Wadsley–Roth phases, specifically niobium tungsten oxides, was studied in Chapter 4. By examining three different Nb/W

oxides we sought to discover common principles governing the cation disorder, lithium insertion mechanism, and electronic structure of these materials. Using an enumeration-based approach, we generated a complete set of cation configurations and obtained their relative energies. We found that tungsten preferentially occupies tetrahedral and block-central sites within the block-type crystal structures. By examining the individual cation configurations we discovered that the local structure of the materials depends on the cation configuration, which implies that both lithium site energies and hopping barriers could vary according to the local cation arrangement. To study the lithium insertion mechanism, we again used enumeration to generate a complete set of lithium-vacancy configurations over the lithium sites of the crystal structure. This allowed us to follow the evolution of the materials over the course of lithium insertion in detail. We found that the lithium insertion proceeds via a three-step mechanism, associated with an anisotropic evolution of the host lattice. The calculations revealed an important connection between long-range and local structural changes: in the second step of the mechanism, the removal of local structural distortions leads to the contraction of the lattice along specific crystallographic directions, buffering the volume expansion of the material. The electronic structure evolution of the materials over the course of lithium insertion follows the general principles introduced in Chapter 3: they host small amounts of localised electrons during initial lithium insertion due to the confining effect of the blocks, but quickly become metallic upon further lithiation. The combination of local, long-range, and electronic structural evolution over the course of lithiation is beneficial to the performance of these materials as battery electrodes. The principles we established are fundamentally linked to the crystallographic structure of the materials, and therefore transferable to niobium titanium oxide or pure niobium oxide crystallographic shear phases.

Building on the results of the previous two chapters, Chapter 5 examined the lithium diffusion mechanism of niobium tungsten oxides. To study the lithium diffusion nudged elastic band (NEB) calculations and *ab initio* molecular dynamics (AIMD) simulations were used. Lithium diffusion was found to occur through jumps between fourfold coordinated window sites with low activation barriers (80–300 meV). The crystallographic shear planes of the structures constrain the lithium motion to be effectively one-dimensional. A number of other processes were identified, including rattling motions with barriers on the order of the thermal energy at room temperature, and intermediate barrier hops between fourfold and fivefold coordinated lithium sites. We found that cavities of distinct types host different diffusion pathways: within the block units of the structures, cavities at the corners and edges host more isolated diffusion tunnels than those in the interior. Diffusion coefficients were found to be in the range of 10^{-12}–10^{-11} m^2s^{-1} for lithium concentrations of 0.5 Li/TM. We also identified a curious type of tungsten interstitial defect, formed when a tungsten ion moves out of the tetrahedral site into an adjacent octahedral site. The structure–property relationships regarding diffusion that were identified are transferable to to the entire family of Wadsley–Roth phases, much like the principles regarding electronic structure and lithium insertion studied in the previous two chapters. This is again due to the crystallographic similarity between Wadsley–Roth phases, and the distinct structural features of their block-type crystal structures.

Chapter 6 opened a new direction of research by developing a method to compute phonons in correlated materials. A robust DFT+DMFT force implementation was combined with the direct method for lattice dynamics. The use of non-diagonal rather than diagonal supercells drastically reduces the computational expense associated with the DFT+DMFT calculations. We benchmarked the method for typical correlated materials, and due to the efficiency of non-diagonal supercells we were able to access large phonon **q**-point grids. To further reduce the cost of the DFT+DMFT calculations, we introduced a fixed self-energy approximation, which is expected to hold for materials that are not close to a phase transition.

There are a number of directions along which the work presented in this thesis can be extended and built upon. I believe the niobium suboxides are a very interesting class of compounds and their electronic structure warrants further study. Unfortunately, they are also rather difficult to prepare as single phases, which has probably contributed to the fact that they have not been studied in detail experimentally since the 1990s. There are still open questions: even with first-principles calculations it is not possible to explain satisfactorily why monoclinic $Nb_{12}O_{29}$ shows magnetic order but orthorhombic $Nb_{12}O_{29}$ does not. It would also be interesting to examine the electronic structure of lithiated Wadsley–Roth phases using the same experimental techniques that were used for the niobium suboxides to link the electronic structure to the battery performance. One experiment I would personally like to see is angle-resolved inverse photoemission spectroscopy on any of the pure Wadsley–Roth phases along the dominant BZ direction. I think this would nicely demonstrate the coexistence of the different electronic states within the structures. In regards to future computational work, the interesting interplay between localised and delocalised electrons calls for further studies using beyond-DFT methods such as DMFT or GW.

From an experimental point of view, the Wadsley–Roth phases present a huge design space, and this will probably one of the most promising directions for future work in the field. A large number of cations could be doped into existing phases, replacing the Ti/Nb/W with Zr/Mo/Hf or other elements. Initial work in this direction has already been reported [184], but detailed characterisation studies are still missing. Going a step further, the mix of cations could be expanded even further and their ratios equalised. One could envision block-type structures including Ti, Nb, W and other cations mixing at the atomic level to create 'high-entropy' mixed-metal oxides with block-type structures. The feasibility of this depends of course on the detailed thermodynamics, but I believe it is worth trying. High-entropy alloys have attracted attention in the metallurgical space [185], while high-entropy oxides in the battery cathode space have shown promising performance [186].

There are also a number of fundamental questions that deserve further investigation. How do the details of the local cation configuration impact the lithium diffusion and site energetics? Is there any benefit to a disordered crystal structure? Future studies of diffusion could make use of the recent developments in machine learning potentials to simulate larger system sizes and longer timescales, possibly even disordered systems. Can we detect features of the constrained 1D dynamics in any of the experimental measurements, and measure the hopping barriers for lithium more accurately? The role of defects in Wadsley–Roth phases is another, currently unexplored, area of research. While we have observed one interesting type of defect formation, and there is

preliminary evidence that it might play a role in cycling, a lot more work in this direction is required.

The final chapter developed a method for the calculation of phonons using DFT+DMFT, and this opens up many possibilities for the study of lattice dynamics and associated phenomena in correlated materials. The next direction of research should be a reexamination of the role of phonons in phase transitions of correlated materials, e.g. close to metal-insulator transitions. Do phonons play a role? Are the electronic and structural transitions coupled? Another very promising second direction that is now open is the development of electron-phonon coupling methods using DFT+DMFT, built on available finite-difference approaches [187].

While I have outlined some my own thoughts for further research, I am sure there are many other directions of future scientific research into the Wadsley–Roth phases and lattice dynamics of correlated materials. The coming years should see great progress in both areas.

Appendix A

Supporting Information for Chapter 4

This appendix contains additional figures and tables relevant to the study of the cation disorder and lithium insertion mechanism of niobium tungsten oxides in Chapter 4.

Site	DFT (1050 °C)	DFT (1200 °C)	DFT (1350 °C)
M1	0.023	0.030	0.037
M2	0.020	0.026	0.033
M3	0.016	0.022	0.028
M4	0.024	0.031	0.038
M5	0.563	0.557	0.549
M6	0.506	0.505	0.503
M7	0.086	0.100	0.110
M8	0.686	0.637	0.594
M9	0.058	0.068	0.076
M10	0.018	0.024	0.031
M11 (tet.)	1.0	1.0	1.0

Table A.1: Tungsten occupancies on cation sites in $Nb_{16}W_5O_{55}$. The occupancy of the tetrahedral M11 site was fixed to one during the enumeration. All sites except M11 have a multiplicity of two. Taking into account the degeneracies, the total W occupancy in a single block is five, as required. The synthesis temperature is reported as 1350 °C [17] or 1200 °C [13].

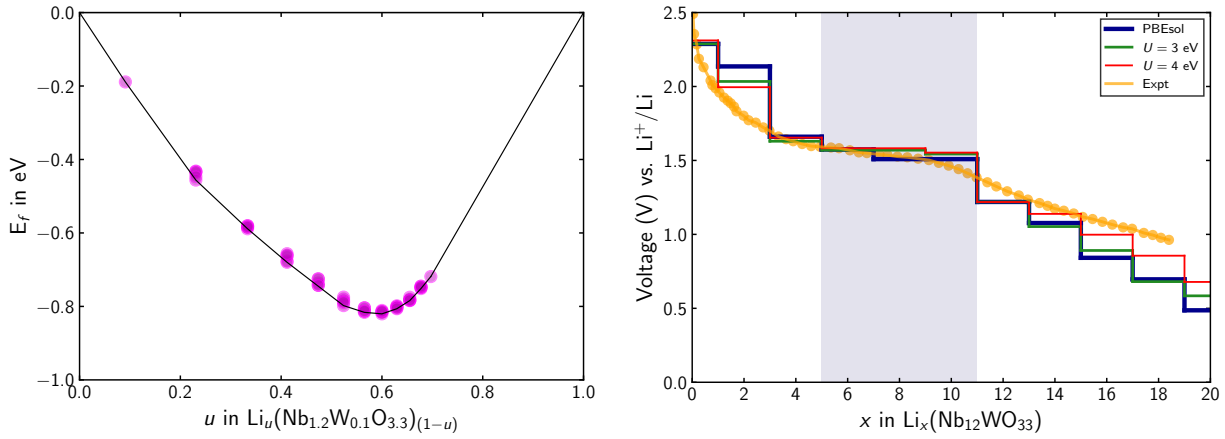

(a) (b)

Figure A.1: (a) Convex hull of lowest energy $Li_xNb_{12}WO_{33}$ structures. At every stoichiometry, structures on the convex hull tieline or very close to it can be found. (b) Comparison of DFT predicted voltage profiles to an experimental profile (Ref. [99]). The DFT predicted profiles have been shifted so that experimental and DFT predictions for the average insertion voltages agree.

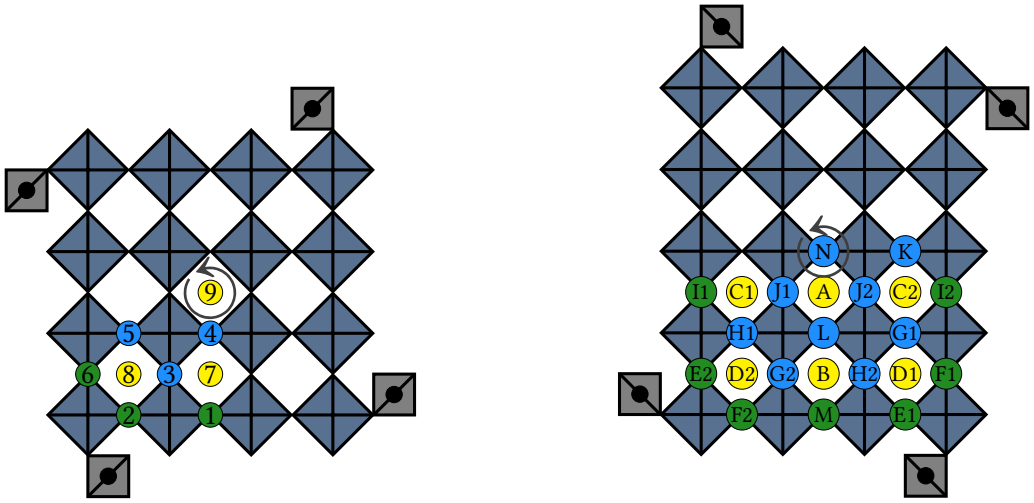

(a) $Nb_{14}W_3O_{44}$ (b) $Nb_{16}W_5O_{55}$

Figure A.2: Labelling convention for lithium positions in $Nb_{14}W_3O_{44}$ and $Nb_{16}W_5O_{55}$. Lithium sites in single blocks of (a) $Nb_{14}W_3O_{44}$, and (b) $Nb_{16}W_5O_{55}$ that were included in this study. Horizontal and vertical window positions (yellow and blue) are fourfold coordinated by oxygens, pocket positions (green) fivefold. Circling arrows mark the twofold ($Nb_{16}W_5O_{55}$) or fourfold ($Nb_{14}W_3O_{44}$) rotation axes of the parent crystal structures, which are perpendicular to the block plane.

Site in $Nb_{12}WO_{33}$	E_f
1	-2.10 eV
2	-2.06 eV
3	-2.06 eV
3	-2.06 eV
4	-2.06 eV
5	-2.07 eV
6	-2.10 eV
7	-2.09 eV
8	-2.15 eV
9	-2.11 eV
10	-2.12 eV
11	-2.06 eV
12	-2.17 eV

Site in $Nb_{14}W_3O_{44}$	E_f
1	-2.19 eV
2	-2.05 eV
3	-2.05 eV
4	-2.14 eV
5	-2.05 eV
6	-2.13 eV
7	-2.12 eV
8	-2.16 eV
9	-2.18 eV

Site in $Nb_{16}W_5O_{55}$	E_f
A	-2.27 eV
B	-2.35 eV
C1	-2.26 eV
C2	-2.33 eV
D1	-2.39 eV
D2	-2.30 eV
E1	-2.22 eV
E2	-2.28 eV
F1	-2.40 eV
F2	-2.36 eV
G1	-2.30 eV
G2	-2.08 eV
H1	-2.10 eV
H2	-2.28 eV
I1	-2.45 eV
I2	-2.45 eV
J1	-2.25 eV
J2	-2.39 eV
K	-1.85 eV
L	-2.41 eV
M	-2.41 eV
N	-2.09 eV

Table A.2: Lithium site energies in $Nb_{12}WO_{33}$, $Nb_{14}W_3O_{44}$, and $Nb_{16}W_5O_{55}$. The E_f values for $Nb_{12}WO_{33}$ were obtained as described in the main text. The E_f values for positions 1-8 in $Nb_{14}W_3O_{44}$ and A-M in $Nb_{16}W_5O_{55}$ were obtained by placing two lithium ions in the primitive cell under constraints of the crystal symmetry. For the special positions 9 and N, a single lithium ion was used.

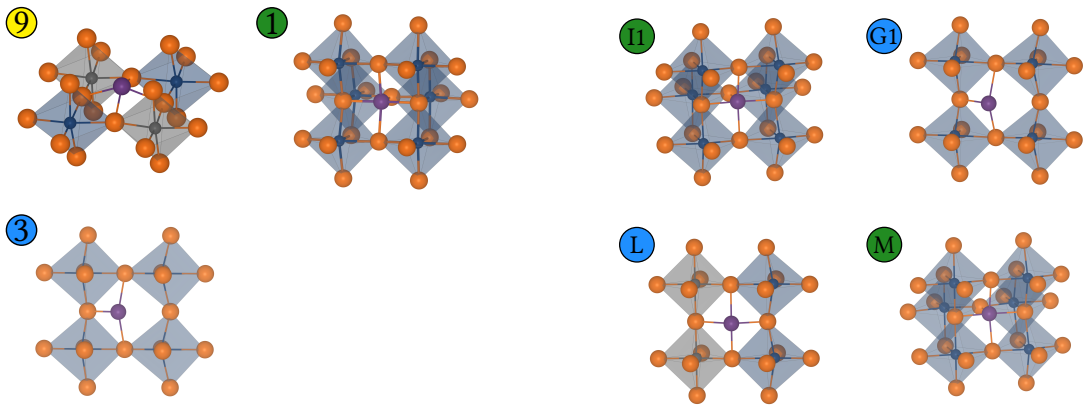

(a) $Nb_{14}W_3O_{44}$ (b) $Nb_{16}W_5O_{55}$

Figure A.3: Examples of local structure of lithium sites in (a) $Nb_{14}W_3O_{44}$ and (b) $Nb_{16}W_5O_{55}$. Note the strong similarity between all three niobium-tungsten oxides (cf. Fig. 4, main text).

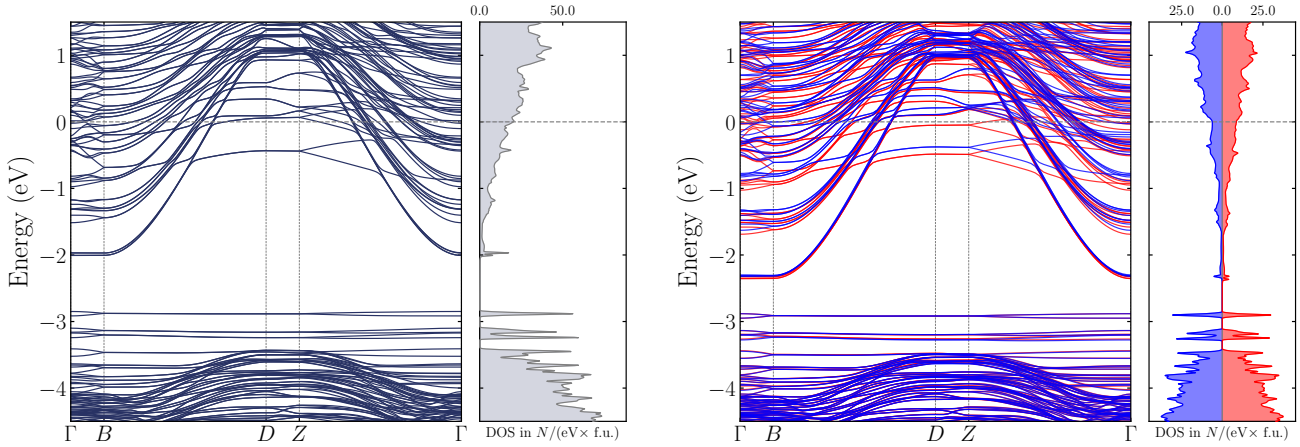

(a) PBEsol

(b) PBEsol+U

Figure A.4: Electronic structure of $Li_{16}Nb_{14}W_3O_{44}$. At the GGA level (a) no spin polarisation is observed. Inclusion of a U value on the metal d orbitals (b) does not lead to the opening of a bandgap. The multitude of strongly dispersive bands suggests a good electronic conductivity of the material. Red and blue correspond to spin up and down bands.

References

[1] The Faraday Institution. https://faraday.ac.uk/.

[2] Dunn, B.; Kamath, H.; Tarascon, J.M. Electrical Energy Storage for the Grid: A Battery of Choices. *Science* **334**, 928–935 (2011).

[3] Urban, A.; Seo, D.H.; Ceder, G. Computational Understanding of Li-Ion Batteries. *npj Computational Materials* **2**, npjcompumats20162 (2016).

[4] Van der Ven, A.; Deng, Z.; Banerjee, S.; Ong, S.P. Rechargeable Alkali-Ion Battery Materials: Theory and Computation. *Chemical Reviews* (2020).

[5] Goodenough, J.B.; Abruña, H.D.; Buchanan, M. Basic Research Needs for Electrical Energy Storage. Tech. rep., US Department of Energy, Office of Science (2007).

[6] Palacín, M.R. Recent Advances in Rechargeable Battery Materials: A Chemist's Perspective. *Chemical Society Reviews* **38**, 2565–2575 (2009).

[7] Mayo, M.; Griffith, K.J.; Pickard, C.J.; Morris, A.J. Ab Initio Study of Phosphorus Anodes for Lithium- and Sodium-Ion Batteries. *Chemistry of Materials* **28**, 2011–2021 (2016).

[8] Bard, A.J.; Faulkner, L.R. *Electrochemical Methods: Fundamentals and Applications*. Wiley, New York, 2nd ed edn. (2001).

[9] McKinnon, W.R. Insertion Electrodes I: Atomic and Electronic Structure of the Hosts and Their Insertion Compounds. In P.G. Bruce, ed., *Solid State Electrochemistry*, 163–198. Cambridge University Press, Cambridge (1994).

[10] Mayo, M.; Morris, A.J. Structure Prediction of Li–Sn and Li–Sb Intermetallics for Lithium-Ion Batteries Anodes. *Chemistry of Materials* **29**, 5787–5795 (2017).

[11] Stratford, J.M.; Mayo, M.; Allan, P.K.; Pecher, O.; Borkiewicz, O.J.; *et al.* Investigating Sodium Storage Mechanisms in Tin Anodes: A Combined Pair Distribution Function Analysis, Density Functional Theory, and Solid-State NMR Approach. *Journal of the American Chemical Society* **139**, 7273–7286 (2017).

[12] Butala, M.M.; Mayo, M.; Doan-Nguyen, V.V.T.; Lumley, M.A.; Göbel, C.; *et al.* Local Structure Evolution and Modes of Charge Storage in Secondary Li–FeS_2 Cells. *Chemistry of Materials* **29**, 3070–3082 (2017).

[13] Griffith, K.J.; Wiaderek, K.M.; Cibin, G.; Marbella, L.E.; Grey, C.P. Niobium Tungsten Oxides for High-Rate Lithium-Ion Energy Storage. *Nature* **559**, 556–563 (2018).

[14] Henriksen, N.E.; Hansen, F.Y. *Theories of Molecular Reaction Dynamics: The Microscopic Foundation of Chemical Kinetics*. Oxford Graduate Texts. Oxford University Press, Oxford ; New York (2008).

[15] Van der Ven, A.; Ceder, G.; Asta, M.; Tepesch, P.D. First-Principles Theory of Ionic Diffusion with Nondilute Carriers. *Physical Review B* **64** (2001).

[16] Heitjans, P.; Kärger, J., eds. *Diffusion in Condensed Matter*. Springer-Verlag, Berlin/Heidelberg (2005).

[17] Roth, R.S.; Wadsley, A.D. Multiple Phase Formation in the Binary System Nb_2O_5–WO_3. I. Preparation and Identification of Phases. *Acta Crystallographica* **19**, 26–32 (1965).

[18] Roth, R.S.; Wadsley, A.D. Multiple Phase Formation in the Binary System Nb_2O_5-WO_3. II. The Structure of the Monoclinic Phases $WNb_{12}O_{33}$ and $W_5Nb_{16}O_{55}$. *Acta Crystallographica* **19**, 32–38 (1965).

[19] Roth, R.S.; Wadsley, A.D. Multiple Phase Formation in the Binary System Nb_2O_5-WO_3. III. The Structures of the Tetragonal Phases $W_3Nb_{14}O_{44}$ and $W_8Nb_{18}O_{69}$. *Acta Crystallographica* **19**, 38–42 (1965).

[20] Roth, R.S.; Wadsley, A.D. Multiple Phase Formation in the Binary System Nb_2O_5–WO $_3$. IV. The Block Principle. *Acta Crystallographica* **19**, 42–47 (1965).

[21] Cava, R.J.; Murphy, D.W.; Zahurak, S.M. Lithium Insertion in Wadsley-Roth Phases Based on Niobium Oxide. *Journal of The Electrochemical Society* **130**, 2345–2351 (1983).

[22] Cava, R.J.; Santoro, A.; Murphy, D.W.; Zahurak, S.; Roth, R.S. Structural Aspects of Lithium Insertion in Oxides: Li_xReO_3 and $Li_2FeV_3O_8$. *Solid State Ionics* **5**, 323–326 (1981).

[23] Cava, R.J.; Batlogg, B.; Krajewski, J.J.; Gammel, P.; Poulsen, H.F.; *et al.* Antiferromagnetism and Metallic Conductivity in $Nb_{12}O_{29}$. *Nature* **350**, 598 (1991).

[24] Cava, R.J.; Batlogg, B.; Krajewski, J.J.; Poulsen, H.F.; Gammel, P.; *et al.* Electrical and Magnetic Properties of $Nb_2O_{5-\delta}$ Crystallographic Shear Structures. *Physical Review B* **44**, 6973–6981 (1991).

[25] Rüscher, C.; Salje, E.; Hussain, A. The Effect of High Polaron Concentration on the Polaron Transport in $NbO_{2.5-x}$: Optical and Electrical Properties. *Journal of Physics C: Solid State Physics* **21**, 3737 (1988).

[26] Rüscher, C.H.; Nygren, M. Magnetic Properties of Phases Possessing Block Type Structures in the Nb_2O_{5-2x} System, with $0 \leq x \leq 0.083$. *Journal of Physics: Condensed Matter* **3**, 3997 (1991).

[27] Rüscher, C. The Structural Effect on the Electrical Properties of $NbO_{2.5-x}$ Block-Type Compounds. *Physica C: Superconductivity* **200**, 129–139 (1992).

[28] Han, J.T.; Goodenough, J.B. 3-V Full Cell Performance of Anode Framework $TiNb_2O_7$/Spinel $LiNi_{0.5}Mn_{1.5}O_4$. *Chemistry of Materials* **23**, 3404–3407 (2011).

[29] Takami, N.; Ise, K.; Harada, Y.; Iwasaki, T.; Kishi, T.; *et al.* High-Energy, Fast-Charging, Long-Life Lithium-Ion Batteries Using $TiNb_2O_7$ Anodes for Automotive Applications. *Journal of Power Sources* **396**, 429–436 (2018).

[30] Kohanoff, J. *Electronic Structure Calculations for Solids and Molecules.* Cambridge University Press, Cambridge (2006).

[31] Martin, R.M. *Electronic Structure: Basic Theory and Practical Methods.* Cambridge University Press, Cambridge (2004).

[32] Capelle, K. A Bird's-Eye View of Density-Functional Theory. *arXiv:cond-mat/0211443* (2002).

[33] Martin, R.M.; Reining, L.; Ceperley, D.M. *Interacting Electrons: Theory and Computational Approaches.* Cambridge University Press, Cambridge (2016).

[34] Paul, A.; Birol, T. Applications of DFT+DMFT in Materials Science. *Annual Review of Materials Research* **49**, 31–52 (2019).

[35] Haule, K. Structural Predictions for Correlated Electron Materials Using the Functional Dynamical Mean Field Theory Approach. *Journal of the Physical Society of Japan* **87**, 041005 (2018).

[36] Kotliar, G.; Vollhardt, D. Strongly Correlated Materials: Insights From Dynamical Mean-Field Theory. *Physics Today* **57**, 53–59 (2004).

[37] Riley, K.F.; Hobson, M.P.; Bence, S.J. *Mathematical Methods for Physics and Engineering.* Cambridge University Press, Cambridge, 3rd edn. (2006).

[38] Hohenberg, P.; Kohn, W. Inhomogeneous Electron Gas. *Physical Review* **136**, B864–B871 (1964).

[39] Levy, M. Universal Variational Functionals of Electron Densities, First-Order Density Matrices, and Natural Spin-Orbitals and Solution of the v-Representability Problem. *Proceedings of the National Academy of Sciences* **76**, 6062–6065 (1979).

[40] Ceperley, D.M.; Alder, B.J. Ground State of the Electron Gas by a Stochastic Method. *Physical Review Letters* **45**, 566–569 (1980).

[41] Perdew, J.P.; Zunger, A. Self-Interaction Correction to Density-Functional Approximations for Many-Electron Systems. *Physical Review B* **23**, 5048–5079 (1981).

[42] Perdew, J.P.; Burke, K.; Ernzerhof, M. Generalized Gradient Approximation Made Simple. *Physical Review Letters* **77**, 3865–3868 (1996).

[43] Sun, J.; Ruzsinszky, A.; Perdew, J.P. Strongly Constrained and Appropriately Normed Semilocal Density Functional. *Physical Review Letters* **115** (2015).

[44] Heyd, J.; Scuseria, G.E.; Ernzerhof, M. Hybrid Functionals Based on a Screened Coulomb Potential. *The Journal of Chemical Physics* **118**, 8207–8215 (2003).

[45] Perdew, J.P.; Ernzerhof, M.; Burke, K. Rationale for Mixing Exact Exchange with Density Functional Approximations. *The Journal of Chemical Physics* **105**, 9982–9985 (1996).

[46] Bloch, F. Über die Quantenmechanik der Elektronen in Kristallgittern. *Zeitschrift für Physik* **52**, 555–600 (1929).

[47] Monkhorst, H.J.; Pack, J.D. Special Points for Brillouin-Zone Integrations. *Physical Review B* **13**, 5188–5192 (1976).

[48] Metzner, W.; Vollhardt, D. Correlated Lattice Fermions in d = Infinity Dimensions. *Physical Review Letters* **62**, 324–327 (1989).

[49] Georges, A.; Kotliar, G. Hubbard Model in Infinite Dimensions. *Physical Review B* **45**, 6479–6483 (1992).

[50] Haule, K. Exact Double Counting in Combining the Dynamical Mean Field Theory and the Density Functional Theory. *Physical Review Letters* **115**, 196403 (2015).

[51] Kato, K.; Tamura, S. Die Kristallstruktur von T-Nb_2O_5. *Acta Crystallographica Section B: Structural Crystallography and Crystal Chemistry* **31**, 673–677 (1975).

[52] Kato, K. Structure Refinement of H-Nb_2O_5. *Acta Crystallographica Section B: Structural Crystallography and Crystal Chemistry* **32**, 764–767 (1976).

[53] Schäfer, H.; Gruehn, R.; Schulte, F. The Modifications of Niobium Pentoxide. *Angewandte Chemie International Edition in English* **5**, 40–52 (1966).

[54] Kunz, M.; Brown, I.D. Out-of-Center Distortions around Octahedrally Coordinated D^0 Transition Metals. *Journal of Solid State Chemistry* **115**, 395–406 (1995).

[55] Bersuker, I. *The Jahn–Teller Effect*. Cambridge University Press, Cambridge (2006).

[56] Andersen, E.N.; Klimczuk, T.; Miller, V.L.; Zandbergen, H.W.; Cava, R.J. Nanometer Structural Columns and Frustration of Magnetic Ordering in $Nb_{12}O_{29}$. *Physical Review B* **72**, 033413 (2005).

[57] McQueen, T.; Xu, Q.; Andersen, E.; Zandbergen, H.; Cava, R. Structures of the Reduced Niobium Oxides Nb12O29 and Nb22O54. *Journal of Solid State Chemistry* **180**, 2864–2870 (2007).

[58] Lappas, A.; Waldron, J.E.L.; Green, M.A.; Prassides, K. Magnetic Ordering in the Charge-Ordered $Nb_{12}O_{29}$. *Physical Review B* **65**, 134405 (2002).

[59] Cheng, J.G.; Zhou, J.S.; Goodenough, J.B.; Zhou, H.D.; Wiebe, C.R.; *et al.* Spin Fluctuations in the Antiferromagnetic Metal $Nb_{12}O_{29}$. *Physical Review B* **80**, 134428 (2009).

[60] Fang, C.M.; van Huis, M.A.; Xu, Q.; Cava, R.J.; Zandbergen, H.W. Unexpected Origin of Magnetism in Monoclinic $Nb_{12}O_{29}$ from First-Principles Calculations. *Journal of Materials Chemistry C* **3**, 651–657 (2014).

[61] Lee, K.W.; Pickett, W.E. Organometalliclike Localization of $4d$-Derived Spins in an Inorganic Conducting Niobium Suboxide. *Physical Review B* **91**, 195152 (2015).

[62] Li, R.; Qin, Y.; Liu, X.; Yang, L.; Lin, C.; *et al.* Conductive $Nb_{25}O_{62}$ and $Nb_{12}O_{29}$ Anode Materials for Use in High-Performance Lithium-Ion Storage. *Electrochimica Acta* **266**, 202–211 (2018).

[63] Waldron, J.E.L.; Green, M.A.; Neumann, D.A. Structure and Electronic Properties of Monoclinic Nb12O29. *Journal of Physics and Chemistry of Solids* **65**, 79–86 (2004).

[64] Clark, S.J.; Segall, M.D.; Pickard, C.J.; Hasnip, P.J.; Probert, M.I.J.; *et al.* First Principles Methods Using CASTEP. *Zeitschrift für Kristallographie - Crystalline Materials* **220**, 567–570 (2005).

[65] Hamann, D.R.; Schlüter, M.; Chiang, C. Norm-Conserving Pseudopotentials. *Physical Review Letters* **43**, 1494–1497 (1979).

[66] Vanderbilt, D. Soft Self-Consistent Pseudopotentials in a Generalized Eigenvalue Formalism. *Physical Review B* **41**, 7892–7895 (1990).

[67] Hellenbrandt, M. The Inorganic Crystal Structure Database (ICSD)—Present and Future. *Crystallography Reviews* **10**, 17–22 (2004).

[68] Koçer, C.P.; Griffith, K.J.; Grey, C.P.; Morris, A.J. First-Principles Study of Localized and Delocalized Electronic States in Crystallographic Shear Phases of Niobium Oxide. *Physical Review B* **99**, 075151 (2019).

[69] Dudarev, S.L.; Botton, G.A.; Savrasov, S.Y.; Humphreys, C.J.; Sutton, A.P. Electron-Energy-Loss Spectra and the Structural Stability of Nickel Oxide: An LSDA+U Study. *Physical Review B* **57**, 1505–1509 (1998).

[70] Nahm, H.H.; Park, C.H. First-Principles Study of Microscopic Properties of the Nb Antisite in $LiNbO_3$: Comparison to Phenomenological Polaron Theory. *Physical Review B* **78**, 184108 (2008).

[71] Hinuma, Y.; Pizzi, G.; Kumagai, Y.; Oba, F.; Tanaka, I. Band Structure Diagram Paths Based on Crystallography. *Computational Materials Science* **128**, 140–184 (2017).

[72] Togo, A.; Tanaka, I. Spglib: A Software Library for Crystal Symmetry Search. *arXiv:1808.01590 [cond-mat]* (2018).

[73] Morris, A.J.; Nicholls, R.J.; Pickard, C.J.; Yates, J.R. OptaDOS: A Tool for Obtaining Density of States, Core-Level and Optical Spectra from Electronic Structure Codes. *Computer Physics Communications* **185**, 1477–1485 (2014).

[74] Pickard, C.J.; Payne, M.C. Extrapolative Approaches to Brillouin-Zone Integration. *Physical Review B* **59**, 4685–4693 (1999).

[75] Pickard, C.J.; Payne, M.C. Second-Order k · p Perturbation Theory with Vanderbilt Pseudopotentials and Plane Waves. *Physical Review B* **62**, 4383–4388 (2000).

[76] Rutter, M.J. C2x: A Tool for Visualisation and Input Preparation for Castep and Other Electronic Structure Codes. *Computer Physics Communications* **225**, 174–179 (2018).

[77] Momma, K.; Izumi, F. VESTA 3 for Three-Dimensional Visualization of Crystal, Volumetric and Morphology Data. *Journal of Applied Crystallography* **44**, 1272–1276 (2011).

[78] Evans, M.L.; Morris, A.J. Matador: A Python Library for Analysing, Curating and Performing High-Throughput Density-Functional Theory Calculations. *Journal of Open Source Software* **5**, 2563 (2020).

[79] Fonari, A. Afonari/Emc. https://github.com/afonari/emc.

[80] Walkingshaw, A.D.; Spaldin, N.A.; Artacho, E. Density-Functional Study of Charge Doping in WO_3. *Physical Review B* **70**, 165110 (2004).

[81] Griffith, K.J.; Forse, A.C.; Griffin, J.M.; Grey, C.P. High-Rate Intercalation without Nanostructuring in Metastable Nb_2O_5 Bronze Phases. *Journal of the American Chemical Society* **138**, 8888–8899 (2016).

[82] Waldron, J.E.L.; Green, M.A.; Neumann, D.A. Charge and Spin Ordering in Monoclinic $Nb_{12}O_{29}$. *Journal of the American Chemical Society* **123**, 5833–5834 (2001).

[83] Imada, M.; Fujimori, A.; Tokura, Y. Metal-Insulator Transitions. *Rev. Mod. Phys.* **70**, 225 (1998).

[84] Allpress, J.G. The Direct Observation of Structural Features and Defects in Complex Oxides by Two-Dimensional Lattice Imaging. *Materials Research Bulletin* **4**, 707–720 (1969).

[85] Anderson, J.S.; Browne, J.M.; Cheetham, A.K.; Dreele, R.V.; Hutchison, J.L.; *et al.* Point Defects and Extended Defects in Niobium Oxides. *Nature* **243**, 81–83 (1973).

[86] Roth, R.S.; Wadsley, A.D. Mixed Oxides of Titanium and Niobium: The Crystal Structure of $TiNb_{24}O_{62}$(TiO_2 - 12 Nb_2O_5). *Acta Crystallographica* **18**, 724–730 (1965).

[87] Wadsley, A.D. Mixed Oxides of Titanium and Niobium. I. *Acta Crystallographica* **14**, 660–664 (1961).

[88] Wadsley, A.D. Mixed Oxides of Titanium and Niobium. II. The Crystal Structures of the Dimorphic Forms Ti_2 $Nb_{10}O_{29}$. *Acta Crystallographica* **14**, 664–670 (1961).

[89] Guo, B.; Yu, X.; Sun, X.G.; Chi, M.; Qiao, Z.A.; *et al.* A Long-Life Lithium-Ion Battery with a Highly Porous $TiNb_2O_7$ Anode for Large-Scale Electrical Energy Storage. *Energy Environ. Sci.* **7**, 2220–2226 (2014).

[90] Preefer, M.B.; Saber, M.; Wei, Q.; Bashian, N.H.; Bocarsly, J.D.; *et al.* Multielectron Redox and Insulator-to-Metal Transition upon Lithium Insertion in the Fast-Charging, Wadsley-Roth Phase PNb9O25. *Chemistry of Materials* **32**, 4553–4563 (2020).

[91] Salje, E.; Güttler, B. Anderson Transition and Intermediate Polaron Formation in WO_{3-x} Transport Properties and Optical Absorption. *Philosophical Magazine B* **50**, 607–620 (1984).

[92] Chen, Z.; Belharouak, I.; Sun, Y.K.; Amine, K. Titanium-Based Anode Materials for Safe Lithium-Ion Batteries. *Advanced Functional Materials* **23**, 959–969 (2013).

[93] Wagemaker, M.; Mulder, F.M. Properties and Promises of Nanosized Insertion Materials for Li-Ion Batteries. *Accounts of Chemical Research* **46**, 1206–1215 (2013).

[94] Griffith, K.J.; Senyshyn, A.; Grey, C.P. Structural Stability from Crystallographic Shear in TiO_2–Nb_2O_5 Phases: Cation Ordering and Lithiation Behavior of $TiNb_{24}O_{62}$. *Inorganic Chemistry* **56**, 4002–4010 (2017).

[95] Lu, X.; Jian, Z.; Fang, Z.; Gu, L.; Hu, Y.S.; *et al.* Atomic-Scale Investigation on Lithium Storage Mechanism in $TiNb_2O_7$,. *Energy & Environmental Science* **4**, 2638–2644 (2011).

[96] Cheng, Q.; Liang, J.; Zhu, Y.; Si, L.; Guo, C.; *et al.* Bulk $Ti_2Nb_{10}O_{29}$ as Long-Life and High-Power Li-Ion Battery Anodes. *J. Mater. Chem. A* **2**, 17258–17262 (2014).

[97] Wu, X.; Miao, J.; Han, W.; Hu, Y.S.; Chen, D.; *et al.* Investigation on $Ti_2Nb_{10}O_{29}$ Anode Material for Lithium-Ion Batteries. *Electrochemistry Communications* **25**, 39–42 (2012).

[98] Saritha, D.; Pralong, V.; Varadaraju, U.V.; Raveau, B. Electrochemical Li Insertion Studies on $WNb_{12}O_{33}$—A Shear ReO_3 Type Structure. *Journal of Solid State Chemistry* **183**, 988–993 (2010).

[99] Yan, L.; Lan, H.; Yu, H.; Qian, S.; Cheng, X.; *et al.* Electrospun $WNb_{12}O_{33}$ Nanowires: Superior Lithium Storage Capability and Their Working Mechanism. *Journal of Materials Chemistry A* **5**, 8972–8980 (2017).

[100] Fuentes, A.F.; Garza, E.B.; de la Cruz, A.M.; Torres-Martínez, L.M. Lithium and Sodium Insertion in $W_3Nb_{14}O_{44}$, a Block Structure Type Phase. *Solid state ionics* **93**, 245–253 (1997).

[101] Yan, L.; Shu, J.; Li, C.; Cheng, X.; Zhu, H.; *et al.* $W_3Nb_{14}O_{44}$ Nanowires: Ultrastable Lithium Storage Anode Materials for Advanced Rechargeable Batteries. *Energy Storage Materials* **16**, 535–544 (2019).

[102] Li, Y.; Sun, C.; Goodenough, J.B. Electrochemical Lithium Intercalation in Monoclinic $Nb_{12}O_{29}$. *Chemistry of Materials* **23**, 2292–2294 (2011).

[103] Patoux, S.; Dolle, M.; Rousse, G.; Masquelier, C. A Reversible Lithium Intercalation Process in an ReO_3 Type Structure PNb_9O_{25}. *Journal of The Electrochemical Society* **149**, A391–A400 (2002).

[104] Cheetham, A.K.; Dreele, R.B.V. Cation Distributions in Niobium Oxide Block Structures. *Nature Physical Science* **244**, 139–140 (1973).

[105] Grau-Crespo, R.; Hamad, S.; Catlow, C.R.A.; de Leeuw, N.H. Symmetry-Adapted Configurational Modelling of Fractional Site Occupancy in Solids. *Journal of Physics: Condensed Matter* **19**, 256201 (2007).

[106] Cheetham, A.K.; Allen, N.C. Cation Distribution in the Complex Oxide, $W_3Nb_{14}O_{44}$; a Time-of-Flight Neutron Diffraction Study. *Journal of the Chemical Society, Chemical Communications* **0**, 1370–1372 (1983).

[107] Perdew, J.P.; Ruzsinszky, A.; Csonka, G.I.; Vydrov, O.A.; Scuseria, G.E.; *et al.* Restoring the Density-Gradient Expansion for Exchange in Solids and Surfaces. *Physical Review Letters* **100**, 136406 (2008).

[108] Bartók, A.P.; Yates, J.R. Regularized SCAN Functional. *The Journal of Chemical Physics* **150**, 161101 (2019).

[109] Bartók, A.P.; Yates, J.R. Ultrasoft Pseudopotentials with Kinetic Energy Density Support: Implementing the Tran-Blaha Potential. *Physical Review B* **99**, 235103 (2019).

[110] Aydinol, M.K.; Kohan, A.F.; Ceder, G.; Cho, K.; Joannopoulos, J. Ab Initio Study of Lithium Intercalation in Metal Oxides and Metal Dichalcogenides. *Physical Review B* **56**, 1354–1365 (1997).

[111] Evans, M. Ml-Evs / Matador. https://bitbucket.org/ml-evs/matador.

[112] Sears, V.F. Neutron Scattering Lengths and Cross Sections. *Neutron News* **3**, 26–37 (1992).

[113] Koçer, C.P.; Griffith, K.J.; Grey, C.P.; Morris, A.J. Cation Disorder and Lithium Insertion Mechanism of Wadsley–Roth Crystallographic Shear Phases from First Principles. *Journal of the American Chemical Society* **141**, 15121–15134 (2019).

[114] Robinson, K.; Gibbs, G.V.; Ribbe, P.H. Quadratic Elongation: A Quantitative Measure of Distortion in Coordination Polyhedra. *Science* **172**, 567–570 (1971).

[115] Ok, K.M.; Halasyamani, P.S.; Casanova, D.; Llunell, M.; Alemany, P.; *et al.* Distortions in Octahedrally Coordinated D^0 Transition Metal Oxides: A Continuous Symmetry Measures Approach. *Chemistry of Materials* **18**, 3176–3183 (2006).

[116] Catti, M.; Ghaani, M.R. On the Lithiation Reaction of Niobium Oxide: Structural and Electronic Properties of $Li_{1.714}Nb_2O_5$. *Physical Chemistry Chemical Physics* **16**, 1385–1392 (2013).

[117] Catti, M.; Pinus, I.; Knight, K. Lithium Insertion Properties of $Li_xTiNb_2O_7$ Investigated by Neutron Diffraction and First-Principles Modelling. *Journal of Solid State Chemistry* **229**, 19–25 (2015).

[118] Dalton, A.S.; Belak, A.A.; Van der Ven, A. Thermodynamics of Lithium in TiO_2(B) from First Principles. *Chemistry of Materials* **24**, 1568–1574 (2012).

[119] Perdew, J.P.; Yang, W.; Burke, K.; Yang, Z.; Gross, E.K.U.; *et al.* Understanding Band Gaps of Solids in Generalized Kohn–Sham Theory. *Proceedings of the National Academy of Sciences* **114**, 2801–2806 (2017).

[120] Richter, J.H.; Henningsson, A.; Karlsson, P.G.; Andersson, M.P.; Uvdal, P.; *et al.* Electronic Structure of Lithium-Doped Anatase TiO_2 Prepared in Ultrahigh Vacuum. *Physical Review B* **71**, 235418 (2005).

[121] Morgan, B.J.; Watson, G.W. GGA+U Description of Lithium Intercalation into Anatase TiO_2. *Physical Review B* **82**, 144119 (2010).

[122] Maxisch, T.; Zhou, F.; Ceder, G. Ab Initio Study of the Migration of Small Polarons in Olivine Li_xFePO_4 and Their Association with Lithium Ions and Vacancies. *Physical Review B* **73**, 104301 (2006).

[123] Zhong, Q.; Dahn, J.R.; Colbow, K. Lithium Intercalation into WO_3 and the Phase Diagram of Li_xWO_3. *Physical Review B* **46**, 2554–2560 (1992).

[124] Ohno, S.; Helm, B.; Fuchs, T.; Dewald, G.; Kraft, M.A.; *et al.* Further Evidence for Energy Landscape Flattening in the Superionic Argyrodites $Li_{6+x}P_{1-x}M_xS_5I$ (M = Si, Ge, Sn). *Chemistry of Materials* **31**, 4936–4944 (2019).

[125] Liu, Y.; Zhu, Y.; Cui, Y. Challenges and Opportunities towards Fast-Charging Battery Materials. *Nature Energy* **4**, 540–550 (2019).

[126] Lennon, A.; Jiang, Y.; Hall, C.; Lau, D.; Song, N.; *et al.* High-Rate Lithium Ion Energy Storage to Facilitate Increased Penetration of Photovoltaic Systems in Electricity Grids. *MRS Energy & Sustainability* **6**, E2 (2019).

[127] Griffith, K.J.; Grey, C.P. Superionic Lithium Intercalation through 2 Nm by 2 Nm Columns in the Crystallographic Shear Phase $Nb_{18}W_8O_{69}$. *Chemistry of Materials* **32**, 3860–3868 (2020).

[128] Griffith, K.J.; Seymour, I.D.; Hope, M.A.; Butala, M.M.; Lamontagne, L.K.; *et al.* Ionic and Electronic Conduction in $TiNb_2O_7$. *Journal of the American Chemical Society* **141**, 16706–16725 (2019).

[129] Henkelman, G.; Uberuaga, B.P.; Jónsson, H. A Climbing Image Nudged Elastic Band Method for Finding Saddle Points and Minimum Energy Paths. *The Journal of Chemical Physics* **113**, 9901–9904 (2000).

[130] Kresse, G.; Furthmüller, J. Efficient Iterative Schemes for Ab Initio Total-Energy Calculations Using a Plane-Wave Basis Set. *Physical Review B* **54**, 11169–11186 (1996).

[131] Blöchl, P.E. Projector Augmented-Wave Method. *Physical Review B* **50**, 17953–17979 (1994).

[132] Koçer, C.; Griffith, K.; Grey, C.; Morris, A. Lithium Diffusion in Niobium Tungsten Oxide Shear Structures - Supporting Dataset. https://doi.org/10.17863/CAM.51613 (2020).

[133] Henkelman, G. Transition State Tools for VASP. https://theory.cm.utexas.edu/vtsttools/.

[134] Zhu, Z.; Chu, I.H.; Deng, Z.; Ong, S.P. Role of Na^+ Interstitials and Dopants in Enhancing the Na^+ Conductivity of the Cubic Na_3PS_4 Superionic Conductor. *Chemistry of Materials* **27**, 8318–8325 (2015).

[135] Bachman, J.C.; Muy, S.; Grimaud, A.; Chang, H.H.; Pour, N.; *et al.* Inorganic Solid-State Electrolytes for Lithium Batteries: Mechanisms and Properties Governing Ion Conduction. *Chemical Reviews* **116**, 140–162 (2016).

[136] Kotliar, G.; Savrasov, S.Y.; Haule, K.; Oudovenko, V.S.; Parcollet, O.; *et al.* Electronic Structure Calculations with Dynamical Mean-Field Theory. *Reviews of Modern Physics* **78**, 865–951 (2006).

[137] Haule, K.; Birol, T. Free Energy from Stationary Implementation of the DFT+DMFT Functional. *Physical Review Letters* **115**, 256402 (2015).

[138] Haule, K.; Pascut, G.L. Forces for Structural Optimizations in Correlated Materials within a DFT+embedded DMFT Functional Approach. *Physical Review B* **94**, 195146 (2016).

[139] Haule, K.; Pascut, G.L. Mott Transition and Magnetism in Rare Earth Nickelates and Its Fingerprint on the X-Ray Scattering. *Scientific Reports* **7**, 1–7 (2017).

[140] Leonov, I.; Anisimov, V.I.; Vollhardt, D. First-Principles Calculation of Atomic Forces and Structural Distortions in Strongly Correlated Materials. *Physical Review Letters* **112**, 146401 (2014).

[141] Savrasov, S.Y.; Kotliar, G. Linear Response Calculations of Lattice Dynamics in Strongly Correlated Systems. *Physical Review Letters* **90**, 056401 (2003).

[142] Leonov, I.; Poteryaev, A.I.; Anisimov, V.I.; Vollhardt, D. Calculated Phonon Spectra of Paramagnetic Iron at the α-γ Phase Transition. *Physical Review B* **85**, 020401 (2012).

[143] Appelt, W.H.; Östlin, A.; Di Marco, I.; Leonov, I.; Sekania, M.; *et al.* Lattice Dynamics of Palladium in the Presence of Electronic Correlations. *Physical Review B* **101**, 075120 (2020).

[144] Han, Q.; Birol, T.; Haule, K. Phonon Softening Due to Melting of the Ferromagnetic Order in Elemental Iron. *Physical Review Letters* **120**, 187203 (2018).

[145] Lloyd-Williams, J.H.; Monserrat, B. Lattice Dynamics and Electron-Phonon Coupling Calculations Using Nondiagonal Supercells. *Physical Review B* **92**, 184301 (2015).

[146] Haule, K.; Yee, C.H.; Kim, K. Dynamical Mean-Field Theory within the Full-Potential Methods: Electronic Structure of $CeIrIn_5$, $CeCoIn_5$, and $CeRhIn_5$. *Physical Review B* **81**, 195107 (2010).

[147] Haule, K. DFT + Embedded DMFT Functional. http://hauleweb.rutgers.edu/tutorials/.

[148] Werner, P.; Comanac, A.; de' Medici, L.; Troyer, M.; Millis, A.J. Continuous-Time Solver for Quantum Impurity Models. *Physical Review Letters* **97**, 076405 (2006).

[149] Haule, K. Quantum Monte Carlo Impurity Solver for Cluster Dynamical Mean-Field Theory and Electronic Structure Calculations with Adjustable Cluster Base. *Physical Review B* **75**, 155113 (2007).

[150] Blaha, P.; Schwarz, K.; Madsen, G.K.H.; Kvasnicka, D.; Luitz, J.; *et al. WIEN2K, An Augmented Plane Wave + Local Orbitals Program for Calculating Crystal Properties*. Karlheinz Schwarz, Techn. Universität Wien, Austria (2018).

[151] Basinski, Z.S.; Hume-Rothery, W.; Sutton, A.L. The Lattice Expansion of Iron. *Proceedings of the Royal Society of London. Series A, Mathematical and Physical Sciences* **229**, 459–467 (1955).

[152] Sasaki, S.; Fujino, K.; Takéuchi, Y. X-Ray Determination of Electron-Density Distributions in Oxides, MgO, MnO, CoO, and NiO, and Atomic Scattering Factors of Their Constituent Atoms. *Proceedings of the Japan Academy. Ser. B: Physical and Biological Sciences* **55**, 43–48 (1979).

[153] Lan, Y.C.; Chen, X.L.; He, M. Structure, Magnetic Susceptibility and Resistivity Properties of $SrVO_3$. *Journal of Alloys and Compounds* **354**, 95–98 (2003).

[154] Fu, L.; Kornbluth, M.; Cheng, Z.; Marianetti, C.A. Group Theoretical Approach to Computing Phonons and Their Interactions. *Physical Review B* **100**, 014303 (2019).

[155] Ackland, G.J.; Warren, M.C.; Clark, S.J. Practical Methods in *Ab Initio* Lattice Dynamics. *Journal of Physics: Condensed Matter* **9**, 7861–7872 (1997).

[156] Kunc, K.; Martin, R.M. Ab Initio Force Constants of GaAs: A New Approach to Calculation of Phonons and Dielectric Properties. *Physical Review Letters* **48**, 406–409 (1982).

[157] Wang, Y.; Shang, S.L.; Fang, H.; Liu, Z.K.; Chen, L.Q. First-Principles Calculations of Lattice Dynamics and Thermal Properties of Polar Solids. *npj Computational Materials* **2**, 16006 (2016).

[158] Lichtenstein, A.I.; Katsnelson, M.I.; Kotliar, G. Finite-Temperature Magnetism of Transition Metals: An Ab Initio Dynamical Mean-Field Theory. *Physical Review Letters* **87**, 067205 (2001).

[159] Körmann, F.; Dick, A.; Grabowski, B.; Hickel, T.; Neugebauer, J. Atomic Forces at Finite Magnetic Temperatures: Phonons in Paramagnetic Iron. *Physical Review B* **85**, 125104 (2012).

[160] Körmann, F.; Grabowski, B.; Dutta, B.; Hickel, T.; Mauger, L.; *et al.* Temperature Dependent Magnon-Phonon Coupling in Bcc Fe from Theory and Experiment. *Physical Review Letters* **113**, 165503 (2014).

[161] Ikeda, Y.; Seko, A.; Togo, A.; Tanaka, I. Phonon Softening in Paramagnetic Bcc Fe and Its Relationship to the Pressure-Induced Phase Transition. *Physical Review B* **90**, 134106 (2014).

[162] Neuhaus, J.; Petry, W.; Krimmel, A. Phonon Softening and Martensitic Transformation in α-Fe. *Physica B: Condensed Matter* **234-236**, 897–899 (1997).

[163] Neuhaus, J.; Leitner, M.; Nicolaus, K.; Petry, W.; Hennion, B.; *et al.* Role of Vibrational Entropy in the Stabilization of the High-Temperature Phases of Iron. *Physical Review B* **89**, 184302 (2014).

[164] Anisimov, V.I.; Belozerov, A.S.; Poteryaev, A.I.; Leonov, I. Rotationally Invariant Exchange Interaction: The Case of Paramagnetic Iron. *Physical Review B* **86**, 035152 (2012).

[165] Sakai, S.; Arita, R.; Held, K.; Aoki, H. Quantum Monte Carlo Study for Multiorbital Systems with Preserved Spin and Orbital Rotational Symmetries. *Physical Review B* **74**, 155102 (2006).

[166] Mandal, S.; Haule, K.; Rabe, K.M.; Vanderbilt, D. Systematic Beyond-DFT Study of Binary Transition Metal Oxides. *npj Computational Materials* **5**, 115 (2019).

[167] Reichardt, W.; Wagner, V.; Kress, W. Lattice Dynamics of NiO. *Journal of Physics C: Solid State Physics* **8**, 3955–3962 (1975).

[168] Massidda, S.; Posternak, M.; Baldereschi, A.; Resta, R. Noncubic Behavior of Antiferromagnetic Transition-Metal Monoxides with the Rocksalt Structure. *Physical Review Letters* **82**, 430–433 (1999).

[169] Wang, Y.; Saal, J.E.; Wang, J.J.; Saengdeejing, A.; Shang, S.L.; *et al.* Broken Symmetry, Strong Correlation, and Splitting between Longitudinal and Transverse Optical Phonons of MnO and NiO from First Principles. *Physical Review B* **82**, 081104 (2010).

[170] Chung, E.M.L.; Paul, D.M.; Balakrishnan, G.; Lees, M.R.; Ivanov, A.; *et al.* Role of Electronic Correlations on the Phonon Modes of MnO and NiO. *Physical Review B* **68**, 140406 (2003).

[171] Coy, R.A.; Tompson, C.W.; Gürmen, E. Phonon Dispersion in NiO. *Solid State Communications* **18**, 845–847 (1976).

[172] Stanislavchuk, T.N.; Pascut, G.L.; Litvinchuk, A.P.; Liu, Z.; Choi, S.; *et al.* Spectroscopic and First Principle DFT+eDMFT Study of Complex Structural, Electronic, and Vibrational Properties of $M_2Mo_3O_8$ (M=Fe, Mn) Polar Magnets. *Physical Review B* **102**, 115139 (2020).

[173] Pascut, G.L.; Haule, K. Role of Orbital Selectivity on Crystal Structures and Electronic States in $BiMnO_3$ and $LaMnO_3$ Perovskites. *arXiv:2005.12179 [cond-mat]* (2020).

[174] Gielisse, P.J.; Plendl, J.N.; Mansur, L.C.; Marshall, R.; Mitra, S.S.; *et al.* Infrared Properties of NiO and CoO and Their Mixed Crystals. *Journal of Applied Physics* **36**, 2446–2450 (1965).

[175] Plendl, J.N.; Mansur, L.C.; Mitra, S.S.; Chang, I.F. Reststrahlen Spectrum of MnO. *Solid State Communications* **7**, 109–111 (1969).

[176] Wagner, V.; Reichardt, W.; Kress, W. Lattice Dynamics of MnO. *Proc. Conf. Neutron Scattering* 175 (1976).

[177] Wdowik, U.D.; Legut, D. *Ab Initio* Lattice Dynamics of MnO. *Journal of Physics: Condensed Matter* **21**, 275402 (2009).

[178] Floris, A.; de Gironcoli, S.; Gross, E.K.U.; Cococcioni, M. Vibrational Properties of MnO and NiO from DFT+U-Based Density Functional Perturbation Theory. *Physical Review B* **84**, 161102 (2011).

[179] Linnera, J.; Karttunen, A.J. Lattice Dynamical Properties of Antiferromagnetic MnO, CoO, and NiO, and the Lattice Thermal Conductivity of NiO. *Physical Review B* **100**, 144307 (2019).

[180] Sekiyama, A.; Fujiwara, H.; Imada, S.; Suga, S.; Eisaki, H.; *et al.* Mutual Experimental and Theoretical Validation of Bulk Photoemission Spectra of $Sr_{1-x}Ca_xVO_3$. *Physical Review Letters* **93**, 156402 (2004).

[181] Haule, K.; Birol, T.; Kotliar, G. Covalency in Transition-Metal Oxides within All-Electron Dynamical Mean-Field Theory. *Physical Review B* **90**, 075136 (2014).

[182] Gutmann, M.J.; Graziano, G.; Mukhopadhyay, S.; Refson, K.; von Zimmermann, M. Computation of Diffuse Scattering Arising from One-Phonon Excitations in a Neutron Time-of-Flight Single-Crystal Laue Diffraction Experiment. *Journal of Applied Crystallography* **48**, 1122–1129 (2015).

[183] Girard, A.; Ilakovac, V.; Stekiel, M.; Morgenroth, W.; Berger, H.; *et al.* Soft-Phonon Driven Hexagonal-Orthorhombic Phase Transition in $BaVS_3$. *Physical Review B* **99**, 144104 (2019).

[184] Li, R.; Liang, G.; Zhu, X.; Fu, Q.; Chen, Y.; *et al.* $Mo_3Nb_{14}O_{44}$: A New Li+ Container for High-Performance Electrochemical Energy Storage. *ENERGY & ENVIRONMENTAL MATERIALS* **4**, 65–71 (2021).

[185] George, E.P.; Raabe, D.; Ritchie, R.O. High-Entropy Alloys. *Nature Reviews Materials* **4**, 515–534 (2019).

[186] Lun, Z.; Ouyang, B.; Kwon, D.H.; Ha, Y.; Foley, E.E.; *et al.* Cation-Disordered Rocksalt-Type High-Entropy Cathodes for Li-Ion Batteries. *Nature Materials* **20**, 214–221 (2021).

[187] Monserrat, B. Electron–Phonon Coupling from Finite Differences. *Journal of Physics: Condensed Matter* **30**, 083001 (2018).